A Study of Atmospheric Excitation and Gravity Response to Earth's Wobble

Yuichi AOYAMA

Acknowledgements

This study was preformed under the supervision of Professor Masatsugu Ooe of National Astronomical Observatory (NAO), Mizusawa. I would like to express my cordial gratitude to Professor Isao Naito of NAO, Mizusawa for his many meaningful guidance, continuous encouragement, and valuable discussions on the Earth's rotation dynamics, and Professor Tadahiro Sato of NAO, Mizusawa for his instructive advice, support and helpful suggestions about the gravity. Without their advices this work would not have been successful.

I wish to thank Dr. Yoshiaki Tamura of NAO, Mizusawa for his kindly helps on the data processing, computation and analysis in this study. I am indebted to Professors Katsutada Kaminuma and Kazuo Shibuya of National Institute of Polar Research (NIPR), Professor Toshiyasu Nagao of Tokai University, and Professor Yoshiteru Kono of Kanazawa University for providing the chance to carry out this study.

Fortunately, I could observe the gravity change at Syowa station in Antarctica as a member of 36th Japanese Antarctic Research Expedition (JARE-36) through the many supports by staffs of NIPR and NAO, and other members of JARE-36.

The author wishes to express his appreciation to Drs. Takashi Takanezawa, Tetsuya Iwabuchi, Koji Matsumoto, and Katsushi Chida for frequent, stimulating, and helpful discussions. I am grateful to Drs. N. Kikuchi and T. Ishikawa for their kind help on my analysis.

I also thank the Japan Meteorological Agency (JMA) and the National Centers for Environmental Prediction/National Center for Atmospheric Research (NCEP/NCAR) for the use of the global analysis data sets that have made this work possible, and R. S. Gross for providing SPACE97 data. The superconducting gravimeter (SG) data used in this study were obtained from a global network of SG measurement called GGP-Japan network. We also thank R. Rosen, B. F. Chao, R. D. Ray for discussion and helpful comments.

Finally, I would like to thank my wife, Yukiko Aoyama, and my family who have always been supported me. Without their continuous supports and encouragement, I could not accomplish this work .

Extended Abstract

Wobble and length of day (LOD) change are known as variations in the Earth rotation. The wobble are dominated by two periodic circular motion: the Chandler wobble that is Earth's free motion with a period of about 14 month, and the annual wobble that is forced motion with a period of one year. The wobble and LOD change are observed with a high accuracy by space geodetic techniques for over two decades. On the other hand, those variations perturb the Earth's gravitational potential that affects surface gravity measurements. Such surface gravity change is detected by the superconducting gravimeter (SG) which has very high sensitivity and long-term stability. Precise measurements of wobble, LOD change and gravity changes can provide us valuable information about a dynamics of the whole Earth.

The major dynamical processes causing the wobble and LOD change are mass redistribution and motion of the geophysical fluids on Earth's surface (i.e. the atmosphere, ocean, and hydrosphere), by which angular momentum exchanges arise between the fluids and the solid Earth (the crust and mantle). Seasonal variations in LOD are almost explained by atmospheric contributions, but excitation sources of the annual wobble and the Chandler wobble also remains uncertain. One of this reason is little knowledge about the wind contributions, comparing to those about the pressure contribution. The atmospheric contributions have been discussed through the atmospheric angular momentum (AAM) functions that consist of effects of mass redistribution (pressure contribution) and relative angular momentum (wind contribution), which are calculated from the global objective analysis data in four dimensional data assimilation (4DDA) system for numerical weather prediction.

The solid Earth is deformed by responding to variations in the centrifugal force due to the wobble. This response of the Earth is observed through the gravity change, which is referred to as a gravity response. The gravity response is generally represented by the gravimetric factor and phase, which imply the physical properties of Earth's interior. These parameters concerning the Chandler and annual wobbles are important to investigate Earth's dynamical response to the long-term forcing (several months to years). The surface gravity change, however, contains the gravimetric effects of other dynamical processes besides the

gravity response to the wobble. For the purpose of evaluating the gravity response to the wobble, it is required to separate these effects from the observed gravity change, although there are little knowledge about the gravimetric effects of the geophysical fluids at periods from several months to a few years.

Thus we examine (1) atmospheric excitation of the wobble and (2) gravity response to the wobble, in an attempt to discuss the relationship of "cause and effect" about the wobble from a self-consistent viewpoint of the Earth system dynamics.

At first (in chapter 2), we discuss the atmospheric contributions to the annual wobble examining the angular momentum budget for the atmosphere - mantle system. The data used here are EOPC04 for wobble data and two AAM functions which are calculated from the operational objective analysis data of the Japan Meteorological Agency (JMA) and the reanalysis data of the National Centers for Environmental Prediction/National Center for Atmospheric Research (NCEP/NCAR) during 1983 - 1998. The two equatorial AAM functions show different wind contributions to the observed annual wobble each other. Thus we precisely calculate the wind contributions to the annual wobble, dividing wind AAM functions into two wind contributions from zonal and meridional winds. It is discovered that the wind contribution depends upon its corresponding difference between the large zonal and meridional wind contributions, which have almost the same amplitudes but with out-of-phase relationship. We further find that the different wind contributions between JMA and NCEP/NCAR arise from the different regional meridional winds in troposphere associated with the Asian monsoon that shows the most remarkable seasonal signal over the world. Since JMA is thought to have a responsibility of forecasting the Asian monsoon, we consider the wind contribution based on JMA to show a better agreement with the function inferred from the annual wobble. It is found that the atmospheric variations have power enough to excite the Chandler wobble. The AAM function around the Chandler frequency varies with time having a similar amplitude and phase lead within 30° with respect to those in the function inferred from the observed wobble during 1987 - 1995, and there are good agreements in the amplitude with zero phase difference between both functions in 1989 and 1991. Though the wind contribution dominates over the pressure contribution to the Chandler wobble, the wind and pressure contributions vary with time to complement each other, so that the atmospheric excitation power can have almost same power as that from the observed wobble. Therefore we confirm that the atmosphere has enough power to excite the Chandler wobble.

At second (in chapter 3), we study the Earth's gravity response to the Chandler and annual wobbles, using the EOPC04 for wobble, and three SG data observed at Esashi in

Japan (1580 days from Jan. 2, 1995), Canberra in Australia (800 days from Jan. 28, 1997), and Syowa station in Antarctica (1740 days from Mar. 23, 1993). We first separate the tidal components (1/3 day to 31 days), atmospheric gravimetric effect, and step-like perturbations caused by the earthquakes and the maintenance of SG, from the SG data sets, for the purpose of examining long-period gravity changes with periods from 6 to 14 months. It is indicated that the observed annual gravity change corrected for atmospheric gravimetric effect agrees well with the predicted one within a discrepancy of 0.25 μGal ($1\mu Gal = 1 \times 10^{-8} m/s^2$) at each observation site, applying five gravimetric effects connected with the solid tide, the ocean tide, the wobble, the equilibrium pole tide, and sea surface height (SSH) variations. It is found that SSH variation is a significant source to cause annual gravity change at each site. The observed gravity response to the wobble, which is extracted by removing the four gravimetric effects (solid tide, ocean tide, pole tide, and SSH) from the observed annual gravity change, agrees roughly with theoretical elastic response. Comparing the nonseasonal observed gravity change with that predicted from the nonseasonal wobble, we determine the gravimetric factor and phase difference for the Chandler wobble at each observation site. The results show the phase difference of about 10°, which is too large to be explained not only by the effect of mantle anelasticity but also by the gravimetric effect of equilibrium pole tide. We suggest a possibility that the SG observes the gravity change around the Chandler period arising from geodynamical phenomena accompanying with mass redistribution in the ocean and the fluid core.

We discussed the excitation of the wobble and the gravity response to the wobble. On the annual wobble, the remaining angular momentum budget for atmosphere - mantle system would probably be expected to be explained by a contribution of SSH variation. This is because the observed annual gravity change agree well with the predicted model in the case of adding its gravimetric effect with a large amplitude. On the Chandler wobble, it is found that the atmospheric excitation power excessively supplies enough energy to excite the Chandler wobble, where the excess excitation power mentioned above is found to have correlation with the activity of El Niño, suggesting an oceanic contribution to the Chandler wobble. On the other hand, large phase difference for gravity response to the Chandler wobble may be explained by gravimetric effects of such oceanic phenomena. All these facts suggest that dynamics of atmospheric excitation of the Chandler wobble link with whole phenomena in the Earth system dynamics. The SG data in combination with satellite gravity mission such as GRACE (Gravity Recovery and Climate Experiment) scheduled for launch in 2001, is expected to monitor the mass transports in Earth system and provide useful information about the dynamics of Earth system.

Contents

List of Tables

List of Figures

Chapter 1

Introduction

1.1 Earth's Wobble and Earth System Dynamics

Observed variations in Earth's rotation are defined as three phenomena: (1) the precession and nutation, (2) wobble or polar motion, and (3) change in the length of day (LOD). The precession and nutation are changes in an instantaneous rotational axis of the Earth with respect to the space, which are caused by Luni-Solar attractions on Earth's equatorial bulge. On the other hand, the wobble or polar motion is the variation in an orientation of instantaneous rotational axis of the Earth with respect to its figure axis. The LOD change is connected to the change in the rotational speed of the Earth.

Among them, both the wobble and LOD change are described by variable components of the instantaneous angular velocity vector of the mantle as defined in Figure 1.1. Namely, the LOD change corresponds to its axial component, while the wobble corresponds to its two equatorial components. By virtue of precise space geodetic techniques such as VLBI (Very Long Base-line Interferometer), SLR(Satellite Laser Ranging), and GPS (Global Positioning System), these variable components are determined with an accuracy better than 1 milliarc-second (mas) for the wobble and 0.1 milliseconds (ms) for the LOD change [see *Smith and Turcotte,* 1993, for a review], and they are published as Earth orientation parameters (EOP) from the International Earth Rotation Service (IERS).

The wobble and LOD change are recognized to be as one of the global changes, and they are tightly connected with dynamical processes within the whole Earth, such as elastic or anelastic deformations of the mantle and irregular motions of geophysical fluids (i.e., atmosphere, ocean, hydrosphere, cryosphere, and fluid core) [for a review, *Munk and MacDonald,* 1960; *Lambeck,* 1980]. The major dynamical processes causing the wobble and LOD change are exchanges of angular momentum between the mantle and the geophysical fluids, under

the conservation of total angular momentum of the whole Earth. These exchanges are due to mass redistribution on/within the Earth (including the mantle deformation) through inertia products of the whole Earth and to relative angular momentum of the geophysical fluids to the mantle in the absence of external torques. We can identify the source to maintain the wobble and LOD change through axial and equatorial angular momentum budgets between the geophysical fluids and the mantle, in which the angular momentum of the mantle is inferred by deconvolving EOP. Fortunately, the recent precise measurements of the wobble and LOD change enable to discuss these dynamical processes.

In general, non-tidal variations in the LOD are decomposed into long period, interannual, seasonal, and high frequency variations. The seasonal and high frequency variations in the LOD are attributed primarily to the exchange of angular momentum between the atmosphere and the mantle, and contributions from other geophysical fluids are not significantly larger than an uncertainties in the observation [*Hide and Dickey,* 1991; *Dickey,* 1993, for a review]. Although the interannual variations (fluctuations on time scales between one and five years) in the LOD are maintained mostly by atmospheric variations, they are also reliably connected with El Niño/Southern Oscillation and/or Quasi-Biennial Oscillation (QBO) [*Chao,* 1989; *Dickey et al.,* 1994]. The long period variations in the LOD are considered to be caused mainly by tidal dissipation and post-glacial rebound for secular variations, and by core-mantle interactions for decade variations [*Eubanks,* 1993, for a review]. Thus we may have sufficient knowledge about excitation sources of the LOD changes.

The wobble is dominated by the Chandler wobble, a free oscillation of the Earth, with a period of about 14 months and the annual wobble, a forced motion, with a period of one year. The Chandler and annual wobbles have been argued by a lot of investigators since their discoveries by S. C. Chandler in 1891 and by Küstner in 1884, respectively. This is because their dynamics are of broad interests over astronomy, climatology, oceanography, hydrology, and geophysics [*Munk and MacDonald,* 1960; *Lambeck,* 1980; *Eubanks,* 1993, for a review]. For example, the eigenfrequency of the Chandler wobble reflects physical properties and dynamics of the Earth, such as figures and density structures within the mantle and ocean, elasticity or anelasticity of the mantle, and dynamical interaction between the fluid core and the mantle [e.g. *Smith and Dahren,* 1981]. Though both frequency and dissipation sources (that are mantle anelasticity and ocean bottom frictions due to ocean response to the wobble) of the Chandler wobble are almost well understood [e.g. *Smith and Dahren,* 1981; *Eubanks,* 1993], the excitation sources of the Chandler wobble remain a mystery [*Munk and MacDonald,* 1960; *Lambeck,* 1980; *Eubanks,* 1993, for a review]. In addition, the excitation sources of the annual wobble have not been fully accounted for [e.g., *King and Agnew,* 1991].

On the other hand, the wobble and LOD change cause perturbations in the centrifugal potential of the Earth, which deform the mantle. Then mass redistribution due to the deformation generates additional perturbations in the gravitational potential of the Earth. Consequently, surface gravity changes due to the wobble and LOD change (hereafter referred to as a gravity response) involve the variation in the centrifugal force, the effect of displacement of observation point, and the additional perturbations in the gravitational potential. Observed gravity responses to the Chandler and seasonal wobbles provide us useful information about the physical properties of Earth's interior such as the frequency-dependent anelastic behavior in a frequency band much lower than seismic and short-periodic tidal bands, in which Earth's response is rarely measured [see, *Wahr and Bergen*, 1986].

The surface gravity changes are affected by other gravimetric effects which are attributable to tidal response and the mass redistribution of the geophysical fluids with periods from several months to a few years. Hence, we can never examine the gravity response to the wobbles without separating these gravimetric effects from the observed gravity changes. There, however, are a little knowledge about the gravity changes caused by geophysical fluids dynamics that has a slight possibility to excite or dissipate the wobble at such period.

The study of both excitation and gravity response to the wobble is useful in understanding the complicated dynamics of the wobble. As mentioned above, the excitation and gravity response can be discussed by using the theory and data obtained from other geophysical fields such as meteorology, oceanography, and hydrology. Thus these discussions should be carried out from the viewpoint of the Earth system dynamics.

1.2 Atmospheric Excitations of Wobbles and Numerical Weather Prediction Data

The seasonal variations in the geophysical fluids on the Earth's surface have been considered as presumable sources to maintain the annual wobble; these variations are mass redistribution of the atmosphere [e.g., *Wilson and Haubrich*, 1976; *Wahr*, 1983] and of the land water and snow-ice [e.g., *Chao and 'Conner*, 1988; *Kuehne and Wilson*, 1991], and fluctuations in the ocean bottom pressure and the ocean currents [e.g., *Wahr*, 1983; *Celaya et al.*, 1999; *Ponte and Stammer*, 1999]. Atmospheric pressure variation and wind are known as the typical mass redistribution and relative angular momentum, respectively, dominating in these seasonal variations. Thus we focus on the atmospheric contribution. Though the pressure contribution was recognized to be a significant source to maintain the annual wobble, the

wind used to be considered as a slight source until *Chao and Au* [1991] found a significance of the wind contribution. Yet there are few studies that are concerned with the wind contribution after their finding. We suspect that this historical lack of attention induce the failure in explaining the complete excitation of the annual wobble.

The sources to excite the Chandler wobble (hereafter referred to as CW source) has still remained a mystery [*Eubanks,* 1993]. What have been considered as the plausible CW source are great earthquakes [e.g., *Mansinha and Smylie,* 1967; *Dahlen,* 1973; *O'Connell and Dziewonski,* 1976], atmospheric mass redistribution [e.g., *Wilson and Haubrich,* 1976; *Wahr,* 1983], and mass redistribution of land water [e.g., *Hinnov and Wilson,* 1987; *Kuehne and Wilson,* 1991]. Both seismic energy release of the great earthquakes and the inertia products of the mantle associated with the displacements of the faults of the great earthquakes are found to be too small to excite the observed Chandler wobble [e.g. *Kanamori,* 1977; *Gross,* 1986]. The contribution from atmospheric mass redistribution is largest among them but it gives only 20 - 30% of a necessary power as the CW source [*Wilson and Haubrich,* 1976; *Wahr,* 1983]. Recently, *Furuya et al.* [1996, 1997] pointed out the possibility that the wind contribution plays a major roles in the CW source.

For a quantitative discussion on the atmospheric contributions to the wobble in these decades, global objective analysis data in four-dimensional data assimilation (4DDA) system for numerical weather prediction have been employed as spatially homogeneous meteorological data over the world. The atmospheric contributions based on the 4DDA data set are referred to as the atmospheric angular momentum (AAM) function [*Barnes et al.,* 1983].

The AAM functions have been computed from the global analysis data produced at several world meteorological centers. They have been known to show different behavior in equatorial wind contribution, despite that these meteorological centers all use essentially the same meteorological data as input to their 4DDA system [e.g., *Eubanks et al.,* 1988; *Gross and Lindqwister,* 1992]. On the time scale of about 14 months, the equatorial wind contributions based on the Japan Meteorological Agency (JMA) and the National Centers for Environmental Prediction (NCEP) were also found to excite the Chandler wobble to a different extent [*Furuya et al.,* 1996]. These differences are probably in the way of evaluating the wind contribution to the Chandler and annual wobbles.

In order to clarify the atmospheric excitations of the Chandler and annual wobbles, it is important to solve the cause of the different behavior in equatorial wind contributions and to evaluate precise wind contributions using the AAM function computed from the global analysis data.

1.3 Earth's Responses to the Wobbles and Superconducting Gravimeter Measurements

In general, the gravity response to the wobble is represented by the amplitude ratio (hereafter referred to as the gravimetric factor) and phase difference between the observed gravity change and that predicted from EOP archived in IERS on the assumption of purely rigid Earth [*Loyer et al.,* 1999]. If the Earth is elastic, the gravity factor is considered to be 1.155 with zero phase difference at long period [*Dehant et al.,* 1999].

A maximum amplitude of the predicted gravity change is about $4\mu Gal(10^{-8}m/s^2)$ at 14-month periods. Such small and long period gravity change can be detected by a superconducting gravimeter (SG), which is superior to the classical spring gravimeters in sensitivity and long-term stability [e.g., *Richter,* 1983, 1990; *Richter et al.,* 1995; *Sato et al.,* 1997a; *Loyer et al.,* 1999]. The high sensitive property of SG, however, prevents simply interpreting the observed gravity changes, because SG can detect simultaneously other gravimetric effects associated with mass redistribution of the geophysical fluids through Newtonian attraction and surface loading effects. Atmospheric gravimetric effect has been argued by a lot of investigators and is evaluated at the accuracy of the order of $0.1\mu Gal$ despite that its maximum amplitude exceeds $10\mu Gal$ [e.g., *Mukai et al.,* 1995]. On the other hand, little is known about oceanic gravimetric effect due to non-tidal sea surface height variations at seasonal period.

The annual signal obtained from SG is demonstrated in previous studies, although its dynamical interpretation is insufficient [see, *Richter,* 1983, 1990]. On the other hand, SG data provides the gravimetric factor and phase for the gravity response to the Chandler wobble, and in consequence a considerable phase lag of about 20 days has been observed [*Sato et al.,* 1997b; *Loyer et al.,* 1999]. However, the geophysical meaning of this phase lag have never yet been explained.

Under the Global Geodynamics Project (GGP), a global network of SG has set up in 1997, and measurements will be continued until 2003 [*Crossley et al.,* 1999]. Unfortunately, there has never been any reports that make a comparison between the SG data sets obtained from the GGP network in order to discuss the gravity response to the wobble.

1.4 Purposes and Constructions of Thesis

Purposes of Thesis

The goal of this thesis is to investigate the dynamic structures of the Chandler and annual wobbles through two studies: (1) precise examination into the atmospheric excitation of both wobbles and (2) the evaluation of gravity response to both wobbles. Since those two studies cannot be discussed without the understanding of the geophysical fluids dynamics besides solid dynamics, they are argued from a self-consistent viewpoint of the Earth system dynamics.

The major purpose of (1) is to confirm the sources to excite the Chandler and annual wobbles. For this purpose we reveal the cause of the difference in the wind contribution between JMA and NCEP AAM functions and select the adequate one for the excitation source of the wobbles. (2) aims at geophysical interpretation of the gravity changes with period between 12 and 14 months observed by SG and at estimation of the Earth's responses to the wobbles in order to give the geophysical meaning of the considerable phase lag pointed out by previous studies.

Constructions of Thesis

In Chapter 2, we discuss the atmospheric contributions to the Chandler and seasonal (annual and semiannual) wobbles through the angular momentum budgets for the atmosphere-mantle system. First its axial and equatorial angular momentum budgets in seasonal variations based on the observed LOD change and wobble and the JMA and NCEP AAM functions during 1988-1997 are illustrated. Subsequently, we present regional and partial contributions from zonal and meridional winds in the troposphere and the stratosphere and describe a precise evaluation of the wind contribution to the annual wobble. Finally, the atmospheric contributions to the excitation of the Chandler wobble that has been a longstanding issue are discussed.

In Chapter 3, we analyze the SG data obtained at Esashi in Japan, Canberra in Australia, and Syowa station in Antarctica, in order to research long period gravity changes (with period from 6 to 14 months). First, it is described that the observed annual gravity change is accounted for by several gravimetric effects due to the mass redistribution of geophysical fluids. Subsequently, we discuss the geophysical meaning of the gravity responses to the Chandler and annual wobbles obtained from the SG data.

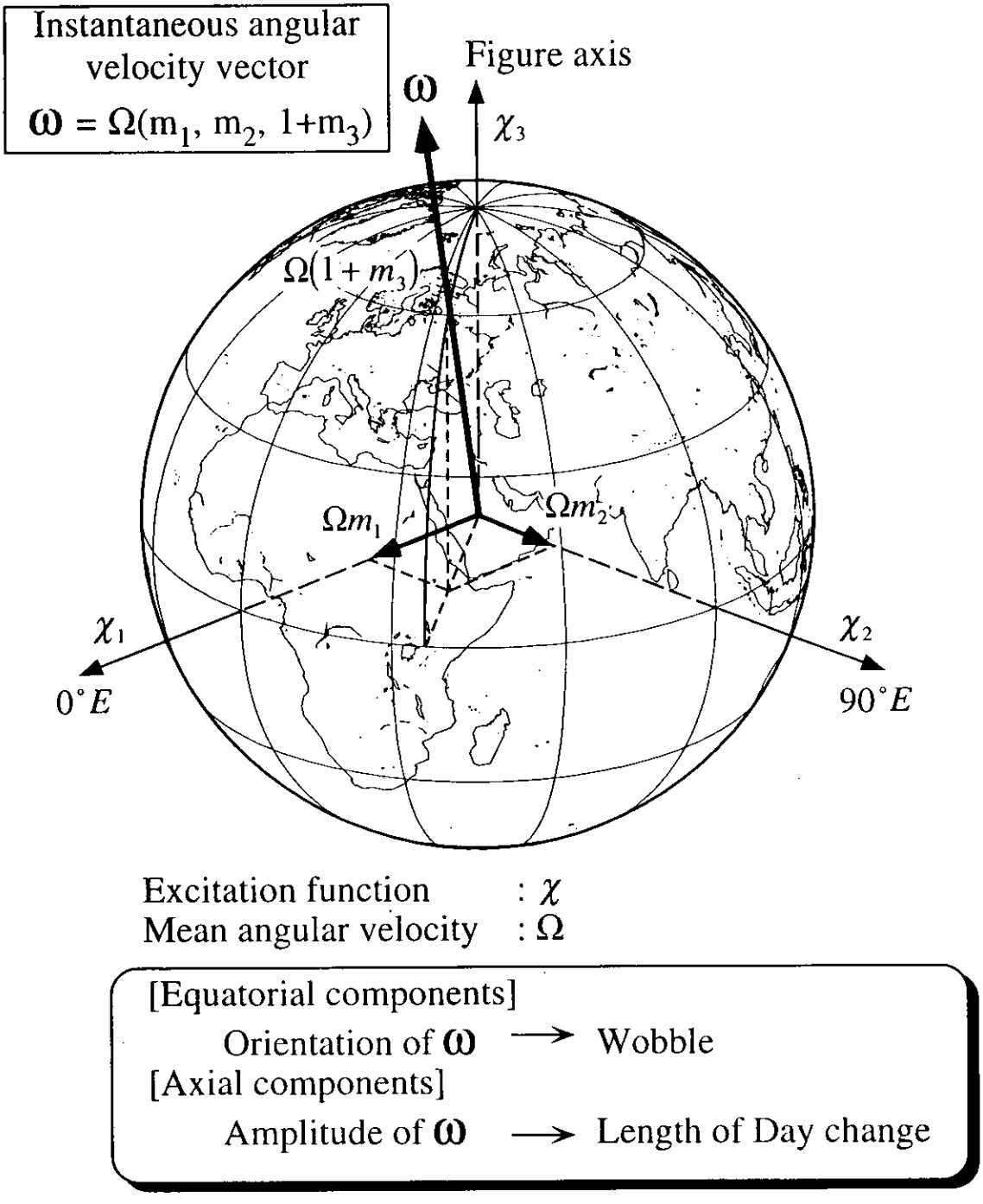

Figure 1.1: Illustrating components of the instantaneous angular velocity vector and the reference frame. Detailed descriptions about the excitation function and m_i are shown in Chapter 2 or Appendix A.

Chapter 2

Atmospheric Excitations of the Wobbles

2.1 Abstract

The atmospheric contributions to the seasonal and the Chandler wobbles are discussed through the angular momentum budgets for the atmosphere-mantle system. The data sets used here are SPACE97 and EOPC04 for length of day (LOD) and wobble, respectively. The two atmospheric angular momentum (AAM) functions are calculated from the operational objective analysis data of the Japan Meteorological Agency (JMA) and the reanalysis data of the National Centers for Environmental Prediction/National Center for Atmospheric Research (NCEP/NCAR). First axial and equatorial angular momentum budgets for the atmosphere-mantle system in seasonal (annual and semiannual) variations are reexamined for the period 1988-1997. Subsequently a precise evaluation of the wind contribution to the annual wobble are performed by using regional and partial contributions from zonal and meridional winds in the troposphere and stratosphere. Finally, the excitation of the Chandler wobble by atmospheric wind and pressure variations is discussed for the period 1983-1998.

Both axial AAM functions based on the JMA and the NCEP/NCAR agree well in annual variation and roughly in semiannual variation with the function inferred from the observed LOD. The two equatorial AAM functions show the different wind contributions to the function inferred from the observed wobble, in both annual and semiannual variations. The AAM function based on the JMA gives a better agreement with the functions inferred from the observed annual wobble. Since there are large discrepancy between the AAM functions and the

function inferred from the semiannual wobble, it is required to consider other contributions such as those from the ocean and land water plus snow-ice.

The equatorial wind contributions in annual variation depend upon its corresponding difference between the large zonal and meridional wind contributions, which have almost the same amplitudes with out-of-phase relationship. On the other hand, the two reasons for the different wind wind contributions to the annual wobble between the JMA and the NCEP/NCAR are verified as follow. Since the NCEP/NCAR AAM function is computed by integrating winds without regard to the surface topography, its wind term is much affected by the spurious winds blowing inside the real mountains, while the JMA AAM function reflects no such spurious winds because its winds are integrated over the real surface topography. Additionally, there is difference in the analysis data themselves, showing the different wind contribution arising from different regional winds in the troposphere associated mostly with the Asian monsoon. As a result, the wind contribution based on JMA, showing a better agreement with functions inferred from the observed annual wobble, is considered to be a more natural one, because the JMA is thought to have a responsibility of forecasting the Asian monsoon.

In the vicinity of the Chandler frequency (0.847 cycle per year), the JMA AAM function has remarkable spectral peak with a little dominant amplitude and about 30° advance in phase to those inferred from the observed wobble, in which their coherence exceeds 95% confidence threshold. In addition, the temporal variation in the Chandler wobble excitation calculated from the shifted eight years data of the AAM function is found to show almost the same pattern as that inferred from the observed wobble, in which the wind and inverted-barometer (IB) pressure contributions complementarily vary with time each other. These reveal that the atmospheric wind and IB pressure variations by themselves maintain the observed Chandler wobble during the analysis period.

2.2 Introduction

The Earth's rotational variations have been observed with a high accuracy by space geodetic techniques for over two decades and are described by variable components of an instantaneous angular velocity vector of the mantle [see *Smith and Turcotte*, 1993, for a review]. Namely, the LOD change corresponds to its axial component, while the wobble corresponds to its two equatorial components. The LOD change and wobble are recognized to be as one of the global changes, so that they provide valuable information about physical properties and dynamics of the whole Earth, such as Earth's figures and density structures, elasticity

or anelasticity of the mantle, and dynamics of geophysical fluids (i.e., atmosphere, ocean, hydrosphere, cryosphere, and fluid core), which are useful in understanding the dynamics of the Earth system.

Under the conservation of total angular momentum of the Earth, the LOD change and wobble are caused by exchanges of angular momentum between the mantle and geophysical fluids and variations in Earth's inertia tensor due to the mantle deformations. These exchanges are due to mass redistribution on/within the Earth through inertia products of the whole Earth and to relative angular momentum of the geophysical fluids to the mantle. Namely the LOD changes and wobbles are the result of excitations that are specified by variations of the angular momentum of the geophysical fluids. Therefore, axial and equatorial angular momentum budgets of the whole Earth provide us information about the source to maintain the LOD change and wobble.

The wobble is dominated by the Chandler wobble, a free oscillation of the Earth, with a period of about 14 months and the annual wobble with a period of one year. On the other hand, non-tidal variations in the LOD are generally decomposed into long period, interannual, seasonal, and high frequency variations. In this thesis, we focus the Chandler wobble and the seasonal LOD changes and wobbles. The excitation source of the Chandler wobble (hereafter referred to as CW source) has remained a mystery since the discovery of CW by S. C. Chandler in 1891 [*Munk and MacDonald,* 1960; *Lambeck,* 1980, for a review]. The major excitation sources for the seasonal LOD changes and wobbles, are believed to be the seasonal mass transport in the geophysical fluids on the Earth's surface (except for the fluid core inside the mantle). The seasonal LOD change has been confirmed to be mainly caused by changes in the atmospheric relative angular momentum, due to zonal wind [*Rosen and Salstein,* 1985; *Naito and Kikuchi,* 1990; etc.]. The seasonal wobble has long been considered to be excited with those in redistribution of atmospheric mass and land water, but no complete understanding has been obtained so far [see *Eubanks,* 1993 and *Dickey,* 1993, for a review].

There have been many studies for the annual wobble since it discovered by Küstner in 1884. *Wilson and Haubrich* [1976] argued that much of the annual wobble could be accounted for by the redistribution of atmospheric mass and land water. In addition to the atmospheric mass contribution, *Wahr* [1982] estimated that the contribution of the atmospheric relative angular momentum (that is, the wind contribution) amounts to 10-50% of the atmospheric mass contribution. *Chao and O'Conner* [1988] pointed out the overestimation of the land water contribution in the previous estimates. *Chao and Au* [1991] noticed that the wind contribution has a comparable order with the land water contribution. The wind contribution

is one of the major sources to be studied for the annual wobble.

For a more quantitative discussion on the atmospheric contributions to the Earth's rotational variations in these decades, global objective analysis data in four-dimensional data assimilation (4DDA) system for numerical weather prediction have been employed as spatially homogeneous meteorological data over the world. The atmospheric contributions based on the 4DDA data set are referred to as the atmospheric angular momentum (AAM) function [*Barnes et al.*, 1983]. The AAM function has three components: one axial component exciting LOD change and two equatorial components exciting wobble. Each component consists of pressure and wind terms, corresponding to the atmospheric mass redistribution and the atmospheric relative angular momentum, respectively. They have been calculated twice a day and archived in the Sub-Bureau for AAM (SBAAM) (presently the Special Bureau for the Atmosphere in the Global Geophysical Fluids Center) of the International Earth Rotation Service (IERS) [*Salstein et al.*, 1993] based on the world's four meteorological centers.

These AAM functions have been known to show different behavior, despite that the world meteorological centers all use essentially the same meteorological data as input to their 4DDA (for a comparison studies of axial atmospheric angular momentum fluctuations simulated by global circulation models, see *Hide et al.* [1997]). *Eubanks et al.* [1988], for example, found that the two pressure terms in the equatorial AAM functions from the National Center for Environmental Prediction (NCEP) and the Japan Meteorological Agency (JMA) have a higher correlation than 0.9, but their wind terms have a correlation of less than 0.4. Similar differences were found in the high-frequency changes from a few weeks, to a few months, between the wind terms from the United Kingdom Meteorological Office (UKMO), NCEP, and JMA [*Gross and Lindqwister*, 1992]. These disagreements in the wind terms of the equatorial AAM functions are considered to be caused in part by lack of data in sparse regions, such as the South Pacific [*Eubanks et al.*, 1988], and are also partly attributed to different methods in the 4DDA systems of the meteorological centers being responsible for different forecasting areas [*Eubanks*, 1993]. As a result, these equatorial wind AAM functions on a timescale of about 14 months were found to excite the Chandler wobble to a different extent [*Furuya et al.*, 1996, 1997].

There have been differences in the vertical integration method for the AAM functions between NCEP and JMA. The NCEP wind terms are computed by integrating wind from the bottom pressure level (1000 hPa) to the top pressure level [*Rosen and Salsten*, 1985]. The JMA wind terms are obtained by integrating wind from surface pressures on real mountains to the top (10 hPa) pressure level [*Naito et al.*, 1987]. It is important to assess the influences of the difference in the methods on the wind term in the AAM function in order to discuss

the wind contribution to the seasonal wobble.

There have been many studies for the Chandler wobble since the discovery of the Chandler wobble by S. C. Chandler in 1891 [*Munk and MacDonald,* 1960; *Lambeck,* 1980, for a review]. Consequently, both frequency and dissipation sources of the Chandler wobble are almost well understood [e.g. *Smith and Dahren,* 1981; *Eubanks,* 1993]. However, the excitation source of the Chandler wobble (hereafter referred to as the CW source) has remained a mystery.

At one time the CW source was considered to be seismic energy release of great earthquakes or the inertia products of the mantle associated with the displacements of the faults of the great earthquakes [e.g., *Mansinha and Smylie,* 1967; *Dahlen,* 1973; *O'Connell and Dziewonski,* 1976]. However, these seismic excitation were found to be too small to excite the observed Chandler wobble [e.g. *Kanamori,* 1977; *Gross,* 1986]. Based on the high correlation between the amplitude of the Chandler wobble and the global seismic activity, *Kanamori* [1977], for example, pointed out the possibility that the increase in amplitude of the Chandler wobble triggers the seismic activity.

It has also been discussed that the CW sources are mass redistribution of atmosphere [*Wilson and Haubrich,* 1976; *Wahr,* 1983] and land water [*Hinnov and Wilson,* 1987; *Kuehne and Wilson,* 1991]. *Wilson and Haubrich* [1976] stated a significant coherence between the contribution from the atmospheric mass redistribution and the excitation inferred from the observed wobble data in the International Latitude Service (ILS) during 1901-1970 and concluded that atmospheric pressure variations play an important role to excite CW. *Wahr* [1983] further examined the relative angular momentum contribution due to winds using hybrid approach (combining the mountain torque approach with the angular momentum approach), but he failed to sufficiently estimate its contribution because of absence of the spatially homogeneous meteorological data. From these results, it is specified that the excitation by the atmospheric mass redistribution supplies only 20-30% of a necessary power as the CW source. In addition, *Kuehne and Wilson* [1991] stated that conbinated contributions of the atmospheric mass redistribution and the land water storage are too small to account for the observed Chandler wobble.

Using the AAM function based on the European Centre for Medium-range Weather Forecast (ECMWF) data set for the period 1980-1990, *Kuehne et al.* [1993] and *Chao* [1993] found a significant correlation between the geodetic excitation function and the atmospheric contribution, focusing the contribution from the atmospheric mass redistribution, and suggested that the atmosphere plays an important role in the CW source, although its contribution by itself cannot completely account for the geodetic excitation.

Furuya et al. [1996] compared the amplitude of power spectrum of the geodetic excitation

function with that of the AAM functions based on the JMA and the NCEP for the period 1983-1994, and suggested that the wind plays a major role in the CW source. In addition, they pointed out that there is a considerable difference in the wind contributions between JMA and NCEP AAM functions, although an explanation of reason for this difference is deferred for the future study.

In this chapter, we investigate with three subjects as following. (1) we reexamine the axial and equatorial angular momentum budgets for the atmosphere-mantle system in annual and semiannual variations, using the reanalysis data set of the NCEP/National Center for Atmospheric Research (NCAR) [*Kalnay et al.*, 1996] and the operational objective analysis data set of the JMA [*JMA*, 1993] during 1988-1997. (2) The wind contribution to the annual wobble are evaluated precisely using the wind terms based on NCEP/NCAR and JMA during 1988-1997. (3) Consequently, we evaluate the atmospheric excitation of the Chandler wobble. In section 2.3, we describe a three dimensional angular momentum budget model. In section 2.4, we outline data, computations, and the method of analysis used in this chapter. In section 2.5, we discuss the three dimensional angular momentum budgets in seasonal variations (subsection 2.5.1), the zonal and meridional wind contributions and their regional wind contributions to the annual wobble (subsection 2.5.2), and the atmospheric excitation of the Chandler wobble (subsection 2.5.3). A conclusion is given in section 2.6.

2.3 Three Dimensional Angular Momentum Budget Models for Atmosphere-Mantle System

2.3.1 Basic Formulations

The Earth's rotation can be described by an instantaneous angular velocity vector of the mantle. In the absence of external torques the variation in its orientation with respect to the Earth's figure axis is associated with the polar motion or the wobble, while its axial variation is described as the LOD change. These variations are observed by space geodetic techniques as small dimensionless quantities, m_3 for the axial component and m_1 and m_2, representing angular distance along 0°E and 90°E longitude, respectively, for the equatorial components. The wobble is often described as complex form of $\tilde{m} = m_1 + im_2$ in plane coordinate system.

The wobble and LOD are basically subject to the following excitation equations for the equatorial and axial angular velocities, respectively. Under the conservation of total angular momentum of the Earth, with an elastic mantle decoupled to core, and with fluids on the

Earth [*Barnes et al.*, 1983; *Eubanks*, 1993],

$$\tilde{m} + \frac{i}{\tilde{\sigma}_c}\frac{d\tilde{m}}{dt} = \tilde{\chi} \tag{2.1}$$

$$\frac{d}{dt}(m_3 + \chi_3) = 0. \tag{2.2}$$

In eq.(2.1) $\tilde{\sigma}_c = 2\pi f_c(1 + i/2Q_c)$ is the complex Chandler frequency of the reflecting the dissipation of the Earth at the Chandler frequency, f_c, in terms of the quality factor, Q_c. The left hand side of eq. (2.1) corresponds to the geodetic excitation function inferred from the observed wobble, $\tilde{m}$. In eq. (2.2), the geodetic excitation function inferred from the LOD change is described with a relation $m_3 = -\Delta\Lambda/\Lambda_0$, where Λ_0 and $\Delta\Lambda$ are a standard LOD and its deviation, respectively. The terms $\tilde{\chi} = \chi_1 + i\chi_2$ in eq. (2.1) and χ_3 in eq. (2.2) are the excitation functions for the wobble and the LOD change, representing dimensionless angular momentum changes due to fluctuations of inertia tensors of the geophysical fluids and their relative angular momentum to the mantle. Hence the equatorial and axial angular momentum budgets of the Earth are discussed through eqs. (2.1) and (2.2), respectively (see Appendix A for more details).

Eq.(2.1) can be expressed as follows:

$$\tilde{m}(t) = e^{i\tilde{\sigma}_c t}\left[\tilde{m}_0 - i\tilde{\sigma}_c \int_{-\infty}^{t} \tilde{\chi}(\tau)e^{-\tilde{\sigma}_c \tau}d\tau\right] \tag{2.3}$$

where $\tilde{m}_0$ is an arbitrary complex constant [*Munk and MacDonald*, 1960; *Lambeck*, 1980]. In eq. (2.1), we can find the balance between the excitation function and the function inferred from the observed wobble with the assumption of $\tilde{\sigma}_c$.

2.3.2 Atmospheric Angular Momentum Functions

Here we use the excitation functions associated with atmosphere variations as $\tilde{\chi}$ and χ_3 in order to discuss the atmospheric contribution to the excitation sources of the wobble and LOD change. The excitation functions, based on the objective analysis data in a numerical weather prediction system, have been called the atmospheric angular momentum (AAM) function [*Barnes et al.*, 1983]. It consists of two terms: pressure and wind terms. The pressure term describes atmospheric mass redistribution effect through the inertia products due to surface pressure variations, while the wind term reflects the relative angular momentum due to wind. Their formulations are shown in Appendix B in detail.

In order to discuss the angular momentum budgets of the real Earth, with a nonrigid mantle, a fluid core inside the mantle, and fluids on the mantle, the transfer functions described below should be taken into account in the AAM functions (see Appendix B).

The transfer functions are coefficient functions of Love numbers, accounting for departures from perfect rigidity of the mantle arising from the effects of mantle deformation and oceanic yielding due to rotation and atmospheric loading. There is a degree of coupling between the fluid core and the mantle (see Appendix A for more details). Since the core-mantle decoupling can be assumed to be on a timescale of less than 5 years [*Yoder et al.*, 1981], the fluid core cannot respond to the seasonal LOD change. In such cases, the axial principal moment of inertia and Love number for only the mantle can be used instead of those for the whole Earth in the axial angular momentum budget. In the equatorial angular momentum budgets the equatorial principal moment of inertia for the whole Earth is replaced by that for only the mantle, because the fluid core can hardly affect the seasonal wobble [*Wahr*, 1982]. Therefore the transfer functions depend on the principal moments of inertia, employed for the angular momentum budget model.

This study uses the principal moments of inertia and the transfer functions employed and evaluated by *Eubanks* [1993] based on the preliminary reference Earth model (PREM) [*Dziewonski and Anderson*, 1981]. Note here that the AAM functions archived in the SBAAM of IERS have conventionally employed the numerical values used by *Barnes et al.* [1983], in which the principal moments of inertia and transfer functions differ from those of *Eubanks* [1993]. In particular, *Barnes et al.* [1983] employs $(C_m - A_m)$ in $\tilde{\chi}$ instead of $(C - A)$ used by *Eubanks* [1993]. These numerical values are shown in Table 2.1 for comparison.

2.4 Data, Computation, and Analysis

2.4.1 Data

LOD and Wobble Data

The axial component of the geodetic excitation functions is calculated from the observed LOD data given by the SPACE97 [*Gross*, 2000] series, in which the effects of the solid Earth tide and the ocean tide (Mf, Mf', and Mm) on the LOD change have been removed by using the models of *Yoder et al.* [1981] and *Desai* [1996]. The equatorial components of the geodetic excitation functions are inferred from the observed wobble data in EOPC04 of IERS [*IERS*, 1999]. For numerical differentiation of the left-hand side of (2.1), its discrete form of equation (2a) of *Wilson* [1985] is employed. In the analysis for the seasonal LOD changes and wobbles these daily series of axial and equatorial geodetic excitation functions are converted into monthly series from March 1988 to December 1997 by averaging. On the other hand, we employ the daily series of the equatorial geodetic excitation during September

28, 1983-December 31, 1998 for evaluating the CW source.

Archived AAM Functions

Though the AAM functions from NCEP, JMA, European Centre for Medium-Range Weather Forecasts (ECMWF), and UKMO have been archived in the
SBAAM of IERS [*Salstein et al.,* 1993], this analysis employs JMA and NCEP AAM functions from March 1, 1988, to December 31, 1997. The NCEP AAM functions are given four times a day, based on the reanalysis data set of NCEP/NCAR [*Kalnay et al.,* 1996]. The JMA AAM functions are given twice a day, based on the operational analysis data set [*Naito et al.,* 1987]. In this study, these series of both the AAM functions are converted into monthly series from March 1988 to December 1997 by averaging. Since this study employs the transfer functions shown in Table 2.1, these archived AAM functions are adjusted to those by *Eubanks* [1993]. In addition, the NCEP AAM function is also multiplied by a scale factor of 9.81/9.80, for adjusting gravity constants.

Objective Analysis Meteorological Data

Since the wind terms in the archived NCEP and JMA AAM functions are calculated using different vertical wind integration methods, as mentioned in section 2.2, we recompute the AAM functions from both the NCEP/NCAR and JMA data sets for the period March 1988 to December 1997. For the NCEP/NCAR AAM function we employ the reanalysis data mentioned above. The NCEP/NCAR reanalysis data used here are monthly data of geopotential heights and eastward and northward wind velocities at 17 standard pressure levels from 1000 to 10 hPa and of temperatures at 1000 hPa on $2.5° \times 2.5°$ latitude-longitude grids, for the period March, 1988-December, 1997.

The JMA AAM function is computed from the operational objective analysis data set of JMA starting from September 28, 1983 [*JMA,* 1993]. The JMA data set includes meteorological values of geopotential height, eastward and northward wind velocities, temperature at 15 standard pressure levels from 1000 to 10 hPa (but note that the number of pressure level was changed to 17 levels on March 1, 1996) on a spatially homogeneous latitude-longitude grid, where there were three horizontal grid size: 2.5×2.5 degrees from September 28, 1983 to February 29, 1988, 1.875×1.875 degrees from March 1, 1988 to February 29, 1996, and 1.25×1.25 from March 1, 1996 downward.

The original JMA data set are provided at half-day intervals, but they are given by daily averaged values from December 12, 1983 to June 30, 1986. We average the AAM function

at 00 UTC and 12 UTC in order to avoid the influences by considerably large intraday variations in the wind velocities which have a seasonal modulation [*Bell et al.,* 1991]. In the case of analysis for the seasonal LOD changes and wobbles, these data are also converted into monthly series during March, 1988-December, 1997, by averaging. For evaluating the CW source, we employ the daily series for the period September 28, 1983-December 31, 1998.

2.4.2 Computation

Recomputation of AAM Functions

For the recomputation of AAM functions from both the analysis data sets of JMA and NCEP, we use the global 5 arc min gridded topography data ETOPO-5 [*National Geophysical Data Center,* 1988], ffrom which 1.25°, 1.875°, and 2.5°square grid topography data are made. On the basis of these topography data, the surface pressures on real mountains are estimated from sea level pressures and geopotential heights at standard pressure levels by a cubic nonperiodic spline method with a hydrostatic equation [*Naito et al.,* 1987], where the sea level pressures are estimated from temperatures and geopotential heights at 1000 hPa assuming a hydrostatic relation.

For calculating the pressure term, the response of the ocean to atmospheric pressure loading is generally considered in terms of two extreme models. One is based on an inverted barometer (IB) approximation that assumes an isostatic response of oceans to the atmospheric loading under conservation of total atmospheric mass over the oceans. The other is a non-inverted barometer (NIB) approximation that assumes oceans to behave like a solid surface.

It is clear that the equatorial wind term as given in eq. (B.3) in Appendix B consists of two wind components: the zonal and meridional winds. In integrating the wind, coefficients of the zonal and meridional winds are functions of both latitude and longitude. However, a function system of their coefficients (hereafter, we call 'weighting function') differ with each other. Thus the regional zonal and meridional winds contribute the wobble effectively in the midlatitude and tropical regions, respectively, as shown in Figure B.2 and B.3 in Appendix B. In addition, we discuss separating the wind term into the tropospheric and stratospheric wind contributions: the former is obtained by wind integration from the surface pressures to 100 hPa and the latter is the wind contribution from 100 hPa to 10 hPa. We also use the regional wind contributions calculated every 7.5 degrees grid.

In the archived JMA AAM functions the wind terms are obtained by integrating winds from surface pressure on the real mountains to 10 hPa. Also, the pressure terms are based

on the surface pressure on real mountains. In the archived NCEP AAM functions the wind terms are obtained by integrating winds from bottom-level pressure (1000 hPa) to 10 hPa, despite the fact that the pressure terms are based on the surface pressure on the model's mountains [*Kalnay et al.*, 1996]. For recomputing the wind terms, we employ the two methods: the surface pressure (SP) method, employed in the archived JMA AAM functions, and the bottom-level pressure (BP) method, employed in the archived NCEP AAM functions. Hereinafter the AAM functions in which the wind terms are computed by the SP method are labeled JMA[SP] and NCEP[SP], while those computed by the BP method are labeled NCEP[BP]. The two methods show no remarkable difference in the pressure terms, as is shown in Fig. 2.1a.

The difference in the wind terms from the two methods only arises from winds blowing inside the real mountains. A maximum mountain height in the topography is about 5500 m above sea level, so that the influences of the two methods on the wind terms appear in the contributions from the lower troposphere.

2.4.3 Analysis

Excitation Domain Approach

In general, the atmospheric excitation of the wobble has been discussed by two methods: comparing geodetic excitation function with the AAM function through eq. (2.1) and comparing the observed wobble with that calculated from the AAM function (calculated wobble) through eq. (2.3). These methods are referred to as "excitation-domain approach" and "wobble-domain approach", respectively [e.g., *Furuya et al.*, 1997]. The wobble-domain approach needs careful choosing of the initial condition of the temporal convolution because of its large influence on the calculated wobble [e.g., *Chao*, 1985]. On the other hand, the excitation-domain approach provide simple discussion on the excitation of the wobble without such attention, and then we here apply this approach.

The comparison bwtween the geodetic excitation and AAM functions is generally made by Fourier transforming them that provides two-sided spectra. Their positive and negative frequency bands correspond to the prograde (counterclockwise) and retrograde (clockwise) circular components of the wobble, respectively. The seasonal LOD change and wobble, which basically consists of annual and semiannual variations, are considered to be the forced motions of the rotation pole, so that they are almost described by a line spectrum. In the analysis for seasonal variations, their annual and semiannual components are extracted by each sinusoids using least square fitting.

Since the Chandler wobble is a prograde normal mode [e.g., *Smith and Dahlen,* 1981], it can be excited by only small background spectral powers near the CW frequency in the AAM function. However, they have never explained the full CW source in previous studies, except *Furuya et al.* [1996] who suggested that narrowband atmospheric excitation at the CW frequency can account for the observed one. In this study, we focus the atmospheric contributions to the geodetic excitation near the CW frequency.

The excitation of the Chandler wobble (hereafter referred to as CW excitation) may not be always steady, showing time dependent power, because the Chandler wobble has shown variable amplitude and phase [see *Lambeck,* 1980, for a review]. We then compute the frequency-time spectra of the geodetic excitation and AAM functions in order to see interdependency among the eight sources for the CW excitation mentioned in section 2.4.2.

Least-square Fittings of Sinusoids

The seasonal variation is basically discussed with its first and second sinusoids: annual and semiannual variations. In this analysis we determine coefficients for cos terms and sin terms of the annual and semiannual sinusoids of the geodetic excitation functions and the AAM functions with their trends, using a least squares fitting, in which their phase angles are defined to January 1, 2000. As mathematical models for the trends, we use fourth-order polynomial functions for axial components (LOD) and linear functions for equatorial components (wobble).

The equatorial components of both the geodetic excitation and AAM functions in the seasonal variations are also separated into their prograde and retrograde components as follow [e.g., *Wilson and Haubrich,* 1976]:

$$\begin{aligned}\tilde{\chi} &= \tilde{\chi}^{+} e^{i\omega t} + \tilde{\chi}^{-} e^{-i\omega t} \\ &= \left[\frac{A_{c1} + A_{s2}}{2} + i\frac{A_{c2} - A_{s1}}{2}\right] e^{i\omega t} \\ &\quad + \left[\frac{A_{c1} - A_{s2}}{2} + i\frac{A_{c2} + A_{s1}}{2}\right] e^{-i\omega t},\end{aligned}$$

where ω, $\tilde{\chi}^{+}$, and $\tilde{\chi}^{-}$ are their angular frequency, the prograde and retrograde components, respectively. A_c and A_s are the coefficients for cos-terms and sin-terms of the annual sinusoid using a least square fitting, respectively.

Multitaper Spectral Analysis

In order to evaluate the CW sources the power spectra are estimated from the geodetic excitation and AAM functions after removing their seasonal components and linear trend by least-square fitting. Their power spectral estimates are computed with using multi-taper method (MTM) developed by *Thomson* [1982], which provides robust and minimum leakage spectral estimates accompanied with their confidence intervals by statistical F-test [see, *Chil and Yiou,* 1996].

Here we employ the application package for the spectral analysis utilizing the MTM approach provided by *Mann and Lees* [1996], and modify it to perform spectral analysis of the complex-valued time series with the prograde and retrograde components. The coherence and phase difference between the geodetic excitation and AAM functions are also estimated using the MTM approach presented by *Mann and Park* [1993].

In estimating power spectra, coherences, and phases, we adopt the seven 4π prolate tapers for the time series. In addition, a red-noise background is assumption is used instead of white-noise background, in order to optimize the fundamental signal-to-noise ratio with spectral estimations of climatic signal through MTM [*Mann and Lees,* 1996].

To obtain the temporal variations in the CW excitation, the frequency-time spectral analysis by MTM (evolutive spectral analysis introduced by *Gill and Yiou* [1996]) is carried out using with a 3000 days (about 8 years) sliding window, shifting 30 days. The features are discussed with the time-varying power spectra, coherences, and phase differences of/between geodetic excitation and AAM functions. We then define the CW excitation power and coherence to be the mean values of power spectra and coherence between 0.8 and 0.9 cpy, respectively, while we define the CW excitation phase difference to be a maximum value of phase difference from 0.8 to 0.9 cpy.

2.5 Results and Discussion

2.5.1 Atmopheric Contributions to Earth's Axial and Equatorial Angular Momentum Budgets in Seasonal Variations

Seasonal Patterns in the AAM Functions

Figure 2.1a shows the yearly mean seasonal patterns of the NIB pressure, IB pressure, and wind terms of the NCEP and JMA AAM functions archived in IERS. The patterns of the three terms, based on the two data sets, agree well each other except in the equatorial

wind terms. Figure 2.1a shows that the pressure terms and the wind terms have out-of-phase relationships, except the χ_2 based on the NCEP data. This exhibits their inphase relationship, although the amplitude of the wind term is very small.

Since the NCEP and JMA AAM functions are known to be based on the BP and SP methods, as mentioned in section 2.4.2, we recompute the seasonal patterns in the equatorial wind terms from the reanalysis data of NCEP/NCAR based on the SP method, as shown in Figure 2.1b. The two wind terms are roughly inphase relationships, but large disagreements still remain. These results make us imagine that the disagreements in the equatorial wind terms of the archived NCEP and JMA AAM functions are caused by the differences, not only in the calculation methods for the wind term, but also in the analysis data themselves between NCEP and JMA.

Axial Angular Momentum Budget

Tables 2.2 and 2.3 show the amplitudes and phases in annual and semiannual variations, respectively, of the geodetic excitation functions, inferred from the observed wobble and LOD data, and of the AAM functions, recomputed by the SP and BP methods from the reanalysis data of NCEP/NCAR and the operational analysis data of JMA. Since the oceans are known to respond isostatically to the atmospheric pressure loading on seasonal timescales [*Trupin and Wahr,* 1990; *Ponte and Rosen,* 1994], we employ here the IB pressure term alone. In the following discussions on the seasonal variations, the IB pressure and wind terms are referred to simply as the pressure and wind contributions.

On the basis of the IB pressure and wind terms in Tables 2.2 and 2.3, the axial angular momentum budgets for the atmosphere-mantle system in annual and semiannual variations are shown in Figure 2.2 in phasor plots, where the lengths of the vectors indicate the amplitudes and the counterclockwise angle of the vectors indicates their phases with respect to January 1. For example, the directions of the JMA[SP] vectors indicate the phases near February and May in annual and semiannual variations, respectively. Note that the vectors of the pressure contributions in semiannual variation are too small to be displayed.

In annual variation the phasor plots reconfirm for us that the three axial budgets can be almost completed with the wind contributions due to zonal wind [*Rosen and Salstein,* 1985, 1991; *Naito and Kikuchi,* 1990, 1991; *Höpfner,* 1998;*Naito et al.,* 2000; etc.]. The budgets, however, indicate that the pressure contributions should never be neglected for more completeness [*Naito and Kikuchi,* 1990; *Naito et al.,* 1999]. Table 2.2 indicates that

the amplitudes in the wind+IB pressure terms, as well as in the IB pressure terms, are larger than their estimation errors. There are the wind contribution from 10 to 1 hPa of 2.9×10^{-10} [*Rosen and Salstein,* 1991], the oceanic contribution of $3 - 4 \times 10^{-10}$ [*Marcus et al.,* 1998], and the land water contribution of 3.1×10^{-10} [*Chao and O'Connor,* 1988], which are comparable orders to the remaining budgets.

In a semiannual variation the wind contribution plays a major role in the budgets. There are a little larger remaining budgets of (4.5×10^{-10}, 217°) in JMA[SP], (5.0×10^{-10}, 217°) in NCEP[SP], and (5.0×10^{-10}, 217°) in NCEP[BP]. Since the semiannual variation in zonal wind prevails in the stratosphere, a major candidate for these discrepancies can be a wind contribution of the upper stratosphere, above 10 hPa, which is not accounted for here. For example, the estimated amplitude and phase of the contribution from the upper stratosphere, above 10 hPa, are about 3.2×10^{-10} and 254°, respectively [*Rosen and Salstein*, 1991]. One can easily confirm that these values well satisfy the remaining budgets, although there are the other contributions from the oceans and land water of about 2×10^{-10} [*Marcus et al.,* 1998] and 1.2×10^{-10} [*Chao and O'Connor,* 1988], respectively.

Equatorial Angular Momentum Budgets

Figure 2.3a shows the equatorial angular momentum budgets in annual variation. The phasor plots reveal that the wind contributions, in JMA[SP], differ considerably from those in NCEP[SP] and NCEP[BP] in both amplitude and phase. Their pressure contributions agree very well each other. In addition, large differences are seen between the wind contributions obtained by the different methods from the NCEP/NCAR data, which indicate contributions from winds blowing inside real mountains. We recomputed the wind term based on JMA[BP] and found that the direction in its vector differs from that based on JMA[SP], suggesting that the AAM functions based on JMA[SP] give a better agreement with the functions inferred from the observed wobble.

It had long been thought that atmospheric pressure and land water contributions are major sources for the budget in annual variation and that wind contributions including effects of mountain torques are much smaller than the above contributions [*Wilson and Haubrich,* 1976; *Wahr,* 1983], although *Wahr* [1982] theoretically pointed out that an effect of atmospheric relative angular momentum has a contribution of 10-50% of pressure contribution. *Chao and Au* [1991] using the ECMWF data, found that the wind contribution is greater

than the land water contribution. It has only 20% of the pressure contribution in the prograde motion. The results shown in Figure 2.3a strongly support the importance of the wind contributions to the annual wobble, in which case the SP method should be employed in their calculations.

There are still large remaining budgets (in amplitude and phase) in annual variation, amounting to (1.9×10^{-8}, 40°) for the χ_1 component and (3.6×10^{-8}, 38°) for the χ_2 component in the case of JMA[SP], for example. These are comparable to the estimated contributions from land water of about (1.7×10^{-8}, 4°) for the χ_1 and about (2.0×10^{-8}, 235°) for the χ_2 [*Chao and O'Connor,* 1988] and to about (2.5×10^{-8}, 181°) for the χ_1 and about (4.2×10^{-8}, 99°) for the χ_2 [*Kuehne and Wilson,* 1991]. Since the oceanic contributions, based on an oceanic general circulation model (OGCM), are as large as these hydrological contributions [*Celaya et al.,* 1999], these estimates suggest that more sophisticated estimations, including oceanic contributions, are necessary to complete the budget.

Figure 2.3b shows the equatorial angular momentum budgets in semiannual variation. The phasor plots indicate that the pressure + wind contributions are too small to complete the budgets. The pressure contributions are also dominant, but the wind contributions are very small in contrast to those in annual variation. In addition, since the disagreements in the wind contributions between JMA[SP], NCEP[SP], and NCEP[BP] are less than their estimation errors, as shown in Table 2.3, these wind contributions seen in Figure 2.3b are insignificant. The other sources for the remaining budgets cannot be evaluated quantitatively; ocean pressure and current contributions based on OGCM are considered to be large [*Ponte et al.,* 1998; *Ponte and Stammer,* 1999], and the contribution from a tidal ocean current may not be negligible. An interesting fact here is that the amplitudes and phases in the wind+NIB pressure terms agree well with those in the function inferred from the observed wobble, as shown in Table 2.3, suggesting oceanic contribution as a source for the remaining budget.

Prograde and Retrograde Angular Momentum Budgets

Figure 2.4 shows the prograde and retrograde budgets of the equatorial angular momentum in annual variation. The annual prograde component of the geodetic excitation function has about two times the amplitude of the retrograde component. The amplitude of prograde and retrograde IB pressure terms are almost equal. Both amplitude and direction of the wind term vector probably plays a major role to explain the difference in the geodetic

excitation function between prograde and retrograde components. There is a considerable difference in both amplitude and direction of the wind term between JMA[SP], NCEP[SP], and NCEP[BP] in the prograde and retrograde budgets. This feature is consistent with the results of χ_1 and χ_2 components shown in Figure 2.3a. Figure 2.4 suggests that the AAM function based on JMA[SP] provides a better agreement with the function inferred from the observed annual wobble in the prograde and retrograde components.

Chao and Au [1991] pointed out the impotance of the wind contribution to the wobble based on the ECMWF data, because the wind contribution was greater than the land water contribution and it has 20% of amplitude of the pressure contribution in the prograde motion. The ampulitudes of the wind contribution based on JMA[SP] in the prograde and retrograde motions are 26% and 38% of those of pressure contribution, respectively. Though *Chao and Au* [1991] pointed out that the phase gap between the geodetic excitation and AAM function is about 40° in the prograde component, our results shows that the phase gaps in the prograde and retrograde components based on JMA[SP] are within 18° and 20°, respectively.

There are remaining budgets (in amplitude and phase), amounting to (2.0×10^{-8}, 24 °) for the prograde component and (2.1×10^{-8}, 100°) for the retrograde component in the case of JMA[SP], for example. The hydrogical contribution is (0.9×10^{-8}, 286°) for the prograde component and (1.6×10^{-8}, 29°) for the retrograde one [*Chao and O'Connor,* 1988] and (0.9×10^{-8}, -23°) for the prograde one and (3.3×10^{-8}, 175°) for retrograde one [*Kuehne and Wilson,* 1991]. *Celaya et al.* [1999] computed the atmospheric, oceanic, and hydrogical contributions to the prograde annual wobble, using data generated by a coupled climate system model in the NCAR. Their estimations of hydrogical (land water and river dischage) and oceanic (ocean bottom pressure and ocean currents) contributions are (2.85×10^{-8}, 83°) and (1.7×10^{-8}, 5°), respectively. Combining JMA[SP] with them, the remaining budget vector in the prograde component becomes (1.1×10^{-8}, -101°). This value is smaller than 2.85×10^{-8} of discrepancy estimated by *Celaya et al.* [1999].

For the retrograde component, the AAM function based on JMA[SP] provides a better agreement with the geodetic excitation function. Its discrepancy is much smaller than that estimated by the previous studies [see *King and Agnew,* 1991]. Though it has considered that the retrograde component of function inferred from observed annual wobble might not be sufficiently accurate [e.g., *Chao and Au,* 1991; *King and Agnew,* 1991], the atmospheric contribution can account for the observed retrograde annual wobble as shown in Figure 2.4. We suggest that the retrograde annual wobble excitation can be evaluated by recent accurate data of fluids on the Earth.

2.5.2 Zonal and Meridional Wind Contributions to the Seasonal Wobble

Zonal and Meridional Wind Contributions

Figure 2.5 shows the eastward (zonal) and northward (meridional) wind contributions to the annual wobble. It turns out from the phasor plots in Figure 2.5 that each wind contribution, based on JMA[SP], NCEP[SP], and NCEP[BP] shown in Figure 2.3a, depends upon its corresponding difference between the large zonal and meridional wind contributions having vectors with almost the same amplitudes, but with almost inverse phases to each other.

In addition, we find that the zonal wind contribution vectors based on JMA[SP] and NCEP[SP] have comparable direction and length, but their meridional wind contribution vectors are different from each other in length. Their disagreement in zonal wind contribution is 0.89×10^{-8} for χ_1 and 1.00×10^{-8} for χ_2, while that in meridional wind contribution is 2.45×10^{-8} for χ_1 and 1.36×10^{-8} for χ_2. In the case of disagreement between NCEP[SP] and NCEP[BP], its magnitude is 1.13×10^{-8} for χ_1 and 1.08×10^{-8} for χ_2, respectively, in the zonal wind contribution and 0.74×10^{-8} for χ_1 and 0.54×10^{-8} for χ_2, respectively, in the meridional one. On the zonal wind contribution, the disagreement arising from different calculation methods in the wind term agrees roughly with that attributed to difference in meteorological data between NCEP/NCAR and JMA. On the meridional wind contribution, the influence of the different meteorological data is 20% larger than that of the different calculation method. These results suggest that the disagreement in the equatorial wind terms of the archived NCEP and JMA AAM functions is caused mainly by the different meridional wind in their meteorological data.

Tropospheric and Stratospheric Wind Contributions

In order to investigate the sources causing the large discrepancies between the JMA and NCEP wind contributions to the annual wobble as mentioned in section 2.5.1, we show the tropospheric and stratospheric wind contributions to the axial and equatorial angular momentum budgets in annual variations based on JMA[SP], NCEP[SP], and NCEP[BP] in Figure 2.6. The figure clearly shows that there is no discrepancy in the phasor plots, not only between NCEP[SP] and NCEP[BP], but also between NCEP[SP] and JMA[SP] in the χ_3 component, suggesting that the annual LOD change are maintained by zonal winds above 500 hPa [also see *Hide and Dickey,* 1991].

In χ_1 and χ_2 components, on the other hand, Figure 2.6 shows that the tropospheric wind contributions are considerably different and that the stratospheric wind contributions are almost the same in both direction and length of the vector between the three estimates. The difference between NCEP[SP] and NCEP [BP] can basically be attributed to the winds blowing inside the real mountains, below about 500 hPa. Between the results based on JMA[SP] and NCEP[SP], however, there is still a large difference. The difference in meteorological data sets is about 20% larger than that in the calculation method.

Figures 2.7a and 2.7b show the tropospheric and stratospheric contributions, separated from zonal and meridional wind contributions of Figure 2.5, respectively. Figure 2.7a reveals that tropospheric zonal wind contribution has a same amplitude of stratospheric one with out-of-phase relationship for χ_1 and in-phase relationship for χ_2. These features are also found in meridional wind contributions as shown in Figure 2.7b.

The disagreement in both zonal and meridional wind terms between NCEP[SP] and NCEP[BP] shown in Figure 2.5 is attributed to only the different contribution from the tropospheric wind. It is clear that the disagreement between JMA[SP] and NCEP[SP] is mainly caused by different meridional wind in the troposphere. These results make us imagine that the difference between the wind contributions, based on JMA[SP] and NCEP[SP], is a reflection of differences in their regional wind contributions in the troposphere.

Regional Wind Contributions to Annual Wobble

Figures 2.8 show the regional contributions to annual wobble from the zonal and meridional winds based on JMA[SP] in χ_1 and χ_2 components in 7.5° square grids. In these figures, the latitude and longitude belt contributions, and their total vectors are also shown. All vectors are displayed by the phasor plot in the same manner as in Figure 2.2. The latitude and longitude belt contributions express the sum of regional vectors along longitude and latitude lines, respectively. Each total vector is equal to the corresponding wind contribution based on JMA[SP] shown in Figures 2.5, 2.7a, and 2.7b.

Figure 2.8a shows the regional contributions from the zonal wind and reveals that their remarkable contributions, for both χ_1 and χ_2, distribute symmetrically about the equator dominating around prevailing westerly zone at mid-latitude on northern and southern hemisphere. Though these regional contributions have a large amplitude, longitude belt contributions exhibit that most of them cancelled out, and their residual corresponds to the global (total) contribution from the zonal wind. There is noteworthy vectors of latitude belt

contribution for χ_2 around $30°N$, which have comparable amplitude and phase to the total vector. These latitude belt contributions appear to reflect the regional zonal wind blowing around southern margin of Eurasia continent. Figure 2.8b shows the regional contributions from the meridional wind and is clear that their remarkable contributions distribute on the continents for χ_1 and over the oceans for χ_2 in the northern hemisphere. The regional and latitude belt contributions from the meridional wind having a significant amplitude are found only in the northern hemisphere.

Figure 2.8c shows the regional contributions from the tropospheric zonal wind. This figure reveals that distributions of their remarkable contributions are basically arranged with north and south symmetry. The longitude belt contributions from the tropospheric zonal wind are also cancelled out, being similar to Figure 2.8a. The latitude belt contributions having comparable amplitude and phase to the total vector are found at $30°N$ in both χ_1 and χ_2 components of tropospheric zonal wind contribution. These belt contributions suggest that global contributions from the tropospheric zonal wind in χ_1 and χ_2, shown in Figure 2.7a, are much affected by the zonal wind blowing over the north Pacific ocean and around southern margin of Eurasia continent, respectively.

Figure 2.8d shows the regional contributions from the tropospheric meridional wind and reveals that their latitude belt contributions are symmetric about the equator and their directions are reversed at the order of $0-30°$, $30-60°$, and $60-90°$. Such reciprocal feature may be characterized by Hadley, Ferrel, and Polar circulations of atmospheric mass. The latitude belt contributions within Ferrel circulation zone in northern and southern hemisphere have same direction to the global contribution from the tropospheric meridional wind. Therefore, we suggest that the tropospheric meridional wind contribution links to global atmospheric circulation in the troposphere, arising from the heat transport from the tropics to the polar region.

Figures 2.8e and Figure 2.8f show the regional contributions from the zonal and meridional winds in the stratosphere, respectively. Each regional contribution vector in the stratosphere has less amplitude than that in the troposphere. The amplitude of their total vector, however, agrees roughly with that in the troposphere, because latitude belt contributions in the stratosphere are not cancelled out in being different from that in the troposphere. This characteristic is considered to arise from monotonous stratospheric wind: eastward wind in summer hemisphere and westward wind in winter hemisphere. When the westward wind blows in the stratosphere, the planetary waves, generated by collisions between tropospheric winds and mountains, can be propagated up to the stratosphere. We suggest that the regional contributions of stratospheric meridional wind, locating on the continents in northern

hemisphere, are related to these phenomena. It is also necessary to consider the dynamics of stratosphere in order to clarify the excitation mechanism of the annual wobble in detail.

Prograde and Retrograde Wind Contributions to Annual Wobble

Figure 2.9 shows zonal and meridional wind contributions to the prograde and retrograde annual wobble, separated from the wind contributions shown in Figure 2.4. It is clear from the phasor plots that each wind contribution, based on JMA[SP], NCEP[SP], and NCEP[BP] shown in Figure 2.4, depends upon its corresponding difference between the large zonal and meridional wind contributions having vectors with almost the same amplitudes, but with almost inverse phases to each other. This figure indicates that disagreements between NCEP[SP] and NCEP[BP], and between JMA[SP] and NCEP[SP] arise mainly from the meridional wind contribution.

Figures 2.10a and 2.10b display the tropospheric and stratospheric wind contributions, separated from zonal and meridional wind contributions of Figure 2.9, respectively. The different properties from those of χ_1 and χ_2 components shown in Figures 2.7 are both zonal and meridional wind contributions in the troposphere are larger for prograde component and smaller for retrograde component than those in the stratosphere. There are insignificant disagreements in the zonal wind contribution in the troposphere and the stratosphere between JMA[SP], NCEP[SP], and NCEP[BP] as shown in Figure 2.10a. On the other hand, the meridional wind contributions in the stratosphere based on three AAM functions agree with each other, but considerable disagreements appear in those in the troposphere. The agreement in prograde and retrograde components of meridional wind contribution in the troposphere are agreeable to those found in χ_1 and χ_2.

Figures 2.11 show regional contributions in prograde and retrograde components instead of χ_1 and χ_2 as shown in Figures 2.8. The remarkable regional contributions from the zonal wind in prograde and retrograde components exhibit same features in χ_1 and χ_2 as shown in Figure 2.8a, except for north and south asymmetry. Comparing total vector with vectors of latitude and longitude belt contributions in Figure 2.11a, the global contribution of zonal wind in prograde and retrograde components as shown in Figure 2.9 are affected by regional zonal winds blowing around Southeast Asia in which the Asian Monsoon, showing the most remarkable seasonal signals over the world, is dominant. The distributions of regional contributions from the meridional wind in prograde and retrograde components equal to those in χ_1 and χ_2 as shown in Figure 2.8b.

Figure 2.11c shows that regional contributions from the tropospheric zonal wind in the

prevailing westerly zone in northern hemisphere are predominant with large amplitudes and phases offset each other. The latitude belt contributions from the tropospheric zonal wind around $30°N$ characterize its global contribution. Figure 2.11d shows that latitude belt contributions of tropospheric meridional wind in prograde and retrograde components correspond to Hadley, Ferrel, and Polar atmospheric circulations. This feature is consistent with that in χ_1 and χ_2 as shown in Figure 2.8d.

The distributions of regional contributions from zonal and meridional winds in the stratosphere for prograde and retrograde components, shown in Figures 2.11e and 2.11f, respectively, resemble those for χ_1 and χ_2 as shown in Figures 2.8e and 2.8f. The different features between Figures 2.7 and Figures 2.10 are caused mainly by the regional contributions from the stratospheric wind as follow: latitude belt contribution from the stratospheric zonal wind from $30°S$ to $60°S$ and latitude belt contributions from the stratospheric meridional wind at high latitude in southern hemisphere. It is suggested that the regional stratospheric wind at high latitude in southern hemisphere involves with the global contributions of stratospheric wind in prograde and retrograde components.

Regional Wind Differences Between the Two Data Sets in Annual Variation

In order to identify the sources for the large difference in wind term between NCEP and JMA AAM functions, we display the differences between the regional wind contributions in annual variation based on JMA[SP] and NCEP[SP] in χ_1 and χ_2 components in 7.5° square grids. The difference between two AAM functions are caused primary by the difference in the meridional wind in the troposphere between NCEP reanalysis and JMA objective analysis as shown in Figure 2.7. Figures 2.12e and 2.12f actually show that the regional contribution of the zonal and meridional wind in the stratosphere based on NCEP[SP] hardly differs from that based on JMA[SP]. The regional difference in entire wind contributions shown in Figures 2.12a and 2.12b agrees roughly with that in tropospheric wind contributions in Figures 2.12c and 2.12d.

Figure 2.12c shows the differences between the regional contributions of the zonal winds in annual variation based on JMA[SP] and NCEP[SP] in χ_1 and χ_2 components, and Figure 2.12d shows those for the tropospheric meridional winds. In the two figures the latitude and longitude belt contributions and their total vectors are also shown. Each total vector is equal to the difference between each tropospheric wind contribution based on JMA[SP] and NCEP[SP]. The total vectors in these figures reveal that the differences between the

meridional wind contributions in the troposphere based on JMA[SP] and NCEP[SP] shown in Figures 2.7 are 2.76 and 1.36 times as large as those in the zonal wind contributions in the χ_1 and χ_2 components, respectively.

In the case of the regional contributions of the zonal winds in Figure 2.12c, major differences between JMA[SP] and NCEP[SP] appear around the Antarctic continent, and in the South Pacific and Indian oceans. In the case of the meridional winds in Figure 2.12d, large differences appear almost throughout the world, except in regions of the North Pacific and North Atlantic Oceans, North America, and Europe. This suggests that the differences depend strongly upon spatial density of meteorological observations, which might affect the difference in the two analysis data sets through the 4DDA system in numerical weather prediction [also see Eubanks et al., 1988; Gross and Lindqwister, 1992; Eubanks, 1993].

Since each total vector in the two figures can be considered to reflect the regional vector with the same direction as that in the total vector, the other regional vectors are cancelled out (see latitude and longitude belt contributions). The most effective area to view the differences between the tropospheric wind terms based on JMA[SP] and NCEP[SP], which affect the equatorial angular momentum budget in annual variation (that is, the annual wobble), is found to be the so-called Asian Monsoon region, which shows the most remarkable seasonal signals throughout the world. For example, the sum of the regional contribution vectors of the meridional wind in the troposphere in Asian Monsoon region (that is specified by range from 60°E to 160°E longitude and from 0°to 30°N latitude) for χ_1 has 92% amplitude of the total vector with 4° phase difference, while the sum of other regional contributions has 13% amplitude of the total vector with 96° phase difference. Therefore the wind terms in the AAM functions in annual variation would strongly reflect the meridional winds in these regions, if the wind terms based on JMA[SP], which show a better agreement with functions inferred from the observed annual wobble, were a more natural one. In addition such meridional winds can be expected to excite the different Chandler wobbles, as mentioned in section 2.1 [see Furuya et al., 1996, 1997]. These features will be clarified by sophisticated studies using a simulation model of the global atmosphere in the near future.

Figure 2.12g shows the differences between the regional contributions of the zonal winds in annual variation based on NCEP[SP] and NCEP[BP] in χ_1 and χ_2 components, and Figure 2.12h shows those for the tropospheric meridional winds. The regional differences arising from calculating method of the wind terms appear in high mountains: Himalaya mountains and Antarctic plateau. These components in Figures 2.12g and 2.12h mean the "spurious" wind contributions included in the archived NCEP AAM function.

Figures 2.13 show the differences in the regional wind contributions to the prograde and

retrograde annual wobble in order to identify the difference between NCEP and JMA AAM functions archived in IERS. These results equal to the features of χ_1 and χ_2 components as shown in Figures 2.12.

2.5.3 Atmospheric Excitation of the Chandler Wobble

Power Spectra, Coherences, and Phases

It is evident from the section 2.5.1 that the JMA AAM function (that is, JMA[SP]) shows better agreement with the geodetic excitation than the NCEP AAM function (that is, NCEP[BP]). Therefore, we evaluate the atmopheric excitation of the Chandler wobble using JMA[SP].

Figures 2.14a, 2.14b, and 2.14c show power spectra, squared coherences, and phase differences of/between the geodetic excitation and the contribution from wind+IB pressure, wind, and IB pressure, respectively, at frequency bands from -3 to 3 cpy for the period 1983-1998, which are accompanied with confidence threshold for the power spectra and coherences by F-test. There are 18 portions of power spectra with respect to the geodetic excitation function having the statistical reliability exceeding 90% confidence threshold shown with small circles in the left figure. Note that one of them appears in the vicinity of the CW frequency.

It is demonstrated in Figure 2.14a that the power spectral amplitude of the wind+IB pressure contribution agrees roughly with that of geodetic excitation at 5 frequency bands (i.e., near -2.7, -1 to -0.8, near 0.2, 0.7 to 1.5, and near 2.7 cpy), where their coherences exceed 95% confidence threshold. This contribution also has remarkable broad spectral peak in the vicinity of the CW frequency.

The power spectrum of the wind contribution in Figure 2.14b exhibits its broad spectral peak around the CW frequency, though its statistical reliability by F-test cannot reach 90% confidence threshold. The reason for this will be discussed in next section. The spectral estimates for the contribution from IB pressure shown in Figure 2.14c clearly indicate that its power spectral amplitude is always much smaller than that of geodetic excitation at frequency bands between -3 to 3 cpy, though there is remarkable broad spectral peak around the CW frequency.

These figures reveal the remarkable broad spectral peaks of wind+IB pressure, wind, and IB pressure contributions at frequency band between 0.7 and 0.9 cpy. At the CW frequency, these power spectral amplitudes reach 117%, 73%, and 50% of amplitude of the geodetic excitation, respectively. However, neither the contribution from wind nor that from IB pressure by itself can account for the geodetic excitation at the CW frequency, but their

sum (the wind+IB pressure contribution) can do. According to analysis by using the wobble-domain approach, the amplitudes of wobble calculated from wind+IB pressure, wind, and IB pressure contributions in the AAM function coincide with 102.1%, 99.5%, and 26.8% of amplitude of the observed Chandler wobble, respectively [*Furuya et al.,* 1997]. Common points to our and their results are that the atmospheric variations have enough power to excite the Chandler wobble, in which the wind contribution dominates over IB pressure contribution.

Additionally it is evident from Figures 2.14 that the wind+IB pressure, wind, and IB pressure contributions have the significant coherence with the geodetic excitation function exceeding 90% confidence threshold around the CW frequency. This feature is almost the same as the those pointed out by the previous studies [e.g., *Wilson and Haubrich,* 1976; *Chao,* 1993; *Kuehne et al.,* 1993]. On the other hand, the phase advances of the wind+IB pressure, wind, and IB pressure contributions to the geodetic excitation at the CW frequency are observed as 27°, −12°, and 71°, respectively, where negative value means phase lag. The interpretation of these phase will be mentioned later.

For comparison, we also show the power spectra, squared coherences, and phases for the wind+IB pressure, wind, and IB pressure contributions based on NCEP[BP] in Figures C.1a, C.1b, and C.1c in Appendix C, respectively. The wind contribution is completely different from that of the JMA[SP] in the following points; (1) its minor role in excitation of the wobble at frequency bands between -3 to 3 cpy; (2) the frequency-depending pattern of its spectral amplitude which does not increase at low frequency in spite of the increase of that based on the JMA AAM function; (3) no remarkable spectral peak in it near the CW frequency. In contrast, there seems no considerably difference between NCEP[BP] and JMA[SP] in power spectra, coherences, and phases for the IB pressure contribution. As a result, it turns out that the wind+IB pressure contribution from NCEP[BP] can hardly account for the geodetic excitation around the CW frequency.

Time Variations in the Chandler Wobble Excitation

Since the wind+IB pressure, wind, and IB pressure contributions have remarkable broad power spectral peaks near the CW frequency, we further examine how these contributions behave as the CW excitation. Figure 2.15a shows the temporal variations in the CW excitation powers, coherences, and phase differences of/between the geodetic excitation and the contributions from wind+IB pressure, wind, and IB pressure calculated as partial cross sections on their frequency-time spectra (see Figures C.3 in Appendix C) through the method

mentioned in section 2.4.3, where the variations are displayed in the center day of the 8 years sliding window for the period 1987-1995. The figure also provides confidence thresholds for their CW excitation powers and cohereces at each time.

It is evident from Figure 2.15a that the geodetic and atmospheric CW excitation powers vary with time, where their statistical reliability exceed 90% confidence threshold by F-test. It is worthy to note that the CW excitation power from wind+IB pressure vary with time having comparable amplitude to that of the geodetic CW excitation. Their amplitude ratio varies within 0.87-1.56 (the averaged value is 1.15), showing the wind+IB pressure contribution is larger than the geodetic excitation in mostly analysis period. The same kinds of temporal variations in the CW excitation were also illustrated by *Celaya et al.* [1999], in which the calculated CW excitation inferred from the observed wobble data for the period 1900-1997 but simulated excitation functions of the atmosphere, ocean, and land water based on non-controlled run of a coupled climate system model developed at the NCAR are used for a comparison, so that no discussion for the real CW excitation was made.

The CW excitation power from wind exceeds 80% of the geodetic one during 1987-1992 but decreases to about 50-60% after 1993. On the other hand, the IB pressure contribution cannot account for only 20-30% of the geodetic CW excitation. This feature is the same as the previous conclusions by *Wilson and Haubrich* [1976] and *Wahr* [1983]. However, interestingly, it increases to reach 60% of amplitude of the geodetic CW excitation after 1993. It turns out that the wind and IB pressure contributions to the CW excitation complementarily vary with time each other, as if they held angular momentum conservation of the atmosphere-mantle system, although the wind contribution always dominates over the IB pressure contribution. In addition, the reason why reliability for the spectral peak of wind contribution near the CW frequency cannot reach 90% confidence threshold as shown in Figure 2.14b is attributable to the temporal variation in the wind contribution to the CW excitation.

The phase advances of the wind+IB pressure contribution with respect to the geodetic CW excitation vary from -4 to 50° (the averaged value is 26°). These phase advances, however, are possibly explained by the contribution from ocean currents and ocean bottom pressure [*Ponte and Stammer,* 1999]. In consequence, it turns out that the atmospheric variations by themselves maintain the observed Chandler wobble.

For comparison, we also show the temporal variations in the CW excitation powers, coherences, and phase differences of/between the geodetic excitation and the contributions from the wind+IB pressure, wind, and IB pressure based on NCEP[BP] in Figure C.2 in Appendix C. Though the temporal variation in the IB pressure contribution to the CW excitation power agrees with that based on the JMA[SP], the wind contribution hardly vary

with time, playing a minor role.

Zonal and Meridional Wind Contributions

Figure 2.15b shows the temporal variations in the CW excitation powers, coherences, and phase differences of/between the geodetic excitation and the contributions from total, zonal, and meridional winds. It is found that the partial contributions from zonal and meridional winds have large amplitudes in comparison with that of the geodetic excitation, but they are almost canceled out due to their out-of-phase relationship, indicating that the total wind contribution to the CW excitation depends on their slight difference. This feature is consistent with the wind contribution to the annual wobble as mentioned in section 2.5.2. Figure 2.15b also reveals that zonal wind contribution dose not have significant power and coherence exceeding 90% confidence threshold with respect to the geodetic one, while the meridional wind contribution dose.

The zonal wind contribution varies with time having in-phase relationship to that of the geodetic CW excitation until 1991, although this relationship becomes out-of-phase one after 1991. The phase difference for the meridional wind contribution is almost opposite to that of the zonal wind contribution, suggesting that the phases of the zonal and meridional wind contributions to CW excitation complementarily also vary with time each other.

Tropospheric and Stratospheric Wind Contributions

Figure 2.15c shows the CW excitation powers, coherences, and phase differences of/between the geodetic excitation and the contributions from total, tropospheric, and stratospheric winds. The tropospheric wind contribution exhibits always stronger CW excitation than that of the stratospheric wind contribution. This dominance in the tropospheric wind contribution is also supported by its higher CW excitation coherence and small phase difference with respect to the geodetic CW excitation, indicating that the tropospheric wind plays an important role to excite the Chandler wobble. This feature corresponds to the result that the winds in the lower troposphere play an important role to maintain the annual wobble as mentioned in section 2.5.2. In addition, we note that the CW excitation power from wind based on NCEP[BP] shown in Figure C.2 in Appendix C has the comparable amplitude with similar phase to that of stratospheric wind contribution in the JMA[SP].

The power spectra of the tropospheric and stratospheric wind contributions like Figures 2.14 (see Figure 2.16) reveal that tropospheric wind contribution has remarkable spectral peak at frequency bands between 0.6 and 0.8 cpy (on a timescale between about 14 and 20

months), while that the stratospheric wind contribution is active at frequency bands between 0.6 and 0.75 cpy (on a timescale between about 15 and 20 months) and between 0.3 and 0.4 cpy (on a timescale between about 29 and 40 months).

These oscillatory variations may be connected with the fluctuations of zonal wind in the upper troposphere such as the Quasi-Biennial Oscillation (QBO) through a nonlinear effect. On the other hand, these variations may link to the ENSO in the tropical Pacific Ocean, since a mean activity period of El Niño is about 16 months [e.g., *Philander,* 1990]. It is well known that the interannual fluctuations in length of day are closely connected with QBO and/or ENSO [*Chao,* 1989; *Dickey et al.,* 1994].

From Figures 2.15a and 2.15c, the major atmospheric CW excitation is confirmed to be the wind contribution, in particular, the tropospheric wind contribution. Hence, the 14-16 months periodicity found in the wind+IB pressure and wind contributions should be attributed to that in the tropospheric wind. One of such oscillatory phenomena in the atmosphere was found in the pole tide [see *O'Conner,* 1986]. *Tsimplis et al.* [1994] verified that the enhanced pole tide in the North Sea is forced by the fluctuation of surface wind stress over the ocean with period of about 14 months.

NIB Pressure Contribution

Figure 2.15d shows the CW excitation powers, coherences, and phase differences of/between the geodetic excitation and the contributions from IB and NIB pressures. It is clear that the NIB pressure contribution has much lager amplitude than that of geodetic CW excitation.

The CW excitation power from IB pressure starts to increase in 1990. This feature is also found in that based on NCEP[BP] in Figure C.2 in Appendix C. Since the temporal variation in the NIB pressure contribution is not very remarkable in that time, we speculate that the atmospheric mass over the ocean fluctuating at the CW frequency begins to move to the land surface from the ocean surface in 1990. The phase shift of the CW excitations from zonal and meridional wind shown in Figure 2.15b may also have some relation to this movement.

Additional Discussions

In our results, there is some gap in the CW excitation power and phase between the geodetic excitation and the wind+IB pressure contribution, indicating somewhat excess amplitude and about 30° phase advance of the wind+IB pressure contribution (hereafter referred to as CW excitation gap). The CW excitation gap implies an existence of other contribution

such as ocean and land water. *Ponte and Stammer* [1999] stated that the ocean plays an important role to excite CW. According to their Figure 7b, showing the phasor diagram for the CW excitation power, the contributions from ocean currents and ocean bottom pressure seems to account for the CW excitation gap.

Gross and Chao [1985] stated the high correlation of the observed Chandler wobble and El Niño, which may link to fluctuations of oceanic angular momentum on the timescale of about 14-16 months, for the period 1982-1983. Thus, we calculate a correlation of the CW excitation gap to the activity of El Niño, using NINO3 and SOI (Southern Oscillation Index) that are the index in terms of the sea surface temperature in the region to monitor El Niño and of the difference in the atmospheric pressure between Tahiti and Darwin, respectively. Figure 2.17 shows the time series and cross correlation coefficients of/between the CW excitation gap and NINO3 and SOI, in which amplitudes of their time series are standardized by their standard deviations. As a result, we obtain their significant correlation (a correlation coefficient of 0.67 for NINO3). This suggests that the ocean (or oceanic angular momentum) behaves like negative contribution to the CW excitation power to cancel out the CW excitation gap.

On the other hand, the simulation study by *Celaya et al.* [1999] indicates an importance of contributions from winds and ocean currents, but they pointed out that the contribution from the hydrosphere, i.e. movements in land water, is nearly negligible in comparison with the atmospheric and oceanic contributions, although it has been considered to be important in previous studies [e.g., *Wilson and Haubrich,* 1976].

If the atmosphere by itself has enough power to excite the Chandler wobble as shown above, we reach an understanding that the large earthquakes are connected with the atmospheric variations through the exchanges of the angular momentum at the CW frequency between the atmosphere and the mantle, taking into account the correlation between the activity of large earthquakes and the amplitude of the Chandler wobble [*Kanamori,* 1977]. Near future, we can expect to have a full understanding of the exchange of angular momentum between the mantle, atmosphere, and oceans near the CW frequency, through which we provide a dynamical information how the Chandler wobble is connected with ENSO.

2.6 Conclusion

The atmospheric pressure and wind contribution to the axial and equatorial angular momentum budgets, in annual and semiannual variation are discussed during 1988 - 1997. The data sets used here are SPACE97 and EOPC04 for the length of day (LOD) change and the

wobble, respectively, and two atmospheric angular momentum (AAM) functions calculated from the operational objective analysis data, of the Japan Meteorological Agency (JMA), and the reanalysis data, of the National Centers for Environmental Prediction / National Center for Atmospheric Research (NCEP/NCAR). The axial AAM functions from the two analysis data sets in annual variation agree well and roughly in semiannual variation, with the function inferred from the observed LOD. In particular, the wind contributions playing major roles in them agree very well with each other. The equatorial AAM functions, from the two data sets, show the different wind contributions to the function inferred from the observed wobble in both annual and semiannual variations. The disagreement in the equatorial wind contributions is attributable in part to the different vertical wind integration methods employed in the archived AAM functions in IERS from JMA and NCEP. There is still a large disagreement in the equatorial wind contributions, calculated by the same method. The AAM function based on JMA give a better agreement with the functions inferred from the observed annual wobble. Though there are the discrepancy between the prograde and retrograde AAM functions, from two data sets, and the functions inferred from the observed annual wobble, the discrepancy based on JMA is smaller than that based on NCEP.

The equatorial wind contribution to the annual wobble depends upon its corresponding difference between the large zonal and meridional wind contributions, which have almost the same amplitudes, but cancel each other. The regional contributions of zonal wind to the annual wobble distribute around prevailing westerly zone remarkably, which almost cancel each other. The global contribution of zonal wind are affected by regional zonal winds blowing above Southeast Asia at $30°N$ in troposphere, and above the ocean around the Antarctic continent at $60°S$ in the stratosphere. The remarkable regional contributions of meridional wind to the annual wobble are found in northern hemisphere, especially above the coast around the Bering Sea, and the northern margin of North America for the stratospheric wind. The latitude belt contribution of meridional wind in troposphere correspond to Hadley, Ferrel, and Polar atmospheric circulations. The distribution of these regional wind contribution suggests that annual wobble is related to the atmospheric circulation accompanying with heat transport. The equatorial wind contributions in troposphere from JMA and NCEP/NCAR data sets calculated by the same method, exhibit discrepancies arising from the different regional meridional winds in troposphere associated with the Asian monsoon that shows the most remarkable seasonal signal over the world. Since JMA must carefully handle the Asian monsoon due to the high quality forecasts, the wind contribution based on JMA, showing a better agreement with functions inferred from the observed annual wobble, is a more natural one.

Comparing the atmospheric angular momentum (AAM) function based on the Japan Meteorological Agency (JMA) with the function inferred from the observed wobble for the period 1983-1998, it is found that a sum of the atmospheric wind and inverted-barometer (IB) pressure variations dominating on the time scale between 14 and 16 months has a little excess power with about 30 degrees phase advance to that required to excite the observed wobble, in which their coherence exceeds 95% confidence threshold. In addition, the temporal variations in the excitation of the Chandler wobble (CW excitation) are calculated from the shifted eight years data of the AAM function and that inferred from the observed wobble by assuming the CW excitation to be the power spectral amplitudes from 0.8 to 0.9 cycle per year. The result shows that the wind and IB pressure contributions to the CW excitation complementarily vary with time each other, although the wind contribution always dominates over the IB pressure contribution throughout the analyzing period of 1987-1995, in which both the temporal variations have almost the same patterns. These reveal that the atmospheric wind and IB pressure variations by themselves maintain the observed Chandler wobble during the analysis period.

	This Study [*Eubanks*, 1993]		*Barnes et al.* [1983]	
	$C-A$	Transfer Function	$C_m - A_m$	Transfer Function
$\tilde{\chi}^P$	$2.610 \times 10^{35} kgm^2$	1.098	$2.344 \times 10^{35} kgm^2$	1.00
$\tilde{\chi}^W$	$2.610 \times 10^{35} kgm^2$	1.5913	$2.344 \times 10^{35} kgm^2$	1.44
	This Study [*Eubanks*, 1993]		*Barnes et al.* [1983]	
	C_m	Transfer Function	C_m	Transfer Function
${\chi_3}^P$	$7.1236 \times 10^{37} kgm^2$	0.753	$7.04 \times 10^{37} kgm^2$	0.70
${\chi_3}^P$	$7.1236 \times 10^{37} kgm^2$	0.998	$7.04 \times 10^{37} kgm^2$	1.00

Table 2.1: Transfer Functions and Principal Moments of Inertia. Shown are the transfer functions and the difference between the Earth's axial and equatorial principal moments of inertia employed in this study [*Eubanks*, 1993] and *Barnes et al.* [1983], where $C - A$ and $C_m - A_m$ denote the whole Earth and the mantle, respectively. Note that the AAM functions archived in SBAAM of IERS are based on *Barnes et al.* [1983].

	χ_1		χ_2		χ_3	
	Amp, $\times 10^{-8}$	Phase	Amp, $\times 10^{-8}$	Phase	Amp, $\times 10^{-9}$	Phase
NIB-Pressure						
JMA	8.5 ± 2.4	$219 \pm 16°$	20.6 ± 2.2	$167 \pm 6°$	0.59 ± 0.10	$234 \pm 10°$
NCEP	9.0 ± 2.3	$216 \pm 15°$	19.9 ± 2.3	$166 \pm 6°$	0.58 ± 0.10	$239 \pm 10°$
IB-Pressure						
JMA	3.1 ± 0.6	$179 \pm 11°$	14.4 ± 0.9	$177 \pm 4°$	0.52 ± 0.06	$204 \pm 6°$
NCEP	3.3 ± 0.6	$176 \pm 11°$	13.9 ± 1.0	$177 \pm 4°$	0.45 ± 0.05	$209 \pm 6°$
Wind						
JMA[SP]	3.1 ± 0.9	$47 \pm 16°$	3.6 ± 0.9	$25 \pm 14°$	4.89 ± 0.45	$37 \pm 5°$
NCEP[SP]	0.7 ± 0.6	$99 \pm 50°$	1.1 ± 0.6	$49 \pm 31°$	4.59 ± 0.43	$38 \pm 5°$
NCEP[BP]	2.0 ± 0.5	$29 \pm 14°$	0.7 ± 0.4	$184 \pm 37°$	4.63 ± 0.43	$38 \pm 5°$
NIB-Pressure + Wind						
JMA[SP]	5.4 ± 3.3	$215 \pm 35°$	17.9 ± 3.1	$160 \pm 10°$	4.33 ± 0.55	$35 \pm 7°$
NCEP[SP]	8.7 ± 3.0	$222 \pm 19°$	19.4 ± 2.8	$163 \pm 8°$	4.05 ± 0.53	$35 \pm 7°$
NCEP[BP]	7.1 ± 2.8	$218 \pm 23°$	20.5 ± 2.7	$167 \pm 8°$	4.09 ± 0.53	$35 \pm 7°$
IB-Pressure + Wind						
JMA[SP]	2.5 ± 1.5	$112 \pm 34°$	11.3 ± 1.8	$169 \pm 9°$	4.38 ± 0.50	$38 \pm 6°$
NCEP[SP]	3.6 ± 1.3	$164 \pm 20°$	13.2 ± 1.5	$174 \pm 7°$	4.15 ± 0.48	$39 \pm 7°$
NCEP[BP]	2.0 ± 1.1	$143 \pm 31°$	14.5 ± 1.4	$178 \pm 6°$	4.19 ± 0.48	$39 \pm 6°$
Geodetic						
Observation	3.6 ± 1.4	$82 \pm 21°$	9.4 ± 2.3	$152 \pm 14°$	4.39 ± 0.49	$36 \pm 6°$

Table 2.2: Estimated Amplitudes and Phases in Annual Variation. The estimated amplitude and phase in annual variation of the geodetic excitations and the AAM functions. JMA[SP], NCEP[SP], and NCEP[BP] denote the data and the methods for the wind integration used in this study (see section 2.4.3 for details). The phases are defined to January 1. The errors in the table are the least-square fitting errors.

	χ_1		χ_2		χ_3	
	Amp, $\times 10^{-8}$	Phase	Amp, $\times 10^{-8}$	Phase	Amp, $\times 10^{-9}$	Phase
NIB-Pressure						
JMA	2.6 ± 2.4	$187 \pm 53°$	2.8 ± 2.2	$2 \pm 45°$	0.18 ± 0.10	$82 \pm 31°$
NCEP	2.9 ± 2.3	$191 \pm 45°$	3.7 ± 2.3	$358 \pm 35°$	0.18 ± 0.10	$82 \pm 32°$
IB-Pressure						
JMA	1.2 ± 0.6	$86 \pm 29°$	3.5 ± 0.9	$30 \pm 15°$	0.10 ± 0.06	$96 \pm 31°$
NCEP	1.3 ± 0.6	$90 \pm 27°$	3.5 ± 1.0	$27 \pm 16°$	0.10 ± 0.05	$98 \pm 28°$
Wind						
JMA[SP]	0.8 ± 0.9	$288 \pm 62°$	0.3 ± 0.9	$11 \pm 156°$	2.67 ± 0.45	$248 \pm 10°$
NCEP[SP]	0.5 ± 0.6	$294 \pm 70°$	0.2 ± 0.6	$212 \pm 177°$	2.63 ± 0.43	$249 \pm 9°$
NCEP[BP]	0.7 ± 0.5	$259 \pm 41°$	0.3 ± 0.4	$115 \pm 81°$	2.63 ± 0.42	$249 \pm 9°$
NIB-Pressure + Wind						
JMA[SP]	2.6 ± 3.3	$205 \pm 72°$	3.1 ± 3.1	$3 \pm 57°$	2.50 ± 0.55	$247 \pm 13°$
NCEP[SP]	2.9 ± 2.9	$202 \pm 59°$	3.5 ± 2.8	$356 \pm 46°$	2.46 ± 0.53	$247 \pm 12°$
NCEP[BP]	3.2 ± 2.8	$202 \pm 49°$	3.5 ± 2.7	$3 \pm 44°$	2.46 ± 0.53	$248 \pm 12°$
IB-Pressure + Wind						
JMA[SP]	0.6 ± 1.5	$56 \pm 148°$	3.8 ± 1.8	$28 \pm 28°$	2.59 ± 0.50	$247 \pm 11°$
NCEP[SP]	0.9 ± 1.3	$75 \pm 83°$	3.3 ± 1.5	$27 \pm 26°$	2.54 ± 0.48	$247 \pm 11°$
NCEP[BP]	0.7 ± 1.1	$101 \pm 91°$	3.5 ± 1.4	$32 \pm 23°$	2.55 ± 0.48	$247 \pm 11°$
Geodetic						
Observation	2.8 ± 1.4	$194 \pm 28°$	5.8 ± 2.3	$21 \pm 23°$	2.99 ± 0.49	$243 \pm 9°$

Table 2.3: Estimated Amplitudes and Phases in Semiannual Variation.

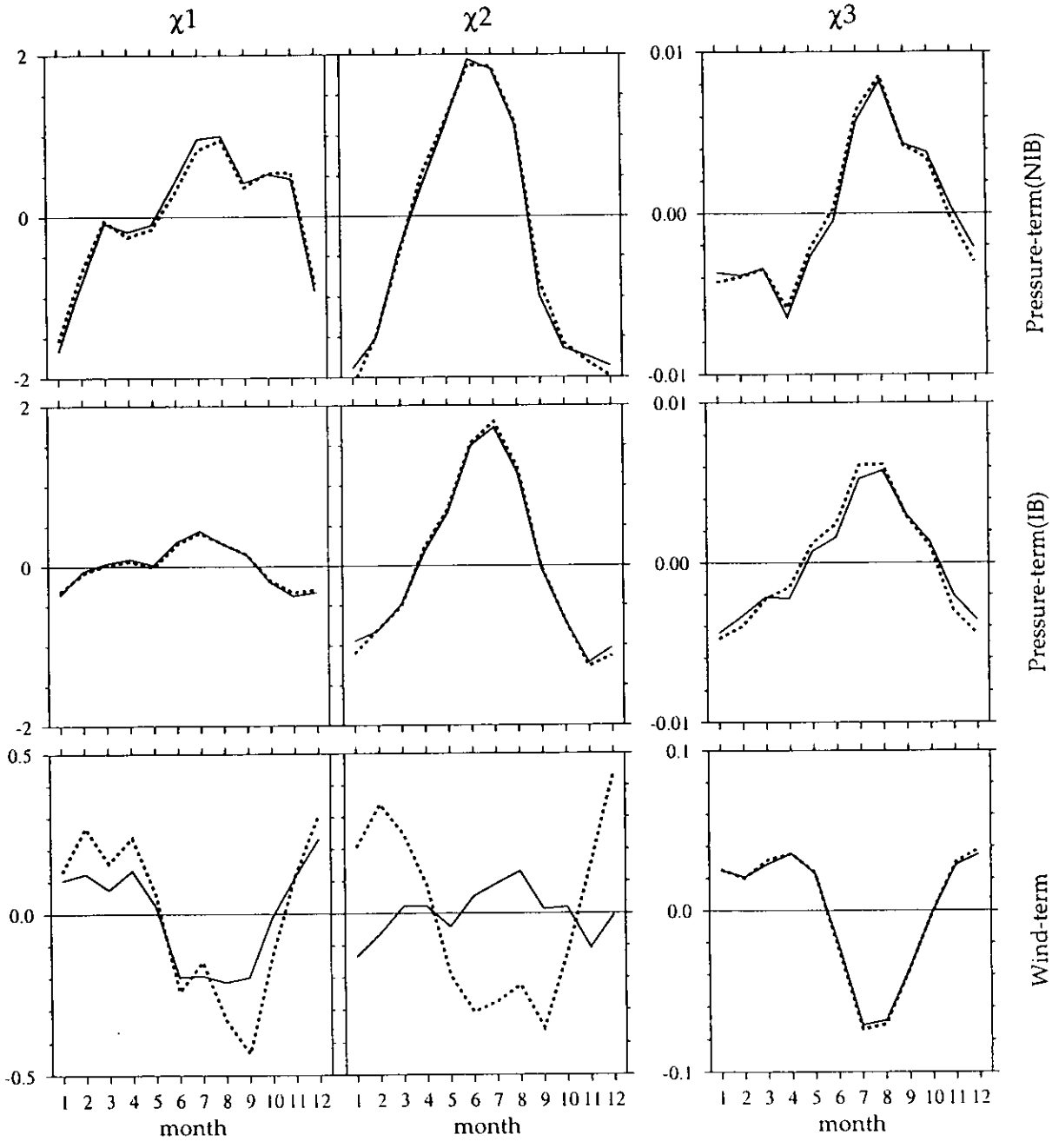

Figure 2.1a: The seasonal patterns in the equatorial and axial components of the archived National Centers for Environmental Prediction (NCEP) (solid line) and Japan Meteorological Agency (JMA) (dotted line) atmospheric angular momentum (AAM) functions in International Earth Rotation Service during 1988-1997. Unit is 10^{-7}.

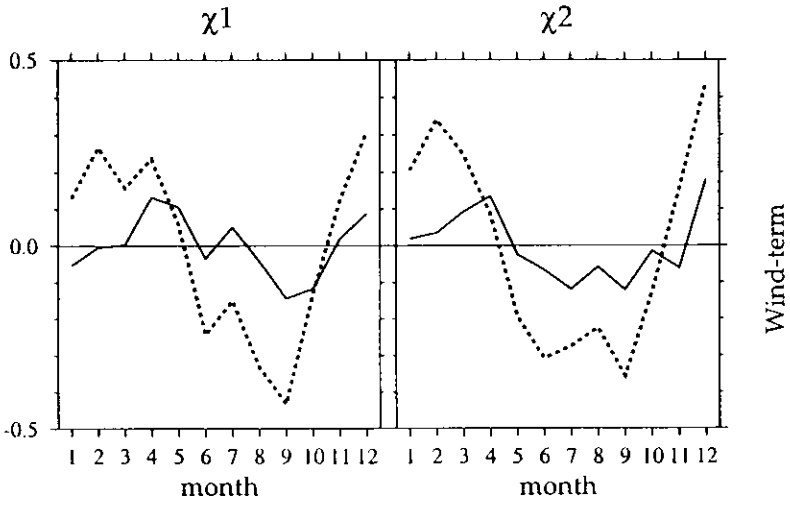

Figure 2.1b: The seasonal patterns in the equatorial wind terms recomputed from the NCEP/National Center for Atmospheric Research (NCAR) (solid line) reanalysis and JMA (dotted line) operational data by the surface pressure (SP) method mentioned in section 2.4.2.

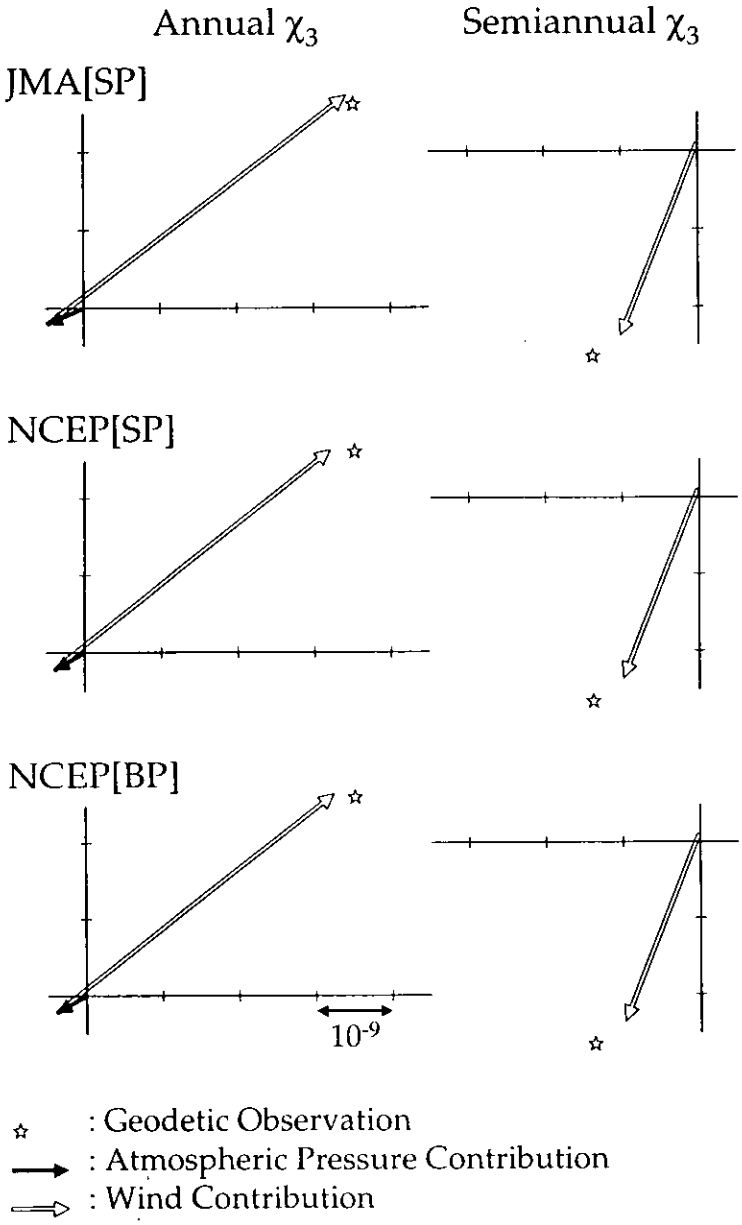

Figure 2.2: The phasor plots showing the axial angular momentum budgets in annual and semiannual variations. Stars denote the functions inferred from the observed length-of-day (LOD) change. Vectors indicate the inverted barometer (IB) pressure and wind terms in JMA[SP], NCEP[SP], and NCEP[BP] (see section 2.4.2 for details) in (left) annual and (right) semiannual variations for the period 1988-1997. Horizontal and vertical axes indicate the coefficients of cosine and sine terms, respectively, in each sinusoid. Length and direction of the vectors denote the amplitude and the phase with respect to January 1. Note that the vectors of the semiannual pressure term are too small to be displayed.

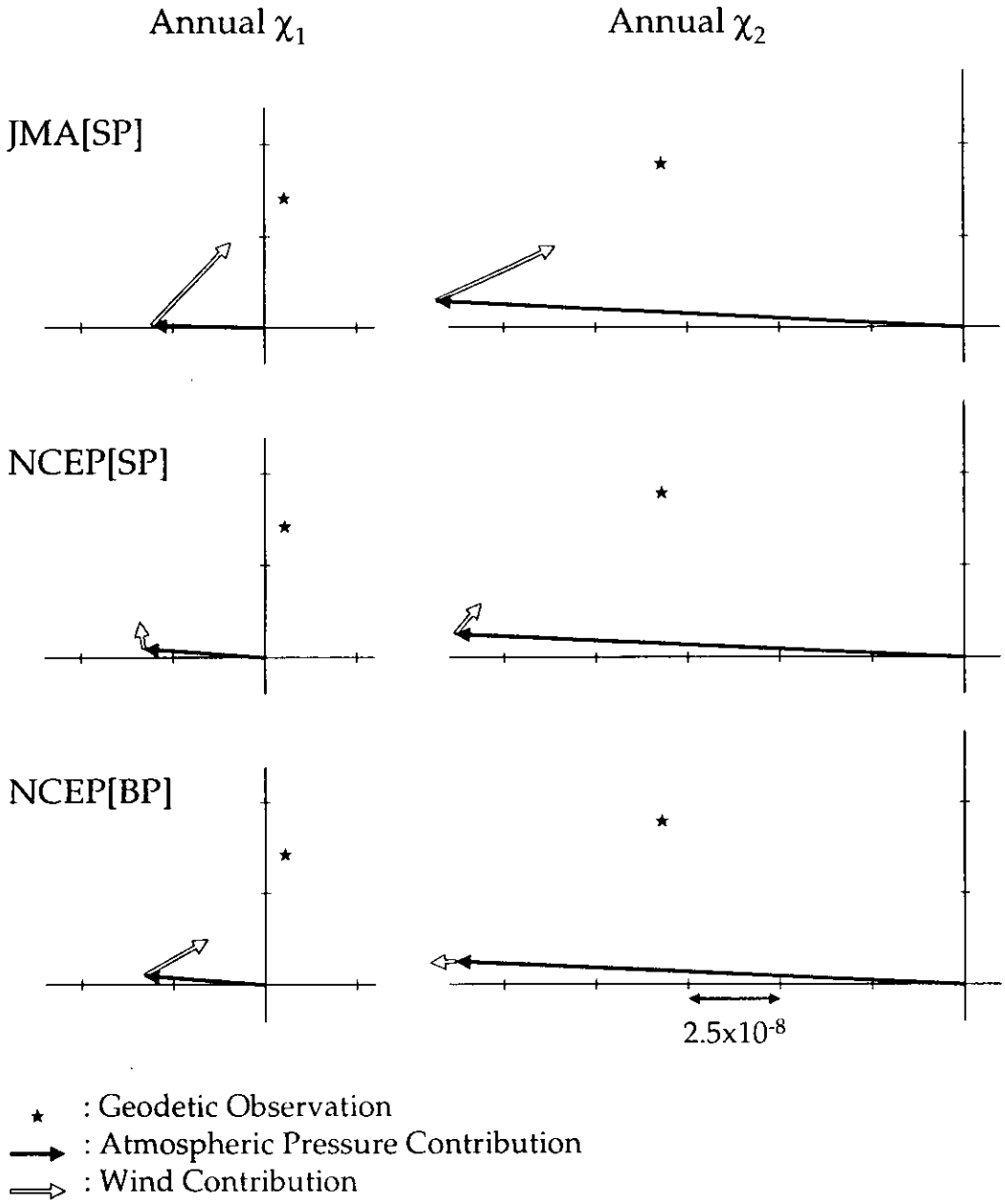

Figure 2.3a: Same as Figure 2.2 but for the equatorial angular momentum budgets in annual variation. Left and right panels show those in χ_1 and χ_2 components, respectively.

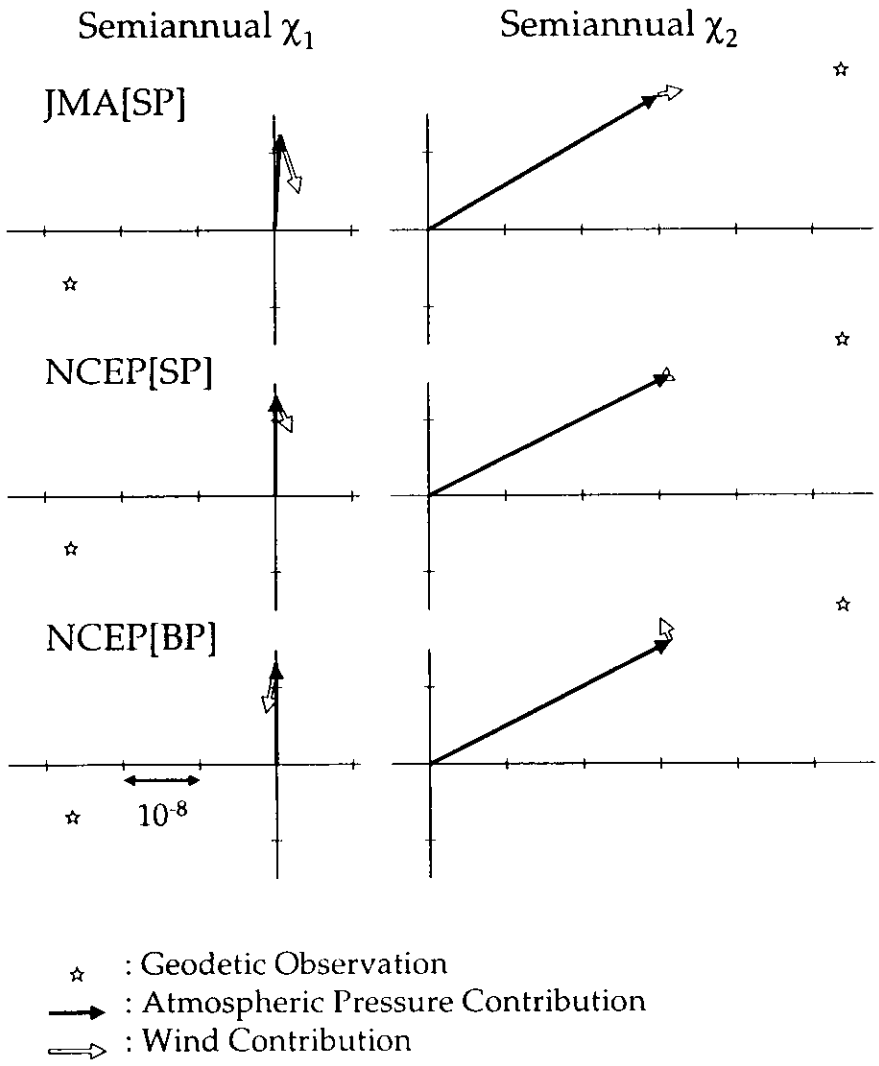

Figure 2.3b: Same as Figure 2.3a but for in semiannual variation.

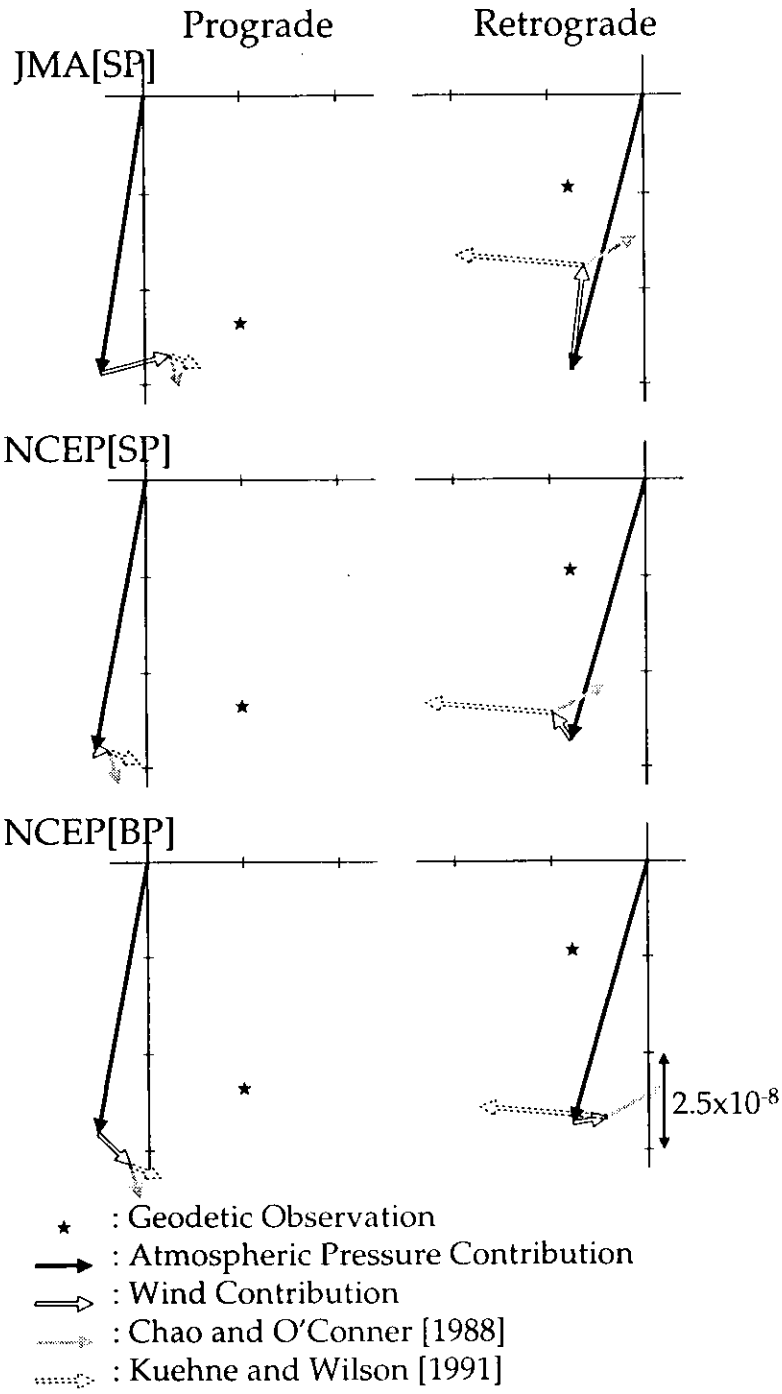

Figure 2.4: Same as Figure 2.3a but for prograde and retrograde components.

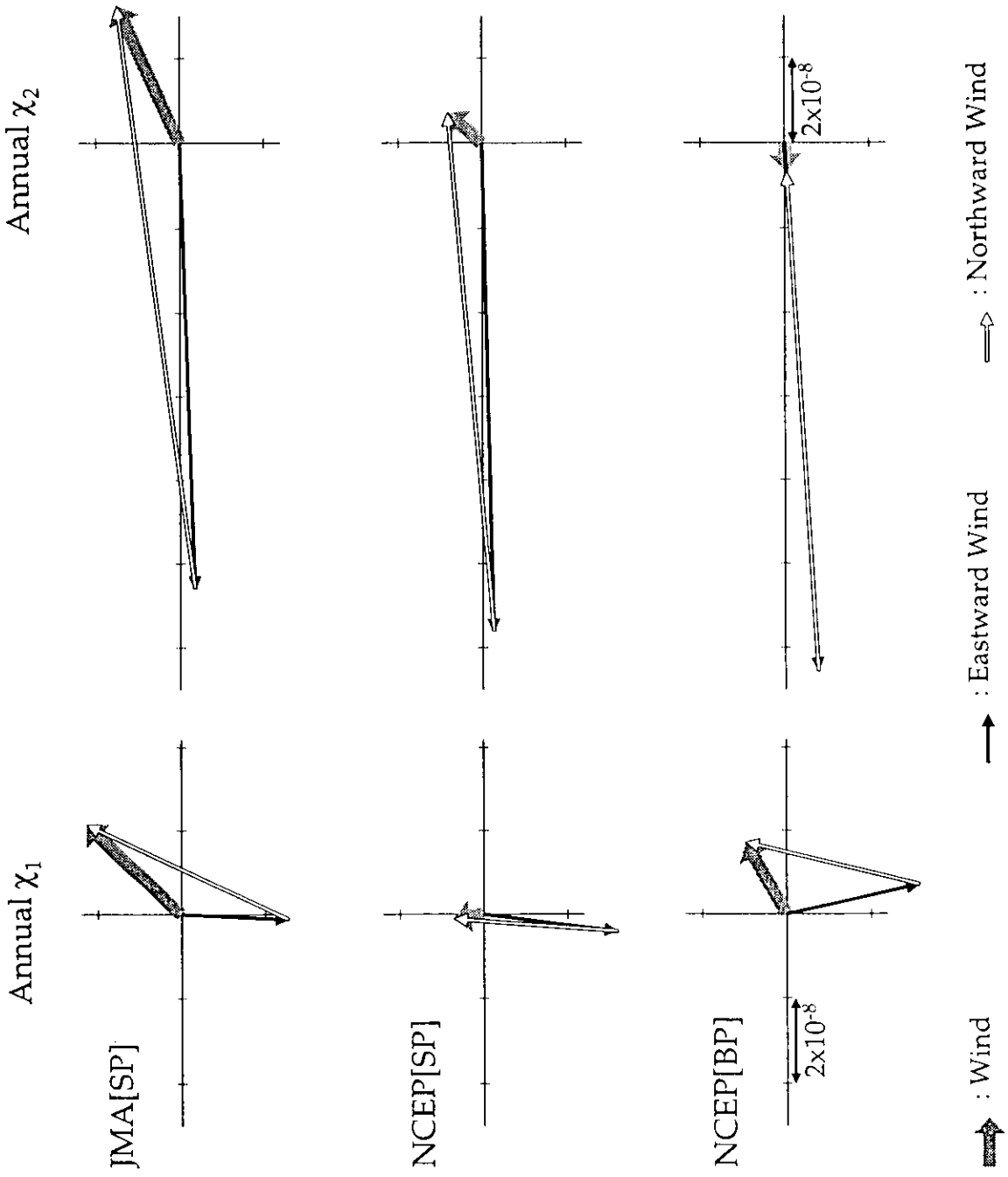

Figure 2.5: The zonal and meridional wind contributions to the equatorial angular momentum budgets in annual variation. Legends are as same as in Figure 2.2. Left and right panels show those χ_1 and χ_2 components, respectively.

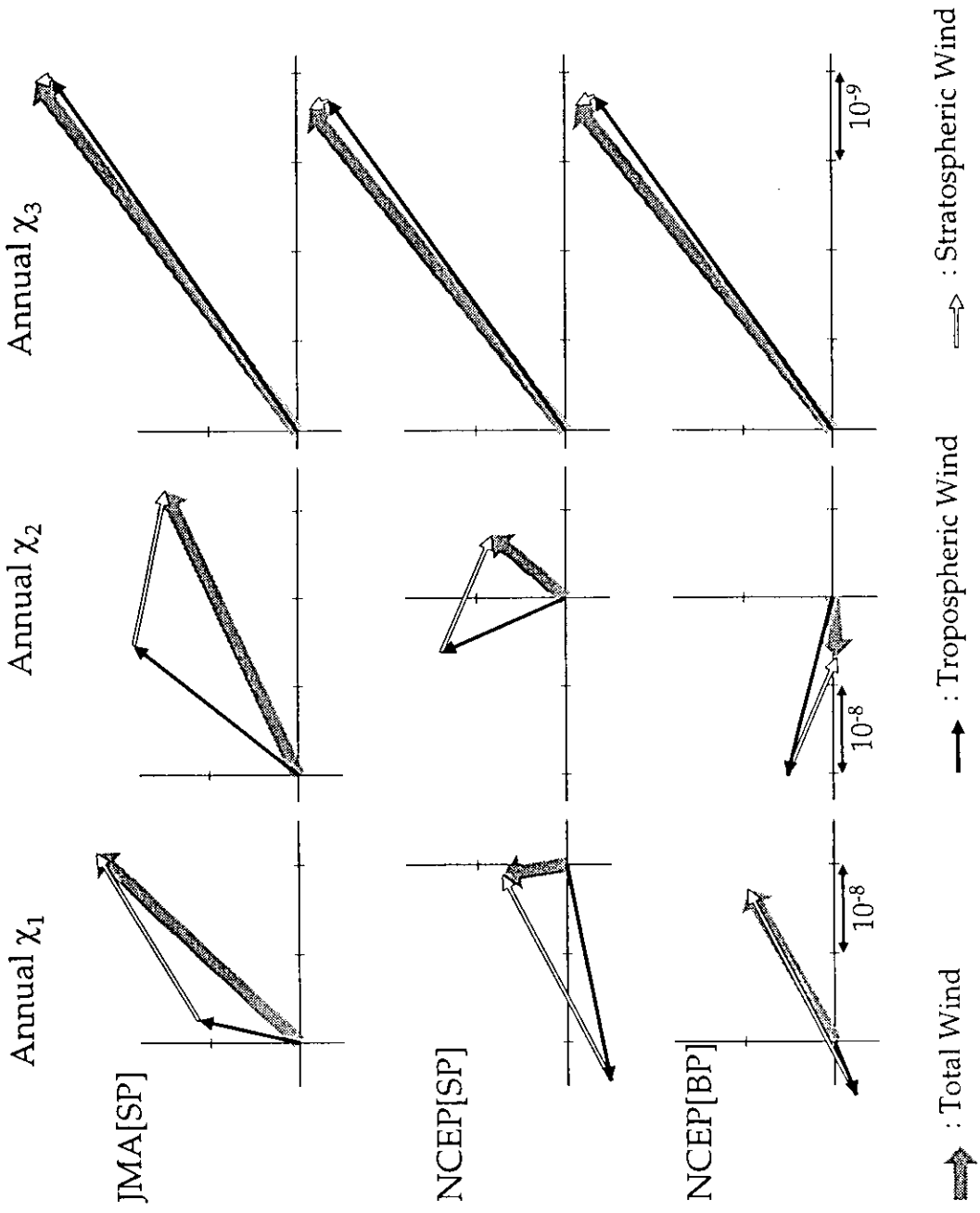

Figure 2.6: The tropospheric and stratospheric wind contributions to the axial and equatorial angular momentum budgets in annual variation. Legends are as same as in Figure 2.2. Left, middle, and right panels show those χ_1, χ_2, and χ_3 components, respectively.

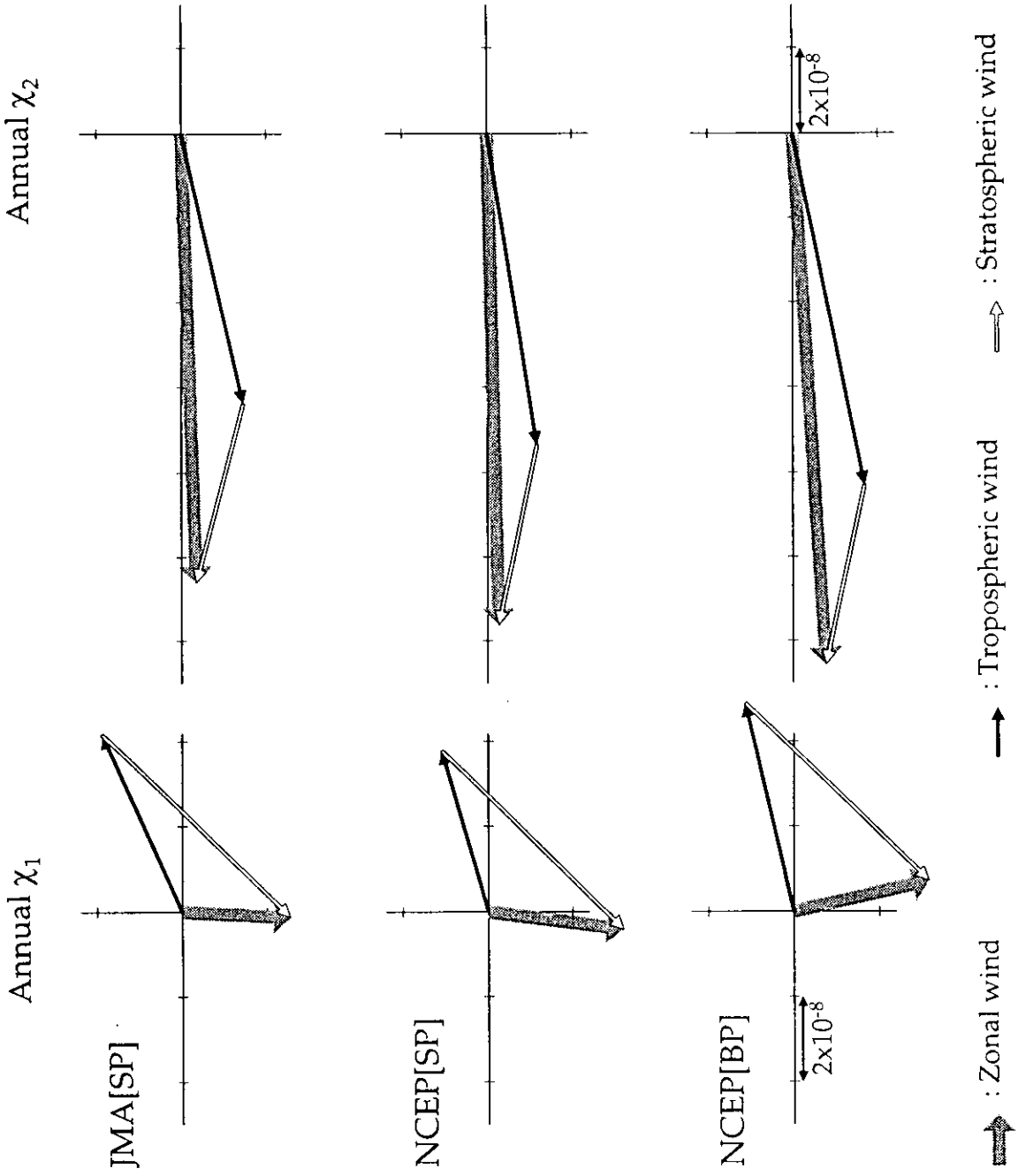

Figure 2.7a: The separate zonal wind contributions of troposphere and stratosphere to the annual wobble. Legends are as same as in Figure 2.2.

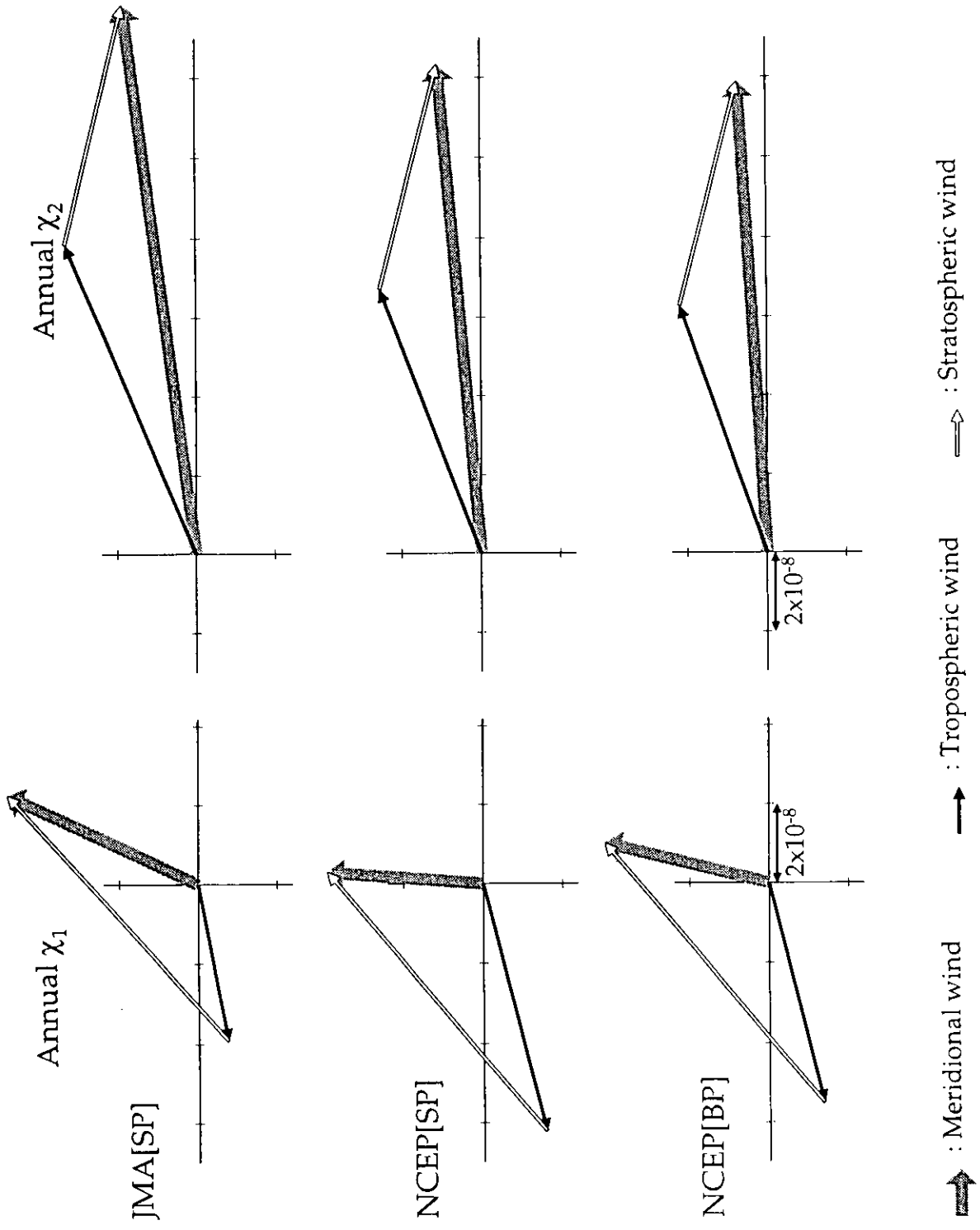

Figure 2.7b: Same as Figure 2.7a but for meridional wind contribution.

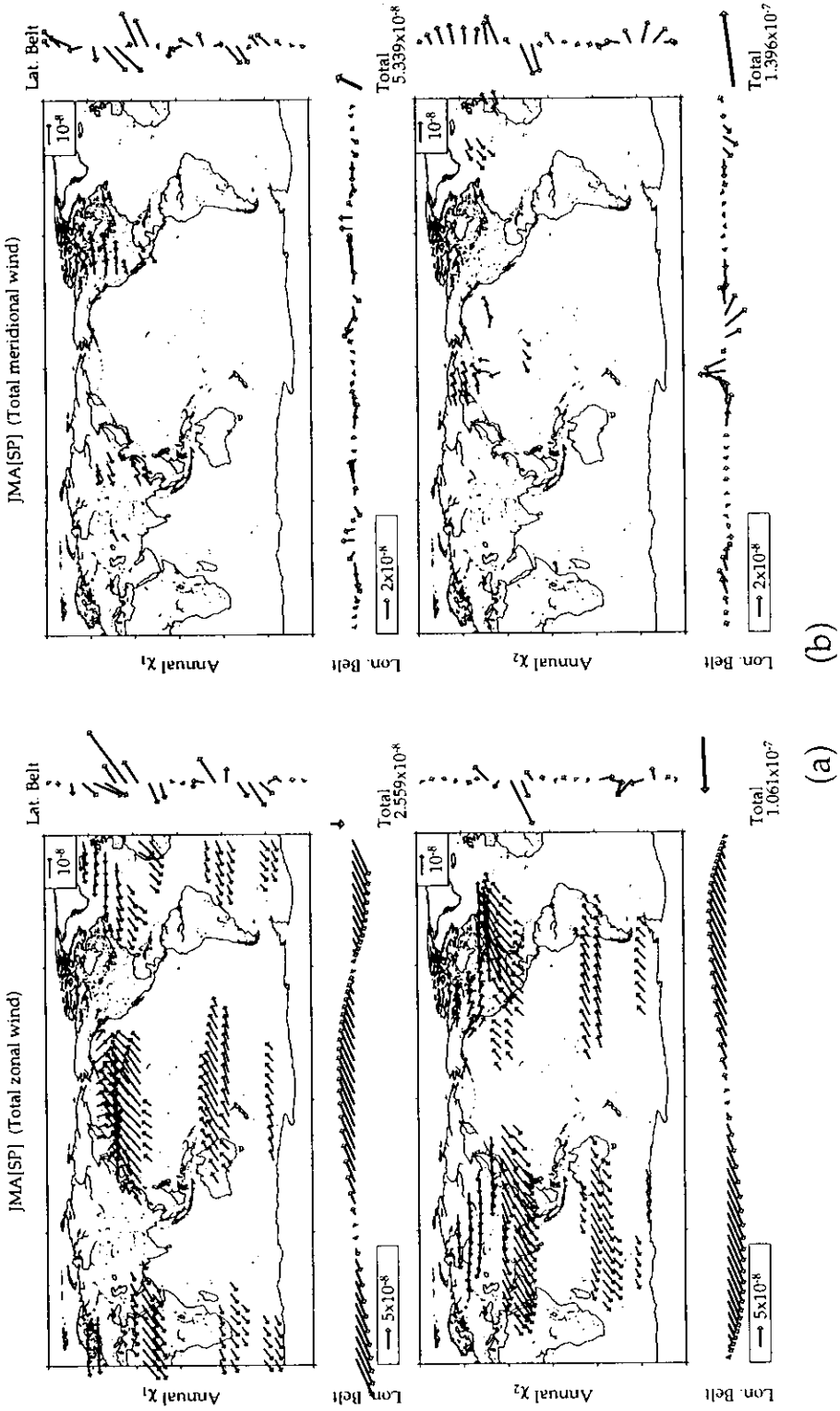

Figure 2.8: The regional wind contributions to the annual wobble, based on JMA[SP]. Each vector is displayed in 7.5° square grid in the same manner as in Figure 2.2. Upper and lower panels show those in χ_1 and χ_2 components, respectively. Note that the regional vectors of less than half the magnitude of the unit shown in the figure are not displayed, but that the latitude and longitude belt contributions, are shown in right sides and lower sides of the each figure, respectively. Vector shown as "Total" at lower right corners of each figure is equal to the zonal or meridional wind contribution based on JMA[SP] in Figure 2.5. (a) zonal wind contribution (b) meridional wind contribution.

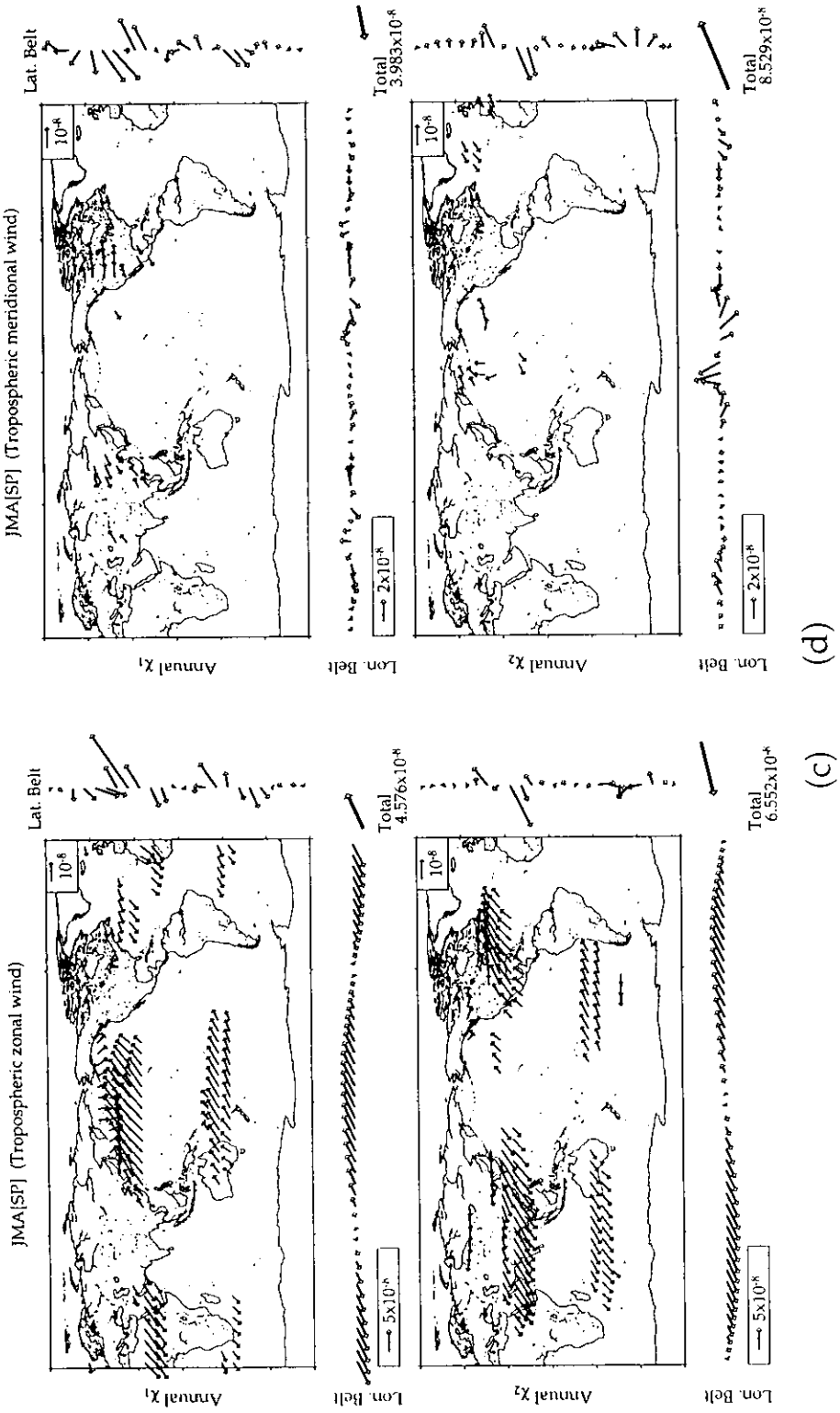

Figure 2.8: (c) zonal wind contribution in the troposphere. Vector shown as "Total" is equal to the tropospheric zonal wind contribution based on JMA[SP] in Figure 2.7a. (d) meridional wind contribution in the troposphere. Vector shown as "Total" is equal to the tropospheric meridional wind contribution based on JMA[SP] in Figure 2.7b.

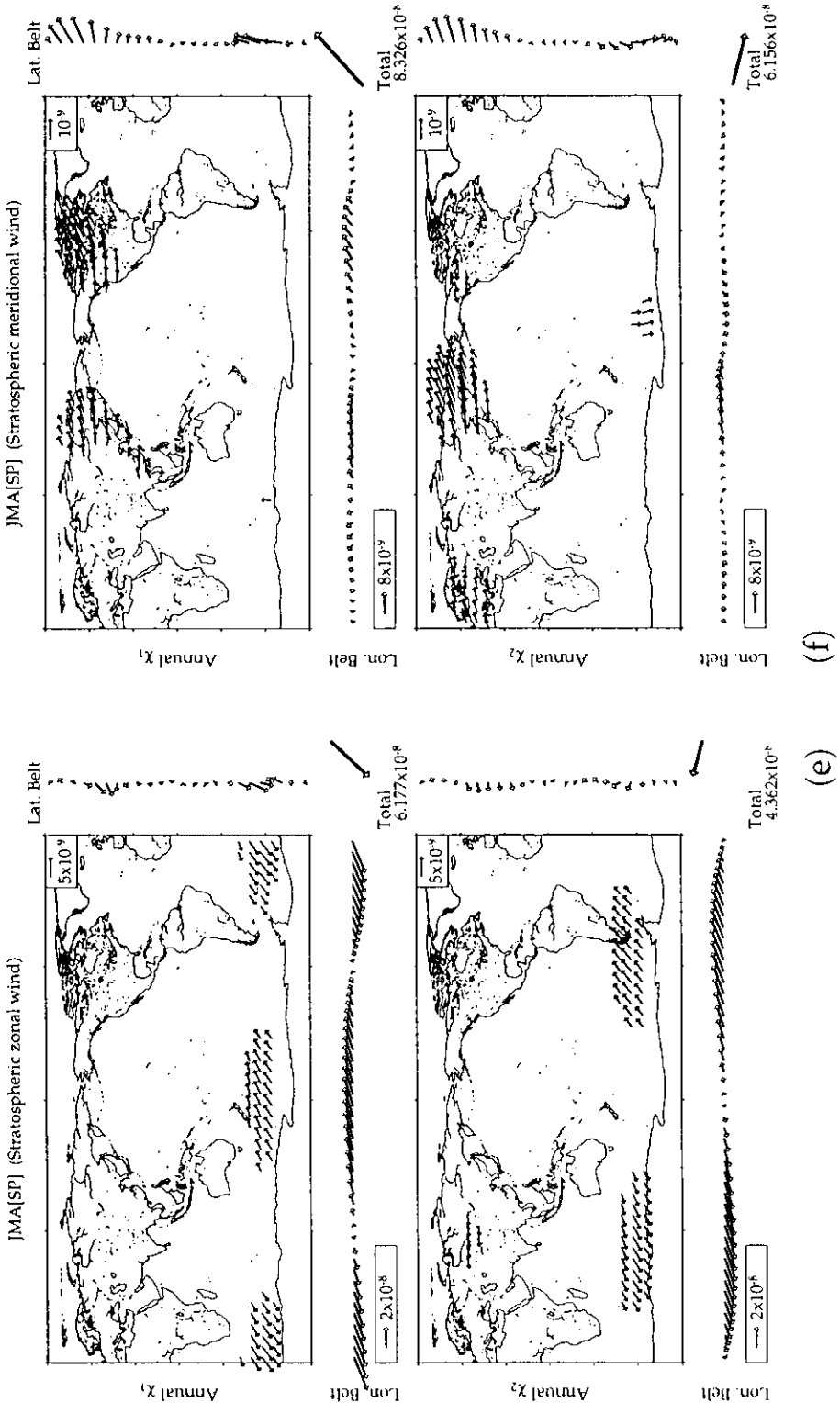

Figure 2.8: (e) zonal wind contribution in the stratosphere. Vector shown as "Total" is equal to the stratospheric zonal wind contribution based on JMA[SP] in Figure 2.7a. (f) meridional wind contribution in the stratosphere. Vector shown as "Total" is equal to the stratospheric meridional wind contribution based on JMA[SP] in Figure 2.7b.

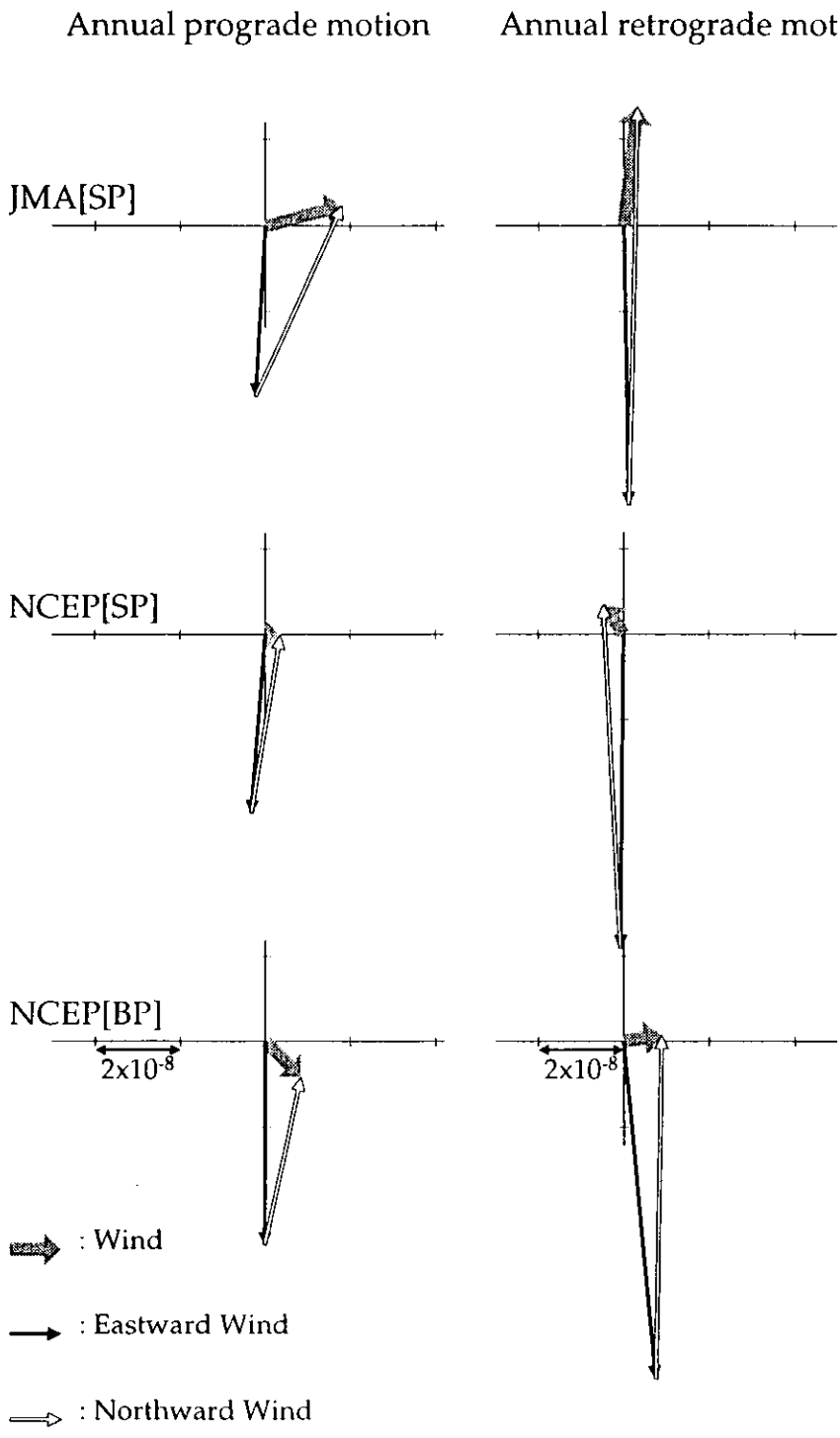

Figure 2.9: Same as Figure 2.5 but for prograde and retrograde components.

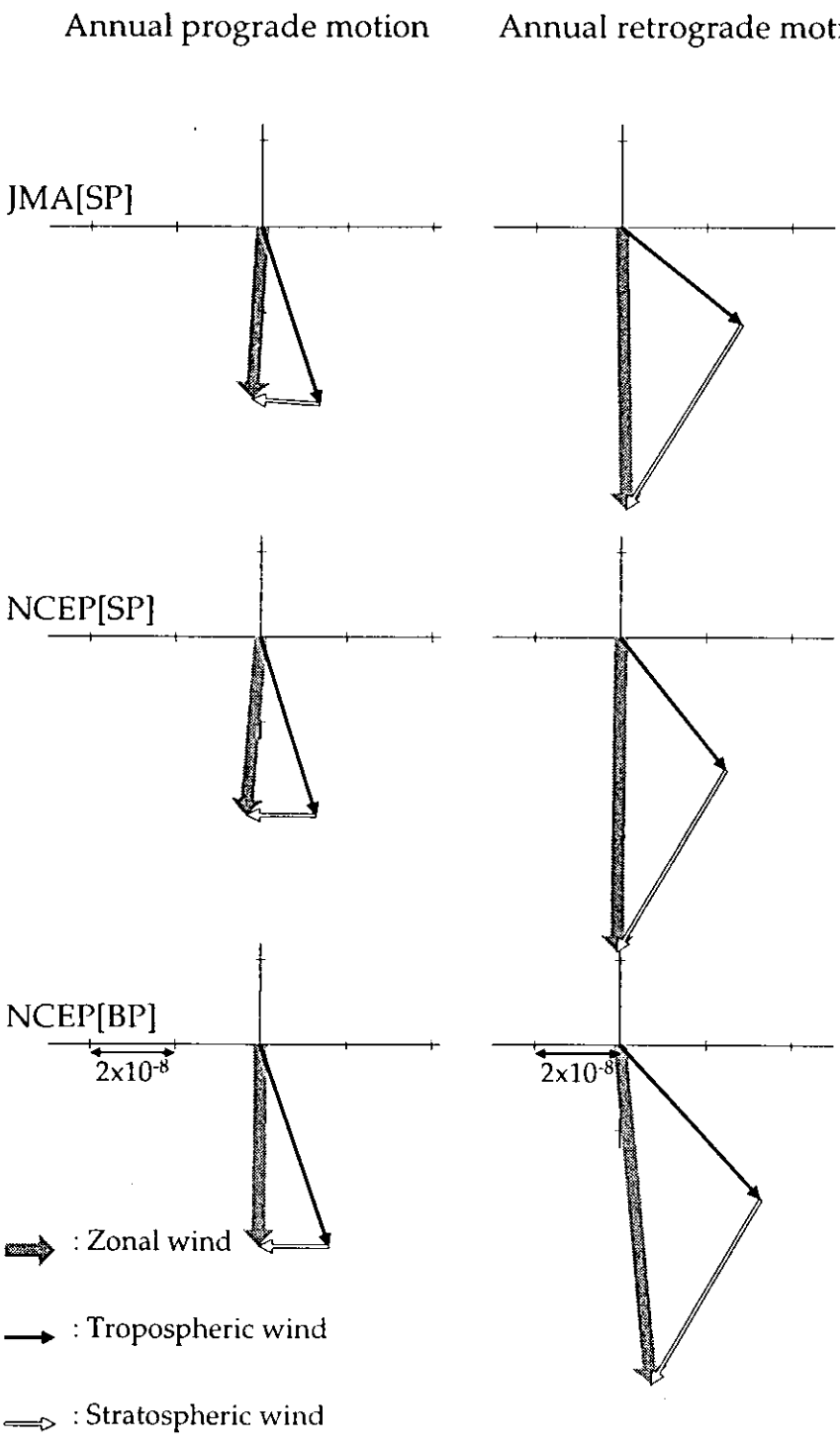

Figure 2.10a: Same as Figures 2.7a but for prograde and retrograde components.

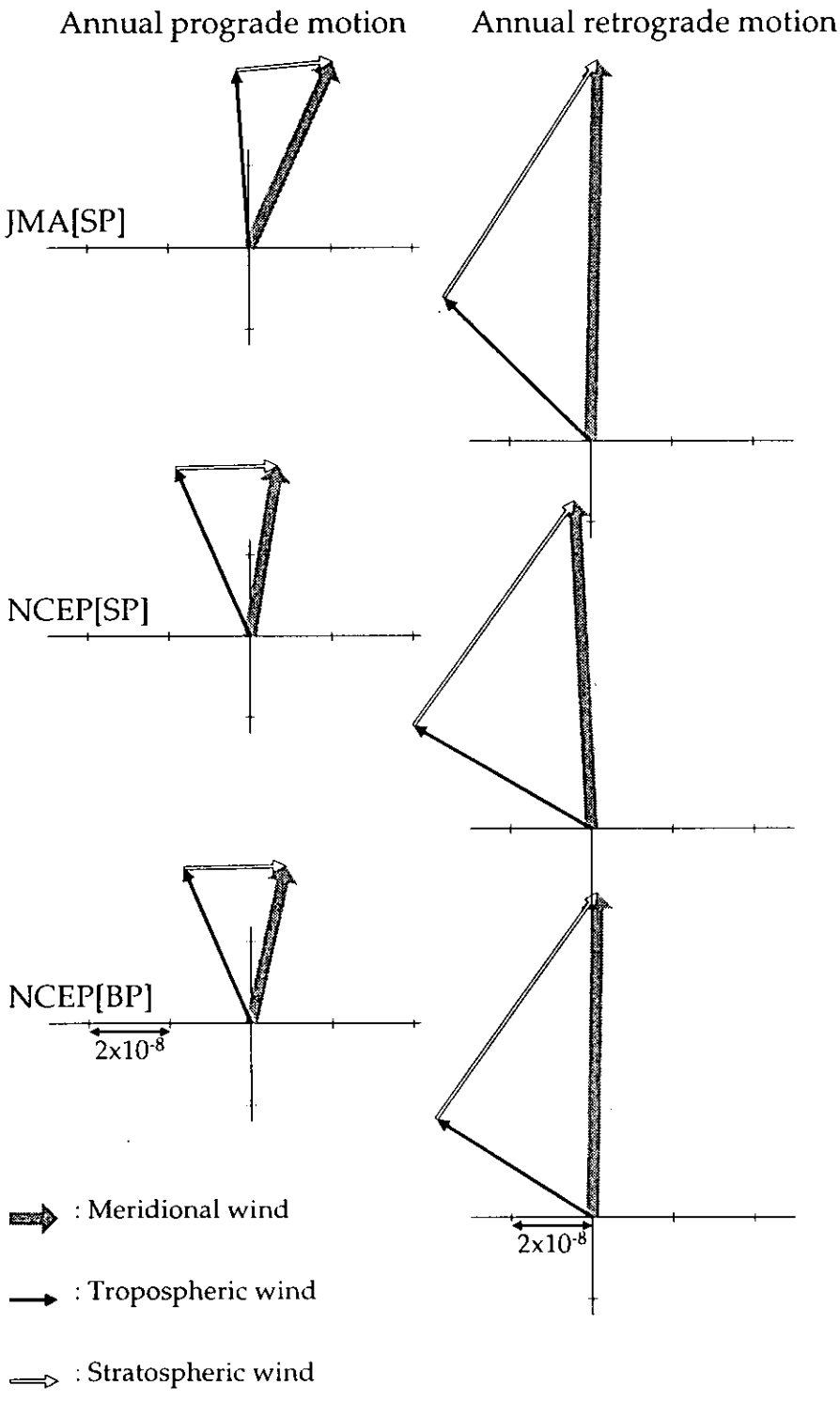

Figure 2.10b: Same as Figures 2.7b but for prograde and retrograde components.

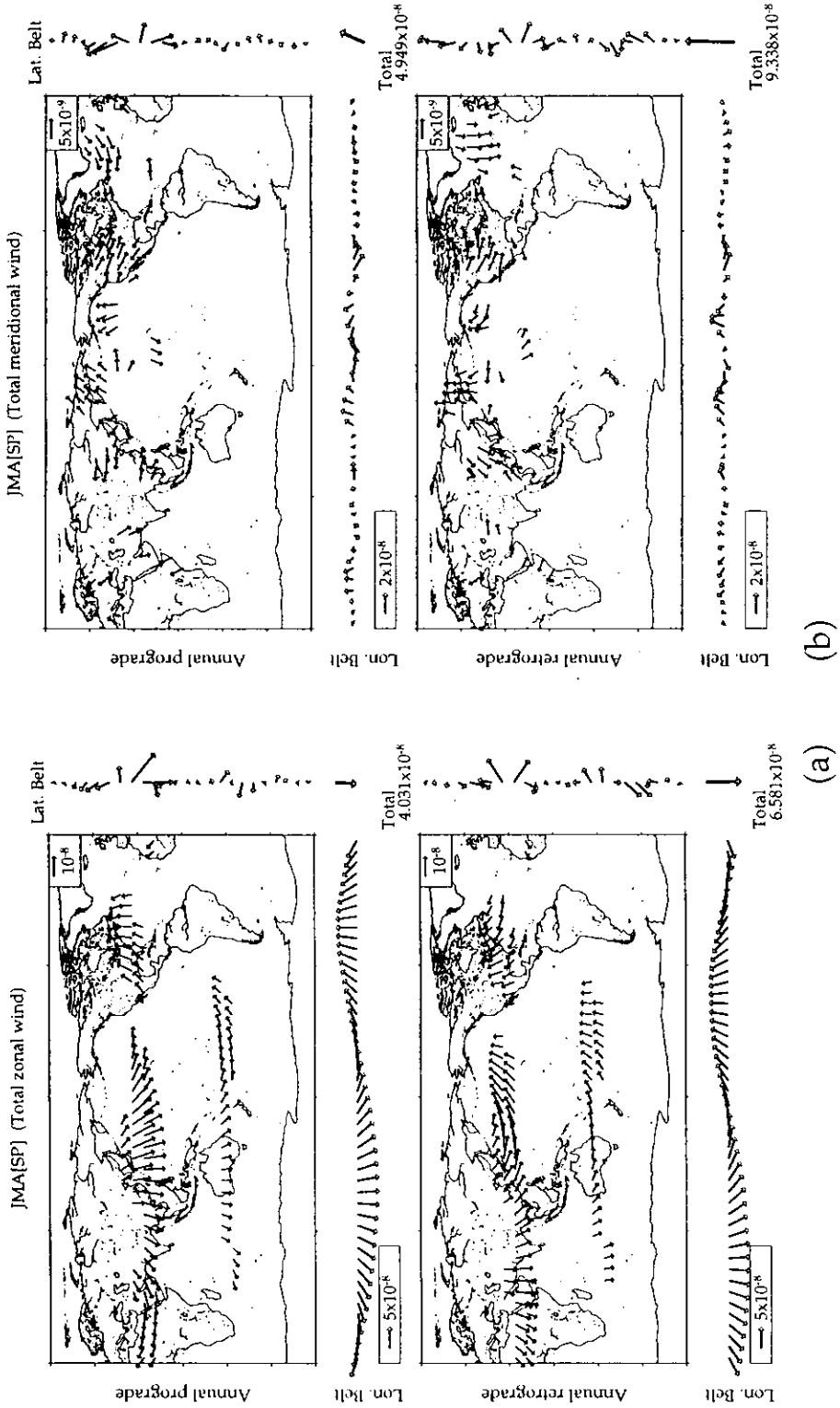

Figure 2.11: Same as Figures 2.8 but for prograde and retrograde components. Upper and lower panels show regional wind contributions in prograde and retrograde components, respectively. Vector shown as "Total" at lower right corners of each figure is equal to the zonal or meridional wind contribution based on JMA[SP] in Figure 2.9. (a) zonal wind contribution (b) meridional wind contribution.

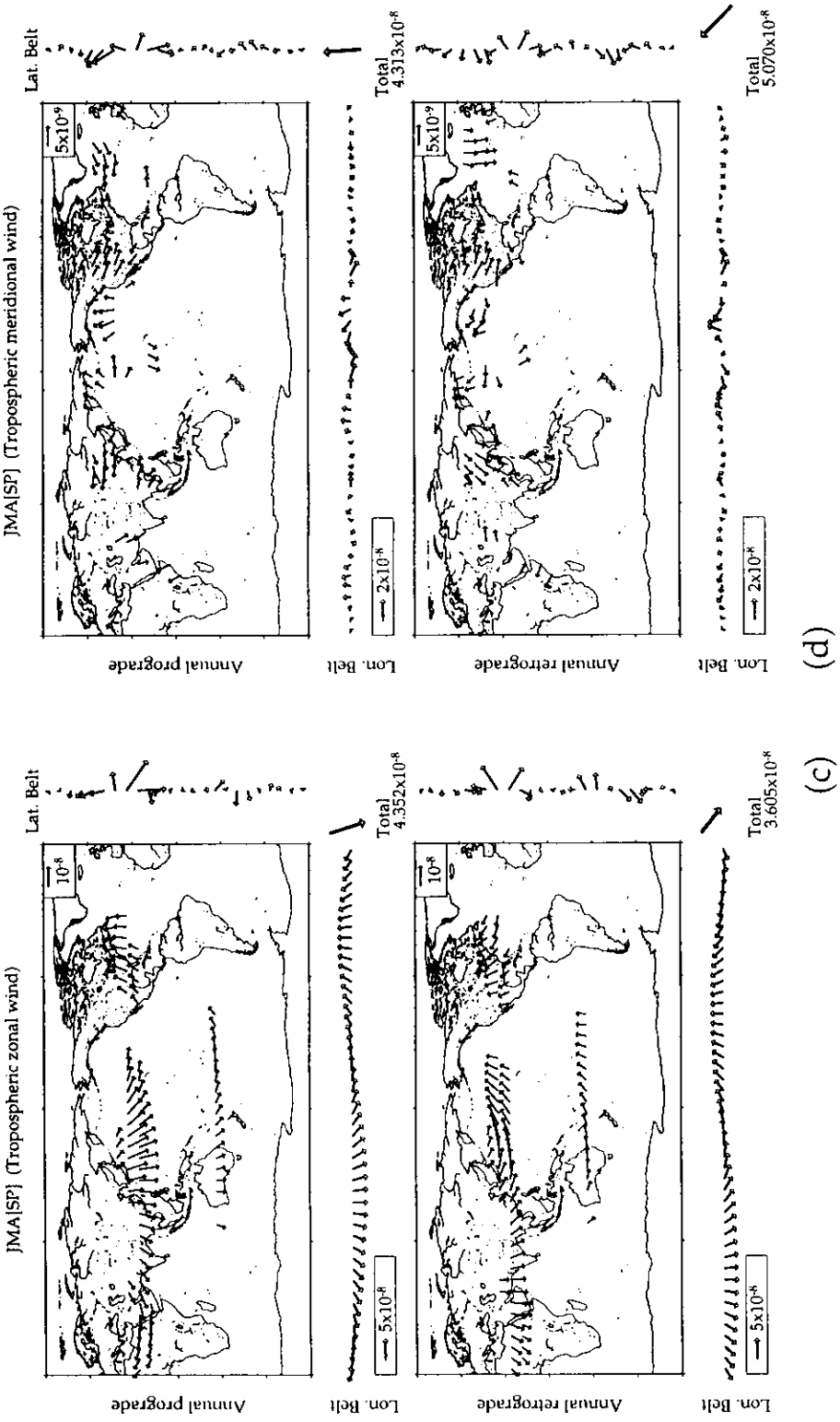

Figure 2.11: (c) zonal wind contribution in the troposphere. Vector shown as "Total" is equal to the tropospheric zonal wind contribution based on JMA[SP] in Figure 2.10a. (d) meridional wind contribution in the troposphere. Vector shown as "Total" is equal to the tropospheric meridional wind contribution based on JMA[SP] in Figure 2.10b.

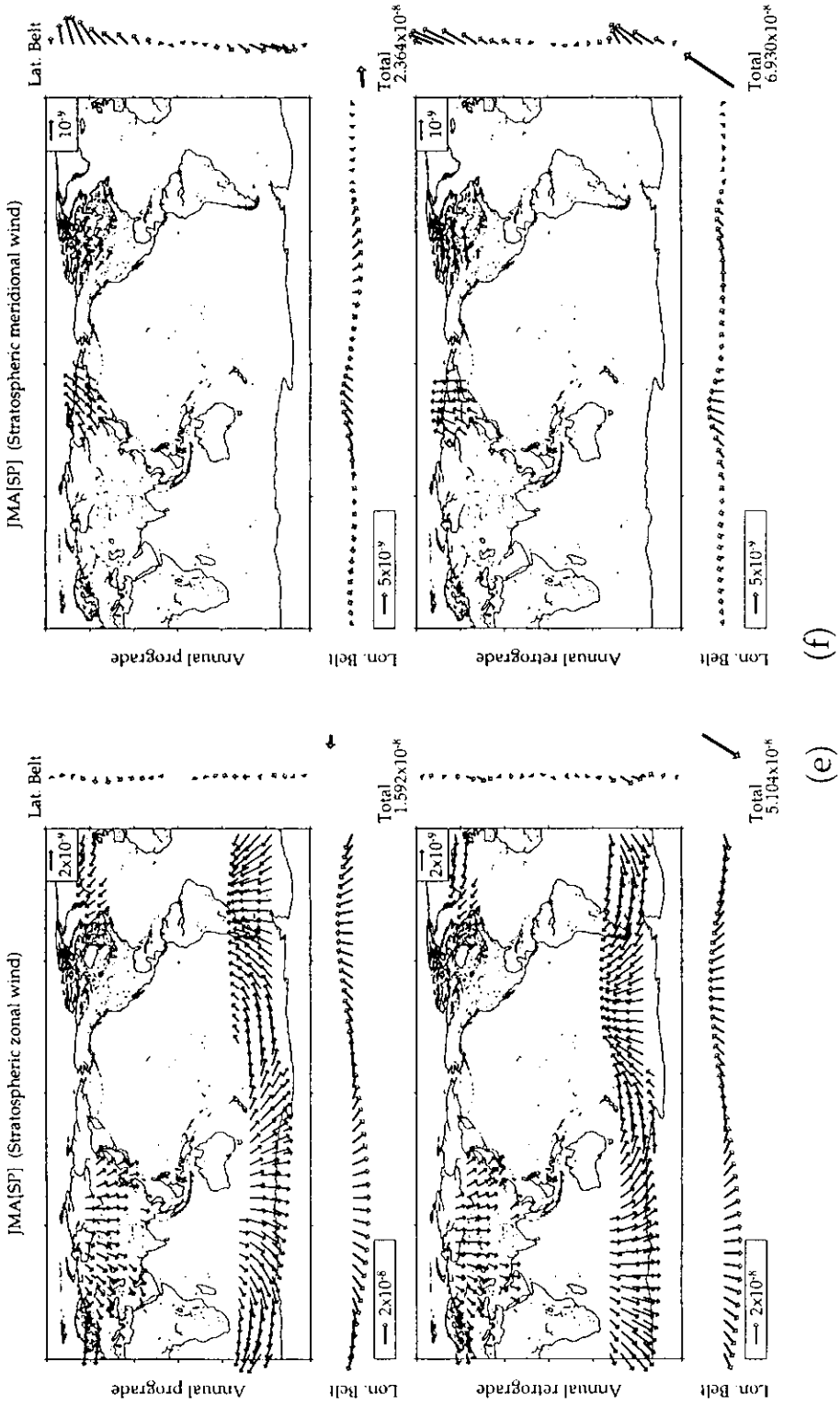

Figure 2.11: (e) zonal wind contribution in the stratosphere. Vector shown as "Total" is equal to the stratospheric zonal wind contribution based on JMA[SP] in Figure 2.10a. (f) meridional wind contribution in the stratosphere. Vector shown as "Total" is equal to the stratospheric meridional wind contribution based on JMA[SP] in Figure 2.10b.

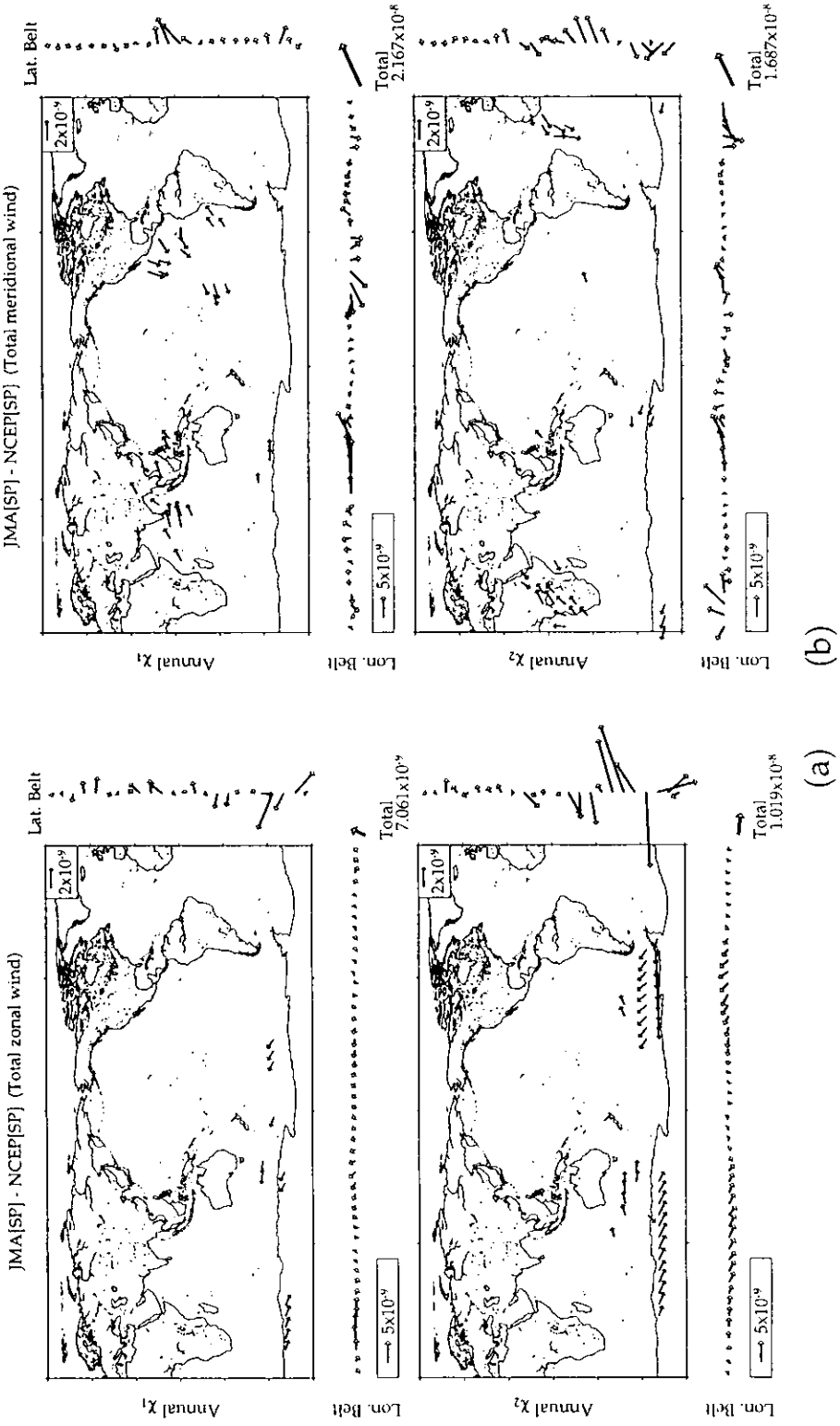

Figure 2.12: The difference between the regional wind contributions based JMA[SP] and NCEP[SP] to the equatorial angular momentum budgets in annual variation. They are displayed in same manner as in Figures 2.8. "Total" Vector at lower right corners of each figure is equal to the difference between the zonal wind contribution (Figure 2.12a) or that between meridional one (Figure 2.12a) based on JMA[SP] and NCEP[SP] in Figure 2.5. (a) zonal wind contribution (b) meridional wind contribution.

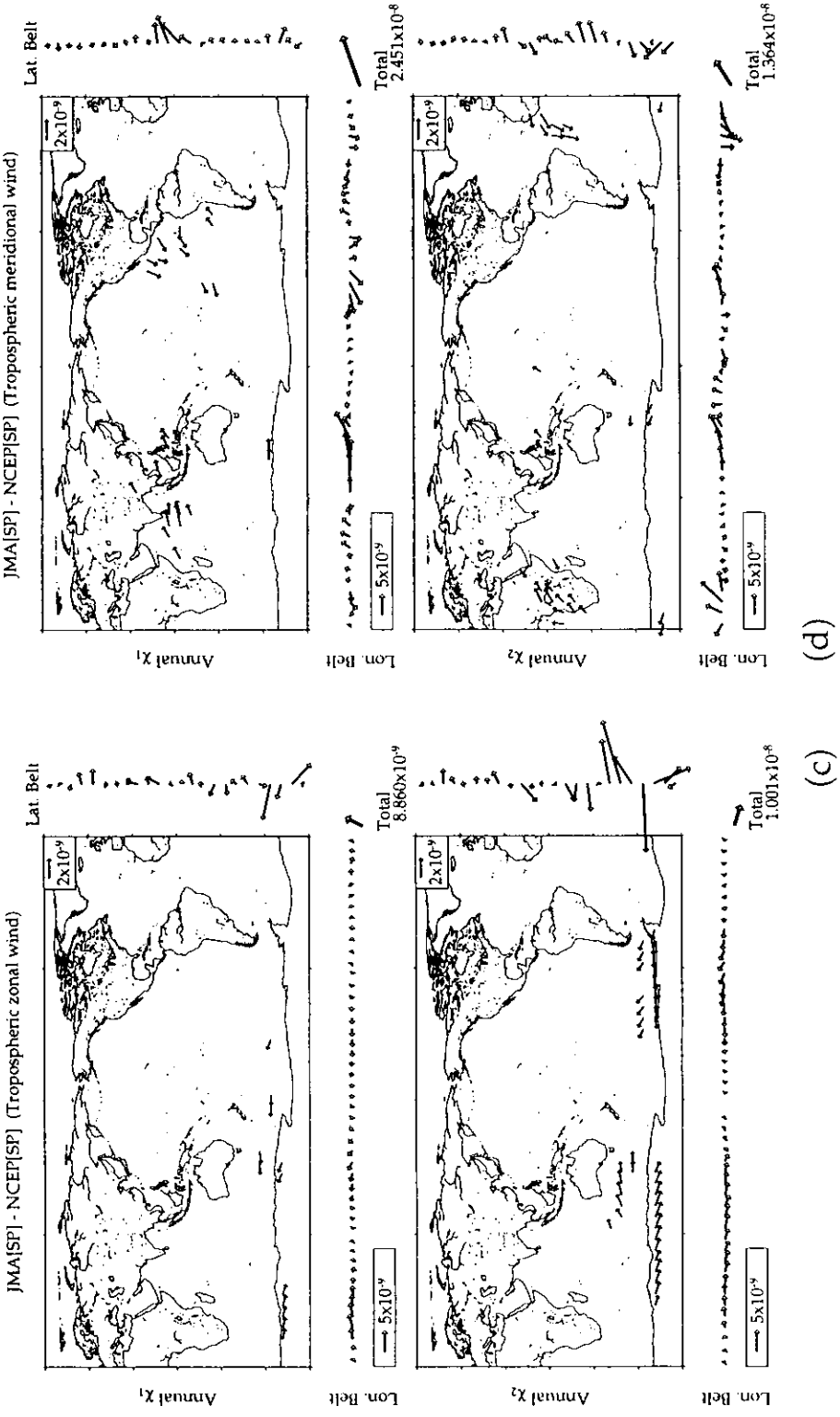

Figure 2.12: (c) zonal wind contributions in the troposphere (d) meridional wind contributions in the troposphere.

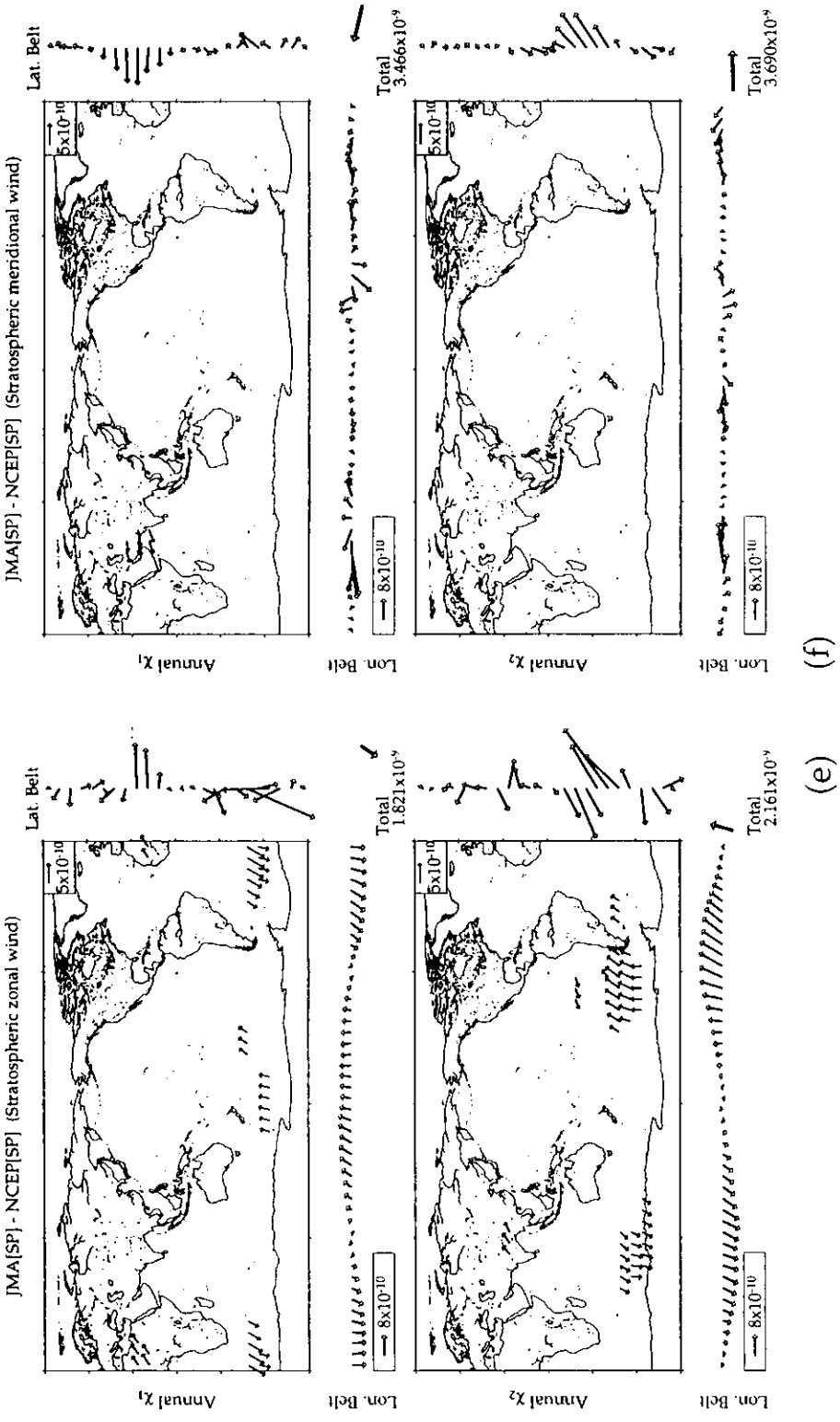

Figure 2.12: (e) zonal wind contributions in the stratosphere (f) meridional wind contributions in the stratosphere.

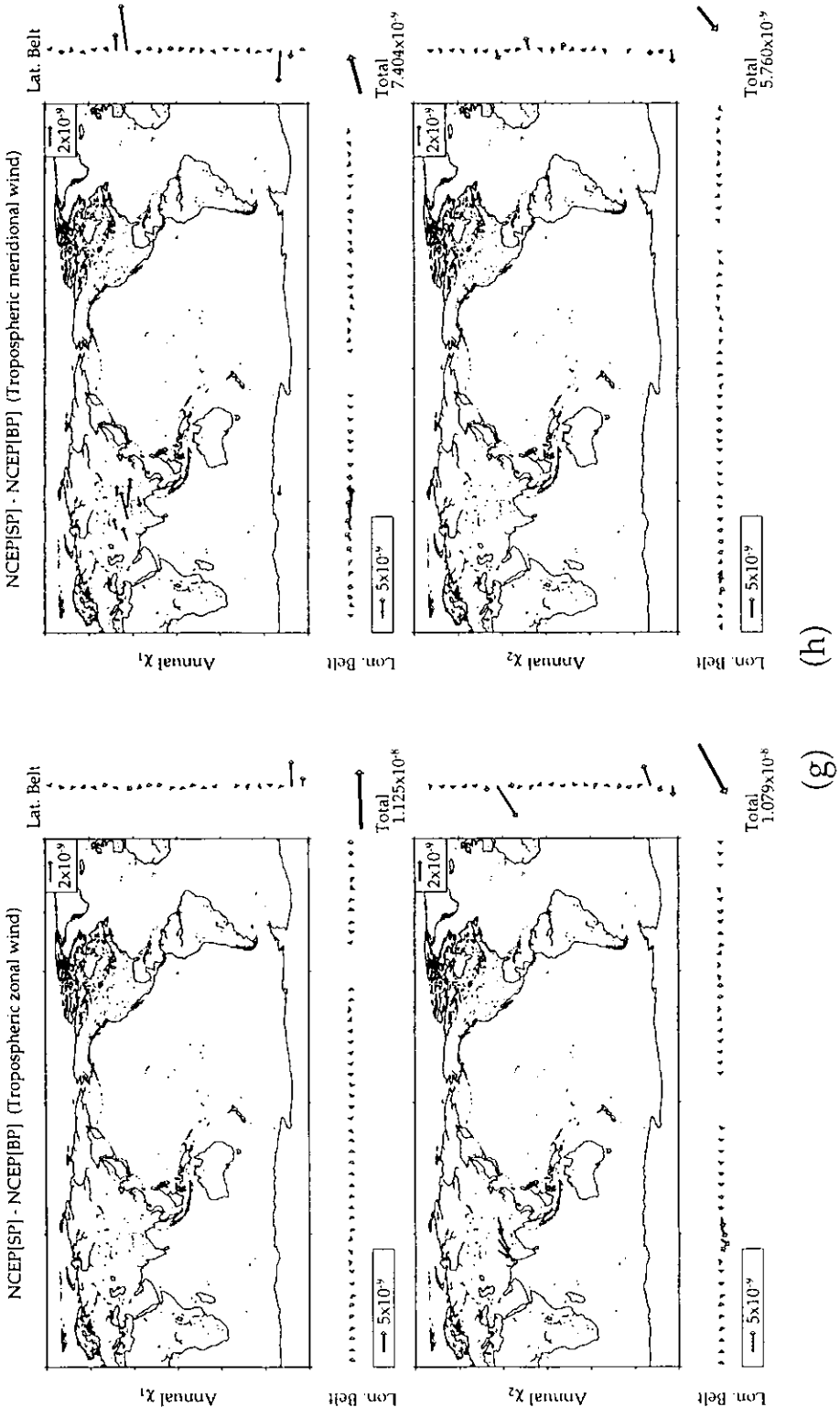

Figure 2.12: (g) the difference between the regional contributions of the zonal winds in the troposphere based NCEP[SP] and NCEP[BP] (h) that of the meridional winds in the troposphere.

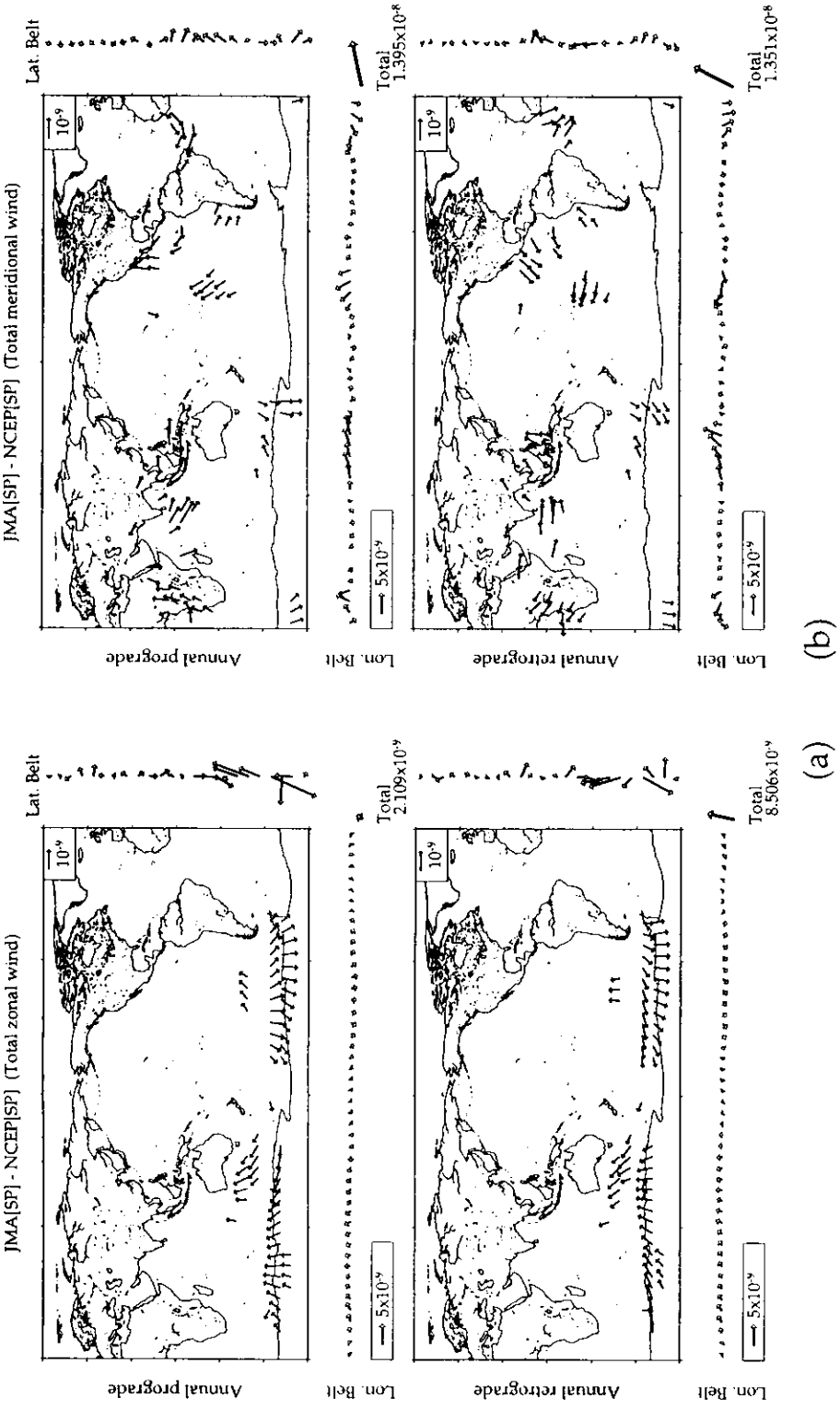

Figure 2.13: Same as Figures 2.12 but for prograde and retrograde components. (a) zonal wind contribution (b) meridional wind contribution.

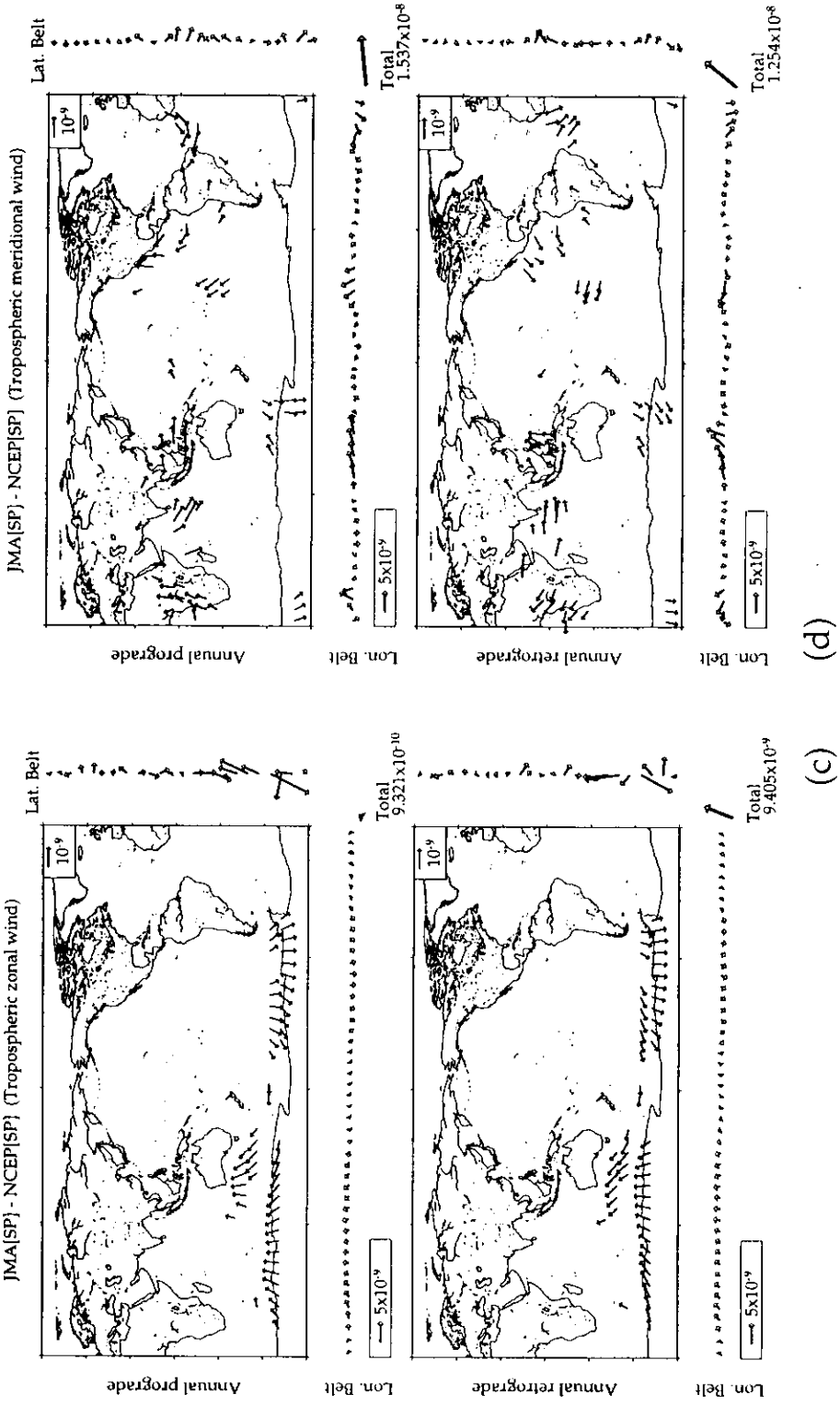

Figure 2.13: (c) zonal wind contributions in the troposphere (d) meridional wind contributions in the troposphere.

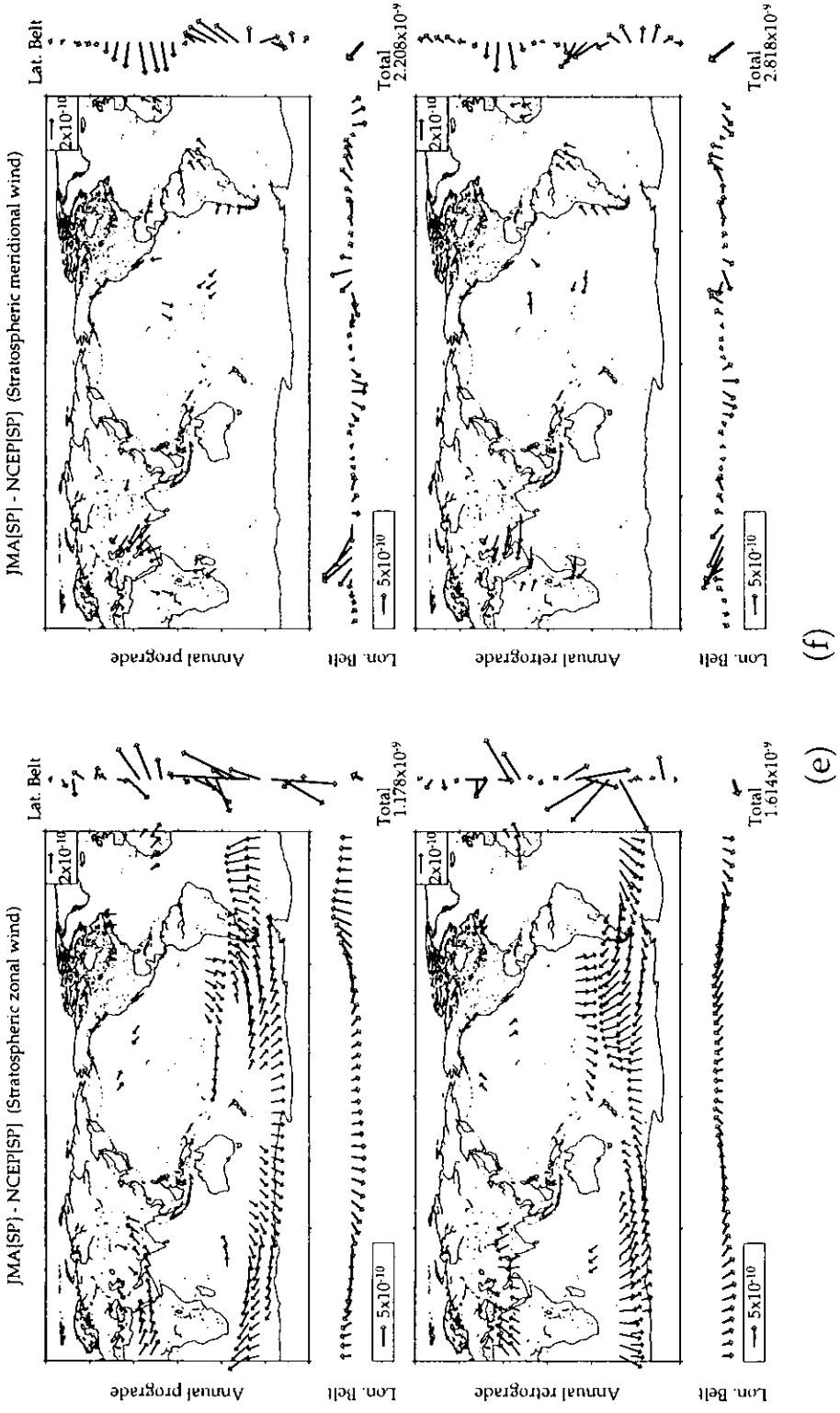

Figure 2.13: (e) zonal wind contributions in the stratosphere (f) meridional wind contributions in the stratosphere.

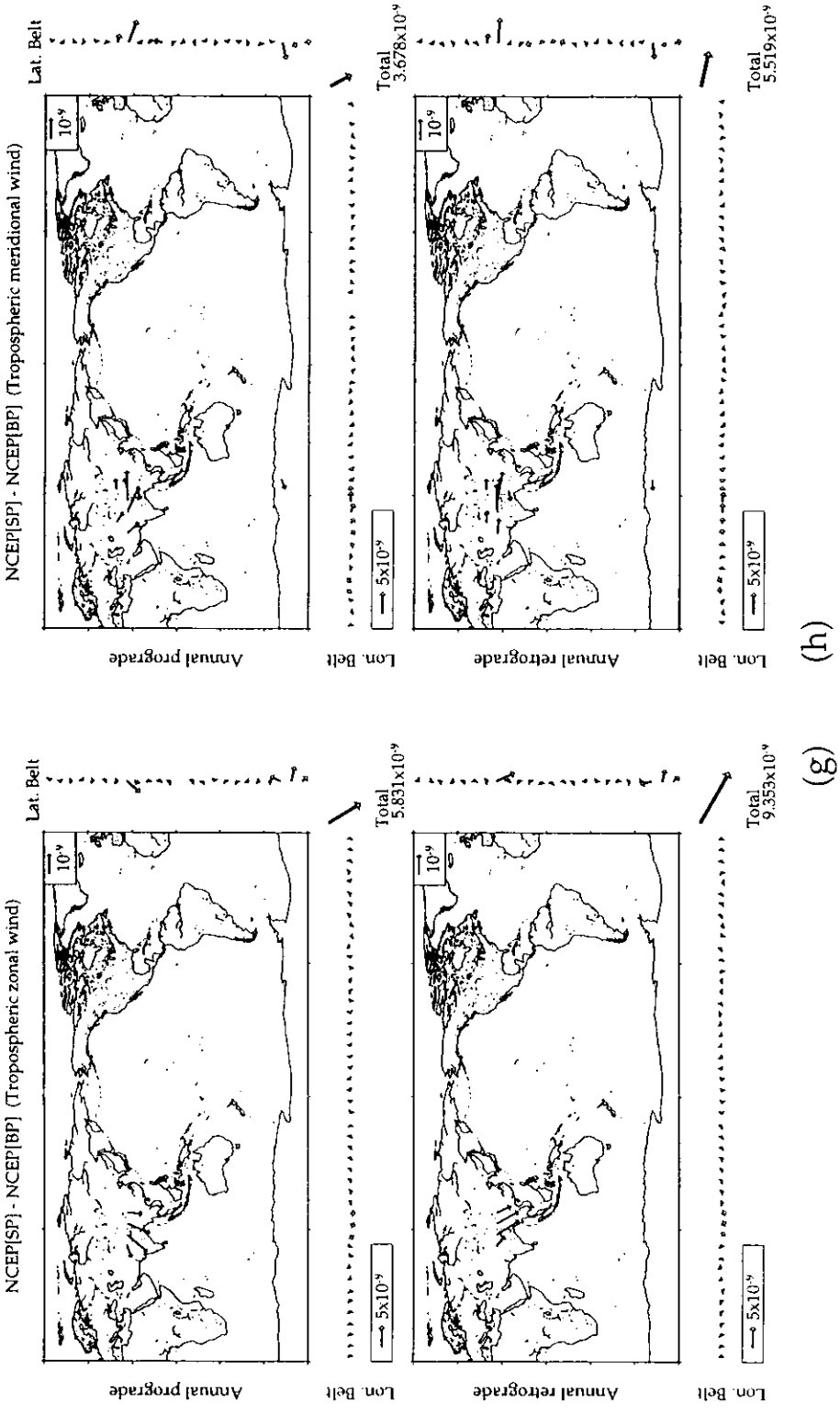

Figure 2.13: (g) the difference in the zonal winds in the troposphere between NCEP[SP] and NCEP[BP] (h) that in the meridional winds in the troposphere.

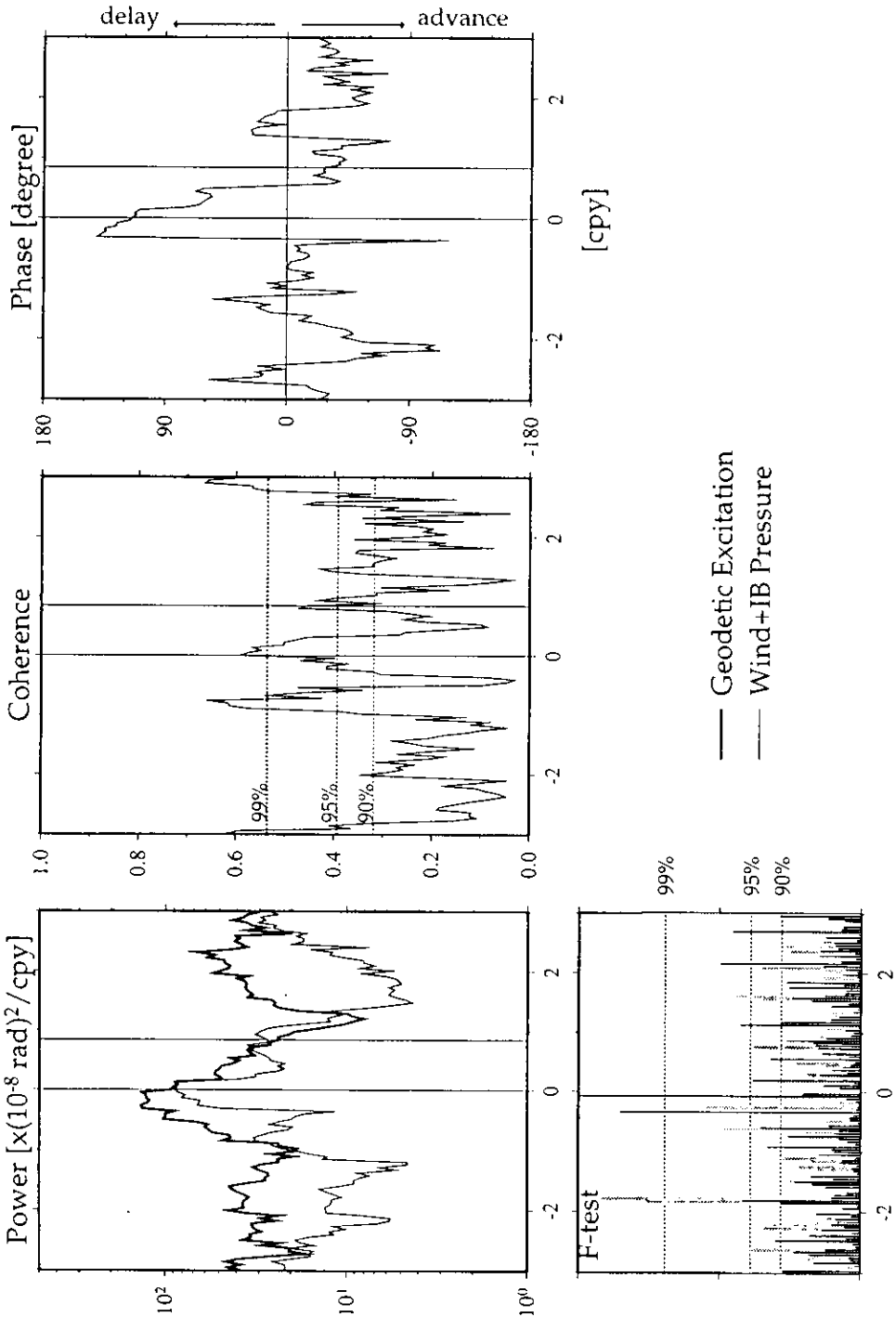

Figure 2.14a: Power spectra (left) for nonseasonal geodetic excitation inferred from the observed wobble and atmospheric contribution based on the JMA[SP], and their squared coherence (center) and phase difference (right), which are estimated for the period 1983-1998, by the multi-taper method (MTM). Note that the atmospheric contribution means a sum of contributions from the wind and inverted barometer (IB) pressure. A vertical line at 0.847 cpy denotes the Chandler frequency. The statistical reliability of power spectra of the geodetic (gray bar) and atmospheric (black bar) excitations by F-test are shown with the confidence thresholds of 90%, 95%, and 99%. Three dashed horizontal lines in the central figure represent the confidence thresholds of 99% (0.54) , 95% (0.40), and 90% (0.32).

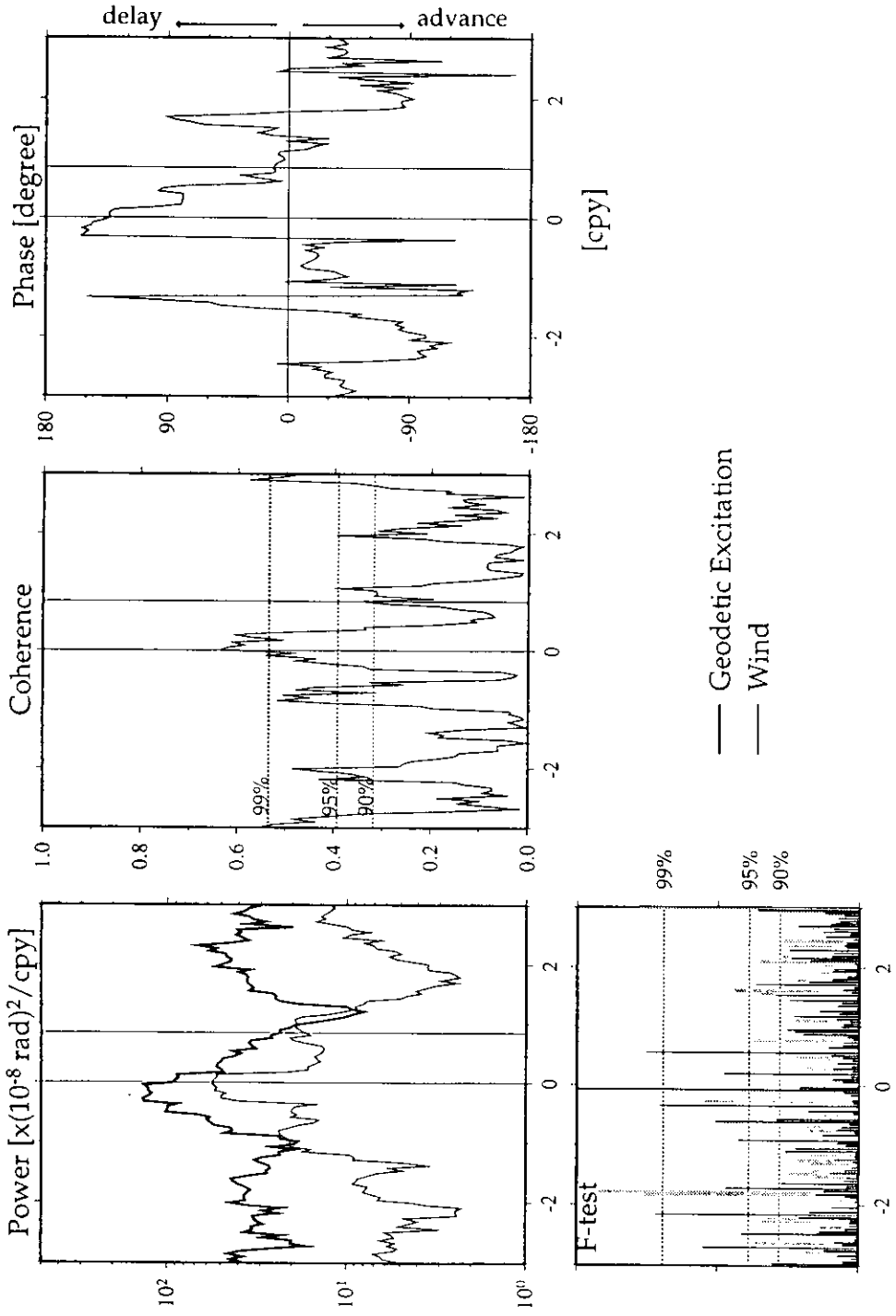

Figure 2.14b: Same as Figure 2.14a, but for the wind contribution.

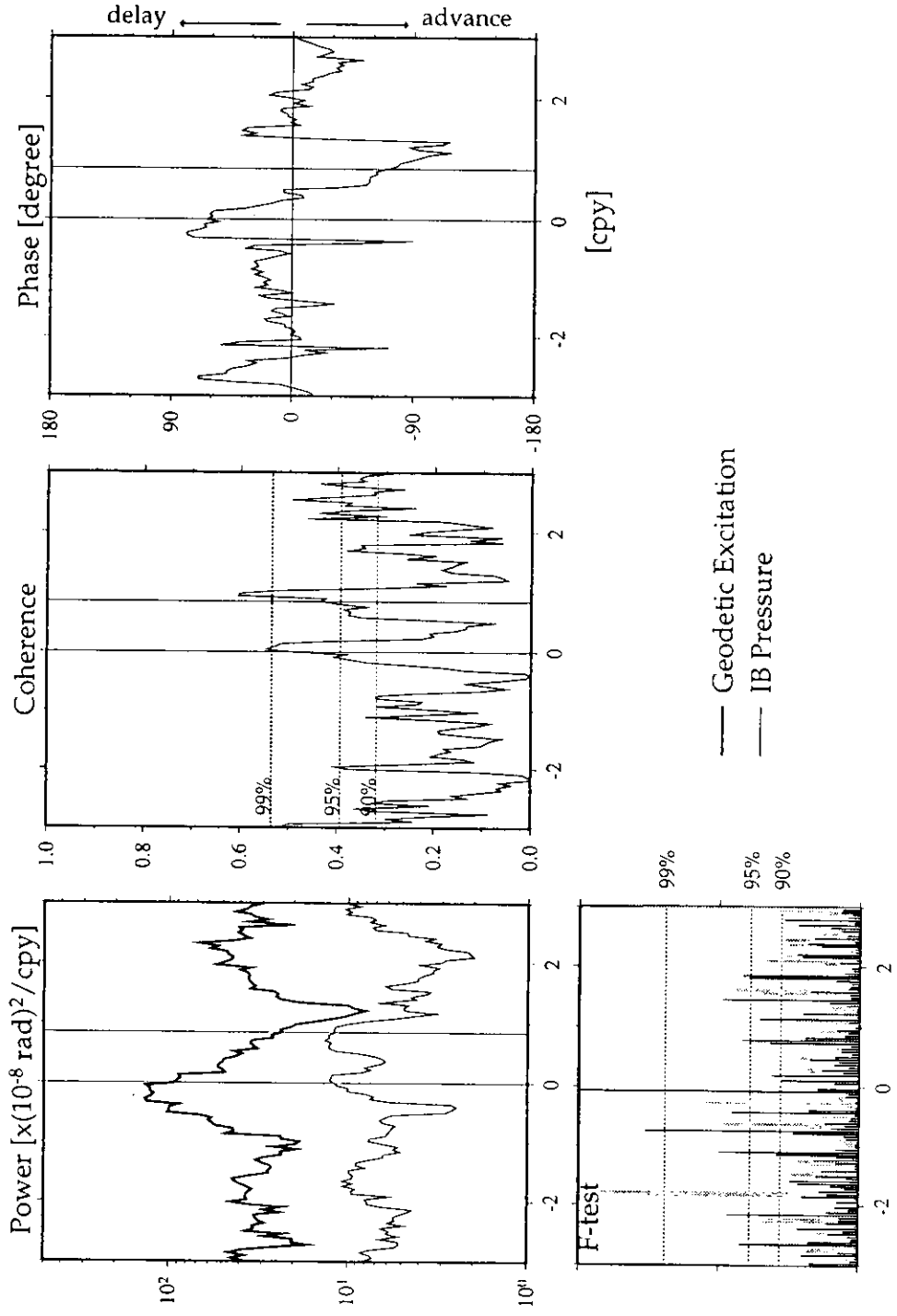

Figure 2.14c: Same as Figure 2.14a, but for the IB pressure contribution.

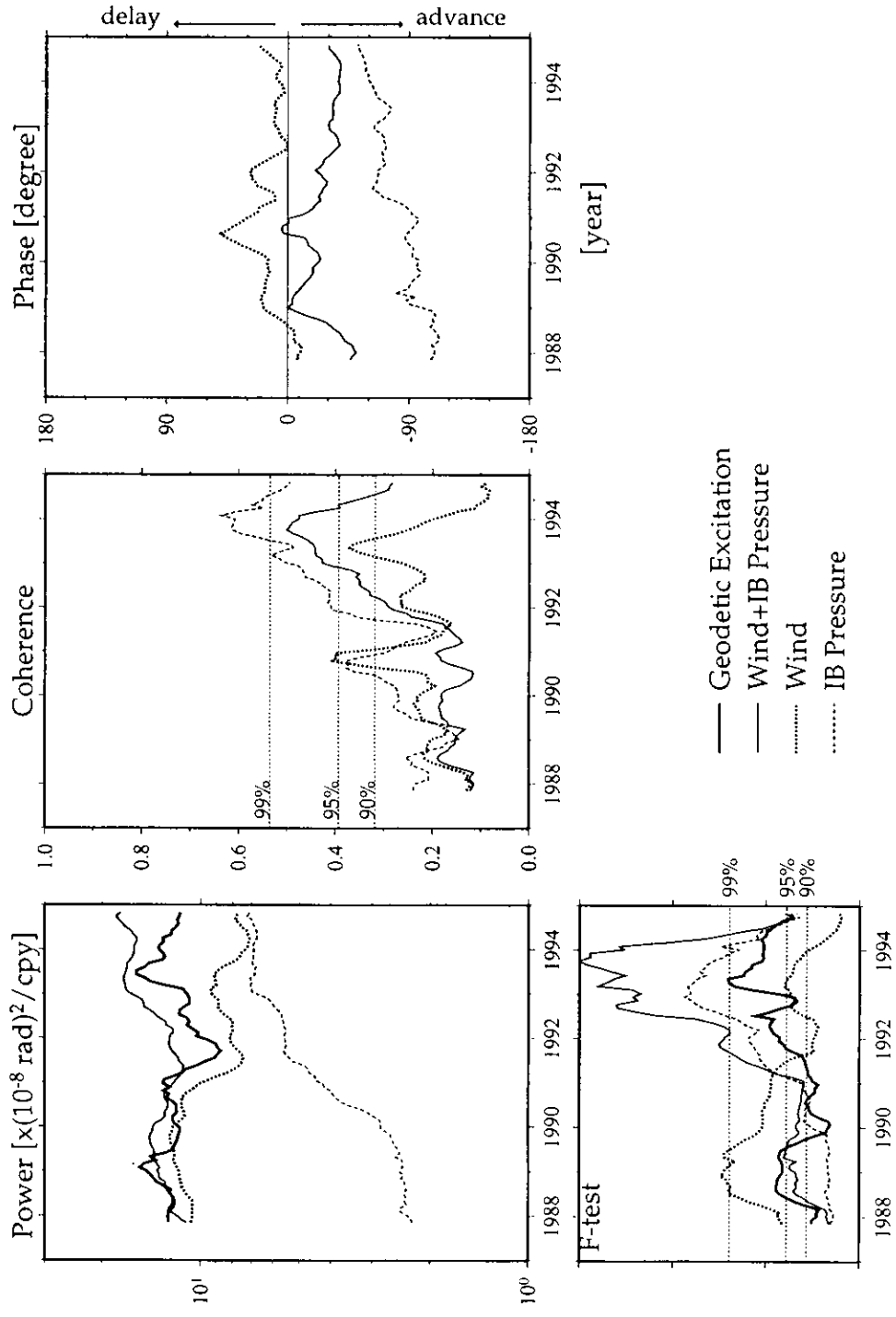

Figure 2.15a: Temporal variations in the power spectra (upper left), F-test (lower left), squared coherence (center), and phase difference (right) of/between the geodetic excitation and contributions from wind+IB pressure, wind, and IB pressure near the CW frequency (0.8-0.9 cpy) for the period 1987-1995. Horizontal dashed lines in the lower left and central figures denote the confidence thresholds of 90%, 95%, and 99%.

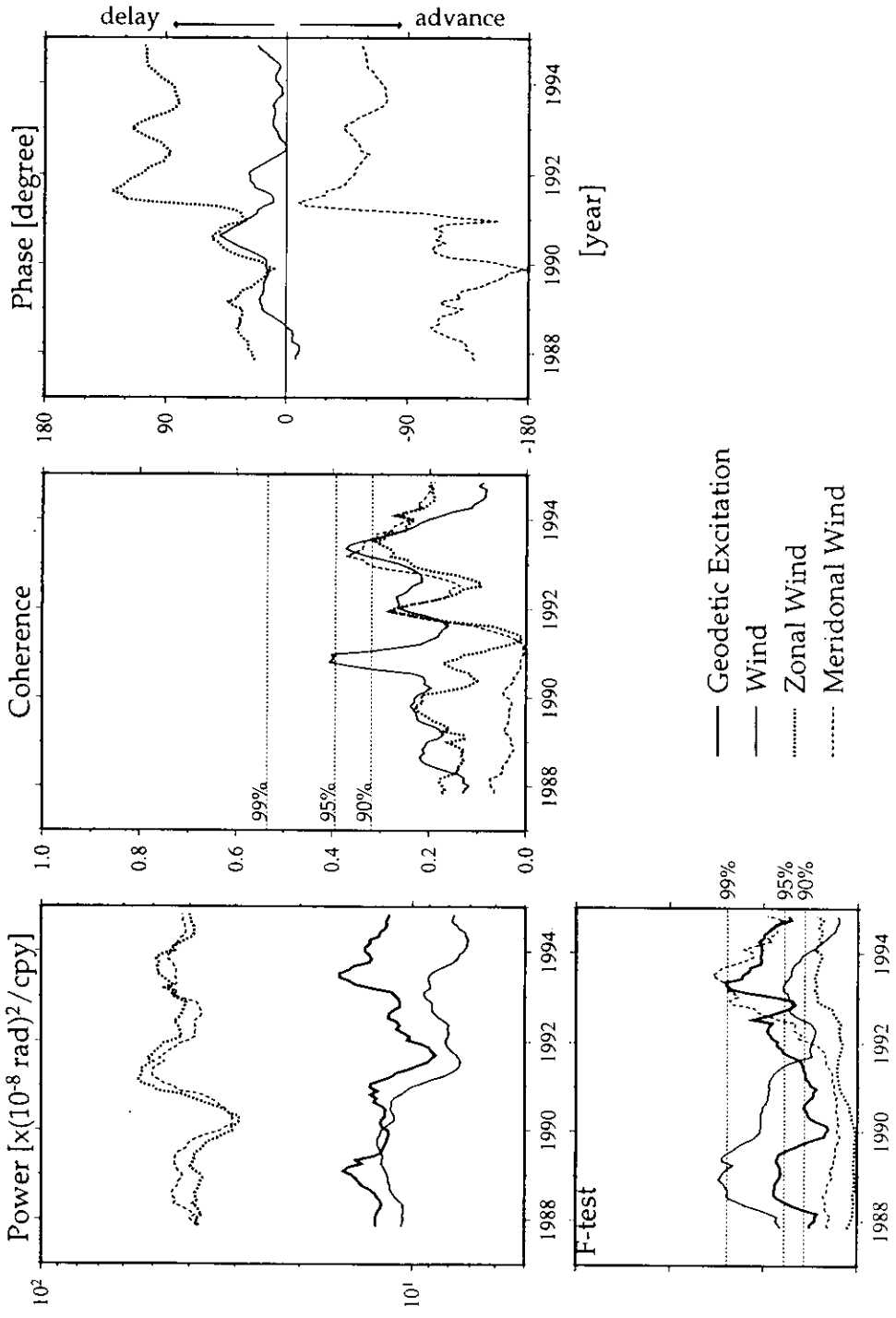

Figure 2.15b: Same as Figure 2.15a, but for the contributions from total, zonal, and meridional winds.

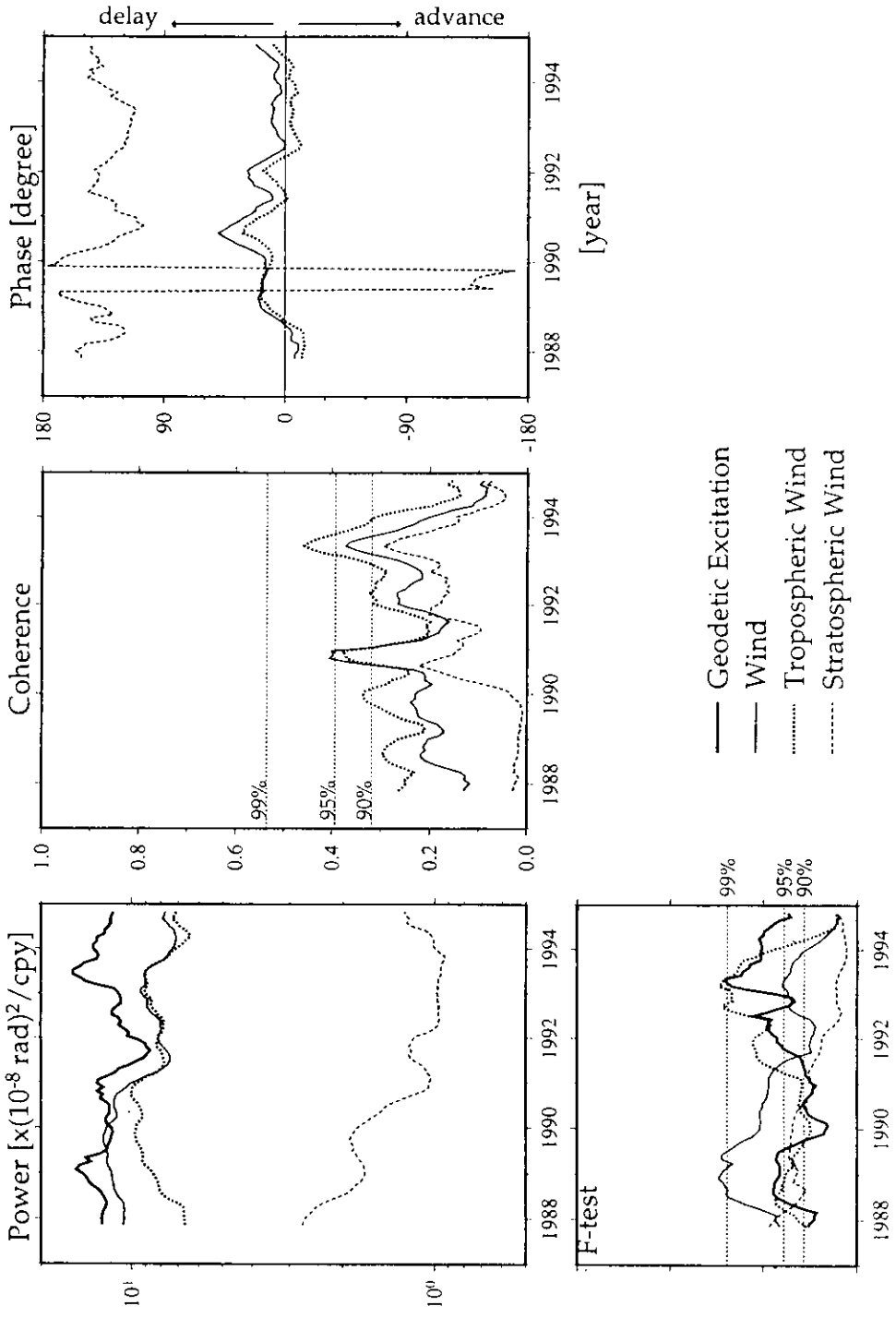

Figure 2.15c: Same as Figure 2.15a, but for the contributions from total, tropospheric, and stratospheric winds.

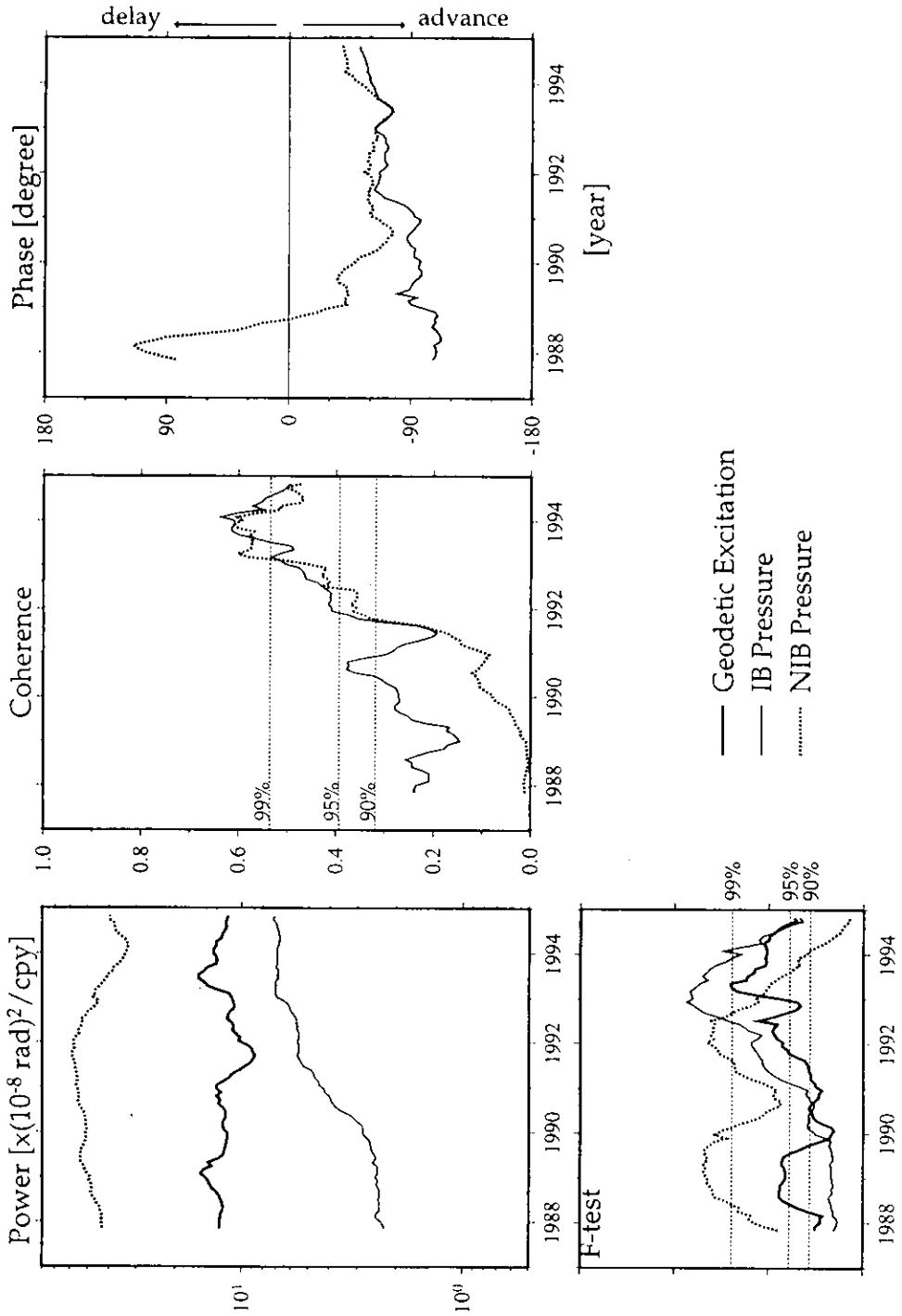

Figure 2.15d: Same as Figure 2.15a, but for the contributions from IB pressure and NIB pressure.

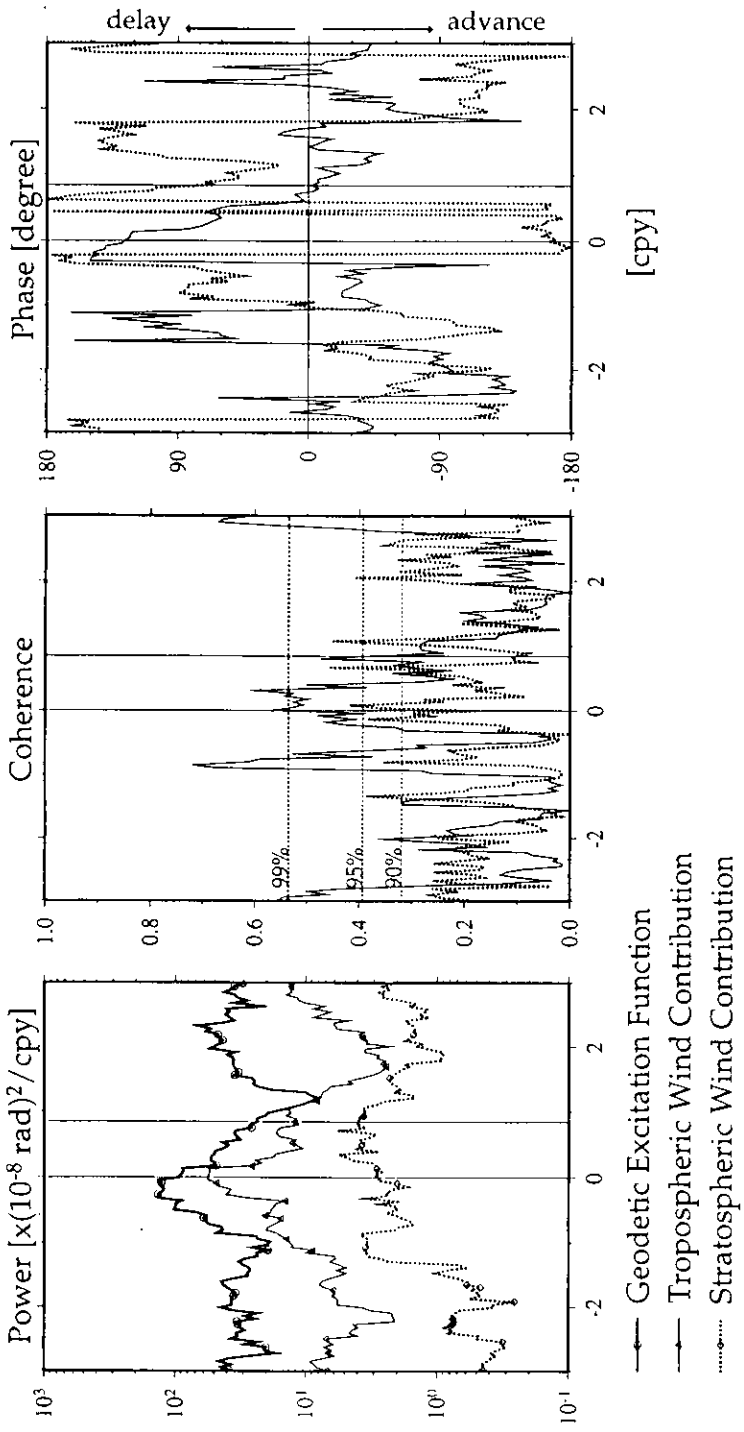

Figure 2.16: Same as Figure 2.14, but for the contributions from tropospheric and stratospheric winds. The small circles, triangles, and diamonds in the left figure indicate their statistical reliability exceeding 90% confidence threshold by F-test.

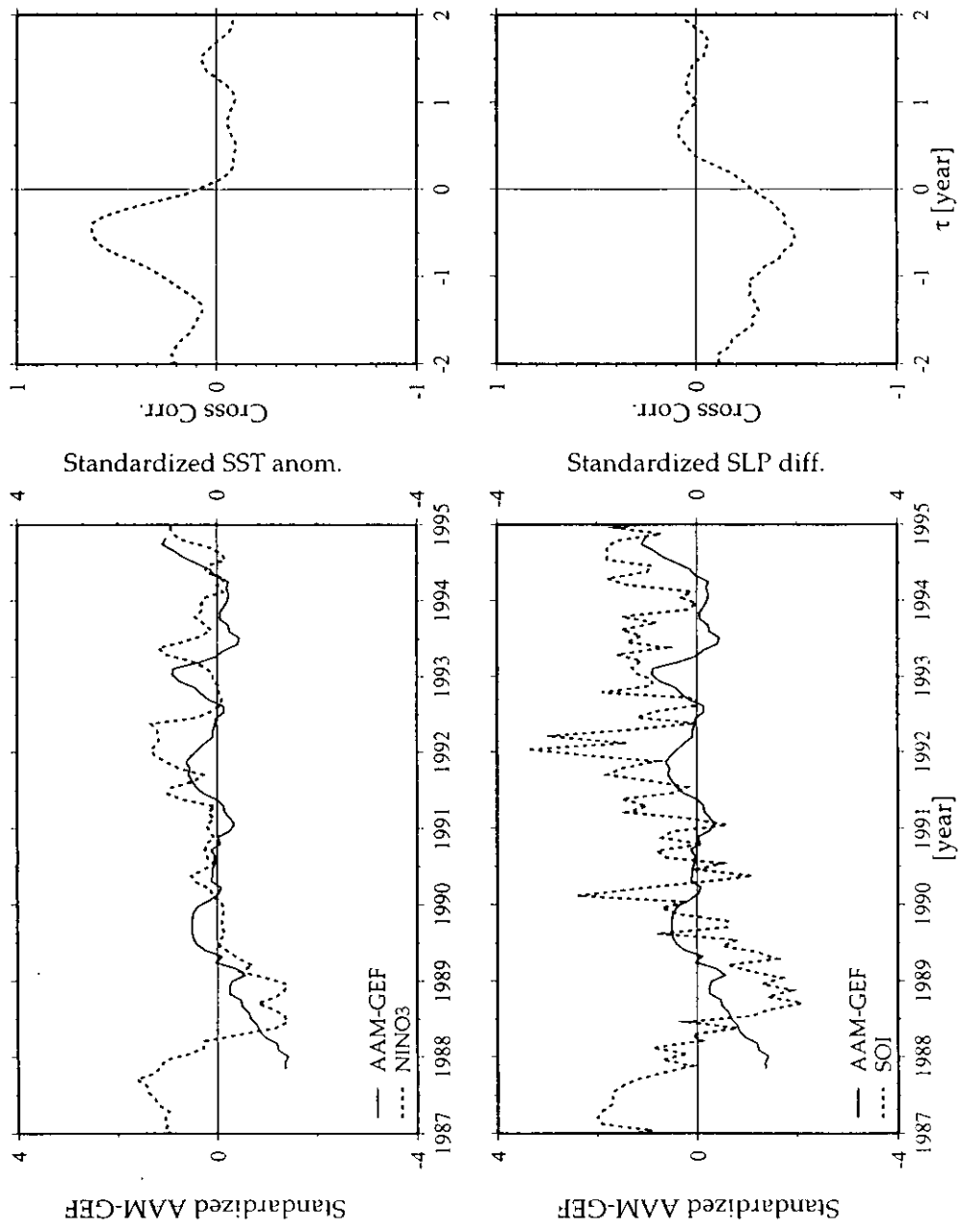

Figure 2.17: Time variations (left two panels) in standardized excess Chandler excitation power and standardized activities of El Niño that are given by NINO3 (upper) and SOI (lower), and their cross correlation coefficients (right two panels) for a period of 1988 - 1995. The excess Chandler excitation power computed from subtracting power spectrum of the geodetic excitation function from that of atmospheric excitation function as shown in Figure 2.16a. The positive τ in the figure for the cross correlation coefficients denote the time advance of NINO3 and SOI relative to the excess Chandler excitation power.

Chapter 3

Earth's Gravity Response to the Wobbles

3.1 Abstract

We discuss Earth's gravity response to the Chandler and seasonal wobbles using data obtained from the superconducting gravimeters (SGs). The data sets used here are three SG data observed at Esashi in Japan (1580 days from Jan. 2, 1995), Canberra in Australia (800 days from Jan. 28, 1997) and Syowa station in Antarctica (1740 days from Mar. 23, 1993), and EOPC04 for the wobble. We first separate the tidal components (1/3 day to 31 days), atmospheric gravimetric effect, and step-like disturbances caused by earthquakes and maintenance of SG, from the SG data sets, for the purpose of examining long-period gravity changes (with period from 6 to 14 months). The residual time series of SG data are fitted by an analysis model consisting of the Chandler, annual and semiannual periodic components with their linear trends, initial drifts of SG (exponential function), and step functions to recorrect for the disturbances throughout long duration. We attempt to interpret the observed annual and semiannual gravity changes using the predicted gravity changes consisting of five gravimetric effects: the solid tide, the ocean tide, the wobble, the equilibrium pole tide, and sea surface height (SSH) variations. Additionally, we discuss a gravity responses to the annual and the Chandler wobbles, comparing the observed annual or nonseasonal gravity change with that predicted from EOPC04, respectively.

It is found that the observed annual gravity change agrees well with the predicted one within a discrepancy of 0.25 μGal ($1\mu Gal = 1 \times 10^{-8} m/s^2$) at each observation site, in particular the discrepancies at Esashi and Canberra are less than 0.1 μGal ($1\mu Gal = 1 \times$

$10^{-8}m/s^2$), which is not significantly larger than the formal error of fitting for amplitude of observed annual gravity change. In that case, we apply a single steric coefficient of 0.60 cm/°C to correction for the thermosteric component of the SSH. We also test other extreme value for the steric coefficient, i.e. 0.0 cm/°C and 1.0 cm/°C. In result, the observed annual gravity changes prefer 0.6 cm/°C, which has been independently determined from the relationship between SST and SSH (sea surface temperature). On gravity response to the annual wobble, a significant departure from theoretically elastic response is found in the case where we separate the three effects of the solid tide, the ocean tide and the equilibrium pole tide from the observed one. However, the departure is reduced by the separation of gravimetric effect of SSH variations besides above three effect, and the observed gravity response agree with theoretical one in the range of its formal error.

In semiannual gravity change, on the other hand, there are discrepancies of 0.1 - 0.5 μGal between observed and predicted values. We suggest that their major source possibly is insufficient correction for the atmospheric gravimetric effect by means of the response method.

Comparing the nonseasonal observed gravity change with that predicted from the non-seasonal wobble, we determine the gravimetric factor and phase difference for the Chandler wobble at each observation site. In result, the observed gravity response to the Chandler wobble disagree with the theoretical elastic one, and their disagreement is too large to be explained not only by the effect of mantle anelasticity but also by the gravimetric effect of equilibrium pole tide. We suggest a possibility that the SG observes the gravity change around the Chandler period arising from other geodynamical phenomena accompanying with mass redistribution in the ocean and the fluid core. Finally, we would propose that the SG data sets can provide valuable information about dynamics of Earth affected by various mass at long-term period.

3.2 Introduction

The temporal variations in the instantaneous angular velocity vector of the mantle relative to the terrestrial reference frame (i.e. the LOD change and wobble) are described by Earth orientation parameter (EOP). The EOP is observed by space geodetic techniques at the accuracy better than 1 mas (mill arc second) as shown in previous chapter. If we can observe gravity responses to the LOD change and wobble at the similar relative accuracy (0.01 μGal order), they provide us valuable information about Earth's deformational response properties at periods much longer than seismic and short-periodic tidal bands. Although there are only

few kinds of measurements knowing it, the superconducting gravimeter (SG) is one of the candidate instruments, which has very high sensitivity and long-term stability.

The gravity response to the LOD change and wobble is represented by the amplitude ratio (hereafter referred to as the gravimetric factor) and phase difference between the gravity change observed from SG and that predicted from EOP on the assumption of purely rigid Earth [see, *Hinderer and Legros,* 1989 and *Loyer et al.,* 1999]. Since these parameters represent the physical properties of the Earth utilizing Love number [see *Wahr and Bergen,* 1986 ; *Hinderer and Legros,* 1989], they are expected to give us useful information about the frequency-dependent anelastic behavior at long-term period.

Richter [1983] first reported that SG measurement obviously detected the gravity change induced by the wobbles. Subsequently, he determined the gravimetric factor of 1.27 and zero time difference between observed and predicted values, using SG data obtained at Bad Homburg in Germany during 1981 - 1984 and during 1986 - 1987 [*Richter,* 1990]. *Sato et al.* [1997a] analyzed the gravity response to the wobbles using 2-year SG data obtained at Syowa Station, Antarctica, and reported the gravimetric factor of 1.198 and phase lag of about 20 days. The length of SG data, however, was too short to safely separate the two dominant periodic components of the wobbles such as the Chandler and annual wobbles (with periods of 14-month and 12-month, respectively) . *Loyer et al.* [1999] estimated the gravimetric factor of 1.18 and phase lag of 22 °(that is about 26 days delay in time domain), based on 8-year data (from October, 1987 to March, 1996) of Strasbourg SG in France . The later two analyses reveal considerable phase lags of observed gravity change relative to the predicted one that is computed from EOP change assuming purely rigid Earth. Taking effects of anelastic Earth with extremely low Q-value [*Wahr,* 1985] into consideration, observed phase lag can hardly be explained. Hence, it is required to examine sources of these observed phase lag.

Since annual wobble is a forced motion, we first consider that the gravity response to the annual wobble will be much simpler and better determined that that to the Chandler wobble which is Earth's free motion. However, the gravity response to the annual wobble have never reported. The major reason for this is that the classical spring gravimeters have considerable instrumental drift due to annual thermal variations, so they can hardly observe the geodynamical annual signals. It has been shown that a few SG measurements might detect the geodynamical annual signals [e.g., *Richter,* 1983, 1990]. In these study, the annual gravity change, which is made a correction for the atmospheric gravimetric effect, was described by a tidal gravimetric factor alone. Moreover, the geophysical meaning of obtained value was not explained. Thus we need analyze the gravity response to the annual

wobble using SG data.

It is considered that SG simultaneously detects the several gravimetric effects in addition to the gravity response in seasonal period. These gravimetric effects are connected with mass redistribution in atmosphere and ocean, water table change, and dynamical process in the core. For the purpose of examining the gravity response, it is essential to separate these gravimetric effects from observed gravity change. Thus, the knowledge about their phases besides their amplitude is also required to correctly understand the origin of the observed annual gravity change.

It have been discussed that the redistribution of the atmospheric mass induce broadband gravity changes whose maximum amplitude is more than 10 μGal [e.g., *Mukai et al.,* 1995]. These atmospheric gravimetric effects are estimated by two methods: the response method [e.g. *Spratt,* 1982] or the numerical integrations method [e.g. *Mukai et al.,* 1995]. In the response method, the estimation of atmospheric gravimetric effect is usually conducted statistically only using a response function of local atmospheric pressure measured around the gravity observation site. On the other hand, the effect is inferred convolving global meteorological data with a Green's function which represents the Earth's response to a loading mass, in the numerical integrations method. Both methods can correct for this effect to the observed gravity change at the accuracy of 0.1 μGal order [*Mukai et al.,* 1995].

Although the atmospheric gravimetric effect have been studied in large number of literatures, little is known about oceanic gravimetric effect. The ocean respond to the variations in the gravitational potential. Typical examples of the ocean response are the ocean tide caused by tidal potential changes and the pole tide arising from the changes in centrifugal potential due to the wobble. Redistribution of the oceanic mass due to these ocean response induce the surface gravity change through the effects of Newtonian attraction and surface loading.

The sea level data from tide gauges have proved the presence of 14-month pole tide [e.g., *Trupin and Wahr,* 1990]. The typical amplitude of the equilibrium 14-month pole tide is less than 1 cm [e.g., *Munk and MacDonald,* 1960]. Large amplitudes several times amplitude of the equilibrium pole tide, however, were obtained from the tide gauge data in the North Sea, Baltic Sea, and Gulf of Bothnia. *Tsimplis et al.* [1994] pointed out the possibility that the non-equilibrium pole tide in North Sea is mainly driven by meteorological origin, i.e. surface wind stress with variation in 14-month period.

The gravimetric effect of the pole tide assuming an equilibrium induces only increase of about 2% in gravimetric factor for the gravity response to the Chandler wobble [*Hinderer and Legros,* 1989]. If there are the departures from the equilibrium pole tide as mentioned above

in other sea regions, the gravimetric effect of non-equilibrium pole tide probably induces the phase difference between theoretical elastic gravity response and that obtained from SG data.

For recent years, the TOPEX/POSEIDON (T/P) altimetry data provides us the knowledge of the global sea surface height (SSH) variations at accuracy of about 1 cm. Thanks to improvements of the ocean general circulation model (OGCM) that is driven by surface wind stress and sea surface temperature (SST), we can employ spatially homogeneous data concerning the SSH variations. It is examined that the SSH variations from Parallel Ocean Climate Model (POCM) as the OGCM agree with those from T/P [*Stammer,* 1997] These data sets enable the quantitative evaluation of the oceanic gravimetric effect on the observed gravity changes.

Recently, it begins to evaluate the gravimetric effects of redistribution of oceanic motions caused by meteorological forcing (i.e. wind stress and sea surface pressure loading) using these SSH data [e.g., *Fukuda et al.,* 1999; *Sato et al.,* 2000]. Moreover, it is found that the annual variation is dominant over the SSH variations [*Fukuda et al.,* 1999], and in consequence the SSH is expected to cause a part of annual gravity change observed by SG.

Observation applying a global network of SG have been carried out by Global Geodynamics Project (GGP) since 1997, and will continue until 2003 [*Crossley et al.,* 1999]. Japanese SG observation sites are located in Australia, Indonesia, and Antarctica beside in Japan. SG data obtained from these sites provides valuable information, because other sites of the SG network are set in mid-latitude in the northern hemisphere. Previous studies have never discussed the gravity response to the wobble analyzing multiple SG observation data in terms of the uniform approach.

In this chapter, we analyze three data obtained from SGs at Esashi in Japan, Canberra in Australia, and Syowa station in Antarctica in terms of the uniform approach, and discuss the gravity response to the annual and the Chandler wobbles. The observed annual gravity is decomposed into the gravity response components to solid tide and annual wobble, and attraction and loading effects associated with ocean tide, pole tide, and SSH variations. We evaluate how the observed Chandlian gravity change is affected by the attraction and loading effects of pole tide and SSH variations beside the gravity response to the Chandler wobble. In section 3.3, we describe the origins of the gravity change. In section 3.4, we outline the observation applying the SG, preprocessing data, and method of analysis employed here. In section 3.5, we display the results of analysis on annual and Chandlian gravity changes, and assess the gravity response to the wobbles in the bands from seasonal to Chandler period. We summary in section 3.6.

3.3 Theory of Gravity Changes

3.3.1 Gravity Response to the Wobble

The gravity change is sensitive to redistribution of mass within and on the Earth in terms of three dynamical processes as follow: a gravity response, an attraction effect, and a loading effect. The variation in the Earth's gravitational potential induces an effect from the local gradient of the acting potential, and an effect due to the displacement deformed by the acting potential. The deformation of the Earth perturbs the Earth's gravitational potential. The gravity response means the sum of these effects associated with the variation of potential. The redistribution of mass in geophysical fluids, such as atmosphere, ocean, land water, liquid core, and so on, cause the gravity perturbations in terms of variations in not only the Newtonian attraction, but also the surface loads with the deformations of the Earth. These attraction and loading effects are described in following subsections, and we first give the basic formulations relative to the gravity response. Note that μGal ($10^{-8} m/s^2$) is employed as a unit of gravity change in this chapter.

A rate of rotation and an orientation of an instantaneous rotation axis are changed by the LOD change and wobble, respectively. Consequently, the LOD change and wobble induce the fluctuation in the Earth's centrifugal force. A first-order perturbation in the Earth's centrifugal potential is given as follow :

$$V(r,\theta,\lambda) = \frac{\Omega^2 r^2}{2}\left[2m_3 sin^2\theta - sin2\theta(m_1 cos\lambda + m_2 sin\lambda)\right] \tag{3.1}$$

where Ω is Earth's mean angular velocity, (r,θ,λ) are radial distance, co-latitude, and longitude of the observation point, respectively [*Wahr,* 1985]. m_1, m_2, and $1 + m_3$ are the direction cosines of the instantaneous rotation axis along Greenwich, 90 °E, and the Earth's figure axis. In eq. (3.1) , the term involved with m_3 at right-hand side describes the perturbation caused by the LOD change, while the terms including m_1 and m_2 express the effect of the wobble.

The perturbation in the Earth's centrifugal potential deforms the solid Earth. This deformation affects the surface gravity thought two dynamical processes: the displacement of observation point and a secondary perturbation in the gravitational potential arising from mass redistribution. The surface gravity change due to the LOD change and wobble, which is derived from radial differentiation of the gravitational potential, can be expressed by:

$$\Delta g = \delta\frac{2}{r}V(r,\theta,\lambda) \tag{3.2}$$

where δ is referred to as a gravimetric factor [*Wahr,* 1985]. Using second-order Love number, h and k, which describe the effect of the displacement of surface and of the additional perturbation in the gravitational potential, respectively, the gravimetric factor is given by $\delta = 1 + h - 3/2k$ [see, e.g. *Hinderer and Legros,* 1989]. The gravimetric factor is sensitive to shape and physical property of the solid Earth, and the spherical harmonics and frequency of the external forcing [see e.g. *Dehant et al.,* 1999]. The gravimetric factor can provide information how the Earth respond to the external forcing and how the solid Earth behaves anelasitically. We employ $\delta = 1.159$ as the theoretical gravimetric factor for gravity response to the wobble and LOD change in seasonal to Chandler period, though the spherical harmonics of perturbation in the gravitational potential due to the wobble and the LOD change differ from that of Sa wave.

The gravimetric factor is obtained from the gravity observation using the following relation:

$$\delta(\omega) = \frac{\Delta g_{observed}(\omega)}{\Delta g_{rigid}(\omega)} \tag{3.3}$$

where ω is an angular frequency, and Δg_{rigid} is computed from eq. (3.2) with assumption of a rigid Earth ($\delta = 1.0$) [see, e.g. *Hinderer and Legros,* 1989, *Loyer et al.,* 1999]. The gravity response due to the LOD change and wobble is given by both the gravimetric factor and a phase difference between $\Delta g_{rigid}(\omega)$ and $\Delta g_{observed}(\omega)$. If the Earth does not deform, $\delta = 1.0$ with zero phase lag of the observed gravity change. Since the Earth actually is deformed by external forcing, the gravimetric factor is considered to be 1.155 for a simple elastic solid Earth, and 1.159 for an anelastic body with mantle convection in the case of annual body tide (Sa wave), using a non-rigid Earth model [*Dehant et al.,* 1999]. The phase lag of observed gravity change are expected by anelastic Earth model [*Wahr,* 1985].

The wobble data, such as Earth orientation parameter (EOP), describes a coordinates of celestial ephemeris pole in terrestrial reference frame, but the celestial ephemeris pole does not always correspond to the instantaneous ration axis [*Gross,* 1992]. In the case of using the EOP, m_1, m_2, and m_3 are represented as follow:

$$(m_1, m_2, m_3) = \left(PMX - \frac{1}{\Omega}\frac{dPMY}{dt}, -PMY - \frac{1}{\Omega}\frac{dPMX}{dt}, -\frac{\Delta\Lambda}{\Lambda_0} \right) \tag{3.4}$$

where PMX and PMY are wobble parameters reported in the EOP, and Λ_0 and $\Delta\Lambda$ are a standard LOD and its deviation, respectively [*Gross,* 1992]. Elimination of the differential terms related to m_1 and m_2 in eq. (3.4) produces the maximum amplitude change of 0.5% or less, and the maximum phase difference of 0.5 °or less, for original gravity change.

In eq. (3.1), the maximum effect of the LOD change appears at the equator, and its estimated amplitude is about 0.03 μGal for annual period. On the other hand, the maximum effect of the wobble reaches about 3.5 μGal for the Chandler period and about 1.2 μGal for annual period at mid-latitude in northern and southern hemisphere. The effect of the wobble is two order larger than that of the LOD change. The estimated amplitude of gravity change without the effect of the LOD agree with that including the effect of the LOD within 0.01% for the Chandler period. In the seasonal variation, the effect of the LOD change varies the estimated amplitude by about 0.02 μGal in the equator and 0.002 μGal in polar region. In this study, we eliminate the effect of the LOD change and the differential terms related to m_1 and m_2 in eq. (3.4), treat only the effect of the wobble.

3.3.2 Response of Ocean to the Wobble

The ocean responds to the fluctuations in the centrifugal force due to the wobble, and in consequence the sea level varies. We refer this ocean response to the pole tide. The sea level changes in arbitrary point on the ocean, $\eta(\theta, \lambda)$, arising from an equilibrium pole tide are given by

$$\eta(\theta, \lambda) = (1 + k - h)\left(\frac{V(r, \theta, \lambda)}{g} + d\right) C(\theta, \lambda) \tag{3.5}$$

where g is gravitational acceleration at the Earth's surface, and d is additive constant to conserve the whole ocean mass (actually, to conserve the whole ocean volume) [*Wahr*, 1985]. $C(\theta, \lambda)$ is ocean function, which has either one on ocean area or zero on the land.

3.3.3 Effects of Fluids on the Earth's Surface

The atmospheric and oceanic mass transport arising from ocean tide, pole tide, and meteorological forcing, varies the gravity through the attraction and loading effects. The surface gravity change at arbitrary point can be estimated from the convolution of geophysical fluids' mass over whole Earth' surface, S. Since the distance between mass and observed point, accompanied with mass redistribution, varies the Newtonian force, the attraction effect is represented by

$$\begin{aligned} \Delta g &= \int\int_S \sigma(\theta, \lambda) \Gamma_N dS \\ \Gamma_N &= \frac{G}{r^2} \sum_n \{n P_n(cos\psi)\} \end{aligned} \tag{3.6}$$

where G is the universal gravitation constant, $\sigma(\theta, \lambda)$ is surface density, and ψ is angular distance between mass and observed points. The loading effect is also caused by the redistribution of mass in the geophysical fluids. The surface gravity change associated with the loading effect is given by

$$\begin{aligned} \Delta g &= \int\int_S \sigma(\theta, \lambda)\Gamma_E(\psi)dS \\ \Gamma_E(\psi) &= \frac{G}{r^2}\sum_n\{(2h'_n - (n+1)k'_n)P_n(cos\psi)\} \end{aligned} \tag{3.7}$$

where $\Gamma_E(\psi)$ is Green's function for the loading effect (we employ the Green's function provided by *Farrell* [1972] in our computation using the Gutenberg-Bullen Earth model), and h'_n and k'_n are n-order load Love number, which are dimensionless small quantities, representing how the Earth displaces and how the Earth's gravitational potential perturbs due to surface loads. Eq. (3.7) provides the gravity change due to both the displacement responding to the surface loads and the perturbation in the gravitational potential corresponding to the mantle deformation.

3.4 Observation of the Gravity Changes, Data Processing and Analysis

3.4.1 Observation of the Gravity Changes

Superconducting Gravimeter

Superconducting gravimeter (SG) is relative cryogenic gravimeter utilizing magnetic levitation force instead of classical metallic spring (see Appendix D for detailed explanations about principle and structure of SG). The cryogenic environment (4.2°K) maintaining the superconductive state gives stable thermal and mechanical environments for the gravimeter sensor, consequently it has a great advantage to realize long-term stability and low noise level of SG in comparison with the classical spring gravimeter.

The gravity sensing unit (GSU) are in a dewar filled by liquid helium (LHe) in order to keep cryogenic environment. The SG dewar is hung (supported) from thermal levelers (see Appendix D) fixed to the concrete pier of about 1.5 m in height. Recently, the configuration of support system of the dewar is improved to support it by the thermal leveler directly put on the basement in order to reduce the mechanical noise arising from the pendulum motion

of hanging dewar. The former is called "top mount" system, and the latter is referred to as "bottom mount" system.

It is essential to maintain the cryogenic environment inside the GSU for the high quality observation by SG. To accomplish this, we are forced periodically to fill LHe and to carry out the maintenance of the cryogenic refrigeration system. Since these work disturbs the SG observation, recent type of SG have been improved by additional features such as enhancement in its cooling performance and decrease in loss of LHe, in order to simplify use, increase reliability and reduce manpower requirements.

Observation Sites

The gravity data analyzed here are obtained from the SGs at three sites among the global SG network of Global Geodynamics Project (GGP; see *Crossley et al.* [1999]). They are Esashi in Japan, Canberra in Australia, and East Ongul Island in Antarctica (Syowa station). Their geographical coordinates (latitude, longitude and altitude) are listed in Table 3.1, and Figure 3.1 shows the locations of three observation sites with other sites in GGP network. All SGs at three sites have been installed on stable bedrock, so that an effect of microseism is considered to be comparatively small. Since Esashi site is located near the subduction zone of the Pacific plate, the seismic activities around there often disturb to continuously record gravity changes due to periodic geophysical phenomena. On the other hand, the observations at Canberra and Syowa station are prevented by such local seismicities.

Although gravity are affected by seasonal variations in hydrology such as ground water, there is no ground water and little rain at Syowa station [*Kaminuma,* 1983], and Esashi and Canberra sites are located where it is difficult to receive those effects. These two sites are separated by several 10 km distance from sea. On the other hand, East Ongul Island with about 1 km diameter is located to 3 km offshore from the Antarctic Continent, and it is surrounded with sea (but it is covered in sea ice over most duration of a year). Therefore it is impossible to be negligible the oceanic gravimetric effects.

SGs of TT#007, CT#031 and TT#016 type have been installed at Esashi, Canberra and Syowa station, respectively (Table 3.1). TT#007 and TT#016 adopt the top-mount system, while recent type such as CT#031 employs the bottom-mount system which has lower noise level than previous system. However, TT#007 was changed to the bottom-mount system on December 7, 1997.

The SG observation can not be maintained without liquid helium (LHe). LHe is easily obtained at Esashi and Canberra. On the contrary, difficult access to Syowa station forces

to produce LHe from gaseous helium in that site. This production of LHe are performed during 2 weeks every half year, and this work significantly affects SG observation. A major problem for analysis of SG data at Syowa station is how we eliminate the these considerable perturbations that is worthless for investigations on geodynamics from observed data.

Observed Data Sets

Analog electric signals that are output from SG through an analog low pass filter of time constant of 50 seconds, are sampled at every 2 seconds (but for 1 second at Canberra) with an analog to digital converter of 7.5 digits [see *Sato et al.*, 1995, for a detail]. The sampled digital data apparently are linearly with the gravity change. Then digital data are converted into the relative gravity change applying an individual scale factor (i.e. the value of $\mu Gal/Volt$) of each SG that is calibrated by comparing the absolute gravimeter [*Sato et al.*, 1997b; *Aoyama et al.*, 1997] Converted SG gravity data at three sites are displayed in Figure 3.2 and their analysis periods employed in this study are tabulated in Table 3.1.

3.4.2 Data Processing

Elimination of Gaps

The SG data includes the step-like or spike-like perturbations of short duration arising from the earthquakes, maintenance of SG (for example, refilling of liquid helium), power failures and so on (see Figure 3.2). Such perturbations disturb the determinations of amplitude and phase in the tidal components and long-term gravity changes. Therefore, we should objectively correct the magnitude of step like perturbations from SG data at stage of the 1 minute sampling interval by means of statistical information.

At first, we apply the digital low pass filter whose cut off period is 90 seconds in order to eliminate the aliasing due to microseism at period bands between 10 and 20 seconds, and convert the observed 2 (or 1) seconds sampling data into 1 minute sampling data. The predicted tidal components and the atmospheric gravimetric effect are removed from 1 minute data. The predicted tidal components between 1/3 days and Ssa tidal waves are computed using simultaneously a recent tidal potential [*Tamura*, 1987] with theoretically gravimetric factor and phase for purely elastic Earth [e.g., *Dehant et al.*, 1999]. The atmospheric gravimetric effect are predicted from atmospheric pressure data obtained at SG observation site with the single coefficient of $-0.384 \mu Gal/hPa$) for the response function.

The magnitude of step like perturbations (offset) are evaluated based on daily medians computed from 1 minute data corrected for the tide and atmospheric gravimetric effect.

When there is daily difference with previous day whose absolute amplitude is grater than $1\mu Gal$, we recognize this difference as the magnitude of step and remove this offset from 1 minute data. The long-term gravity changes longer than Ssa tidal wave appear in 1 minute data corrected for the tide and atmospheric gravimetric effect, but amount of gravity change per a day can not reach $0.05\mu Gal$ in maximum. Thus threshold of $1\mu Gal$ seems to be impossible to judge the daily change due to long-term gravity change as the offset. In the case that the step is detected, the time in which the step appears is specified by searching in duration between previous and next days, in order of 1 hour data, 1 minute data. The magnitude of the step at that time is defined by the difference in daily median. We eliminate the spikes from the corrected 1 minute data when absolute difference between daily median and gravity at each 1 minute exceeds threshold of $1\mu Gal$. The smaller remaining spikes will also be removed in tidal analysis as described later. A major problem is found that above correction for the steps and spikes can hardly be correspondent to long-term missing observation and perturbations. However, this problem will mention later.

The resulting 1 minute sampling series include the tidal components and atmospheric gravimetric effect, but they are made corrections for steps and spikes. These cleaned series are adopted by the digital low pass filter whose cut off period is 180 minutes in order to make 1 hour series for tidal analysis.

Decomposition of Tidal Variations and Atmospheric Effects

To separate the short-term tidal components from SG data, a tidal analysis program called BAYTAP-G [*Tamura et al.*, 1991] is applied to the cleaned 1 hour series. BAYTAP-G decomposes the given original data y_i into the four components of the tide T_i, response R_i, trend d_i, and irregular noise e_i, using the following model:

$$\begin{aligned} y_i &= T_i + R_i + d_i + e_i \\ &= \sum_{m=1}^{M} a_m \sum_{n=1}^{N} a^*_{nm} cos(\varpi_{nm} t_i + \phi^*_{nm} + \phi_m) + \sum_{k=1}^{K} b_k x(t_i - t_{i-k}) + d_i + e_i \end{aligned} \qquad (3.8)$$

where i denotes the $i'th$observation time. The unknown parameters to be determined are tidal factor a_m and phase ϕ_m for the $m'th$ tidal group, the response coefficients b_k to the associate data $x(t_i - t_{i-k})$ and trend d_i at each data point. ϖ_{nm}, a^*_{nm}, and ϕ^*_{nm} are the angular frequency, its theoretical amplitude and phase for the $n'th$ wave in the $m'th$ tidal group, respectively, and these parameters are given by BAYTAP-G as known parameters. e_i is equivalent to the residual time series.

BAYTAP-G can estimate the atmospheric gravimetric effect by means of the response

method. The atmospheric pressure data obtained at each observation site are adopted as the associated data in the analysis. *Tamura et al.* [1991] pointed out that BAYTAP-G dose not postulate explicit time function for the trend model, for example as a polynomial function. but only defines its smoothness by assuming an integrated random walk model as trend model. Thus trend components involve the long-term variations such as long-period tide, gravity response to the wobble, instrumental drift, and other gravimetric effects.

The tidal factors determined by BAYTAP-G find that SG data observed at Syowa station are desensitized within 2 % of magnitude for a period from May 25, 1996 to November 14, 1996 because the observation system was connected with the UPS system. The calibration factor in this duration are made a correction using the tidal factor for O_1 and M_2 tidal wave which have large amplitude and are affected by atmospheric variations. The 1 hour series corrected for the sensitivity are reanalyzed by BAYTAP-G. The results for short-term tidal analysis at each site are presented in Figures 3.3, where we adopt such sign convention for the gravity data as an increasing in gravity (i.e. downward acceleration) corresponds to the increasing of the observed value with the plus sign.

Next, the data sampled at the interval of 1 day (every 00 h UTC) from the 1 hour sampled trend data are separated into the long-term tidal components applying the BAYTAP-L program that is a modified version of BAYTAP-G for the analysis of the long-term tidal wave (4-5 days to 31 days). The results for long-term tidal analysis at each site are shown in Figures 3.4.

3.4.3 Method and Analysis

Least-square Fittings of Sinusoids, Trends and Steps

We derive the following three components from the residual daily series, using a non-linear least square fitting by means of Levenberg-Marquardt algorithm. The analysis model fitted to the residual daily series is

$$f(t) = f_{trend}(t) + f_{periodic}(t) + f_{step}(t) \tag{3.9}$$

where t is the observation time in unit of day, and $f_{trend}(t)$, $f_{periodic}(t)$, and $f_{step}(t)$ are models for trend, periodic term, and steps, respectively.

The trend model $f_{trend}(t)$, consists of three components of bias, instrumental drift (exponential function), and linear trend as follow:

$$f_{trend}(t) = a_1 + a_2 e^{a_3(t-t_0)} + a_4(t - t_0) \tag{3.10}$$

where t_0 denotes the start day of the analyzed period. a_2 is parameter for amplitude of exponential term and a_3 equal to the $1/\tau$, where τ is a time constant of the exponential term. At Esashi site, SG was installed on April 20, 1988, and the continuous observation has been performed, but we use SG data beginning on January 1, 1995, in which the atmospheric pressure data by the cylinder vibratory barometer was recorded with SG data. Moreover, SG at Esashi was exchanged to the bottom mount type from the top mount type on December 7, 1997. Therefore, the instrumental drift beginning on December 7, 1997 is beforehand determined, and it is removed from $f_{trend}(t)$ in SG data obtained at Esashi site.

The periodic term $f_{periodic}(t)$ comprises coefficients for cos-terms and sin-terms of the annual and semiannual sinusoids, and gravimetric factor and phase for gravity response to the Chandler wobble as follow:

$$\begin{aligned} f_{periodic}(t) &= a_5 cos\omega_A t + a_6 sin\omega_A t + a_7 cos\omega_S t + a_8 sin\omega_S \\ &\quad + a_9\{g^C_{EOP}(t) - a_{10} \times dg^C_{EOP}(t)/dt\} \end{aligned} \tag{3.11}$$

where ω_A and ω_S are angular frequencies of annual and semiannual components, and $\Delta g^C_{EOP}(t)$ are theoretical gravity change inferred from nonseasonal wobble on the assumption of purely rigid Earth (i.e. $\delta = 1.0$) [see *Mukai et al.*, 1998]. All phase angles are defined to January 1, 2000.

The problem about the correction for the steps as above affects on the phase of periodic terms, seriously. We test this influence using synthetic data that artificial step is added to periodic components consisting of three sinusoids with same data length of observed data in center of day. In the case that artificial step is $5\mu Gal$, the amplitude of the Chandler, annual and semiannual components are disturbed within 0.9 %, 17.5 % and 12.4 % of it, respectively. Their phases also are increased within 9.2, 3.9, and 1.9°, respectively. Since the maximum amplitude of step caused by power failures reaches $600\mu Gal$, the disturbances in amplitude and phase are generated if it is determined at high accuracy of 1 %. The problem about correction for the steps are gotten to contend with the following model:

$$\begin{aligned} f_{step}(t) &= \sum_i a_i \times S(t) \\ S(t) &= \begin{cases} 1 & t < t_i \\ 0 & t \geq t_i \end{cases} \end{aligned} \tag{3.12}$$

where S(t) is step function with 1 beginning on $i'th$ disturbed day and one. The magnitude of step are reestimated by a_i. The date when the step function become 1 from 0 are listed in Table 3.2.

Optimization of Sinusoids

The Chandler wobble is free circular motion. Therefore, its amplitude and phase have varied with time [*Lambeck,* 1980, for a review]. If such time variation with considerably large amplitude is generated even in our analysis period, it prevents to determine the periodic terms using least square fitting. At first, we test the stability of amplitude and phase using EOPC04 during 1962 - 1999. We estimate time variation in amplitude and phase of the Chandler, annual, and semiannual components of the gravity change inferred from EOPC04 on assumption of rigid Earth, Δg_{EOP}, applying 6 years sliding window that is advanced by half year. Every 6 years in length of Δg_{EOP} are fitted to the following analysis model:

$$\begin{aligned} f(t) &= a_1 + a_2 t + a_4 cos a_3 t + a_5 sin a_3 t \\ &\quad + a_6 cos\omega_A t + a_7 sin\omega_A t + a_8 cos\omega_S t + a_9 sin\omega_S \end{aligned} \tag{3.13}$$

where a_3 is unknown parameter for angular frequency of the Chandler wobble.

Figure 3.5 displays these results for Syowa site. This figure reveals that both considerable change in amplitude and phase of the Chandler component appear in 1969 and 1980 and its period seems to vary. Synthetic data that assumes the phase jump can reproduce the similar variations in amplitude, phase and period of Chandler component as shown in Figure 3.5. *Gibert et al.* [1998] reported the similar change in amplitude and phase of the Chandler wobble applying the wavelet analysis and concluded that those changes are caused by torques arising from variations in a pressure of fluid core on core-mantle boundary, because those changes are coincided with magnetic jerk. However, those changes are hardly observed in our analysis period for SG data during 1993 - 1999.

The optimum Chandler period for each 6 years window is stable within the range of 432.4 days to 438.7 days at its center day during 1987 - 1995. On the other hand, Δg_{EOP} of 12 years in length provides 435.0 $\pm$ 0.1 days for the optimum Chandler period during 1987 - 1998. *Smith and Dahlen* [1981] show the theoretical Chandler period of 435.2 days which incorporates four effects of the elastic deformation of mantle (+143 days), dynamical interaction between the mantle and core (-50.5 days), equilibrium pole tide (+29.8 days), and the mantle anelasticity (+8.5 days) in addition to the Euler period of 304.4 days, using 1066A Earth model. In the case of the PREM (Preliminary Reference Earth Model), the Chandler period is 432.3 days which includes the three effects of the elastic deformation (+147.1 days), core-mantle interaction (-51.5 days), and equilibrium pole tide (+30.7 days) besides the Euler period of 306 days [*Rubanks,* 1993]. Our Chandler period agree with these theoretical values within a few days. We recognize that the application of analysis model in eq. (3.13) is not improper.

A data length more than 6 years is considered to be necessary to safely separate the annual component from the Chandler component. Although EOP data has sufficient data length to safe separation, our SG data do not cover this condition. Therefore, we adopt the method that Δg^C_{EOP} that is removed seasonal components from Δg_{EOP} during 1987 - 1998, are fitted to the residual daily series of SG. There are two advantages which Δg^C_{EOP} is preferred to the Chandlian sinusoid; one reason is that the amplitude of Δg^C_{EOP} is monotonously decreased after 1993, another reason is that it is unnecessary to assume the Chandler period from the shorter data.

Figure 3.6 shows the results for trend model and step model, which residual daily series of SG are fitted to the analysis model in eq. (3.9) at three observation sites. Table 3.2 tabulate the reestimated magnitude of step by means of non-linear least square fitting and initial estimates in terms of daily median. This table reveals that a maximum value exceeds $6\mu Gal$. These results propose that long-term observation missing and perturbations are required to be reestimated the magnitude of step.

SG at Syowa station locating in high latitude possibly detect long-period tide such as 18.6 years tidal wave. This tidal effect for Syowa station as shown in Figure 3.6 may disturb the trend terms, so that we remove this effect from residual daily series. The residual series corrected for 18.6 years tide and reestimated steps are presented in Figure 3.7. This figure shows that observed long-term gravity change agrees well with fitting model at each observation site. The fitting parameters are listed in Table 3.3.

3.4.4 Computation of Effects of Surface Fluids

Atmospheric Gravimetric Effects

Atmospheric motion affects the surface gravity measurement over the broad frequency bands. Precise estimations of atmospheric gravimetric effects are carried out by means of response method and integral method. In application of the response method, the atmospheric gravimetric effects are calculated by multiplying meteorological data by coefficients of response function which are fitted to gravity data [e.g. *Sparatt,* 1982]. In application of the integral method, on the other hand, the atmopsheric effects on gravity measurement are evaluated by convolving global objective analysis data with a function for the attraction and the load Green's function (see eqs. (3.6) and (3.7)) over the world [e.g. *Mukai et al.,* 1995]. The estimation of atmospheric gravimetric effect by the integral method is considered to be more precise than that by the response method. However, the gravity change that estimated by

using a single response coefficient and atmospheric pressure data obtained from SG observation site can represent more than 90 % of that estimated by applying the integral method [*Sato et al.*, 1991; *Mukai et al.*, 1995]. Although we have applied the response method that has advantage of its simplicity of calculation, to the data processing mentioned above, the influence (i.e. failure in estimation of atmospheric effect) due to this application is considered to be small.

Oceanic Gravimetric Effects

The attraction and loading effects of the ocean tide are computed from output of ocean tide model for Ssa and Sa tidal waves [*Takanezawa*, 1999, a private communication], applying the computer program called GOTIC which is developed to make a correlation for effect of ocean tidal loading to the data obtained from gravimeter or tiltmeter [*Sato and Hanada*, 1984]. The topographic data used in GOTIC is global 5-arcmin gridded topography data called ETOPO-5 [National Geophysical Data Center, 1988]. The Green's function for the Gutenberg-Bullen Earth model provided by *Farrell* [1972] is applied as $\Gamma_E(\psi)$ in eq. (3.7). The sea level changes due to the equilibrium pole tide over the whole ocean are computed from EOPC04 in terms of eq. (3.5) using h=0.602 and k=0.298. Its gravimetric effect is also estimated applying the GOTIC.

The gravimetric effect of SSH variations are evaluated by convolving SSH data over the whole oceans. We employ the SSH data generated by Parallel Ocean Climate Model (POCM) [*Stammer*, 1992], and that obtained by TOPEX/POSEIDON (T/P) satellite altimeter. The POCM is ocean general circulation model which is driven by climatic forcing such as surface wind stress and sea surface temperature (SST). The data of POCM used here are SSH in every 1/4 degrees grid in the ocean regions from -75°S to 75°N, at 10 days intervals for a period of October 7, 1992 to December 22, 1995 (i.e. 1171 days). For the computation in this study, we average the original data over the 1° × 1°. On the other hand, the data of T/P used here are compiled by Naval Post Graduate School of USA (NPS), and their grid size is 2 degrees square which covers the ocean regions between 0°to ±66°in latitude. The ocean region in south of 66°S is interpolated by means of spline, because of absence of data in T/P.

In SSH variations, there are components which are not accompanied with mass change exist; one of them is thermal expansion of water column that is referred to as thermosteric component and it hardly cause any gravity changes [see, *Fukuda et al.*, 1999; *Sato et al.*, 2000]. EOFs (Empirical Orthogonal Function) of SSH and SST obviously indicate that a

most dominant signal of the SSH variations is connected with the annual thermal change. Thus thermosteric correction is required to estimate the gravimetric effect of the SSH variations [*Fukuda et al.*, 1999].

We attempt to evaluate the thermosteric component using a single coefficient alone. We estimate the coefficient for the thermosteric correction at each grid $\alpha_{i,j}$ as linear regression coefficient between SSH and SST by fitting following equation by means of the least squares method:

$$SSH(\theta_i, \lambda_j, t) = \alpha_{i,j} \times SST(\theta_i, \lambda_j, t), \tag{3.14}$$

where θ_i and λ_j are co-latitude and longitude of each ocean grid; t denotes time of each data point; $SSH(\theta_i, \lambda_j, t)$ and $SST(\theta, \lambda, t)$ are the deviatory parts of SSH and SST on each grid by subtracting their mean values.

From the fitting based on the POCM SSH data, we have obtained the values for $\alpha_{i,j}$ within the range between -1.30 and $1.58 cm/°C$. In order to see the characteristics in the spatial distribution of the obtained $\alpha_{i,j}$ values, we averaged them zonally over 10°wide belts across each ocean basin of the Pacific, Atlantic and Indian Oceans. The averaged values vary between -0.06 and $1.09 cm/°C$. Low $\alpha_{i,j}$ values (0.2 to $0.3 cm/°C$) were found at high latitude in both the northern and southern hemispheres. In the equatorial regions within ±20°, the values of $\alpha_{i,j}$ show large and complex spatial variations, and the averaged values range from -0.06 to $1.09 cm/°C$. In mid latitude regions , ocean regions where strong western currents such as Kuroshio or the Gulf stream flow also showed a complex spatial distribution of $\alpha_{i,j}$, but $\alpha_{i,j}$ itself distributed around a value of $0.6 cm/°C$. Similar results were obtained from the analysis using the T/P data.

The coefficient $\alpha_{i,j}$ clearly varies with the location but as an approximation, we have evaluated an average coefficient $\alpha_{i,j}$ over the central regions of the Pacific and Atlantic oceans. Consequently, we obtained values of $0.60 cm/°C$ from the POCM SSH data, and $0.52 cm/°C$ from the T/P data [*Sato et al.*, 2000, for a detail]. We employ $0.60 cm/°C$ as the single coefficient for the thermosteric correction.

Figure 3.8 shows the annual fields of the T/P SSH and SST. SST data are multiplied by the thermosteric coefficient of $0.6 cm/°C$, and in consequence correspond to the thermosteric components. The annual SSH field corrected for thermosteric components is also displayed in Figure 3.8. It appears that the north and south symmetric phase pattern are dominant in the annual field of the original SSH and thermosteric components, while the zonally phase pattern in the equator are remarkable in that of corrected SSH (see Figure 3.8b). Comparing the original SSH and corrected SSH, it reveals that the extensive high amplitude region in the central parts of both the Pacific and Atlantic oceans in the northern hemisphere is

considerably reduced by corrections for the thermosteric effect, but the high amplitude areas accompanying with the two western boundary currents (i.e. Kuroshio and Gulf stream) still remain (Figure 3.8a). The remarkable high amplitude region also appears in the El Niño region around the equator.

The mass of ocean should conserve after making the correction for the thermosteric components to the SSH variations. We have to take into account all of the water cycle over the oceans and profile for the density and temperature in the seas, for the purpose of carrying out rigorous mass conservation. Thus we apply the volume conservation instead of the mass conservation in calculation of the attraction and loading effects of SSH variations which are already removed thermosteric components.

3.5 Results and Discussion

3.5.1 Seasonal Gravity Changes

Gravity Change at Annual Period

We first attempt to quantitatively explain the observed annual gravity change corrected for atmospheric gravimetric effect, using five geodynamical model: two gravity responses to the solid tide and to the annual wobble, and three gravimetric effects of ocean tide, equilibrium pole tide, and SSH variations driven by climatic forcing. The observed annual gravity changes are compared with predicted values by means of the phasor plots (see section 2.5.1 in detailed explanation of phasor plot) in Figure 3.9. These gravity responses are computed on the assumption of purely elastic response of the Earth (i.e., $\delta = 1.16$ with zero phase lag). The elastic gravity response to the annual wobble are computed from the EOPC04 for the period of 12 years from 1987 to 1998. The gravimetric effect of equilibrium pole tide on the annual gravity change is extracted from time series generated by equilibrium sea level change given by eq. (3.5) and by applying GOTIC, using least square fitting. The gravimetric effect of SSH variations are estimated using POCM and T/P SSH data which are corrected for thermosteric components with the thermosteric coefficient of $0.6cm/^{\circ}C$.

Both effects of the solid and ocean tides of Sa wave are very small at Esashi and Canberra located in mid latitude. In the order of Esashi, Canberra and Syowa station, their amplitudes are 0.109, 0.094 and 0.922 μGal for solid tide of Sa wave, and 0.002, 0.003 and 0.070 μGal for ocean tide, respectively. The gravimetric effects of equilibrium pole tide have the amplitude of 0.054, 0.043 and 0.029 μGal for Esashi, Canberra and Syowa station, respectively. Both gravimetric effects of the ocean tide and the equilibrium pole tide are not significantly larger

than the formal error of fitting for the observed annual gravity change.

We compare the gravimetric effect of POCM SSH with that of T/P SSH, these results are shown in Figures 3.9a and 3.9b, respectively. The POCM SSH and T/P SSH induce different gravimetric effects. We possibly attribute this difference mainly to different grid size of those data. Their vector differences have about 0.2 μGal in amplitude and about 25°in phase at all sites, except for -160°of phase at Syowa station. Since T/P SSH data around Antarctica are interpolated by means of spline, we avoid its physical interpretation about the phase difference. In view of the amplitude of the vector differences, there is a possibility that these differences are caused by different correction for ocean response to the atmospheric loading, which is whether or not it incorporates the effect of mean surface pressure over the whole oceans. This means that source of this difference may give us information about ocean response to the atmospheric loading.

As a test, we have computed the gravimetric effects of SSH variations corrected for thermosteric components using two extreme thermosteric coefficients of $0.0cm/°C$ (i.e. no correction for thermosteric effect) and $1.0cm/°C$, and they are displayed in Figure 3.9 for the purpose of comparisons. Figure 3.9 clarifies that the case of $0.6cm/°C$ is consistent rather than other two cases. This result means that the gravity observations support the single coefficient of $0.6cm/°C$ for thermosteric corrections, which has independently estimated from the SSH and SST data.

Figure 3.9 shows that gravity response to the annual wobble is a major source of annual gravity change, and the gravimetric effect of SSH variations is secondary source except for annual gravity change observed at Syowa station (they are secondary and thirdly sources, respectively). Therefore, the gravimetric effect of SSH variation can not be ignored to explain the observed annual gravity change with the accuracy better than 1 μGal.

Figure 3.9a clearly show that observed annual gravity change agree well with a sum of predicted gravity changes at all observation sites. The discrepancies between observed and predicted gravity changes are 0.080, 0.047 and 0.222 μGal for Esashi, Canberra and Syowa station, respectively, which are less than formal errors of fitting for the observed gravity change, except for value at Syowa station. The annual components of atmospheric gravimetric effects, which have been already removed from SG data, have magnitude of 0.530, 1.493 and 0.051 μGal for Esashi, Canberra and Syowa station, respectively. Their estimation errors may hardly affect these discrepancies, because the error is considered to little reach 10% of the magnitude of annual components (see *Sato et al.* [1991] and *Mukai et al.* [1995]). Since there are no ground water [*Kaminuma,* 1983], it is difficult to be considered that the discrepancy at Syowa station is connected with that gravimetric effect. Therefore,

we doubt that the maintenance of SG in every half year disturbs observed annual gravity change. Consequently, the significant agreements between observed and predicted annual gravity changes suggest that gravity data obtained from SG can prove information about geodynamics at time scale of a year with high accuracy equal to 0.1 μGal.

Gravity Change at Semiannual Period

Figure 3.10 shows the comparison between observed and predicted gravity change in semiannual variation as same as that in annual variation. In semiannual gravity change, the elastic gravity response to the semiannual wobble is very small at all sites, and the gravimetric effect of equilibrium pole tide are negligible. The amplitude of the gravimetric effect of SSH variations are too small to discuss the difference between POCM SSH and T/P SSH as shown in Figures 3.10a and 3.10b, respectively.

The discrepancies are 0.430, 0.353 and 0.145 μGal for Esashi, Canberra and Syowa station, respectively, in the case of the application of POCM SSH (Figure 3.10a). The semiannual components of atmospheric gravimetric effects have the magnitude of 0.723, 0.190 and 0.964 μGal for Esashi, Canberra and Syowa station, respectively, and their estimation errors possibly explain the 15 - 65% of these discrepancies. The future work is to study the geophysical meaning about the discrepancies in semiannual gravity change.

Observed Gravity Response to the Annual Wobble

Table 3.4 tabulates the gravimetric factors and phases with respect to the gravity response to the annual wobble. We first correct for the three gravimetric effects (due to solid tide, ocean tide and equilibrium pole tide) to the observed annual gravity change. The gravimetric factor and phase are derived from comparing the corrected gravity change with that computed from the observed annual wobble assuming rigid Earth, in terms of the relation in eq. (3.3). These values considerably disagree with theoretical elastic values, i.e. 1.159 and 0 for gravimetric factor and phase, respectively. However, their disagreements are decreased by further correction for the gravimetric effect due to SSH variations besides three effects. The approximations of theoretical values are remarkable in phase for Esashi and Syowa station, which are reduced by about 10°. The gravimetric factors contain noticeable errors (about ± 0.25), so that all gravimetric factors determined here can correspond with theoretical elastic value. Unfortunately, it is difficult to discuss the physical properties of Earth's interior such as the frequency-dependent anelastic behavior at frequency band much lower than seismic and short-periodic tidal bands without a betterment in the accuracy on

SG data and SSH data.

Our results indicate a necessity of precise evaluation on the gravimetric effect of SSH variations, in order to discuss the gravity response to the annual wobble. Since mass redistribution in the ocean affect the gravity measurements at SG observation sites locating at various latitude, we speculate that these oceanic variations possibly connect with the remaining budget for annual wobble as discussed in section 2.5.1. If this assumption is supported by the future work, we suggest a possibility that SG can detect the excitation source of annual wobble through the mass transports.

3.5.2 Gravity Change at Chandler Period

Observed Gravity Response to the Chandler Wobble

The gravity change in the vicinity of the Chandler period (defined here to the change with periods between 400 and 450 days) are represented by gravimetric factor and phase with respect to the gravity response to the Chandler wobble. Based on the eq (3.3), these values are estimated from comparing observed gravity change with wobble-induced one which are computed by assuming rigid Earth from the observed nonseasonal wobble (defined here to be wobble in which seasonal components and its trend are removed) during 1987 - 1998. Table 3.4 tabulates the gravimetric factors and phases for the gravity response to the Chandler wobble with their formal errors of fitting at three observation sites.

The gravimetric factors for Canberra and Syowa station are unusually smaller than theoretical values, and their disagreements exceed their formal errors by fitting. The phase lags of observed gravity change are -9 ± 2, 4 ± 2 and -10 ± 3 days for Esashi, Canberra and Syowa, respectively. In our results, there doesn't seems to be the considerable phase lag such as about 20 days reported by *Sato et al.* [1997a] and *Loyer et al.* [1999]. *Sato et al.* [1997] analyzed using two year SG data obtained at Syowa station, and obtained the about 20 days time lag of the observed gravity change against the wobble-induced one. The difference in phase lag at Syowa station between our results and *Sato et al.* [1997a] despite same data except for data length probably are attributed to the following reasons; (1) different data length of SG data; (2) different corrections for step-like perturbations; (3) they compared observed gravity change with induced one which contained the seasonal components. Thus we propose that the major source of large phase lag given by *Sato et al.* [1997a] are the effect of unseparated annual components.

On the other hand, *Loyer et al.* [1999] analyzed 8-year SG data obtained at Stratsbourg, France, and evaluated the phase lag that vary within the ranges of 9°to 22°, i.e. delaying of

10 days to 27 days in time domain. We possibly attribute the difference between our results and these large phase lag to the different analyzing method; *Loyer et al.* [1999] used sinusoid with period of 435 days in order to evaluate the gravity response to the Chandler wobble, but we employ the observed nonseasonal wobble, which shows the decreasing or increasing amplitude with time. Moreover, although *Loyer et al.* [1999] did not describe observed annual gravity change, it should be discussed dynamically in order to clarify the geophysical meaning of their phase lag for response to the Chandler wobble.

Phase difference within 10 days in our results are hardly based on the separation of annual gravity change because the observed annual gravity change agrees well with predicted one (we will further discuss the separation problem later) . The effect of mantle anelasticity varies the gravimetric factor and phase difference [*Wahr and Bergen,* 1986]. In the case of using the anelastic mantle based on the extremely low Q-value, the gravimetric factor increases 3.8% and the phase is delayed by 0.8°(i.e. about 1 day) [*Wahr,* 1985].

About 0.7 μGal magnitude of the gravity change is required to explain the phase difference of about 10 days. The atmospheric gravimetric effects at Chandler period have amplitudes of 0.216, 0.442 and 0.866 μGal for Esashi, Canberra and Syowa station, respectively, so that the effects of their estimation error are considered to be insufficient.

The disagreement between observed and theoretical elastic values are too large to be explained by the effect of mantle anelasticity and estimation error of atmospheric gravimetric effect. Thus we need assume that the observed gravity change around the Chandler period involves the gravimetric effects due to oceanic motion.

Effect of Pole Tide

It is impossible to ignore the pole tide as interannual variations in the geophysical phenomena. We subtract the induced gravity change that is computed from observed nonseasonal wobble assuming the purely elastic Earth from observed nonseasonal gravity change (which include neither seasonal components nor its trend term), in order to discuss the gravimetric effect due to pole tide on the gravity change around the Chandler period. The residual gravity change are converted into 10 day sampling data by averaging.

Figure 3.11a shows a comparison the residual gravity change with that due to the nonseasonal equilibrium pole tide during 1993 - 1995. It seems that residual gravity change contain the gravimetric effect of equilibrium pole tide, but its amplitude is much smaller than that of the residual.

The tide gauges around globe have observed sea level changes arising from ocean response

to the wobble, i.e. pole tide, and their observations have indicated several times amplitude of the equilibrium pole tide in the North Sea, Baltic Sea, and Gulf of Bothnia [e.g., *Trupin and Wahr*, 1990]. These non-equilibrium pole tide probably is driven by meteorological forcing such as surface wind stress with period of 14 months [*Tsimplis et al.* 1994]. It should be considered that oceanic gravimetric effect due to the meteorological origin in addition to the attraction and loading effects of equilibrium pole tide.

Figure 3.11b displays a sum of the gravimetric effects due to nonseasonal equilibrium pole tide and nonseasonal SSH variations in POCM, with a view to examining the effect of these non-equilibrium pole tide on the gravity change. It appears that the gravimetric effect of virtual nonseasonal non-equilibrium pole tide can partly reproduce the observed residual gravity change to the short-term variation. It is possibly appropriate to consider that the gravimetric factor and phase with respect to the gravity response to the Chandler wobble are affected by the nonseasonal oceanic motions, which are not only driven by meteorological forcing but also induced by the wobble. We, however, can not give a sufficient proof of this presumption, because the POCM SSH data are too short in data length to cover the analyzing period of SG data.

Gravity Change Due to Other Geodynamical Processes

On the assumption that the residual gravity change contain the periodic variation, we determine their amplitude and phase using the analysis model given in eq. (3.13) by means of non-linear least square fitting. In result, optimum periods of primary periodic component are 712 ± 93, 448 ± 270 and 435 ± 23 days for Esashi, Canberra and Syowa station, respectively. These results suggest that there seems the periodic gravity change with period similar to the Chandler one (i.e. 435 days).

In order to stabilize the estimation by fitting, the period of the primary periodic component are fixed on 435.0 days which is the optimum Chandler period obtained from observed wobble during 1987 - 1998. The results for refitting give us the evidence that the annual component are sufficiently separated from the observed gravity change, because annual component in the residual gravity change has amplitude less than 0.05 μGal, which is quantity of no significance. Therefore, the separation of annual component hardly affect the evaluation of the gravity response to the Chandler wobble.

Figure 3.12 shows the gravity changes at the Chandler period which are involved in the residual gravity change, wobble-induced one, the effect of equilibrium pole tide, that of SSH variations, and that of virtual non-equilibrium pole tide. The vectors of the Chandlian

component of the residual gravity change have the following amplitude and phase: (0.446 μGal, 137°) at Esashi, (0.446 μGal, 137°) at Canberra and (0.446 μGal, 137°) at Syowa station (Figure 3.12a). The amplitudes of these vectors are less than 1/10 of those of induced gravity changes, and there are difference in phase angle between them.

The Chandlian components of the gravimetric effect due to equilibrium pole tide display the different phase angle between Esashi, Canberra and Syowa station, while those due to SSH variations have similar phase angle at all sites as shown in Figures 3.12c and 3.12d, respectively. This means that equilibrium pole tide is distributed by spatial pattern which is represented by the second order and second degree spherical harmonics, i.e. tesseral function, but the SSH variations seem to be zonally.

Figure 3.12e shows the gravimetric effect of virtual non-equlibrium pole tide at the Chandler period, which is derived from the sum of effects of equilibrium pole tide and SSH variations driven by meteorological forcing, based on the conclusion of *Tsimplis et al.* [1994] in which non-equilibrium pole tide probably is driven by surface wind stress. These vectors for Esashi and Syowa are amplified by comparison with those in Figures 3.12c and 3.12d. Consequently, the residual gravity change corrected for these effects gives us interesting information; the directions of all vectors of corrected residual one agree within 30°. Each direction of the corrected residual vector is clearly different from that of equilibrium pole tide, comparing Figure 3.12c and Figure 3.12g. The vector shown in Figure 3.12g are considered to not contain the gravity change connected with the wobble and equilibrium pole tide. The amplitude of vector in Figure 3.12g are $0.1 - 0.3 \mu Gal$, and these size correspond to the theoretically estimated amplitude of the gravimetric effect arising from fluid core [*Hinderer and Legros,* 1989].

We suggest the possibility that SG detects the interannual signals arising from motions in ocean and fluid core which are little connected with perturbations in gravitational potential due to the wobble. A reliability for this discussion should be increased by the storage of precise data such as gravity and SSH data. In the near future, the precise global gravity field will be shown by satellite gravity mission such as GRACE (Gravity Recovery and Climate Experiment) scheduled for launch in 2001. These satellite gravity data together with SG data may provide new information about ocean and fluid core dynamics in interannual variations.

3.6 Summary and Further Studies

The Earth's gravity response to the Chandler and seasonal wobbles are discussed using data obtained from the superconducting gravimeters (SG). The data sets used here are three SG

data observed at Esashi in Japan (1580 days beginning from Jan. 2, 1995), Canberra in Australia (800 days beginning from Jan. 28, 1997) and Syowa station in Antarctica (1740 days beginning from Mar. 23, 1993), and EOPC04 for the wobble.

The observed annual gravity change corrected for atmospheric gravimetric effect at each observation site agrees well with predicted one consisting of the two elastic gravity responses to the solid tide and the annual wobble, and three gravimetric effects due to the ocean tide, equilibrium pole tide, and sea surface height (SSH) variations driven by meteorological forcing such as surface wind stress, where the SSH variations have been corrected for thermosteric component, using sea surface temperature (SST) and a single steric coefficient of 0.60 cm/°C that was independently determined from the relationship between SST and SSH. Their discrepancies for Esashi and Canberra are less than 0.1 μGal ($1\mu Gal = 1 \times 10^{-8} m/s^2$), and they are not significantly larger than the formal error of fitting for amplitude of observed annual gravity change. Consequently, it is clear that the SG data sets can provide valuable information about dynamics in various constituents of Earth through the mass transports at long-term period.

In semiannual gravity change, on the other hand, there are discrepancies of 0.1 - 0.5 μGal between observed and predicted values, but their major source possibly is insufficient correction for the atmospheric gravimetric effect by means of response method.

The observed gravity response to the annual wobble agree with theoretical elastic one in the range of its formal error of fitting. We suggest that the accuracy of discussing the mantle anelasticity can hardly be obtained in present state. The observed gravity response to the Chandler wobble disagree with the theoretical elastic one, and their disagreement is too large to be explained not only by the effect of mantle anelasticity but also by the gravimetric effect of equilibrium pole tide. We also We suggest a possibility that the SG observes the gravity change around the Chandler period arising from other geodynamical phenomena accompanying with mass transports in the ocean and the fluid core, but we can not give a quantitative discussion on this presumption because of insufficient data length of SSH.

The SG data in combination with satellite gravity mission such as GRACE (Gravity Recovery and Climate Experiment) scheduled for launch in 2001, can monitor the mass transports in Earth system and provide useful information about the dynamics of Earth system.

Site	Lat	Lon	Alt (m)	SG Type	Analysis Period (days)
Esashi	39.148°N	141.335°E	393	TT#007	1995.1.2~1999.4.30 (1580)
Canberra	35.321°S	149.008°E	724	CT#031	1997.1.28~1999.4.7 (800)
Syowa	69.006°S	39.586°E	24	TT#016	1993.3.22~1997.12.25 (1740)

Table 3.1: The SG data used in analysis of gravity response to the wobble. Note that TT or CT denotes the type of SG used. TT and CT means the old type with top mount system and new compact type of SG with bottom mount system, respectively.

Esashi

Date	Step[1](μGal)	Step[2](μGal)	Ratio(%)
1995.08.10	-358.97	-1.046	0.29
1995.09.27	376.16	-0.912	0.24
1997.06.26	-42.30	-1.829	4.32
1997.12.07	-285.71	-2.151	0.75

Canberra

Date	Step[1](μGal)	Step[2](μGal)	Ratio(%)
1997.08.07	-6.37	-0.954	14.98
1997.11.04	71.50	-0.142	0.20
1998.12.15	2.90	-0.411	14.18

Syowa

Date	Step[1](μGal)	Step[2](μGal)	Ratio(%)
1994.01.11	-69.05	0.540	0.78
1994.02.04	-501.58	0.515	0.10
1994.08.02	395.16	-6.723	1.70
1995.01.23	163.61	0.019	0.01
1996.07.16	23.63	1.340	5.67
1997.07.19	-14.78	0.487	3.29

Table 3.2: The magnitude of step-like perturbations estimated by non-linear least square fitting. Note that "$Step^1$" is estimated using "daily median", and "$Step^2$" is additionally estimated by non-linear least square fitting.

Site	Periodic components						Trends			S.D. (μGal)
	Chandler comp.		Annual comp.		Semi-annual comp.		Bias (μGal)	Linear (μGal/yr)	Exponential comp.		
	G. F.	Phs (days)	Amp. (μGal)	Phs. (deg)	Amp. (μGal)	Phs. (deg)			Amp. (μGal)	Tau (10^{-3}/day)	
Esashi	1.177	-8.7	1.296	-2.1	0.857	-167.4	0.360	-3.096	-	-	1.085
	±0.043	±2.1	±0.112	±6.5	±0.085	±4.8	±0.232	±0.164			
Canberra	1.085	4.3	1.878	-147.8	0.292	92.4	46.422	3.014	-6.527	-19.40	0.324
	±0.091	±2.1	±0.091	±7.0	±0.039	±2.5	±0.251	±0.142	±0.462	±2.10	
Syowa	0.861	-9.8	0.772	31.2	5.089	161.5	-420.648	-0.417	41.727	-2.71	0.907
	±0.061	±3.3	±0.083	±5.6	±0.067	±4.2	±1.022	±0.113	±1.207	±0.08	

Table 3.3: The estimated periodic components and trends obtained from three SG site. All estimated parameters are listed with their fitting errors. The phase defined to January 1, 2000. Note that "G.F." means gravimetric factor.

Site	Lat & Lon	Available Period (days)	Annual[1] Factor τ(days)	Annual[2] Factor τ(days)	Chandler Factor τ(days)	SD (μGal)
Esashi (1995.1~1999.4)	39.2°N 141.3°E	1337/1580	1.17±0.09 -21±7	1.09±0.26 -2±7	1.17±0.04 -9±2	1.0850
Canberra (1997.1~1999.4)	35.3°S 149.0°E	776/800	1.29±0.05 -6±6	1.13±0.16 1±6	1.09±0.09 4±2	0.3243
Syowa (1993.3~1997.12)	69.0°S 39.6°E	1552/1740	0.70±0.11 25±7	1.13±0.29 17±7	0.86±0.06 -10±3	0.9068

Table 3.4: The observed gravimetric factor and phase (time lag, τ) for the gravity responses to the annual wobble and the Chandler wobble.

Figure 3.1: Observation sites of the global network of the superconducting gravimeter (SG). Double circles denote the Esashi in Japan, Canberra in Australia, and Syowa station in Antarctica in which the data used here are observed.

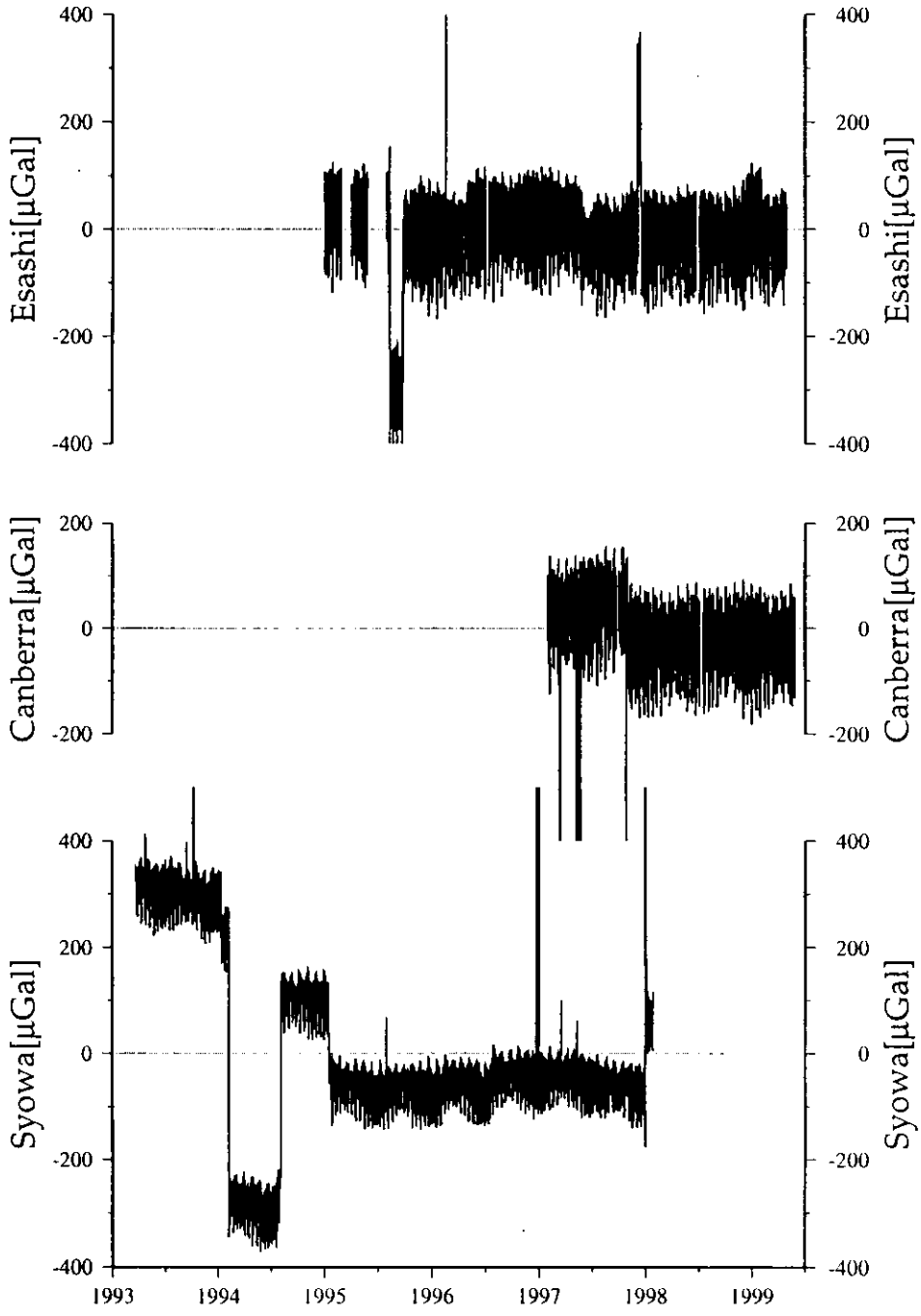

Figure 3.2: The raw gravity signal obtained from the SG at Esashi, Canberra, and Syowa station. Horizontal axis indicates the observed date. The spike-like or step-like changes in the gravity are caused by earthquakes, electric failures, and maintenance of instrument.

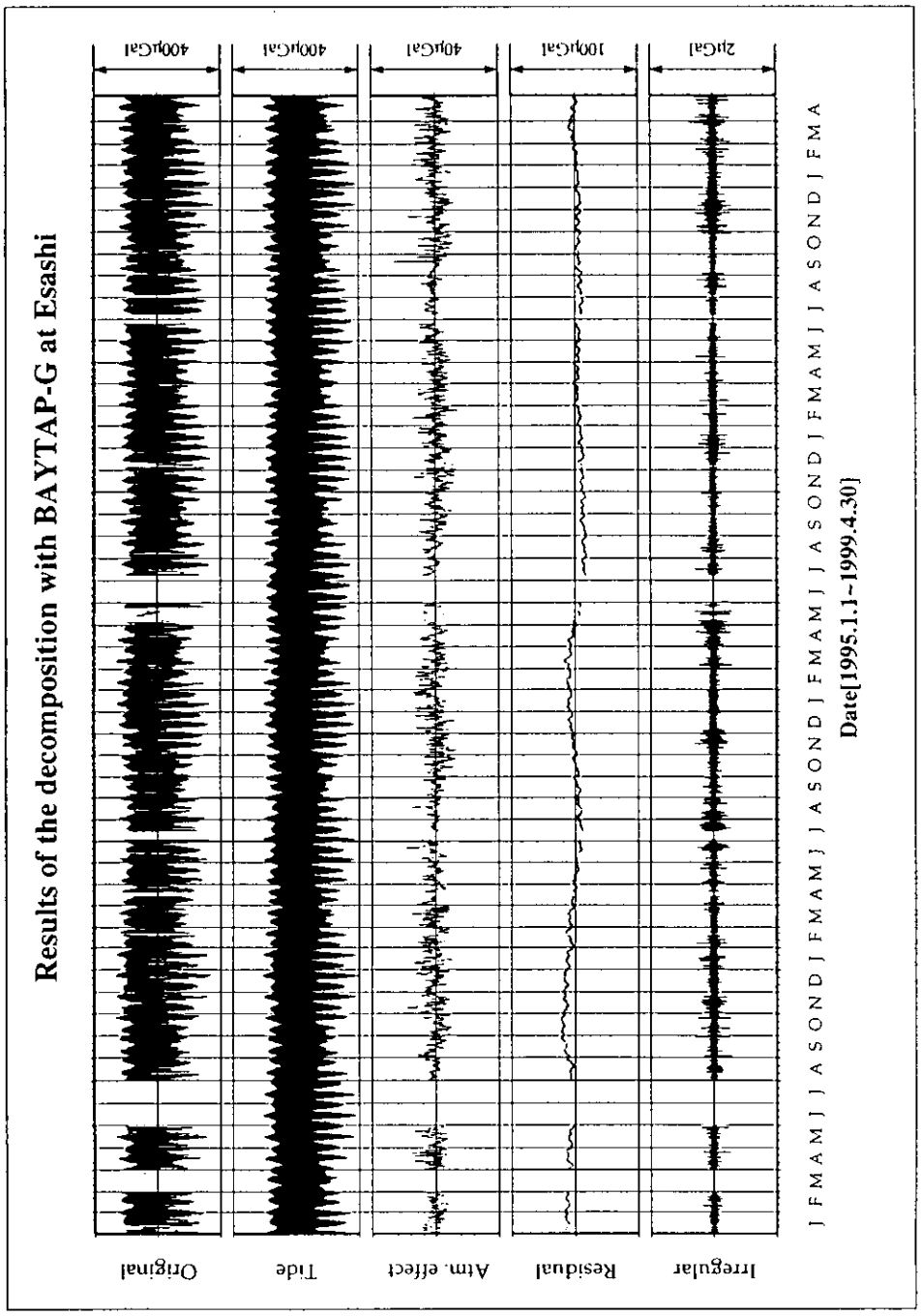

Figure 3.3a: Results of the decomposition applying the tidal analysis package, BAYTAP-G [*Tamura et al.*, 1991]. The following are displayed from the top : Original gravity change, tidal components (1/3 to daily tides), atmospheric gravimetric effect, trend, and short-term irregular component. Plotted data is observed at Esashi.

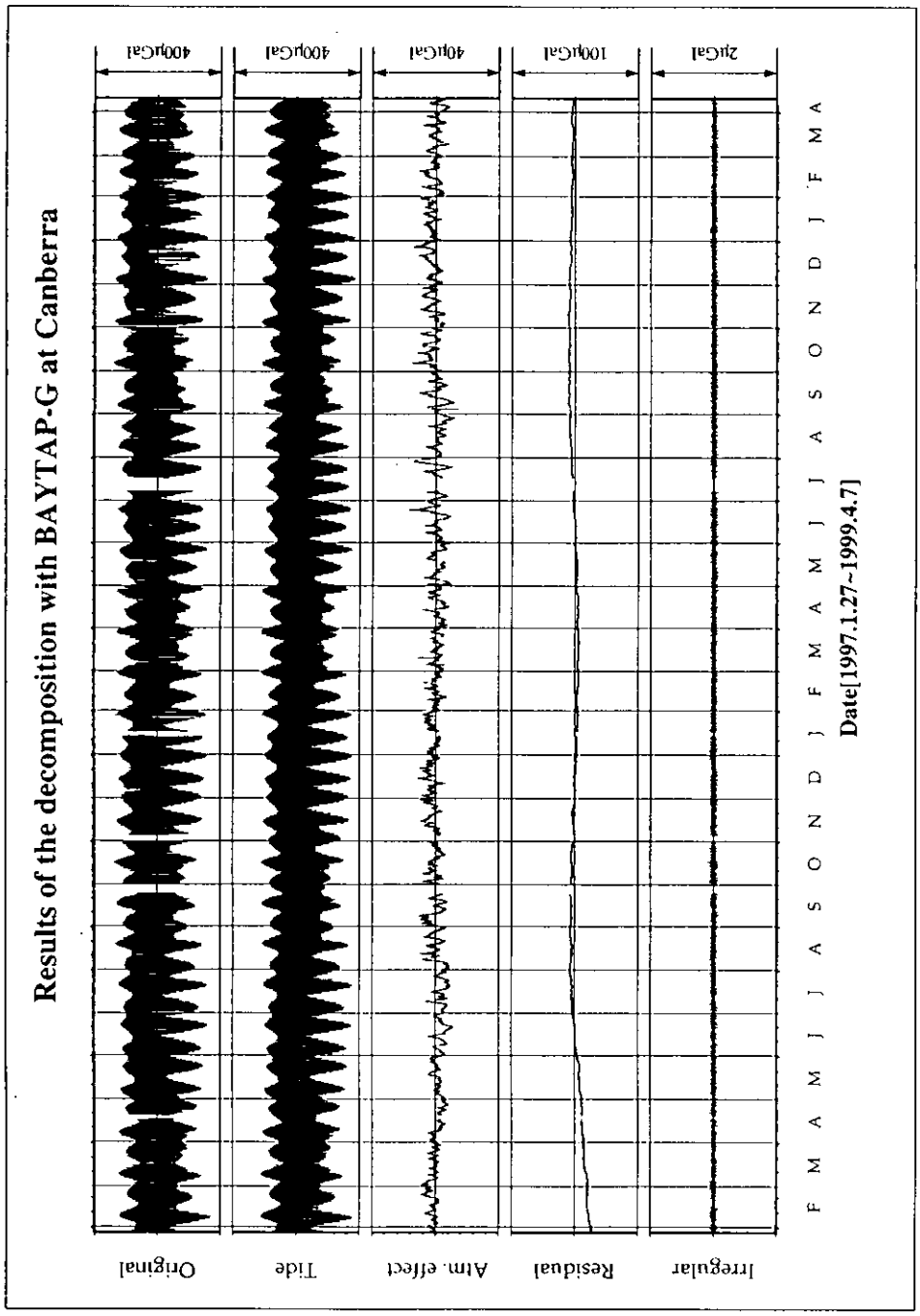

Figure 3.3b: Same as Figure 3.3a, but plotted data is observed at Canberra.

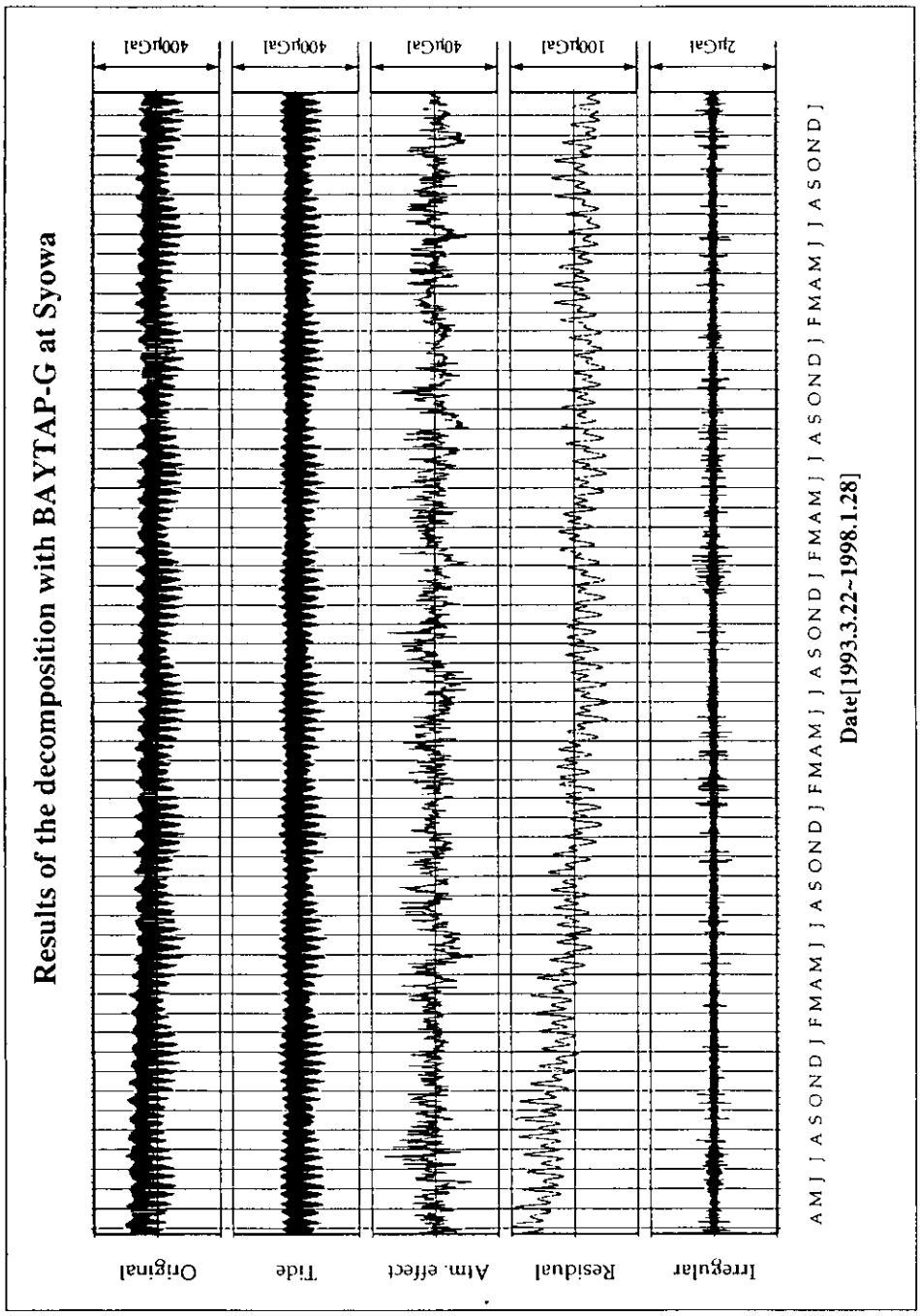

Figure 3.3c: Same as Figure 3.3a, but plotted data is observed at Syowa station.

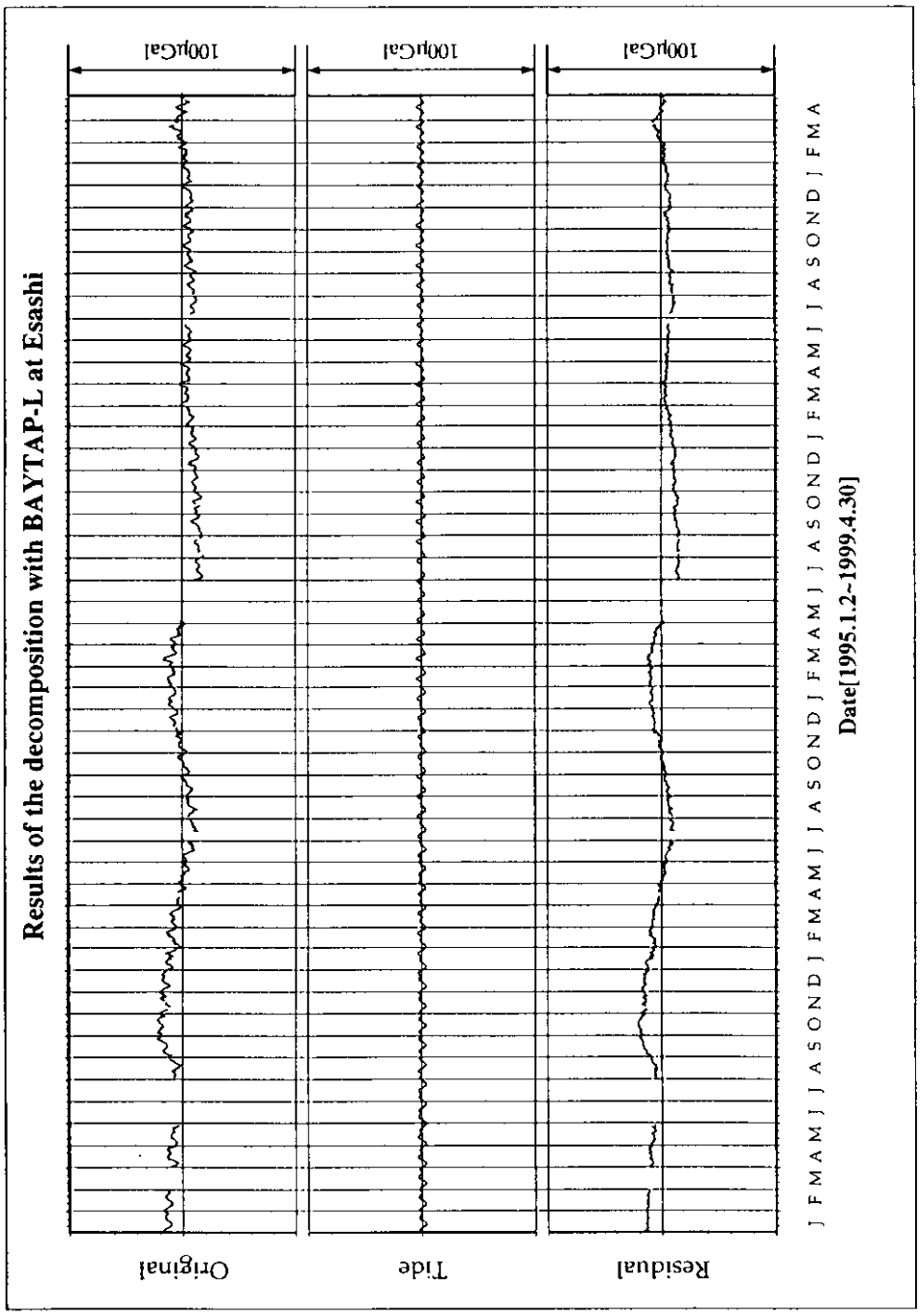

Figure 3.4a: Long-term tidal components (4-5 days to monthly tides) separated from the residual (trend) gravity change as shown in Figure 3.3a. The "residual" means the gravity change separated into the tidal components. Plotted data is observed at Esashi.

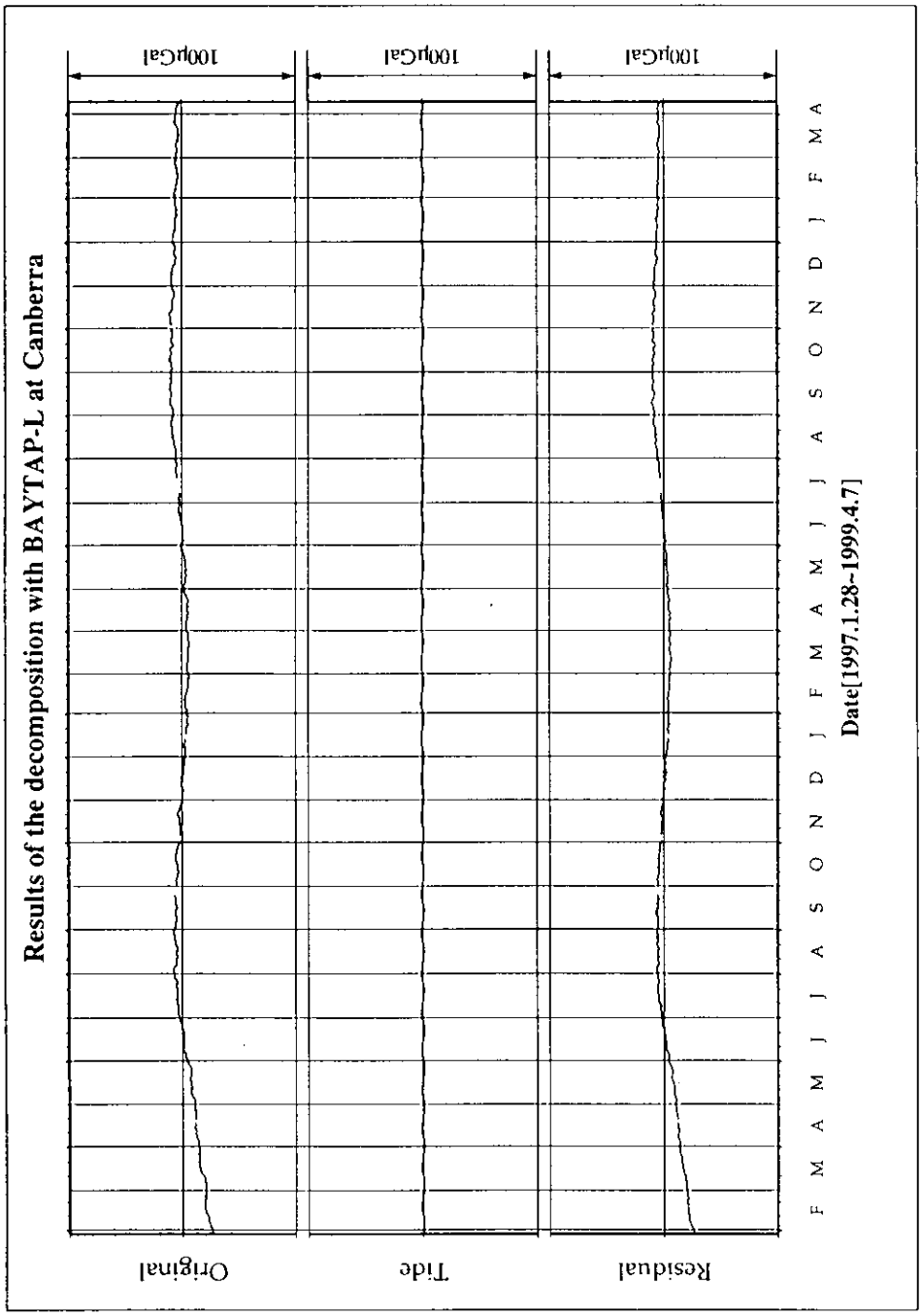

Figure 3.4b: Same as Figure 3.4a, but plotted data is observed at Cnaberra.

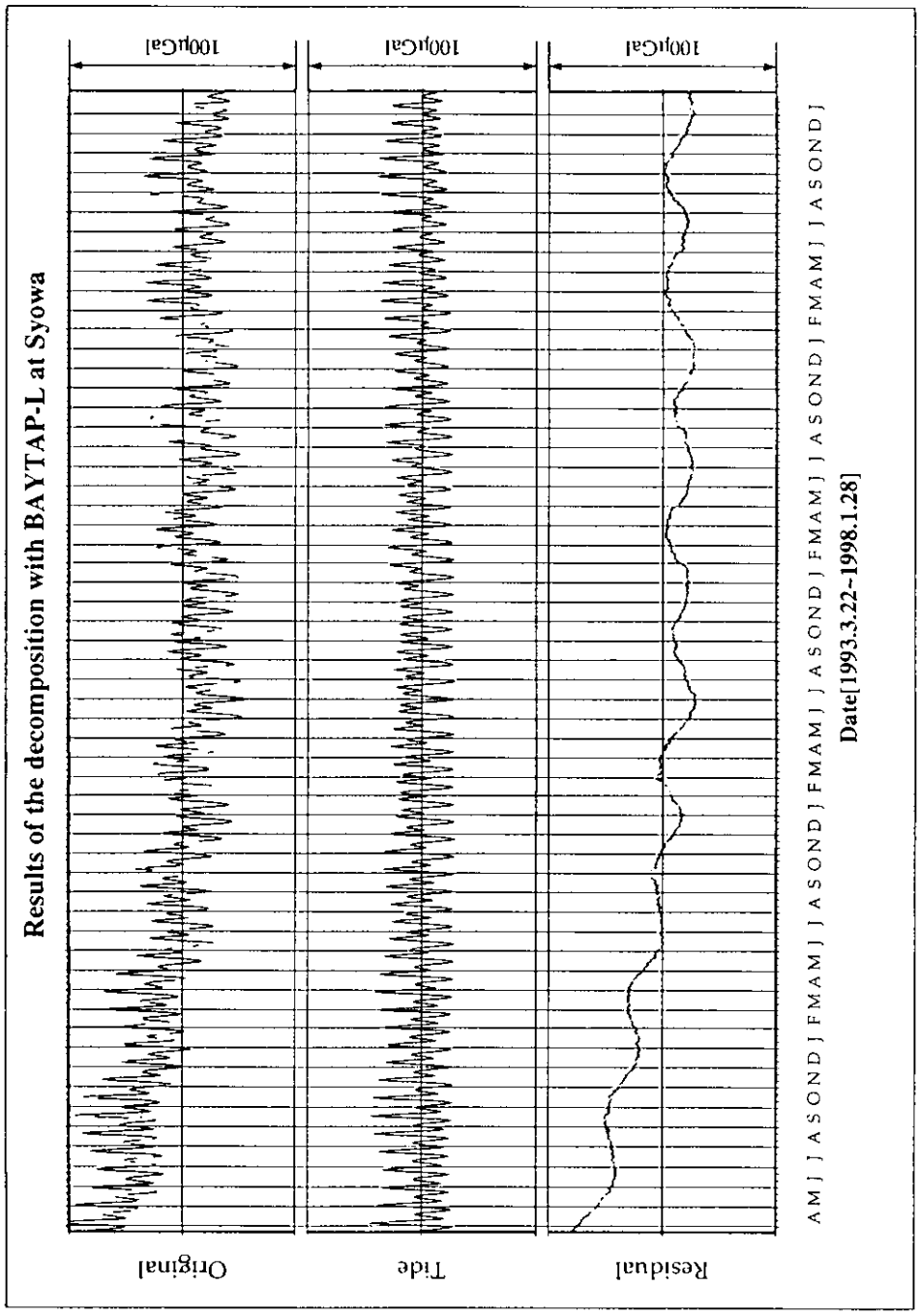

Figure 3.4c: Same as Figure 3.4a, but plotted data is observed at Syowa station.

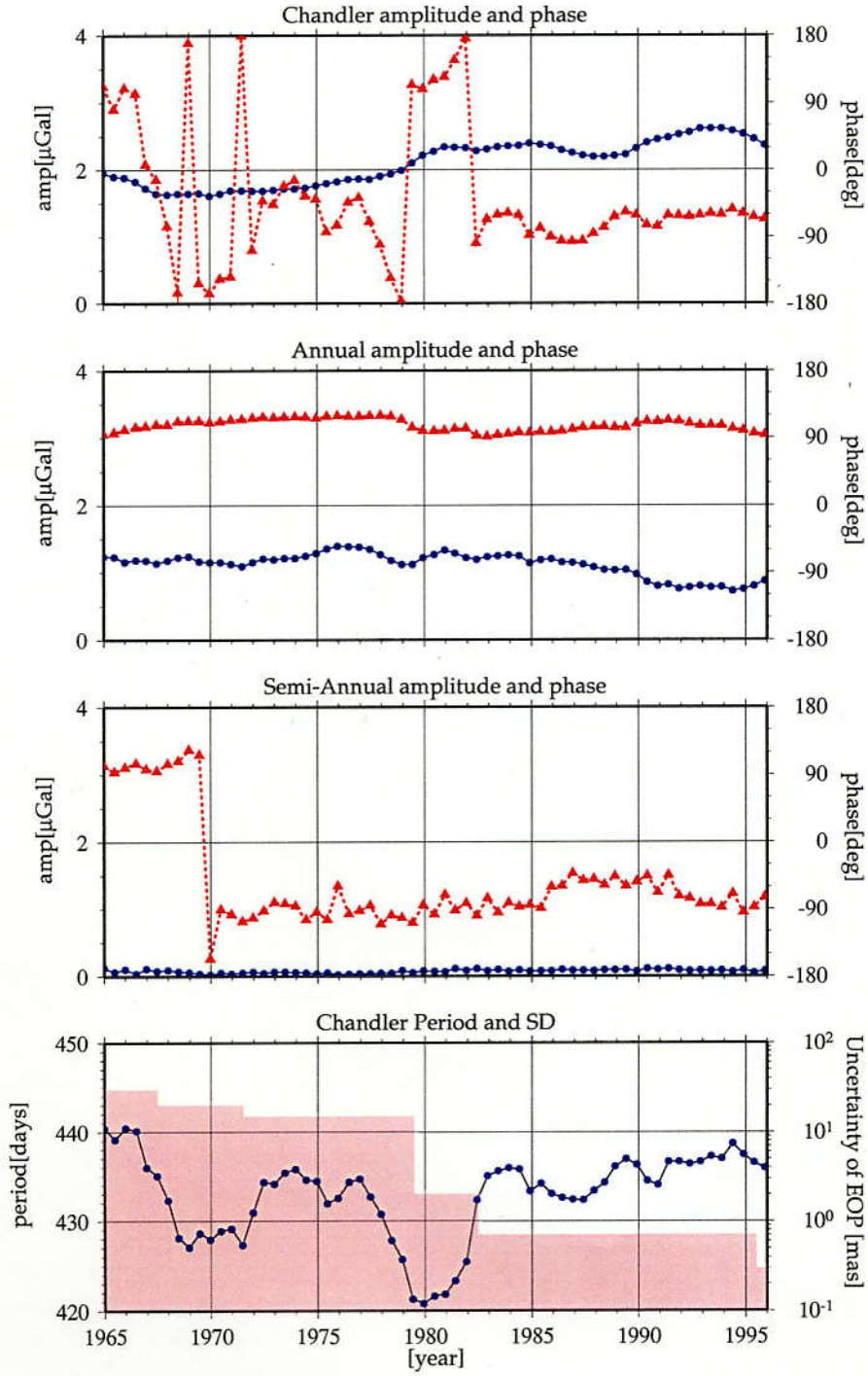

Figure 3.5: Time variations in amplitude and phase of the Chandler, annual, and semiannual components and the variation in the optimum Chandler period of the wobble-induced gravity change at Syowa station computed by assuming purely elastic Earth. These estimates are plotted at central day of a sliding 6 years window that is advanced by an increment of a half year, for a period of 1965 - 1998. Circles and triangles in three panels from the top denote the amplitude and phase with respect to January 1, respectively. In bottom panel, the circle indicate the Chandler period, and uncertainties of EOP is given by pink rectangle.

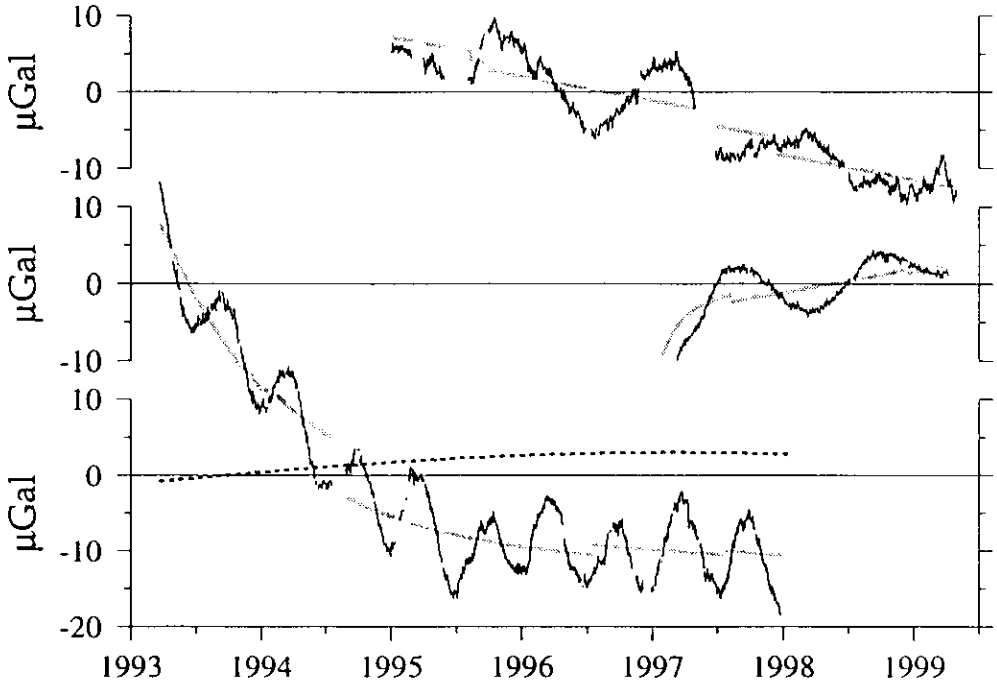

Figure 3.6: Comparison between the observed long-term gravity change and the results for fitting. Thin lines denote the observed data which is residual components shown in Figures 3.4a, 3.4b, and 3.4c, and gray-coloered heavy lines show the trend components (linear trend, initial drift of the instrument, and step-like disturbance) fitted using the analysis model given in section 3.4.4. From the top, three panels show the results for Esashi, Canberra, and Syowa station, respectively. The 18.6 years tidal component at Syowa station is displayed as the dashed curve.

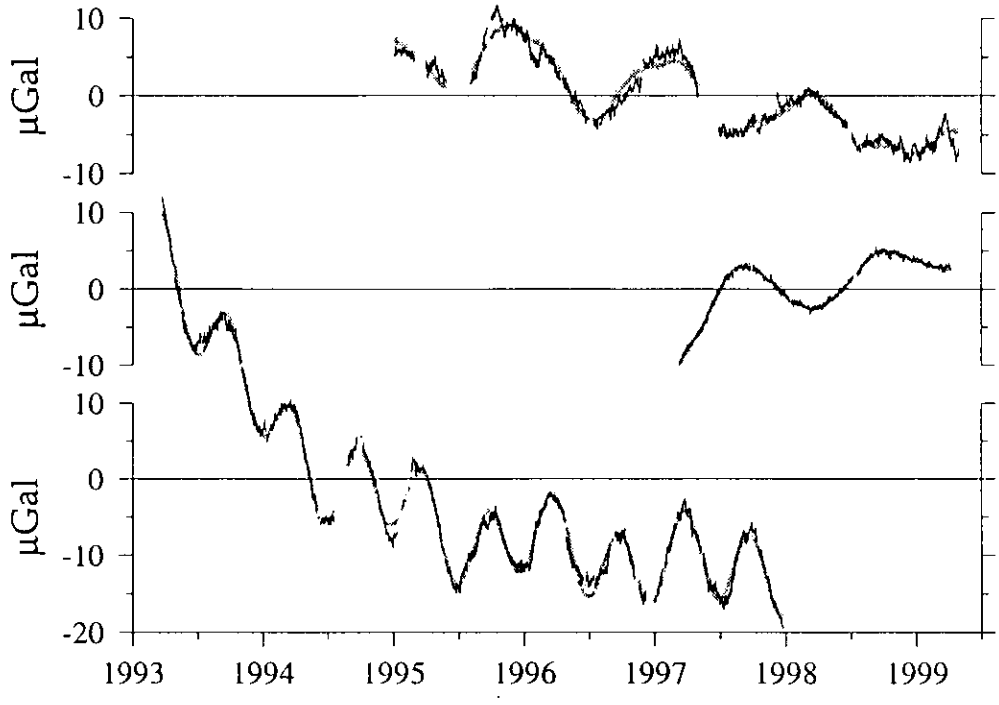

Figure 3.7: Comparison between the observed long-term gravity change that the step-like disturbance (thin line) is removed, and the results for fitting. The gray-colored heavy lines indicate the periodic components with the linear trend and the initial drift of the instrument fitted using the analysis model given in section 3.4.4. From the top, three panels show the results for Esashi, Canberra, and Syowa station, respectively. The 18.6 years tidal component as shown in Figure 3.6 is also deducted from the long-term gravity change observed at Syowa station.

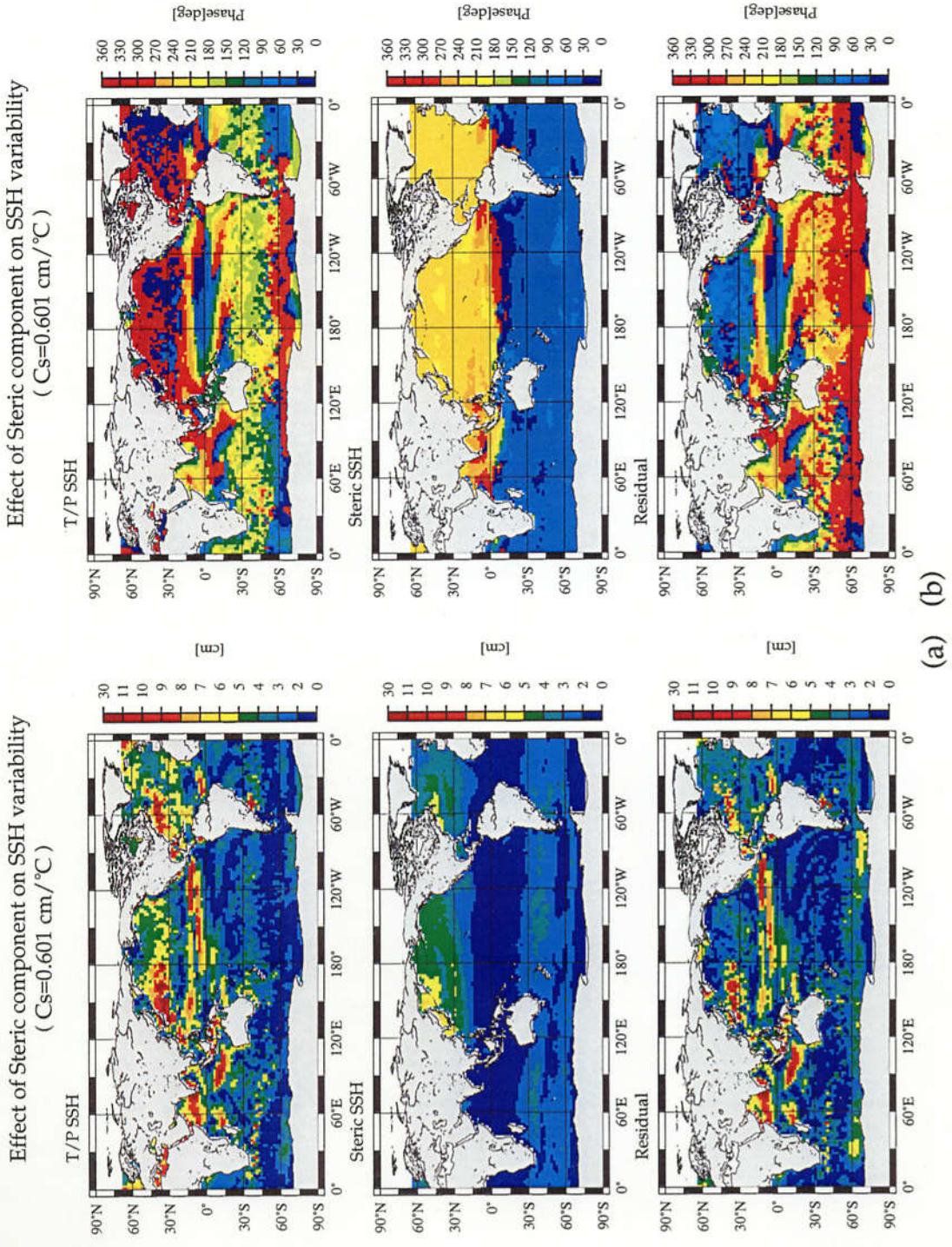

Figure 3.8: Comparison of annual sea surface height (SSH) fields. Original SSH obtained from TOPEX/POSEIDON satellite altimeter data (top), the thermosteric components (center), and SSH corrected for thermosteric components (bottom). The thermosteric components are estimated from sea surface temperature with a single coefficient of 0.60 cm/°C. The colored legends on right hand of each panel indicate the amplitude (Figure 3.8a) and phase (Figure 3.8b) of the annual component.

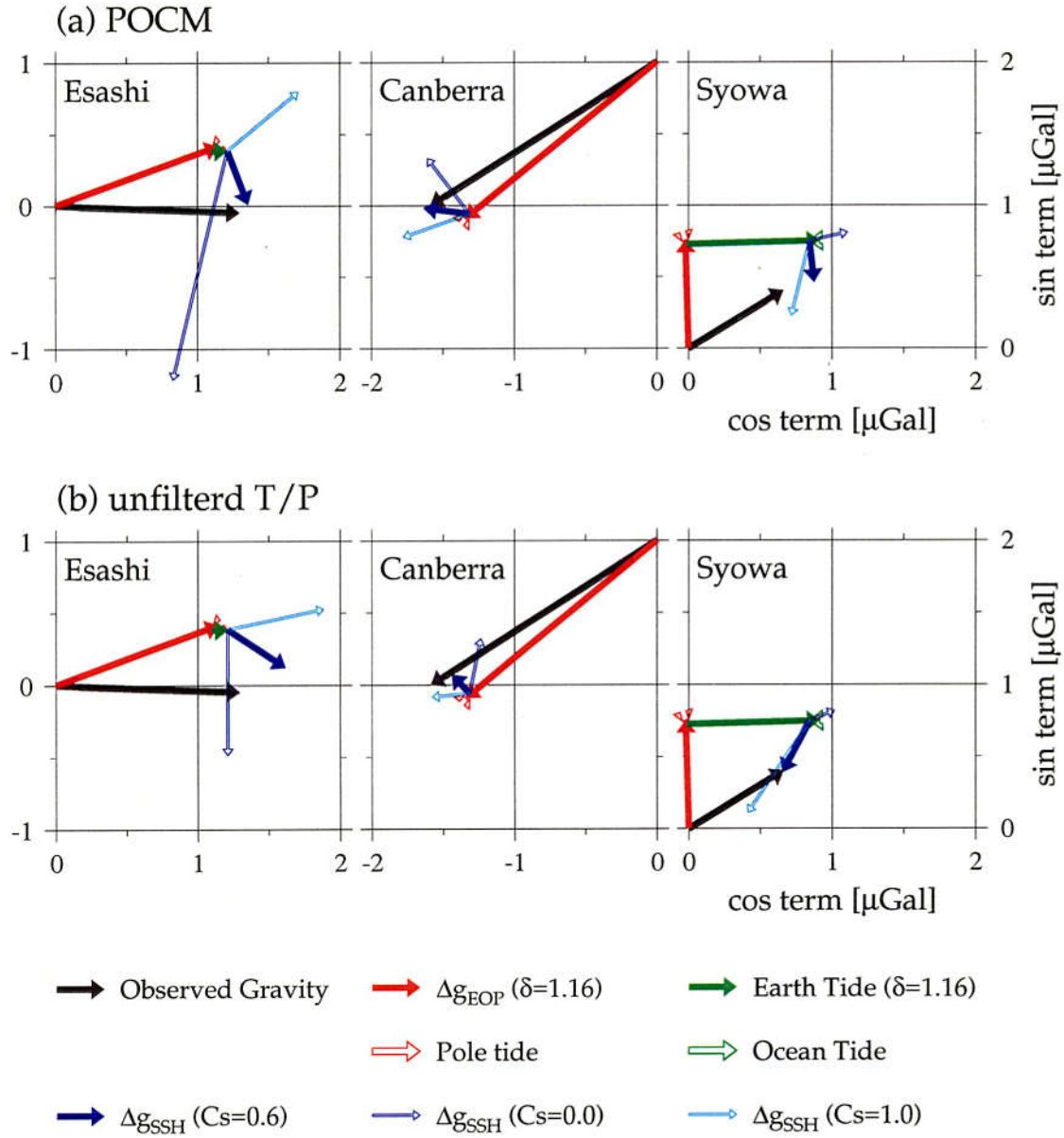

Figure 3.9: The phasor plots showing the observed annual gravity changes and predicted ones. Vectors indicate the annual gravity changes observed by the SG, and predicted from solid tide, ocean tide, annual wobble, equilibrium pole tide, and SSH variations. Horizontal and vertical axes indicate the coefficients of cosine and sine terms, respectively, in each sinusoid. Length and direction of the vectors denote the amplitude and the phase with respect to January 1. The gravimetric effect of the SSH variations are estimated in terms of three approaches: without the correction for thermosteric components, with the correction applying the single thermosteric coefficient of 0.6 cm/°C, and with extreme correction applying the single coefficient of 1.0 cm/°C. The results for Esashi (left), Canberra (center), and Syowa station (right) are shown.
(a) SSH variations based on POCM (Parallel Ocean Climate Model provided by *Stammer*, [1997]) (b) SSH variations based on TOPEX/POSEIDON satellite altimeter data.

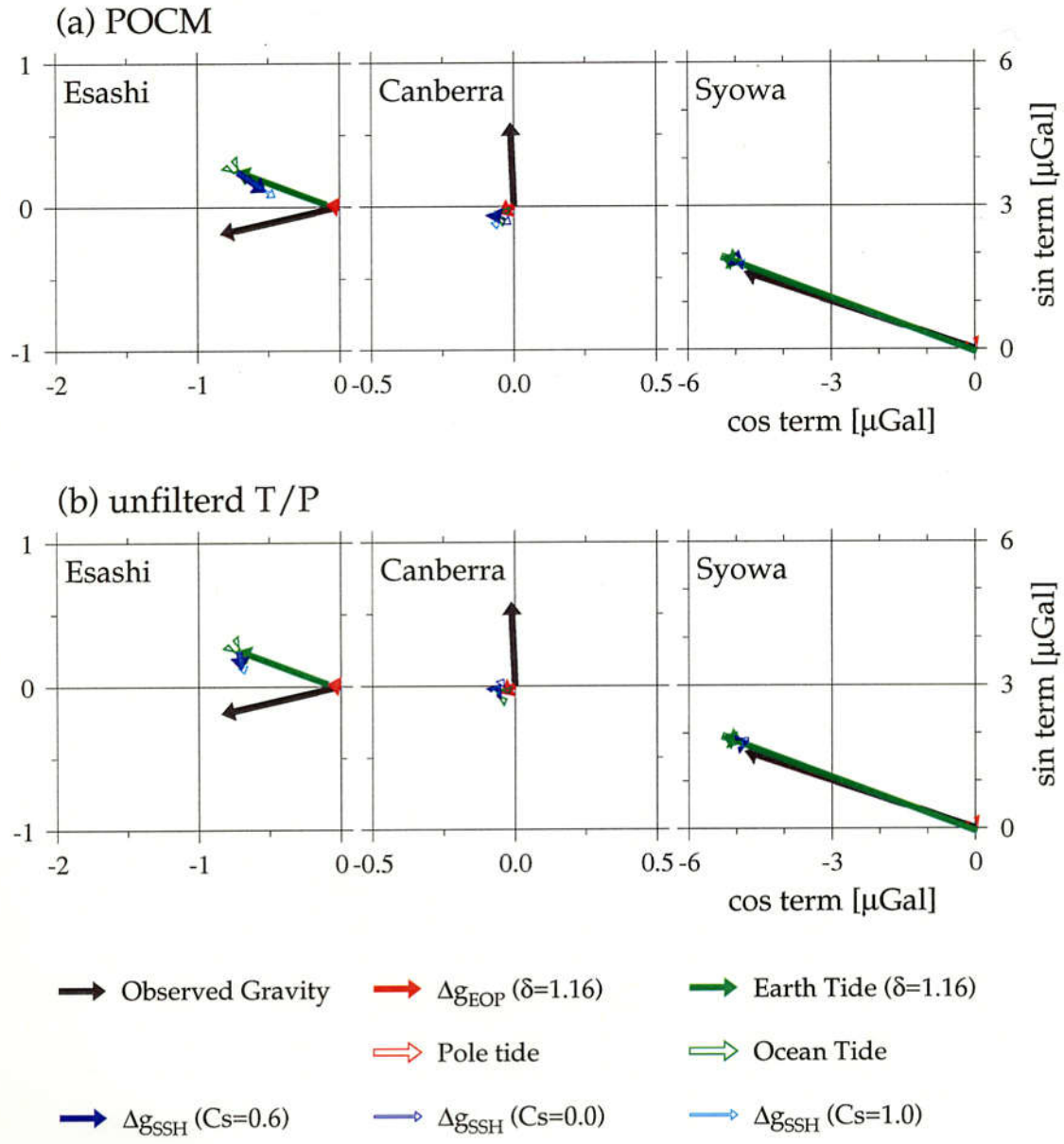

Figure 3.10: Same as Figure 3.9, but for semiannual gravity changes.

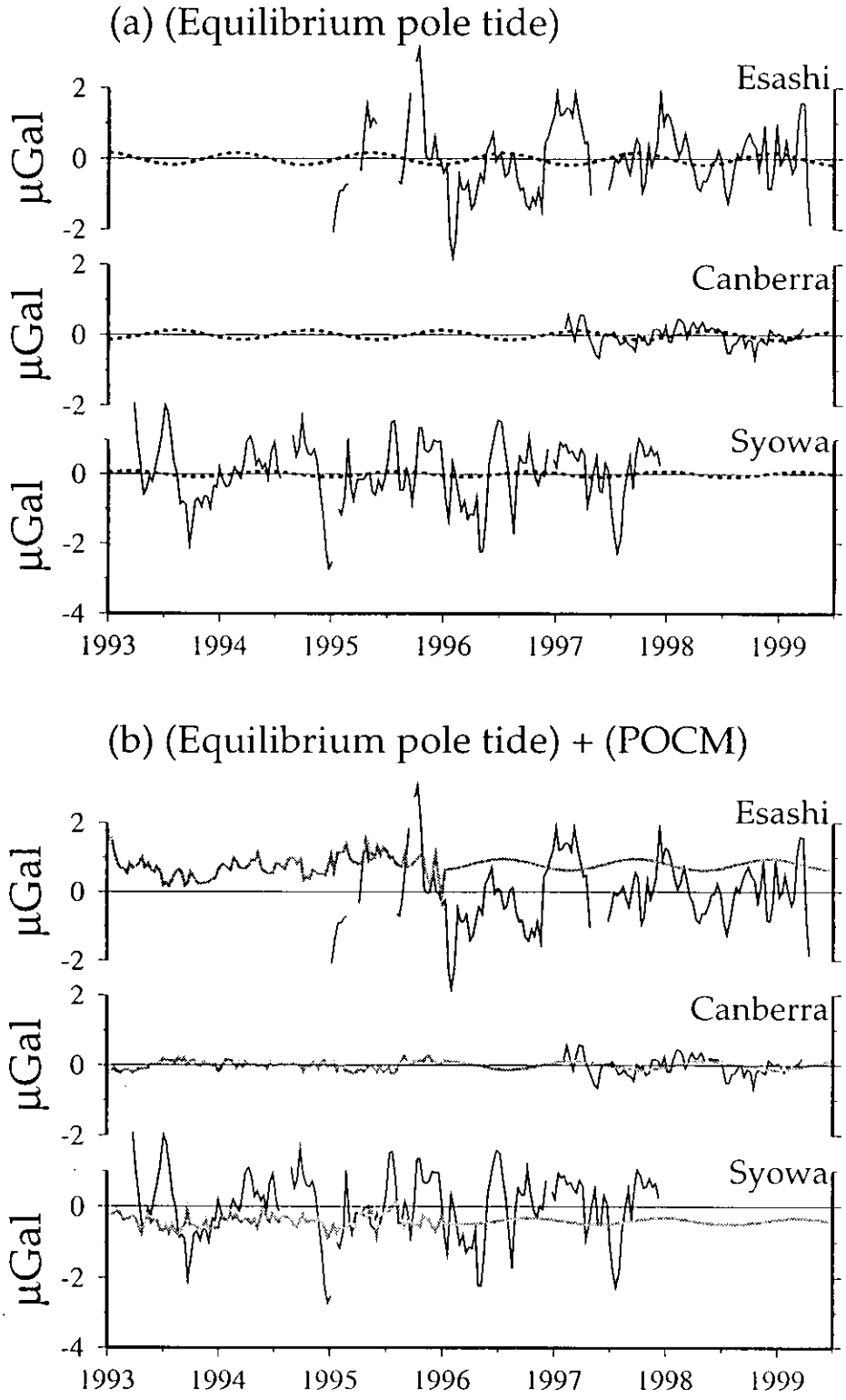

Figure 3.11: Comparison between the nonseasonal residual gravity changes (solid lines) and oceanic gravimetric effect. The residual gravity changes are converted into 10 daily averaged time series, in which theoretical elastic gravity response to the Chandler wobble with their seasonal components, linear trend, and initial drift are removed from long-term gravity change shown in Figure 3.7. (a) oceanic gravimetric effect caused only by equilibrium pole tide (dashed line). (b) oceanic gravimetric effect arising from virtual non-equilibrium pole tide (the sum of equilibrium pole tide and SSH variations based on POCM; gray line).

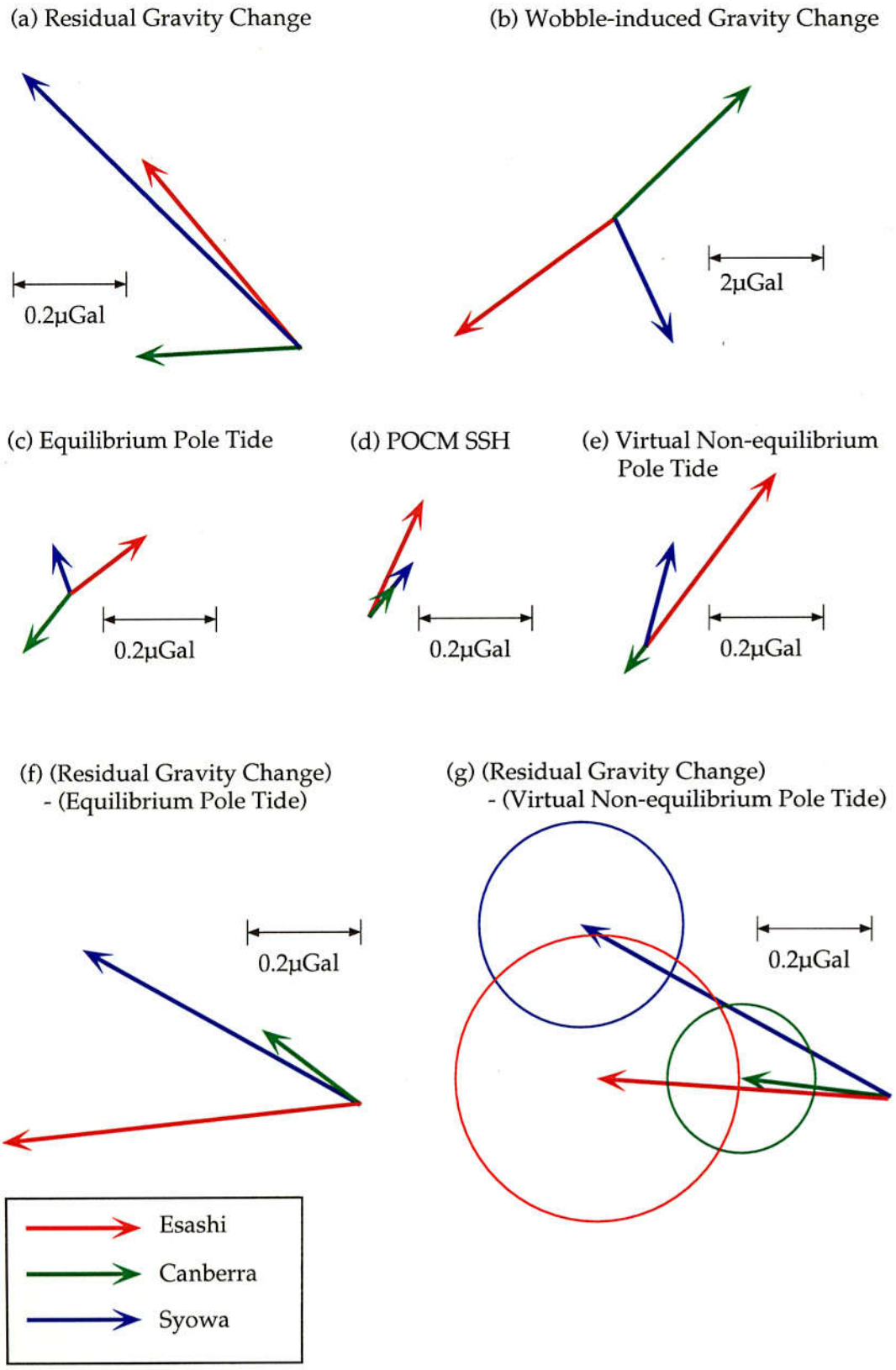

Figure 3.12: Phasor plots showing the residual gravity change shown in Figure 3.11 and oceanic gravimetric effects in the Chandler period (435 days). Their amplitude and phase are determined by fitting of sinusoid on the grounds that the Chandlian component is represented by harmonic function with 435 days of angular velocity. The red, green, and blue vectors indicate the results for Esashi, Canberra, and Syowa station, respectively.

Chapter 4

Epilogue: Toward Earth System Dynamics

We have discussed the atmospheric excitation of the wobble and the gravity response to the wobble.

We show that wind plays significant role to excite the annual wobble, in particular the regional meridional winds in the troposphere connected with the Asian monsoon that shows the most remarkable seasonal signal over the world in Chapter 2. Considering such winds reasonably, the atmospheric excitation function can explain about 70% of the function inferred from observed annual wobble. The remaining angular momentum budget for atmosphere - mantle system in annual variation as shown in Chapter 2 would be expected to be explained by the contribution of oceanic mass redistribution. This reason is that the observed annual gravity change are almost perfectly accounted for by two elastic gravity responses to the solid tide and the annual wobble, and four gravimetric effects due to variations in atmosphere, ocean tide, equilibrium pole tide and sea surface height (SSH) variations, where the SSH variations are corrected for thermosteric components. The effect of SSH variations are largest among oceanic effects, and these SSH variations are driven by meteorological forcing such as surface wind stress. This may mean that dynamical interaction for atmosphere - ocean system is greatly connected with the excitation of annul wobble and the annual gravity change.

In semiannual variation, the pressure contribution is dominant over the wind contribution to the semiannual wobble. In semiannual gravity change, on the other hand, there are discrepancies of 0.1 - 0.5 μGal between observed and predicted values, but their major source possibly is insufficient correction for the atmospheric gravimetric effect by means of response method. Thus variation in atmospheric pressure is a major source to cause the

geophysical phenomena with periods between 150 and 200 days. There are discrepancy in angular momentum budget for atmosphere - mantle system in semiannual variation as shown in Chapter 2. Based on resent literature with respect to oceanic contribution to the semiannual wobble, the discrepancy nearly disappears. Since SSH variations can not affect the semiannual gravity change, these oceanic contribution probably are dominated by the effect of relative angular momentum arising from ocean currents.

Largest result in this paper is that it is confirmed that the atmosphere by itself has enough power to excite the Chandler wobble. We also find that the atmospheric excitation power excessively supplies enough energy to excite the Chandler wobble, where the excess excitation power mentioned above is found to have correlation with the activity of El Niño, suggesting an oceanic contribution to the Chandler wobble. On the other hand, large phase difference for gravity response to the Chandler wobble may be explained by gravimetric effects of such oceanic phenomena. All these facts suggest that dynamics of atmospheric excitation of the Chandler wobble link with whole phenomena in the Earth system dynamics. The SG data in combination with satellite gravity mission such as GRACE (Gravity Recovery and Climate Experiment) scheduled for launch in 2001, is expected to monitor the mass transports in Earth system and provide useful information about the dynamics of Earth system.

Appendix A

Appendix A : Dynamics of the Earth Rotation

Basic Equations

The conservation of the total angular momentum of the whole Earth with respect to the terrestrial reference frame that is fixed the rotating body are represented by

$$\frac{d\boldsymbol{H}}{dt} + (\boldsymbol{\omega} \times \boldsymbol{H}) = \boldsymbol{L}, \tag{A.1}$$

where $\boldsymbol{L}$ is a external torque and $\boldsymbol{\omega}$ is the instantaneous angular velocity vector of the whole Earth. The total angular momentum of the whole Earth, $\boldsymbol{H}$, are separated into the angular momentum of the rigid mantle ($\boldsymbol{H}_{mantle}$) and that of the geophysical fluids ($\boldsymbol{H}_{fluid}$) and they can be described as follow [see *Eubanks*, 1993]:

$$\begin{aligned} \boldsymbol{H}_{mantle} &= \boldsymbol{I}_0 \boldsymbol{\omega} \\ \boldsymbol{H}_{fluid} &= \Delta \boldsymbol{I} \boldsymbol{\omega} + \boldsymbol{h}, \end{aligned} \tag{A.2}$$

where $\boldsymbol{I}_0$ and $\Delta \boldsymbol{I}$ are inertia tensors of the mantle and the fluids, respectively, and $\boldsymbol{h}$ is the relative angular momentum of the fluid with respect to the mantle. When the reference frame used here is aligned with the principal axes of inertia of the mantle, $\boldsymbol{I}_0$ consists of only diagonal components, which are equatorial and axial principal moments of inertia for the whole Earth (A and C, respectively). Here $\boldsymbol{\omega}$ can generally be written by

$$\boldsymbol{\omega} = (\omega_1, \omega_2, \omega_3) = \Omega\,(m_1, m_2, 1 + m_3)\,, \tag{A.3}$$

where Ω is mean angular velocity and m_1, m_2, and m_3 are dimensionless small quantities, representing fluctuations in the Earth's rotation. Using them, the conservation of total

angular momentum in eq. (A.1) are rewritten by the following two perturbation equations for the equatorial and axial angular momentum in the absence of the external torque.

$$-i(C-A)\Omega^2\tilde{m} + A\Omega\frac{d}{dt}\tilde{m} = -i\Omega\left[\Omega\Delta\tilde{I} + \tilde{h}\right] \tag{A.4}$$

$$\Omega C\frac{d}{dt}m_3 = -\frac{d}{dt}\left(\Omega\Delta I_{33} + h_3\right). \tag{A.5}$$

In (A.4), $\tilde{m} = m_1 + im_2$, $\Delta\tilde{I} = \Delta I_{13} + i\Delta I_{23}$, and $\tilde{h} = h_1 + ih_2$ represent complex-valued quantities for the equatorial dimensionless angular velocity, fluctuations in the inertia tensor of the fluids, and equatorial components in the relative angular momentum of the fluids, respectively. In (A.5), m_3, ΔI_{33}, and h_3 represent those for the axial components.

Correction for Deformation of Earth

Because of applying the conservation equations to the real Earth, one needs to consider the departures from perfect rigidity of the mantle arising from effects of mantle deformation and oceanic yielding and a degree of coupling between the fluid core and the mantle. The deformations arise from variations in centrifugal forces in accordance with the fluctuation of ω and load due to redistributions of the fluid mass on the Earth, where the former is called rotational deformation and the latter is called load deformation. These deformations induce changes in the inertia tensors of the mantle and the fluids which can be expanded in only the second-order spherical harmonic series [see *Munk and MacDonald,* 1960; *Lambeck,* 1980; *Eubanks,* 1993]. Thus their effects are described in terms of the second-order rotational Love number and the load Love number.

The degree of core-mantle coupling affects the principal moments of inertia and the Love numbers. Since the core-mantle decoupling for axial rotation can be assumed to be on a timescale of less than 5 years [*Yoder et al.,* 1981], the principal moments of inertia and the Love numbers for only the mantle are used in the axial angular momentum budget. In the equatorial angular momentum budgets the equatorial principal moment of inertia for the whole Earth is replaced for only the mantle, because the fluid core hardly affects the seasonal wobble [*Wahr,* 1982]. The response of the ocean yielding, due to the rotational variation, affects the rotational Love number [see *Eubanks,* 1993]. Consequently, the angular momentum budgets for the deformable mantle with the fluids on it and the fluid core are expressed by following equations:

$$\dot{m} + \frac{i}{\tilde{\sigma}_c}\frac{d}{dt}\dot{m}$$

$$= \left[\frac{k(1+k'_2)}{k-k_2} \Omega \Delta \tilde{I} + \frac{k}{k-k_2} \tilde{h} \right] / (C-A)\Omega = \tilde{\chi} \tag{A.6}$$

$$\frac{\Delta \Lambda}{\Lambda_0} = \left[k_r (1+k'^m_2) \Omega \Delta I_{33} + k_r h_3 \right] / \Omega C_m = \chi_3, \tag{A.7}$$

where $\tilde{\chi} = \chi_1 + i\chi_2$ and χ_3 are dimensionless excitation functions for the wobble and the LOD changes, respectively, C_m and A_m are principal moments of inertia for only the mantle, and $k'_2 = -0.310$ and $k'^m_2 = -0.245$ are the second-order load Love numbers for the whole Earth and for the mantle, respectively. Here $k_2 = -0.348$ is the second-order rotational Love number, which is considered to be the effect of the equilibrium ocean response to the wobble. The term $k_r = 0.998$ represents the correction for the axial component due to the rotational deformation [*Yoder et al.,* 1981], and k is a secular Love number [*Munk and MacDonald,* 1960]. Here $\tilde{\sigma}_c$ is a complex Chandler wobble frequency defined as

$$\tilde{\sigma}_c = \Omega \frac{C-A}{A_m} \frac{k-k_2}{k} \times \left(1 - \frac{k_2}{k} \frac{C-A}{A_m} \right) \left(1 + \frac{i}{2Q} \right), \tag{A.8}$$

where Q is quality factor, indicating the dumping of free motion [*Eubanks,* 1993]. We employ $\tilde{\sigma}_c$ assuming that its real part is 435 days and that $Q = 100$. In the preceding equations the terms

$$(X_1, X_2, X_3, X_4) = \left(k(1+k'_2)/(k-k_2),\ k/(k-k_2),\ k_r(1+k'^m_2),\ k_r \right) \tag{A.9}$$

are called transfer functions, which represent the corrections of departures from perfect rigidity of the mantle due to the deformations and oceanic yielding.

Appendix B

Appendix B : Formulas for Atmospheric Angular Momentum Function

When atmospheric contributions to LOD change and wobble are discussed, $\tilde{\chi}$ and χ_3 in (A.6) and (A.7) are used for the atmospheric excitation functions and are called the atmospheric angular momentum (AAM) function. The AAM function consists of the pressure term χ^P, the effect of redistribution of air mass, and the wind term χ^W, the effect of the relative angular momentum of the atmosphere. These are expressed by using X_i in (A.9):

$$\begin{aligned} \tilde{\chi} &= \tilde{\chi}^P + \tilde{\chi}^W \\ &= \left(X_1 \Omega \Delta \tilde{I} + X_2 \tilde{h}\right) / \Omega (C - A) \\ \chi_3 &= \chi_3^P + \chi_3^W \\ &= \left(X_3 \Omega \Delta I_{33} + X_4 h_3\right) / \Omega C_m . \end{aligned} \tag{B.1}$$

If we describe the inertia tensors, $\Delta \tilde{I}$ and ΔI_{33}, and the relative angular momentum $\tilde{h}$ and h_3 in spherical polar coordinate $(\tilde{R}, \lambda, \phi)$, $\tilde{\chi}^P$, $\tilde{\chi}^W$, χ_3^P, and χ_3^W are expressed as follows:

$$\begin{aligned} \tilde{\chi}^P &= \chi_1^P + i\chi_2^P \\ &= \frac{-1.098 \tilde{R}^4}{g(C-A)} \int_{\phi_1}^{\phi_2} \int_{\lambda_1}^{\lambda_2} p_s \sin\phi \cos^2\phi e^{i\lambda} d\lambda d\phi \end{aligned} \tag{B.2}$$

$$\begin{aligned} \tilde{\chi}^W &= \chi_1^W + i\chi_2^W \\ &= \frac{1.5913 \tilde{R}^3}{g\Omega(C-A)} \end{aligned}$$

$$\times \int_{\phi_1}^{\phi_2} \int_{\lambda_1}^{\lambda_2} \int_{p_{bot}}^{p_{top}} (u \sin\phi + iv) \cos\phi e^{i\lambda} dp d\lambda d\phi \tag{B.3}$$

$$\chi_3^P = \frac{0.753 \bar{R}^4}{g C_m} \int_{\phi_1}^{\phi_2} \int_{\lambda_1}^{\lambda_2} p_s \cos^3\phi d\lambda d\phi \tag{B.4}$$

$$\chi_3^W = \frac{-0.998 \bar{R}^3}{g \Omega C_m} \int_{\phi_1}^{\phi_2} \int_{\lambda_1}^{\lambda_2} \int_{p_{bot}}^{p_{top}} u \cos^2\phi dp d\lambda d\phi, \tag{B.5}$$

where $\bar{R}$ is Earth's mean radius; λ and ϕ are longitude and latitude of an arbitrary point on the Earth, respectively; $g = 9.80$ m/s^2 is gravity acceleration; p_s is surface pressure; and u and v are eastward and northward wind velocities, respectively. In computation of the wind term the atmospheric surface pressures on the real mountains and the pressure at the top level in the global objective analysis are used for p_{bot} and p_{top}, respectively. Tropospheric and stratospheric wind contributions are calculated by integrating from $p_{bot} = p_s$ to $p_{top} = 100$ hPa and from $p_{bot} = 100$ hPa and $p_{top} = 10$ hPa, respectively.

Coefficients of p_s for the pressure terms, and u and v for the wind term are function of latitude and longitude. However, the function system of their coefficients (hereafter, referred to as 'weighting function') differ with each other. Effectively spatial pattern of the weighting functions for p_s, u and v are shown in Figure B1, B.2 and B.3, respectively.

The surface pressures on real mountain are used in the calculation of AAM function. They are estimated using mountain height data, pressure at sea surface level, and geopotential heights at each standard pressure levels in the global objective analysis data, by means of interpolation using a cubic non-periodic spline method combined with the hydrostatic equation. The real mountain height data are obtained from the global 5-arcmin gridded topography data ETOPO-5 [*National Geophysical Data Center*, 1988]. On the other hand, the pressures at sea level are computed by means of the following relation:

$$p_{sea\_level} = 1000 \times \left(\frac{T_{1000hPa} - z_{1000hPa}\Gamma}{T_{1000hPa}} \right)^{\frac{g}{R_d \Gamma}}, \tag{B.6}$$

where $R_d = 287 \quad m^2/s^2 K$ is gas constant for dry air, and $T_{1000hPa}$ and $z_{1000hPa}$ are temperature and height at 1000 hPa level, respectively. A temporal and spatial function, $\Gamma = -\Delta T/\Delta z$ is estimated from the temperatures and heights from 1000 to 700 hPa levels.

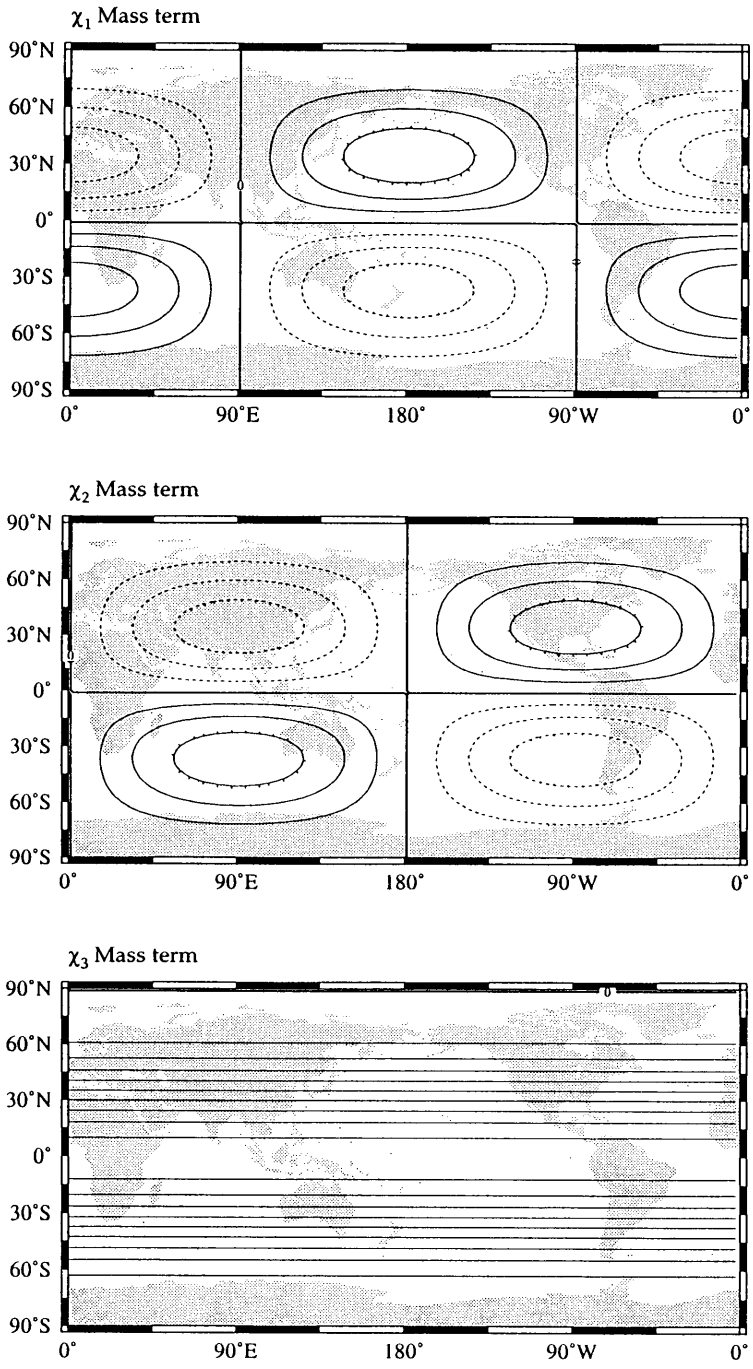

Figure B.1: Effective area of the weighting function for surface pressure in eqs. B.2 and B.4. Solid and dashed lines denote their positive and negative values, respectively.

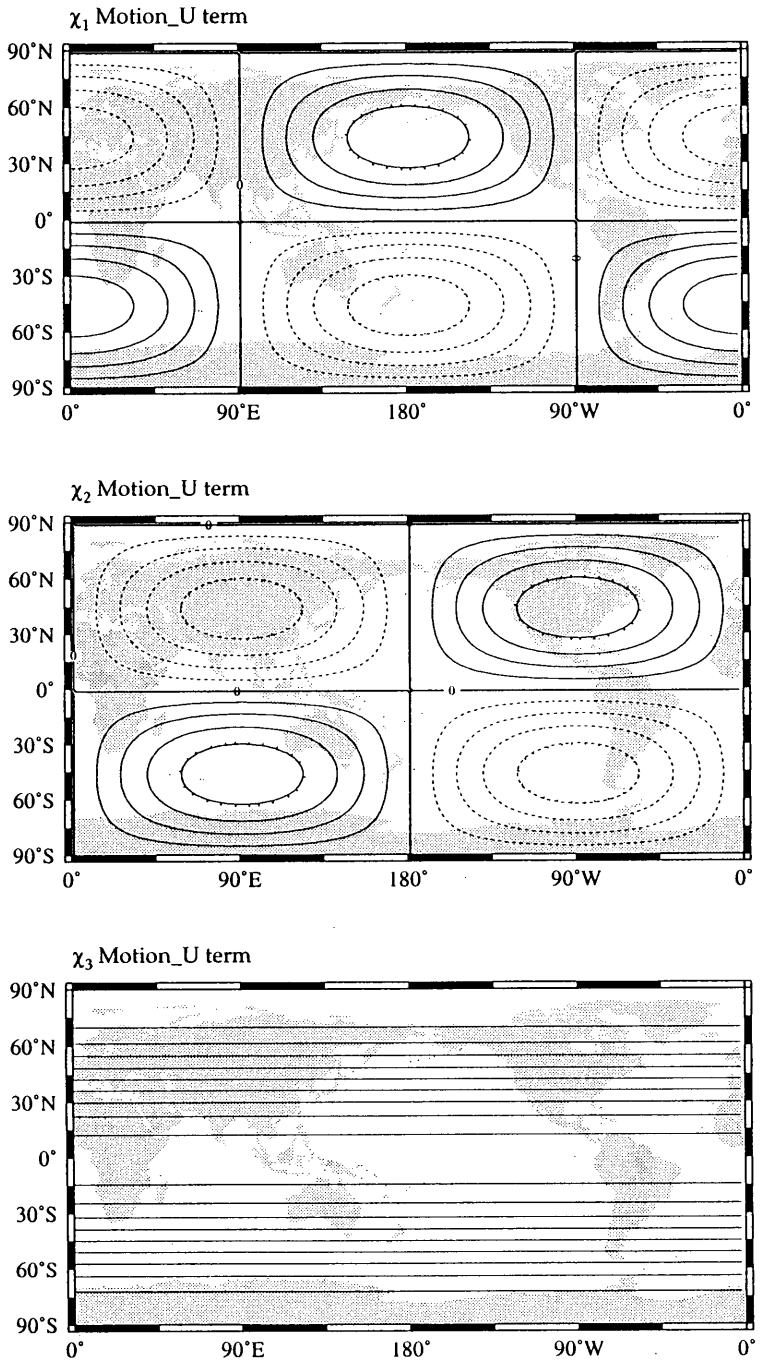

Figure B.2: Effective area of the weighting function for zonal wind in eqs. B.3 and B.5.

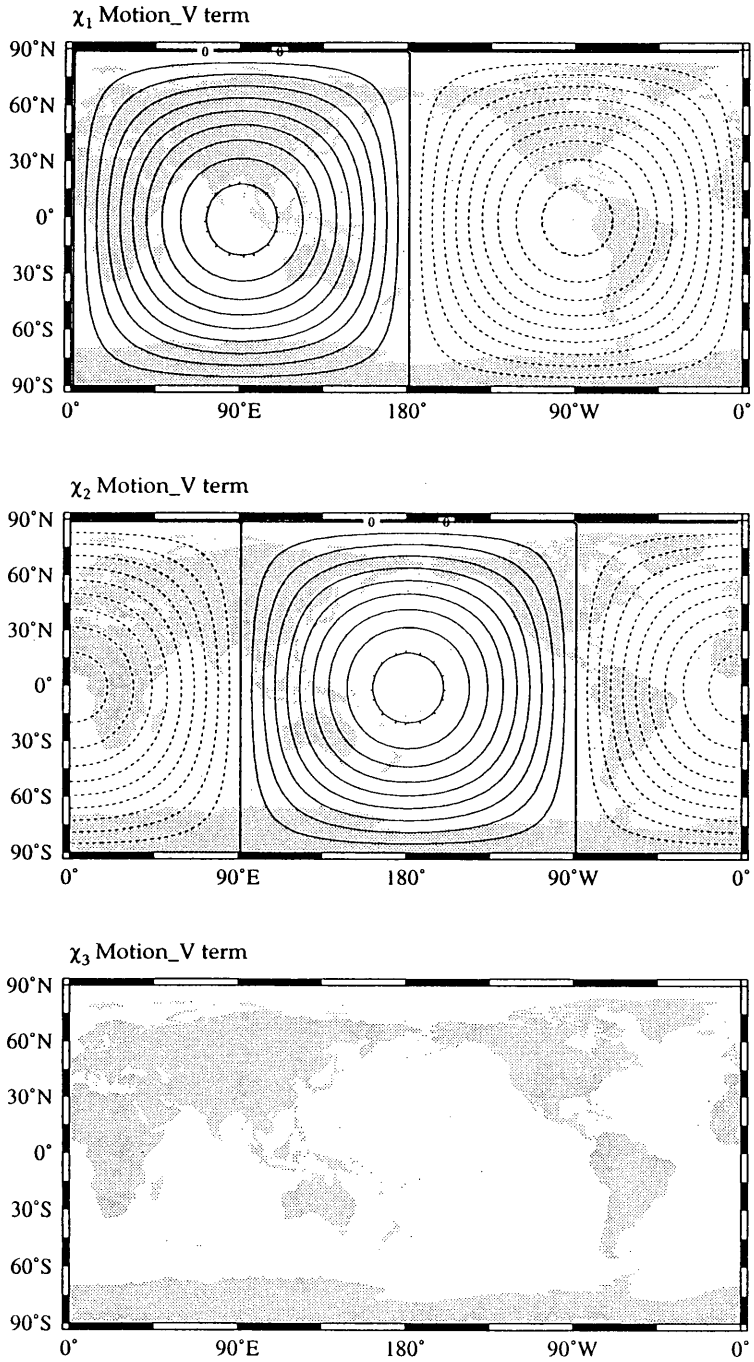

Figure B.3: Effective area of the weighting function for meridional wind in eqs. B.3 and B.5.

Appendix C

Appendix C : Supplementary Analyses of Excitation of the Chandler Wobble

Atmospheric Excitation Based on the NCEP AAM Function

We exemplify the contributions to the excitation of the wobble from the wind+IB pressure, wind, and IB pressure in the NCEP AAM function archived in IERS (that is, NCEP[BP]) for comparison with those in the JMA AAM function (that is, JMA[SP]). Figures C.1a, C.1b, and C.1c display power spectra, squared coherences, and phase differences of/between the geodetic excitation function and contributions from wind+IB pressure, wind, and IB pressure like Figures 2.14 (see section 2.5.3) but using the NCEP[BP]. The confidence threshold for the power spectra and coherences by F-test are also shown in these figures. Figure C.1a reveals that the wind+IB pressure contribution is too small to explain the geodetic excitation near the CW frequency, although their significant coherence exceeding 95% confidence threshold and phase advance of about 30° of the AAM function as well as the result of JMA[SP] function are shown.

This small amplitude of the wind+IB pressure contribution in comparison with that of the geodetic excitation is attributed to the slight wind contribution as shown in Figure C.1b. Its power spectrum is considerably different from that of wind contribution in the JMA[SP]. This feature is consistent with previous indication that there is difference in the wind contribution to the wobble between the NCEP and JMA AAM functions [*Eubanks et al.*, 1988; *Gross and Lindqwister*, 1992; *Furuya et al.*, 1996]. In the case of the wind contribution to the annual wobble, the difference is partly caused by different vertical wind integration methods employed in the two AAM functions as mentioned section 2.5.2. As

opposed to the wind contribution, a behavior of the IB pressure contribution as shown in Figure C.1c coincides with that based on the JMA[SP].

Figure C.2 shows temporal variations in the CW excitation powers, coherences, and phases of/between the geodetic excitation function and contributions from wind+IB pressure, wind, and IB pressure based on the NCEP/NCAR AAM function during 1987-1995 by the same manner in Figure 2.15a. The temporal variations in the wind+IB pressure and IB pressure contributions are also observed, but that in the wind contribution is not very remarkable. A time-varying pattern of the IB pressure contribution is similar to that in the JMA[SP].

The amplitude ratio between the geodetic CW excitation power and wind+IB pressure contribution varies within 0.16-0.65 (the averaged value is 0.38). Namely, the amplitude of the wind+IB pressure contribution is always smaller than that of the geodetic excitation. The ranges of time-varying amplitude ratios for the wind and IB pressure contributions are 0.06-0.13 (the averaged value is 0.09) and 0.18-0.54 (the averaged value is 0.33), respectively. The CW excitation coherences for the wind+IB pressure, wind, and IB pressure contributions exhibit similar time-varying patterns to those based on the JMA[SP]. The phase advances of the wind+IB pressure and IB pressure contributions to the geodetic CW excitation correspond to those in the JMA[SP], while time-varying pattern of the phase of the wind contribution resemble that of the stratospheric wind contribution in the JMA[SP]. These features suggest that the failure to account for the geodetic CW excitation by using the NCEP[BP] are caused by its vertical wind integration method.

Frequency-Time Spectral Analysis

We compute the frequency-time spectra of nonseasonal geodetic excitation and three AAM functions, using a 3000 days sliding window that is advanced by an increment of 30 days. It is clear that the amplitude of the remarkable spectral peaks of the geodetic excitation (Figure C.3a), and the contributions from the wind+IB pressure (Figure C.3b), wind (Figures C.3c) and IB pressure (Figures C.3d) vary with time.

Figure C.3a shows the three remarkable spectral peaks at broad bands around ± 2 cpy and from -1 to 1 cpy, with regard to the geodetic excitation functions. Three atmospheric contributions, on the other hand, have no spectral peaks around ± 2 cpy. The broad spectral peaks of the geodetic excitation around ± 2 cpy make a display of the rapid change of their amplitude in 1993. Such rapid change in the partition of 1993 appears in broad bands around ± 3 cpy and 0 to 1 cpy for entire AAM function, from -0.5 to 0.5 cpy for wind AAM function, and around -1.5 cpy and from 0.5 to 1.2 cpy for IB pressure contribution. These

temporal variations in power spectra may be affected by global motions of atmospheric mass in broad band.

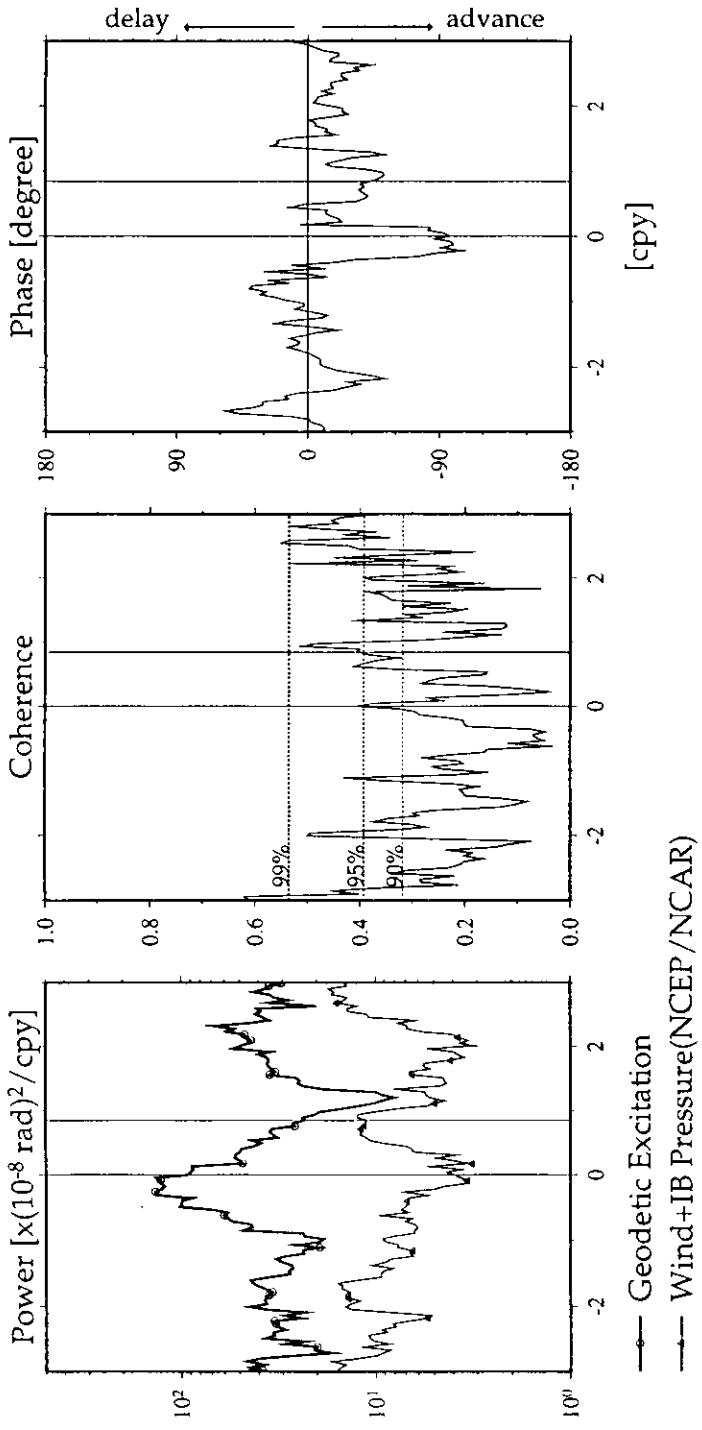

Figure C.1a: Same as Figure 2.14a, but for the atmospheric contribution based on the NCEP[BP]

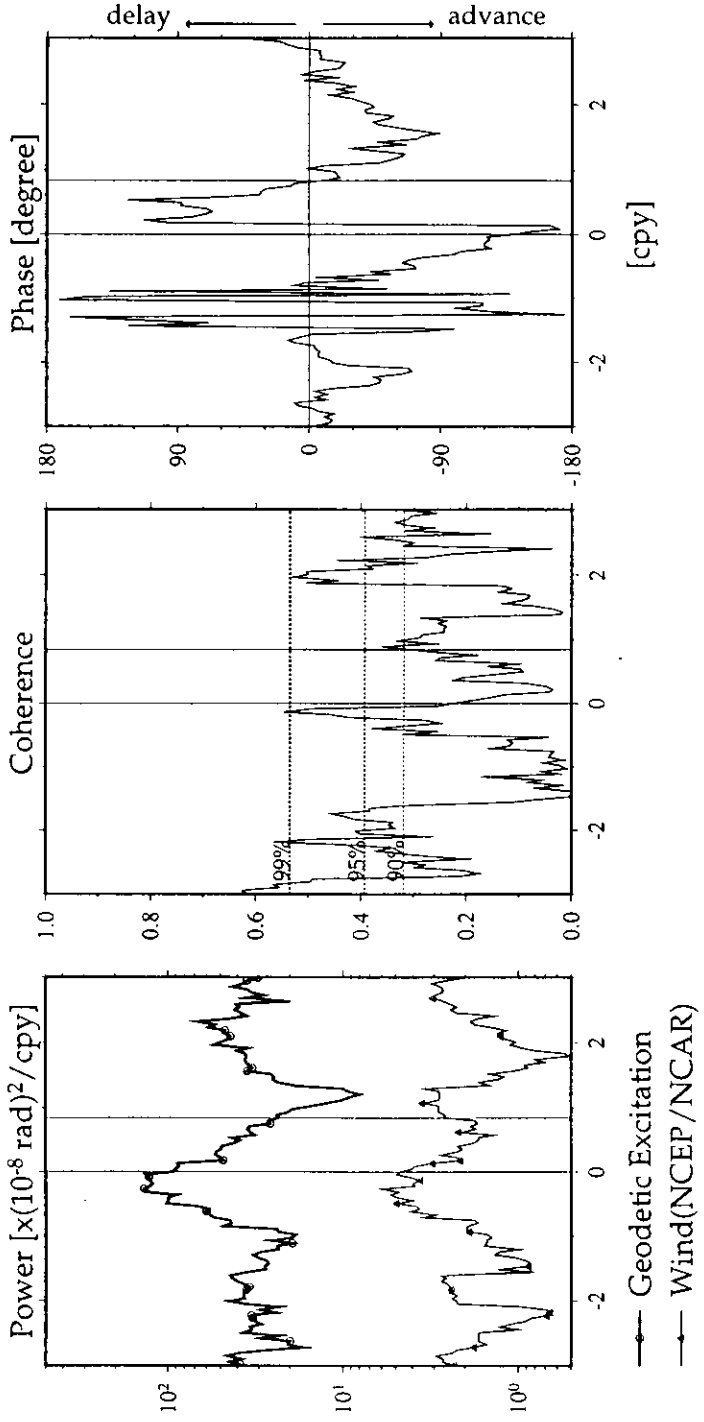

Figure C.1b: Same as Figure 2.14b, but for the wind contribution based on the NCEP[BP]

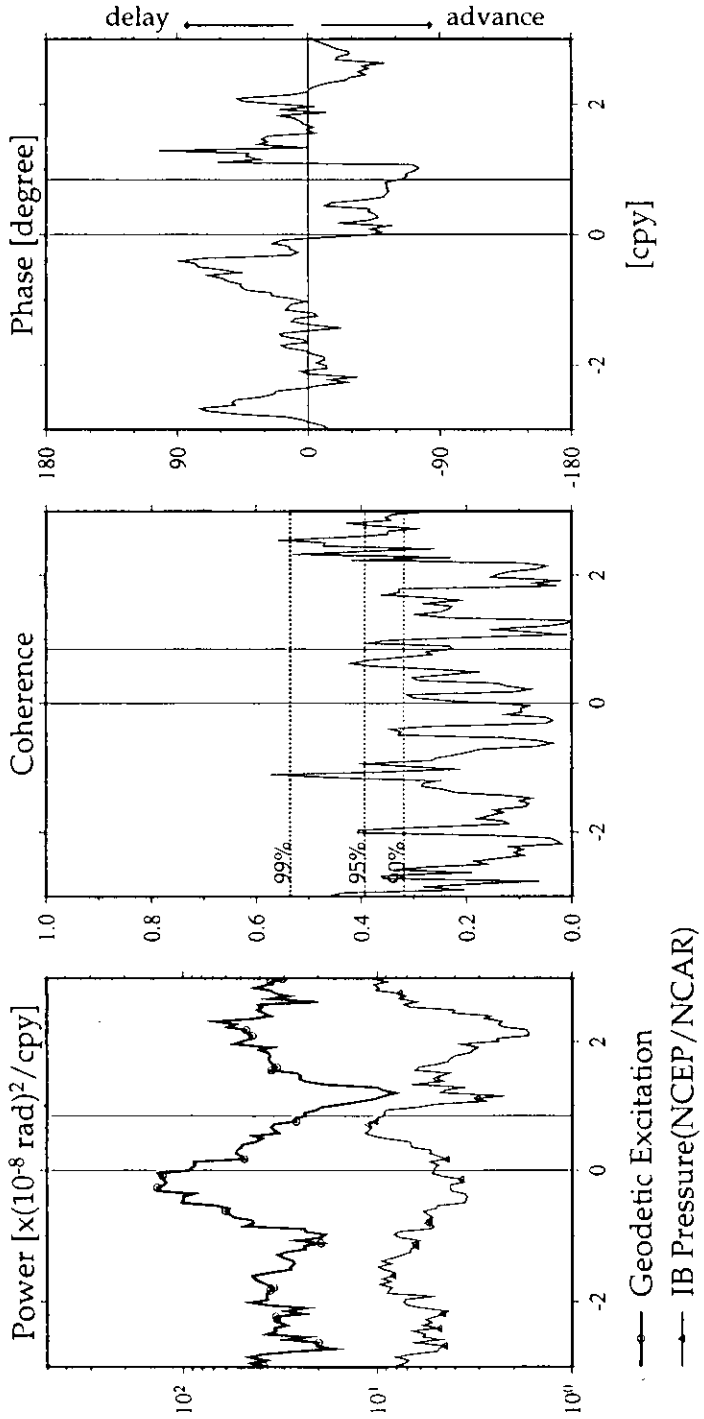

Figure C.1c: Same as Figure 2.14c, but for the IB pressure contribution based on the NCEP[BP].

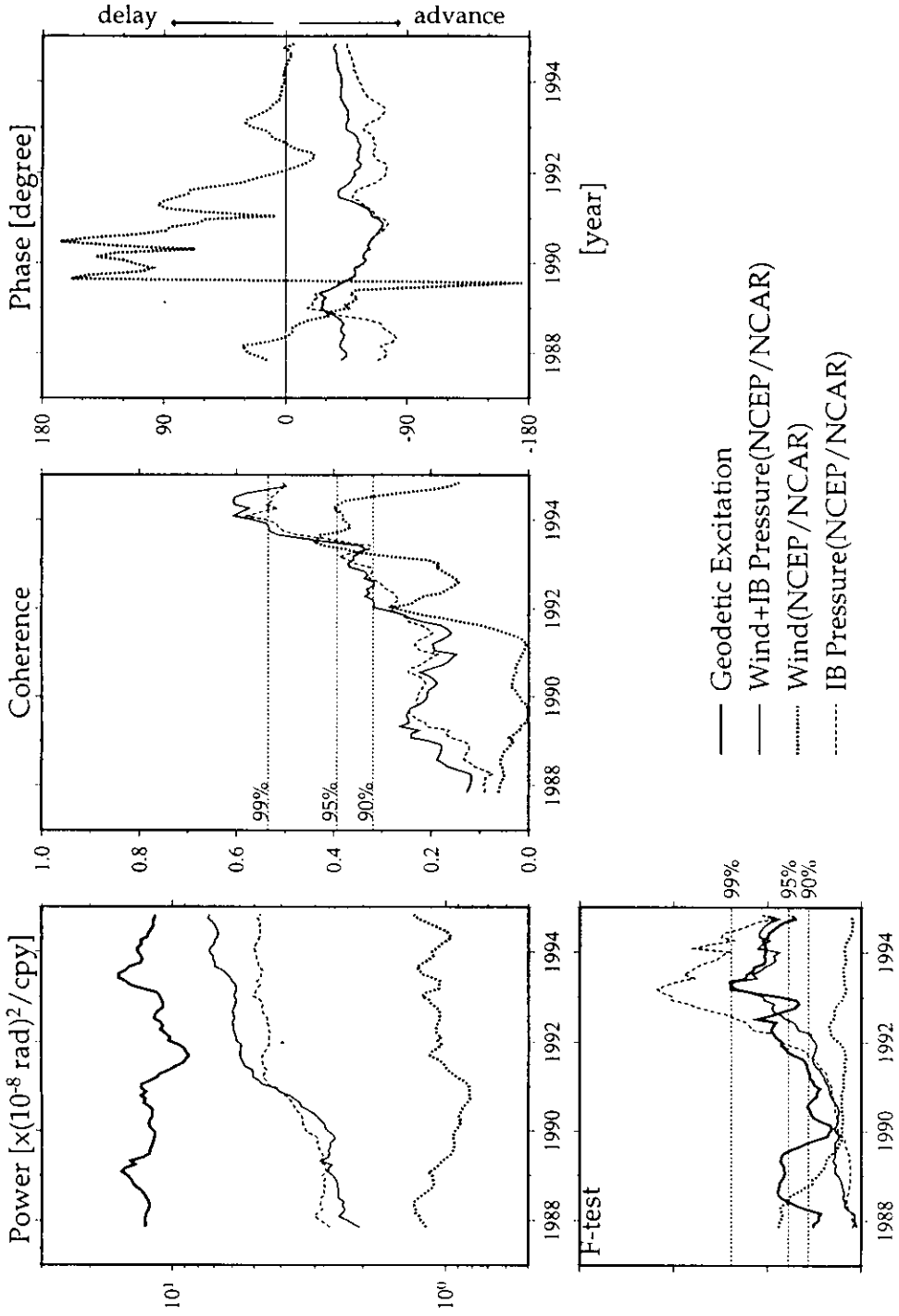

Figure C.2: Same as Figure 2.15a, but for the contributions from wind+IB pressure, wind, and IB pressure based on the NCEP[BP]

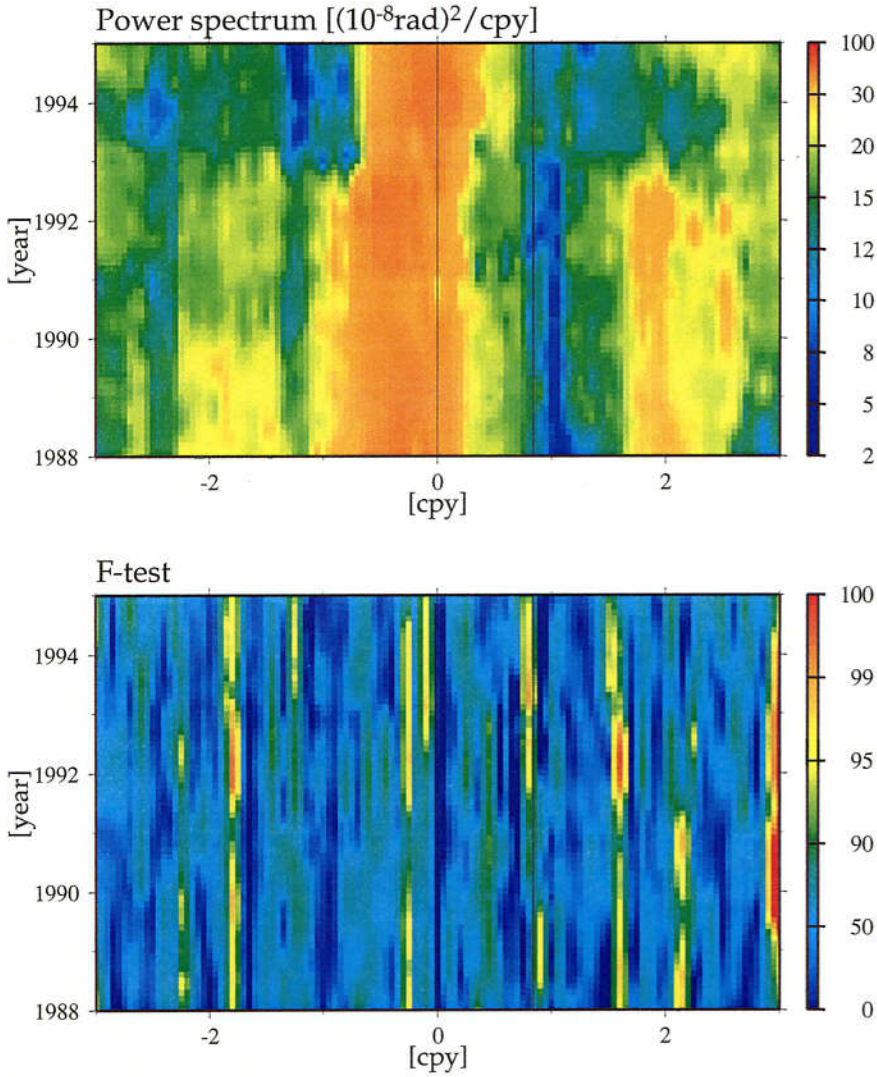

Geodetic Excitation Functions

Figure C.3a: Frequency-time power spertrum (upper) and frequency-time F-test (lower) for the nonseasonal geodetic excitation. These estimates are plotted at central day of a sliding 3000 days window that is advanced by an increment of 30 days, for a period 1988-1995. Their amplitudes are displayed by color legends in right sides of each panel. A vertical line at 0.847 cpy denotes the frequency of the Chandler wobble.

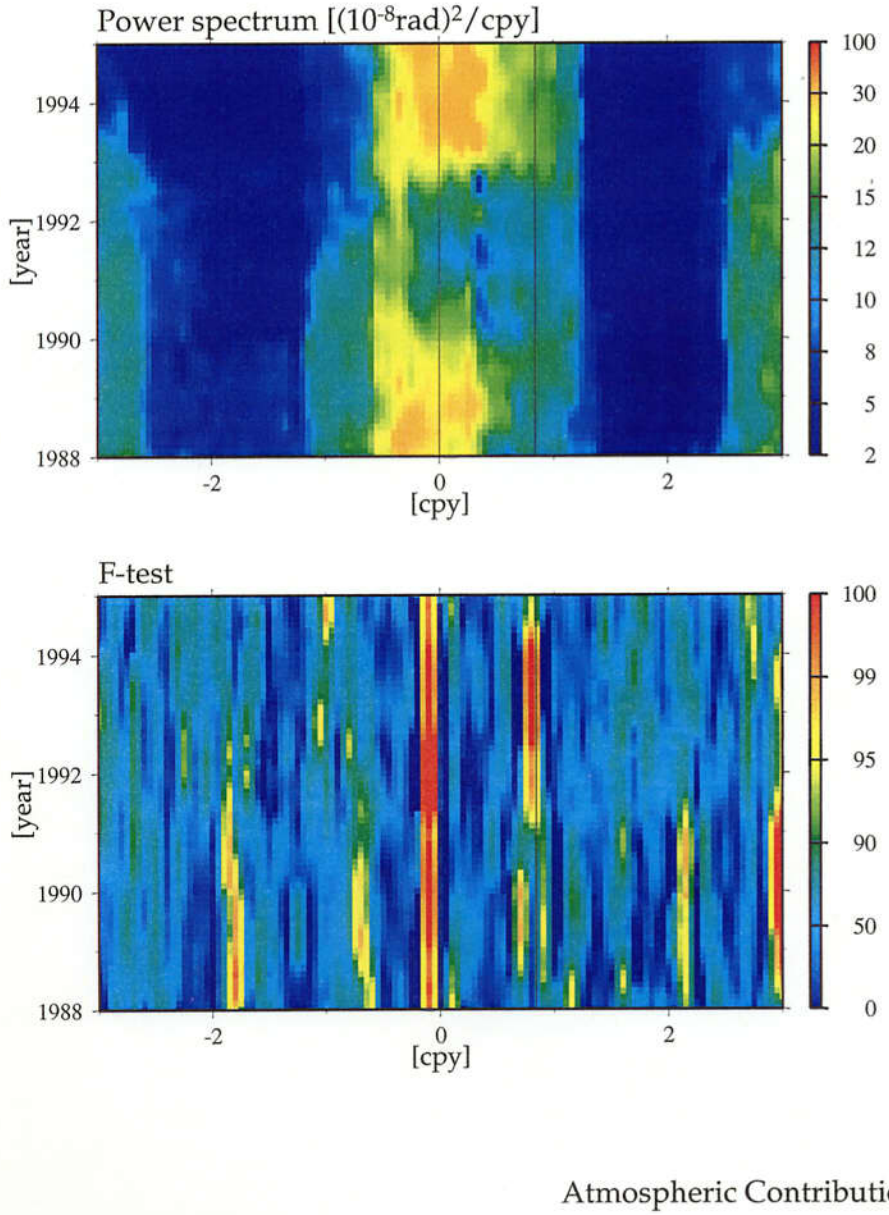

Figure C.3b: Same as Figures C.3a but for the nonseasonal wind+IB pressure contribution.

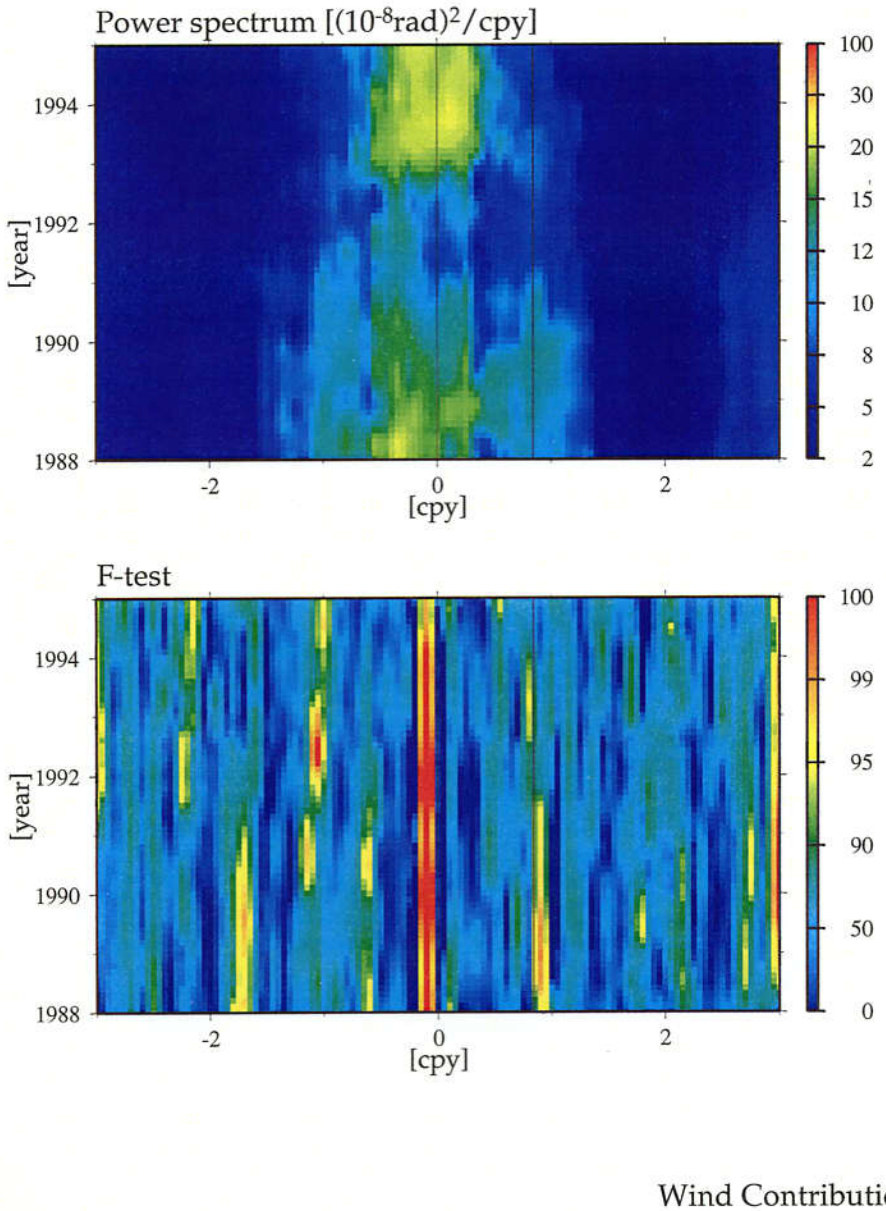

Figure C.3c: Same as Figures C.3a but for the nonseasonal wind contribution.

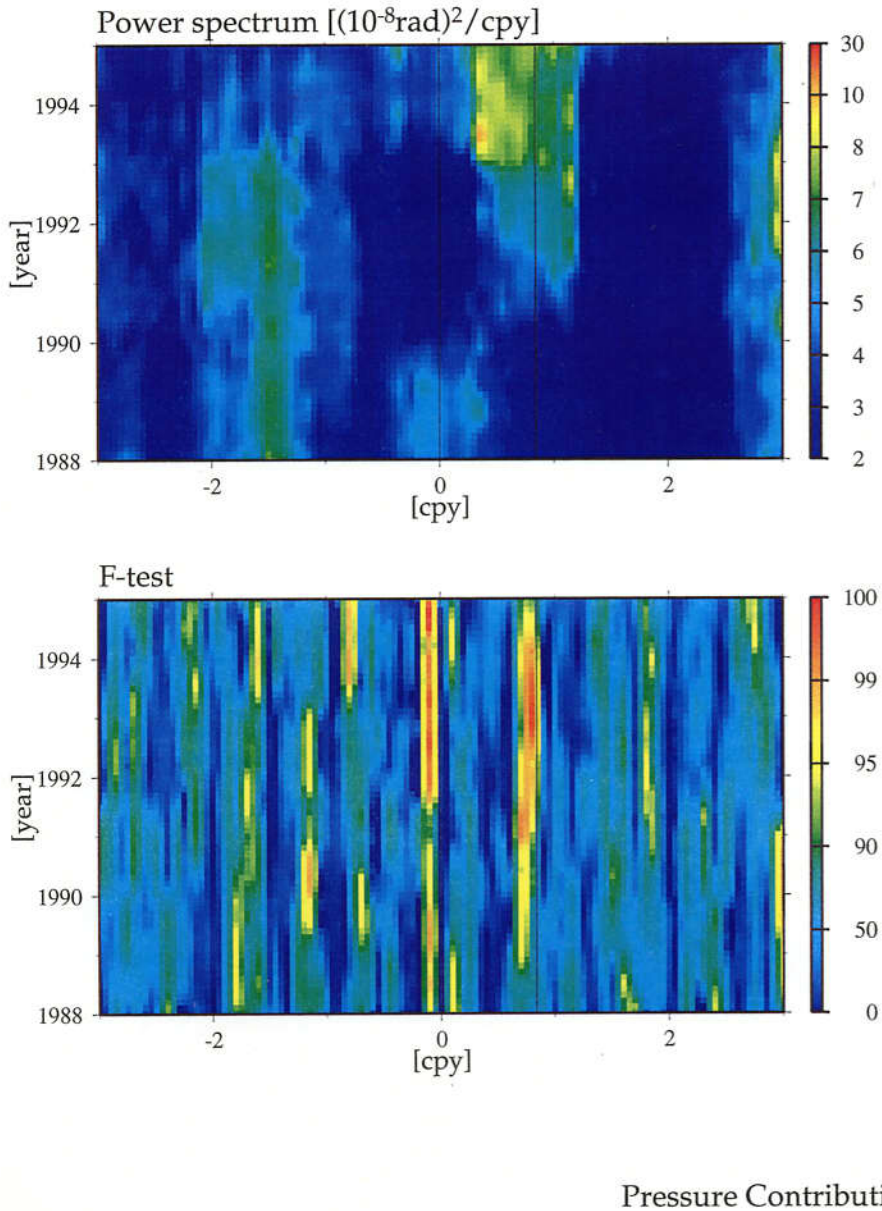

Figure C.3d: Same as Figures C.3a but for nonseasonal IB pressure contribution.

Appendix D

Appendix D : A Principle of Superconducting Gravimeter

Superconducting gravimeter (SG) is relative cryogenic gravimeter utilizing the superconductive phenomenon under temperature of 4.2°K [see, *Goodkind,* 1999 for a review of SG] . The SG applies magnetic levitation force which is maintained by magnetic field induced from persistent current flowing in superconducting coil using magnetic repulsion force in terms of Meissner effect, instead of classical metallic spring. The cryogenic environment (4.2°K) maintaining the superconductive state also gives us the advantages as follow; show instrumental drift because thermal expansion and creep of the metallic material in instrument can be disregarded under such temperature; low noise because cryogenic environment also reduces thermal noise and Brownian motion inside the instrument to almost zero. Thus the SG have obtained the long-term stability (i.e. slow drift) and sensitivity improvement of 2 or 3 order higher than the classical spring gravimeter.

Niobium sphere with the 2.54 cm diameter that becomes perfect diamagnetic material by Meissner effect is levitated in the magnetic field induced by superconducting current. The levitation of that sphere are performed by using two superconducting coils, because the gradient of magnetic field decreases to stably levitate the sphere. A sphere position is varied by the perturbations in gravity field. Fluctuation in its position is detected by gravity capacitive sensing plate which cylindrically surrounds the width side of the levitating sphere, and the sphere is kept to the fixed position by magnetic feedback coil. The amount of current flowing in respect to the feedback coil is linearly with the gravity change and it is output. The superconducting coils and sphere, the capacitive sensing plate, and the feedback coil are put in gravity sensing unit (GSU) which is demagnetized and covered by mu-metal magnetic shield. GSU also has the germanium thermometer and tilt capacitive sensing plates in order

to keep cryogenic environment and for the purpose of setting the GSU to a tilt-insensitive position, respectively.

The GSU are inserted into SG dewar filled by LHe. The GSU are always adjusted by thermal leveler in order to point to the vertical direction using signals from tilt capacitive sensing plates. The SG dewar is hung (supported) from these thermal levelers above the concrete pier with about 1.5 m of height. Recently, the support system of the dewar is improved into the system in which the dewar is supported from the bottom by thermal leveler that are directly put in the basement for the purpose of reducing noise level to lower one. The former is called "top mount" system, and the latter is referred to as "bottom mount" system.

It is essential to maintain the cryogenic environment inside the GSU for the high quality observation by SG. To accomplish this, we are forced periodically to fill LHe and to carry out the maintenance of the cryogenic refrigeration system consisting of the coldhead inserted in the dewar, the compressor, and water chiller. Since these work disturbs the SG observation, recent type of SG have been improved by additional features such as enhancement in its cooling performance and decrease in loss of LHe in order to simplify use, increase reliability and reduce manpower requirements.

References

Aoyama, Y., K. Nawa, H. Yamamoto, K. Doi, K. Shibuya, and T. Sato, Calibration of the SG at Syowa station using an absolute gravimeter FG5, *Proc. 6th Workshop on the SG*, eds. K. Kaminuma and Y. Imanishi, 48-49, 1997 (in Japanese).

Barnes, R. T. H., R. Hide, A. A. White and C. A. Wilson, Atmospheric angular momentum fluctuations, length-of-day changes and polar motion, *Proc. R. Soc. London, Ser. A*, **387**, 31-73, 1983.

Bell, M. J., R. Hide, and G. Sakellarides, Atmospheric angular momentum forecasts as novel tests of global numerical weather prediction models, *Phil. Trans. R. Soc. Lond.*, Ser. A, **334**, 55-92, 1991.

Celaya, M. A., J. M. Wahr, and F. O. Bryan, Climate-driven polar motion, *J. Geophys. Res.*, **104**, 12813-12829, 1999.

Chao, B. F., On the excitation of the Earth's polar motion, *Geophys. Res. Lett.*, **12**, 526-529, 1985.

Chao, B. F., Length-of-day variations caused by El Niño-southern oscillation and quasi-biennial oscillation, *Science*, **243**, 923-925, 1989.

Chao, B. F., Excitation of Earth's polar motion by atmospheric angular momentum variation, 1980-1990, *Geophys. Res. Lett.*, **20**, 253-256, 1993.

Chao, B. F. and W. P. O'Connor, Global surface-water-induced seasonal variations on the earth's rotation and gravitational field, *Geophys. J.*, **94**, 263-270, 1988.

Chao, B. F. and A. Y. Au, Atmosperic excitation of Earth's annual wobble: 1980-1988,*J. Geophys. Res.*, **96**, 6577-6582, 1991.

Crossley, D., J. Hinderer, G. Casula, O. Francis, H.-T. Hsu, Y. Imanishi, G. Jentzsch, J. Kääriänen, J. Merriam, B. Meurers, J. Neumeyer, B. Richter, K. Shibuya, T. Sato, and T. vanDam, Network of superconducting gravimeters benefits a number of disciplines, *Eos Trans. AGU*, **80**, 123-125, 1999.

Dahlen, F. A., A correction to the excitation of the Chandler wobble by earthquakes, *Geophys. J. R. Astron. Soc.*, *32*, 203-217, 1973.

Dehant, V., P. Defraigne, and J. M. Wahr, Tides for a convective Earth, *J. Geophys. Res.*, **104**, 1035-1058, 1999.

Desai S. D., Ocean tides from TOPEX/POSEIDON altimetry with some geophysical applications, Ph.D. thesis, 254 pp., Univ. of Colorado, Boulder, 1996.

Dickey, J. O., Atmospheric excitation of the Earth's rotation: Progress and prospects via space geodesy, in *Contributions of Space Geodesy to Geodynamics, Geodyn. Ser.*, **24**, edited by D. E. Smith and D. L. Turcotte, pp. 55-70, AGU, Washington, D. C., 1993.

Dickey, J. O., S. L. Marcus, R. Hide, T. M. Eubanks, and D. H. Boggs, Angular momentum exchange among the solid Earth, atmosphere, and oceans: A case study of the 1982-1983 El Niño event, *J. Geophys. Res.*, *99*, 23,921-23,937, 1994.

Dziewonski, A. M. and D. L. Anderson, Preliminary reference Earth model, *Phys. Earth. Planet. Int.*, **25**, 297-356, 1981.

Eubanks, T. M., Variations in the orientation of the Earth, in *Contributions of Space Geodesy to Geodynamics, Geodyn. Ser.*, **24**, edited by D. E. Smith and D. L. Turcotte, pp. 1-54, AGU, Washington, D. C., 1993.

Eubanks, T. M., J. A. Steppe, J. O. Dickey, R. D. Rosen and D. A. Salstein, Causes of rapid motions of the Earth's pole, *Nature*, **334**, 115-119, 1988.

Farrell, W. E., Deformation of the Earth by surface loads, *Rev. Geophys.*, **10**, 764-797, 1972.

Feissel, M., D. Bourquard, P. Charlot, E. Eisop, N. Essaifi, J. F. Lestrade, E. F. Arias, C. Boucher, and Z. Altamimi, Earth orientation and related reference frames, in *Contributions of Space Geodesy to Geodynamics, Geodyn. Ser.*, **24**, edited by D. E. Smith and D. L. Turcotte, pp. 99-111, AGU, Washington, D. C., 1993.

Fukuda, Y., T. Sato, and Y. Aoyama, The effects of sea-surface height variations on the long-period gravity changes -Results of EOF analysis -, *Proceedings of Symposium on Studies of Ocean and Solid Earth Dynamics Using Satellite Altimetry Data*, 125-133, 1999.

Furuya, M., Y. Hamano and I. Naito, Quasi-periodic wind signal as a possible excitation of Chandler wobble, *J. Geophys. Res.*, **101**, 25537-25546, 1996.

Furuya, M., Y. Hamano and I. Naito, Importance of wind for the excitation of Chandler wobble as inferred from wobble domain analysis, *J. Phys. Earth*, **45**, 177-188, 1997.

Gibert, D., M. Holschneider, and J. L. Mouel, Wavelet analysis off the Chandler wobble, *J. Geophys. Res.*, **103**, 27069-27089, 1998.

Goodkind, J. M., The superconducting gravimeter, *Rev. Sci. Instrum.*, **70**, 4131-4152, 1999.

Gross, R. S., The influence of earthquakes on the Chandler wobble during 1977-1983, *Geophys. J. R. Astron. Soc.*, **85**, 161-177, 1986.

Gross, R. S., Correspondence between theory and observations of polar motion, *Geophys. J. Int.*, **109**, 162-170, 1992.

Gross, R. S., Combinations of Earth orientation measurements: SPACE97, COMB97, and POLE97., *J. Geod.*, **73**, 627-637, 2000.

Gross, R. S. and B. F. Chao, Excitation study of the LAGEOS-derived Chandler wobble, *J. Geophys. Res.*, **90**, 9369-9380, 1985.

Gross, R. S. and U. J. Lindqwister, Atmospheric excitation of polar motion during the GIG' 91 measurement campaign, *Geophys. Res. Lett.*, **19**, 849-852, 1992.

Hide, R. and J. O. Dickey, Earth's variable rotation, *Science*, **253**, 629-637, 1991.

Hide, R., J. O. Dickey, S. L. Marcus, R. D. Rosen, and D. A. Salstein, Atmospheric angular momentum fluctuations during 1979-1988 simulated by global circulation models, *J. Geophys. Res.*, **102**, 16423-16438, 1997.

Hinderer, J. and H. Legros, Elasto-gravitational deformation, relative gravity changes and earth dynamics, *Geophys. J.*, **97**, 481-495, 1989.

Hinderer, J., H. Legros, and D. Crossley, Global Earth dynamics and induced gravity changes, *J. Geophys. Res.*, **96**, 20257-20265, 1991.

Hinnov, L. and C. R. Wilson, An estimate of the water storage contribution to the excitation of polar motion, *Geophys. J. R. Astron. Soc.*, **88**, 437-459, 1987.

Höpfner, J., Seasonal variations in length of day and atmospheric angular momentum, *Geophys. J. Int.*, **135**, 407-437, 1998.

International Earth Rotation Service, *1998 IERS Annual Report*, 174pp., 1999.

apan Meteorological Agency, *Outline of Operational Numerical Weather Prediction at Japan Meteorological Agency*, 128 pp., Tokyo,1993.

Kalnay, E., M. Kanamitsu, R. Kistler, W. Collins, D. Deaven, L. Gandin, M. Iredell, S. Saha, G. White, J. Woollen, Y. Zhu, A. Leetmaa, R. Reynolds, M. Chelliah, W. Ebisuzaki, W.Higgins, J. Janowiak, K. C. Mo, C. Ropelewski, J. Wang, Roy Jenne and Dennis Joseph, The NCEP/NCAR 40-year reanalysis project. *Bull. Amer. Meteor. Sor.*, **77**, 437-471, 1996.

Kaminuma, K., Core drilling at Syowa station, Antarctica, *Nankyoku Shiryo (Antarct. Rec.)*, **77**, 134-143, 1983 (in Japanease with English abstract).

Kanamori, H., The energy release in great earthquakes, *J. Geophys. Res.*, **82**, 2981-2987, 1977.

King, N. E. and D. C. Agnew, How large is the retrograde annual wobble?, *Geophys. Res. Lett.*, **18**, 1735-1738, 1991.

Kuehne, J., and C. Wilson, Terrestrial water storage and polar motion, *J. Geophys. Res.*,

96, 4337-4345, 1991.

Kuehne, J., S. Johnson, and C. R. Wilson, Atmospheric excitation of nonseasonal polar motion, *J. Geophys. Res.*, **98**, 19973-19978, 1993.

Lambeck, K., *The Earth's Variable Rotation*, 449 pp., Cambridge Univ. Press, New York, 1980.

Loyer, S., J. Hinderer, and J.-P. Boy, Determination of the gravimetric factor at the Chandler period from Earth orientation data and superconducting gravimetry observations, *Geophys. J. Int.*, **136**, 1-7, 1999.

Mann, M.E., and J. Park, Spatial correlations of interdecadal variation in global surface temperatures, *Geophys. Res. Lett.*, **20**, 1055-1058, 1993.

Mann, M.E., and J.M. Lees, Robust estimation of background noise and signal detection in climatic time series, *Clim. Change*, **33**, 409-445, 1996.

Mansinha, L. and D. E. Smylie, Effects of earthquakes on the Chandler wobble and secular pole shift, *J. Geophys. Res.*, **72**, 4731-4743, 1967.

Marcus, S. L., Y. Chao, J. O. Dickey and P. Gegout, Detection and modeling of nontidal oceanic effects on Earth's Rotation Rate, *Science*, **281**, 1656-1659, 1998.

Mukai, A, T. Higashi, S. Takemoto, I. Nakagawa, and I. Naito, Accurate estimation of atmospheric effects on gravity observations made with a superconducting gravity meter at Kyoto, *Phy. Earth Planet. Inter.*, **91**, 149-159, 1995.

Mukai, A., S. Takemoto, Y. Fukuda, T. Higashi, and T. Tanaka, *Proceedings of the 8th Workshop on SG*, **8**, 1-4, 1998 (in Japanese).

Munk , W. H. and G. J. F. MacDonald, *The rotation of the Earth*, 323 pp., Cambridge Univ. Press, Cambridge, 1960.

Naito, I., N. Kikuchi and K. Yokoyama, Results of estimating the atmospheric effective angular momentum functions based on the JMA global analysis data, *Publ. Int. Latitude Obs. Mizusawa*, **20**, 1-11, 1987.

Naito, I. and N. Kikuchi, A seasonal budget of Earth's axial angular momentum, *Geophys. Res. Lett.*, **17**, 631-634, 1990.

Naito, I. and N. Kikuchi, Reply to Rosen & Salstein's comment, *Geophys. Res. Lett.*, **18**, 1927-1928, 1991.

Naito, I., Y. H. Zhou, M. Sugi, R. Kawamura, and N. Sato, Three dimensional atmospheric angular momentum simulated by the Japan Meteorological Agency model for the period of 1955-1994, *J. Met. Soc. Japan*, **78**, 111-122, 2000.

National Geophysical Data Center, ETOPO-5 bathymetry /topography data, *Data Announc. 88-MGG-02*, Natl. Oceanic and Atmos. Admin., U.S. Dep. Commer.,

Boulder, Colo., 1988.

O'Connell, R. J. and A. M. Dziewonski, Excitation of the Chandler wobble by large earthquakes, *Nature*, **262**, 259-262, 1976.

O'Conner, W. P., The 14-month wind stressed residual circulation (pole tide) in the North Sea, *NASA Tech. Memo. TM-87800*, 1986.

Park, J., C.R. Lindberg, and F.L. Vernon III, Multitaper spectral analysis of high-frequency seismograms, *J. Geophys. Res.*, **92**, 12675-12684, 1987.

Philander, S. G., *El Niño, La Niña, and Southern Oscillation*, Academic Press, New York, 1990.

Ponte, R. M. and R. D. Rosen, Oceanic angular momentum and torques in a general circulation model, *J. Phys. Oceanogr.*, **24**, 1966-1977, 1994.

Ponte, R. M., D. Stammer and J. Marshall, Oceanic signals in observed motions of the Earth's pole of rotation, *Nature*, **392**, 476-479, 1998.

Ponte, R. M. and D. Stammer, Role of ocean currents and bottom pressure variability on seasonal polar motion, *J. Geophys. Res.*, **104**, 23393-23409, 1999.

Richter, B. , *IAG Symposium a, 16 Aug. 1983 at Hamburg. Germany*, 1983.

Richter, B. , The long period elastic behavior of the Earth, *Geophys. Monograph IUGG*, **9**, Variations in Earth Rotation, edited by McCarthy, D. D. and W. E. Carter, 21-25, 1990.

Rosen, R. D., and D. A. Salstein, Contribution of stratospheric winds to annual and semiannual fluctuations in atmospheric angular momentum and the length of day, *J. Geophys. Res.*, **90**, 8033-8041, 1985.

Rosen, R. D., and D. A. Salstein, Comment on "a seasonal budget of the Earth's axial angular momentum" by Naito and Kikuchi, *Geophys. Res. Lett.*, **18**, 1925-1926, 1991.

Salstein, D. A., D. M. Kann, A. J. Miller and R. D. Rosen, The Sub-Bureau for Atmospheric Angular Momentum of the International Earth Rotation Service (IERS): A meteorological data center with geodetic applications, *Bull. Amer. Meteor. Soc.*, **74**, 67-80, 1993.

Sato, T. and H. Hanada, A program for the computation of oceanic tidal loading effects 'GOTIC', *Pub. Int. Lat. Obs. Mizusawa*, **18**, 29-47, 1984.

Sato, T., Y. Tamura, N. Kikuchi, and I. Naito, Influences of global pressure changes on gravity measurements, Proc. Natl. Astronomical Observatory Symp. on the Core of the Earth, *Central Core of the Earth*, **I**, 357-361, 1991 (in Japanese).

Sato, T., K. Shibuya, Y. Tamura, M. Kanao, M. Ooe, K. Okano, Y. Fukuda, N. Seama, K.

Nawa, K. Kaminuma, Y. Ida, M. Kumazawa, and T. Yukutake, One year observations with a superconducting gravimeter at Syowa station, Antarctica, *J. Geod. Soc. Japan*, **41**, 75-89, 1995.

Sato, T., K, Nawa, K. Shibuya, Y. Tamura, M. Ooe, K. Kaminuma, and Y. Aoyama, Polar motion effect on gravity observed with a superconducting gravimeter at Syowa station, Antarctica, *Gravity, Geoid and Marine Geodesy*, **117**, 99-106, 1997a.

Sato, T., Y. Tamura, S. Okubo, and S. Yochida, Calibration of the scale factor of superconducting gravimeter at Esashi using an absolute gravimeter FG5, *J. Geod. Soc. Japan*, **42**, 225-232, 1997b.

Sato, T., Y. Fukuda, Y. Aoyama, H. McQueen, K. Shibuya, Y. Tamura, and M. Ooe, On the observed annual gravity variation and the effect of sea surface height variations, to be submitted to *Phy. Earth Planet. Inter.*, 2000.

Smith, M. L. and F. A. Dahlen, The period and Q of the Chandler Wobble, *Geophys. J. Roy. Astron. Soc.*, **64**, 223-281, 1981.

Smith, D. E. and D. L. Turcotte (Eds.), *Contributions of Space Geodesy to Geodynamics Technology*, **25**, 213 pp., AGU, Washington, D. C., 1993.

Stammer, D., Steric and wind-induced changes in TOPEX/POSEIDON large-scale sea surface topography observations, *J. Geophys. Res.*, **102**, 20987-21009, 1997.

Tamura, Y., A harmonic development of the tide-generating Potential, *Marees Terrestres Bulletin d' Informations*, *99*, 6813-6855, 1987.

Tamura, Y., T. Sato, M. Ooe, and M. Ishiguro, A procedure for tidal analysis with a Bayesian information criterion, *Geophys. J. Int.*, **104**, 507-516, 1991.

Thomson, D. J., Spectrum estimation and harmonic analysis, *Proc. IEEE*, **70**, 1055-1096, 1982.

Trupin,A. and J. Wahr, Spectroscopic analysis of global tide gauge sea level data, *Geophys. J. Int.*, **100**, 441-453, 1990.

Tsimplis, M. N., R. A. Flather, and J. M. Vassie, The North Sea pole tide described through a tide-surge numerical model, *Geophys. Res. Lett.*, **21**, 449-452, 1994.

Wahr, J. M., The effects of the atmosphere and oceans on the Earth's wobble - I. theory, *Geophys. J. Roy. Astron. Soc.*, **70**, 349-372, 1982.

Wahr, J. M., The effects of the atmosphere and oceans on the Earth's wobble - II. results, *Geophys. J. Roy. Astron. Soc.*, **74**, 451-487, 1983.

Wahr, J. M., Deformation induced by polar motion, *J. Geophys. Res.*, **90**, 9363-9368, 1985.

Wahr, J. M., and Z. Bergen, The effect of mantle anelasticity on nutations, Earth tide, and tidal variation in rotation rate, *Geophys. J. R. Astron. Soc.*, **87**, 633-668, 1986.

Wilson, C. R., Discrete polar motion equations, *Geophys. J. Astron. Soc.*, **80**, 551-554, 1985.

Wilson, C. R. and R. A. Haubrich, Meteolorogical excitation of the Earth's wobble, *Geophys. J. R. astr. Soc.*, **46**, 707-743, 1976.

Wilson, C. R. and R. O. Vicente, Maximum likelihood estimations of polar motion parameters, in Variation in Earth Rotation, Geophysical Monograph, Vol. 59, ed. D. D. McCarthy and W. Carter, pp. 151-155, Am. Geophys. Union, Washington, D.C., 1990.

Yoder, C. F., J. G. Williams and M. E. Parke, Tidal variations of Earth rotation, *J. Geophys. Res.*, **86**, 881-889, 1981.